NASA Contractor Report 3188

Characteristics of Lightly Loaded Fan Rotor Blade Wakes

B. Reynolds and B. Lakshminarayana

GRANT NSG-3012
OCTOBER 1979

NASA

NASA Contractor Report 3188

Characteristics of Lightly Loaded Fan Rotor Blade Wakes

B. Reynolds and B. Lakshminarayana
The Pennsylvania State University
University Park, Pennsylvania

Prepared for
Lewis Research Center
under Grant NSG-3012

National Aeronautics
and Space Administration

**Scientific and Technical
Information Branch**

1979

TABLE OF CONTENTS

SUMMARY

The highly three-dimensional flow characteristics of a rotor blade wake has been investigated both theoretically and experimentally. The research presented in this report is confined to a study of a low subsonic and incompressible wake flow downstream of a lightly loaded rotor. Theoretically, the equations of motion were solved using the momentum integral technique in the far wake region. An analytical solution for the three components of mean velocity and wake width is derived from the momentum integral equations using suitable approximations. This analysis showed good agreement with experimental results in the far wake region and correctly predicted the effects of varying blade loading on the overall properties of the rotor wake. The experimental investigation included measurements of mean velocity, turbulence intensity, Reynolds stress, and static pressure variations across the rotor wake at various axial and radial locations. Wakes were measured at various rotor blade incidences to discern the effect of blade loading on the rotor wake. Mean velocity and turbulence measurements were carried out with a tri-axial hot wire probe both rotating with the rotor and stationary behind the rotor. The rotating tri-axial probe measurements reported in this investigation represent the first systematic data in the near wake region of a rotor wake using this technique. Static pressure measurements across the rotor wake were made with a conventional static pressure probe rotating with the rotor. Radial, tangential, and axial components of mean velocities and turbulence intensities were found to decay very rapidly near the rotor blade trailing edge. Increased blade loading was shown to slow the decay rates of axial and tangential mean velocity defects and radial velocities in the wake. The presence of large radial velocities

in the rotor wake indicated the extent of the interactions between one radius and another. Similarity in the profile shape was found for the axial and tangential components of mean velocity and in the outer layer for axial, tangential, and radial turbulence intensities. Appreciable static pressure variations across the rotor wake were found in the near wake region.

NOMENCLATURE

A_1, A_2, A_3	Gains for fluctuating voltages in stationary probe measurement technique (defined in Figure 9)
a_{ij}	Direction cosines defining tri-axial probe hot wire configuration (given in Table 1)
B_1, B_2	Constants in Equation (79)
B_3, B_4	Constants in Equation (80)
B_5, B_6	Constants in Equation (81)
B_c	Hot wire calibration constant in Equation (68)
C_1	Constant in Equation (54)
C_2, C_3	Constants in Equation (55)
C_4	Constant in Equation (57)
C_5	Constant in Equation (61)
c	Chord length
c_d	Section drag coefficient
D_1, D_2	Constants in Equation (83)
D_3, D_4	Constants in Equation (84)
D_5, D_6	Constants in Equation (85)
E	Voltage measured by hot wire
e	Fluctuating voltage measured by hot wire
E_1, E_2, E_3	Mean voltages measured by the tri-axial probe hot wires, 1, 2, and 3, respectively
E_k	Turbulent energy (defined in Equation (86))
E_o	Voltage at zero velocity measured by hot wire sensor
e_1, e_2, e_3	Fluctuating components of voltage measured by the tri-axial probe hot wires 1, 2, and 3, respectively
F	Similarity parameter defined in Equation (45)
f	Function defined in Equation (45)
f_1	Function defined in Equation (77)

f_2	Function defined in Equation (78)
f_3	Function defined in Equation (82)
f_k	Frequency of turbulence fluctuations
f_s	Function defined in Equation (70)
G	Similarity parameter defined in Equation (43)
g	Function defined in Equation (43)
H	Similarity parameter defined in Equation (44)
H_1	Wake shape factor (Equation (73))
h	Function defined in Equation (44)
I	Similarity parameter defined in Equation (46)
i	Incidence of inlet flow with rotor blade in relative (rotating) frame of reference
J	Similarity parameter defined in Equation (47)
K	Similarity parameter defined in Equation (48)
$K_1(r)$	Function defined in Equation (58)
$K_2(r)$	Function defined in Equation (60)
K_p	Calibration constant for spherical head static pressure probe (defined in Equation (69))
L_1	Constant in Equation (75)
$L_{L.S.}$, $L_{T.S.}$	Wake width at half the depth on the leading and trailing surface sides of the wake, respectively (defined in Figure 50)
L.S.	Leading surface of rotor blade (Figure 1)
m_1	Exponent in Equation (54)
m_2, m_3	Exponents in Equation (55)
n	Principle normal to streamwise direction (Figure 1)
n_c	Hot wire calibration constant in Equation (68)
n_s	Exponent in Equation (86)
p	Static pressure

P_o	Stagnation pressure
p_{probe}	Actual static pressure measured by spherical head static pressure probe
P^*	Reduced pressure defined by Equation (88)
$\overline{p}$	Passage averaged static pressure defined by Equation (31)
Q	Resultant velocity in the relative (rotating) frame of reference
Q_a	Resultant velocity in the absolute (stationary) frame of reference
q	Generalized parameter
R	Radius ratio (r/r_t)
R_c	Radius of curvature of the wake centerline
r	Radial distance (Figure 1)
S	Blade spacing
s	Streamwise distance (Figure 1)
s_o	Streamwise virtual origin (Equations (79), (80), (81), (83), (84), and (85))
T.S.	Trailing surface of rotor blade (Figure 1)
U	Radial mean velocity
U_n, U_r, U_s	Relative mean velocities in the normal, radial, and streamwise directions, respectively (Figure 1)
u	Radial mean velocity in the wake (Figure 1)
u'_n, u'_r, u'_s	Fluctuating components of relative velocities in the normal, radial and streamwise directions, respectively (Figure 1)
u'	Fluctuating component of radial velocity (Figure 1)
V	Relative tangential mean velocity (Figure 1)
V_c	Velocity measured in hot wire probe calibration
v	Defect in relative tangential mean velocity (Figure 1)
v'	Fluctuating component of tangential velocity (Figure 1)
W	Axial mean velocity (Figure 1)

w	Defect in axial mean velocity (Figure 1)
w'	Fluctuating component of axial velocity (Figure 1)
Y	Tangential distance from the wake centerline non-dimensionalized by blade spacing ($r\theta/S$, $\theta = 0$ at wake centerline, and Y is negative on the suction side and positive on the pressure side of the wake)
Z	Axial distance from rotor blade trailing edge non-dimensionalized by chord length of rotor blade
z	Axial distance (Figure 1)
z_o	Axial virtual origin
α	Relative streamline angle with respect to blade stagger angle
β	Angle between axial and streamwise direction
δ	Semi-wake width ($L_{L.S.} + L_{T.S.}$)
δ^*	Displacement thickness in wake (Equation (74))
η	$r\theta/L_{L.S.}$ or $r\theta/L_{T.S.}$ with $\theta = 0$ at the wake centerline
$\eta_{L.S.}$, $\eta_{T.S.}$	$r\theta/L_{L.S.}$ and $r\theta/T_{T.S.}$, respectively with $\theta = 0$ at the wake centerline
θ	Tangential distance (Figure 1)
θ^*	Momentum thickness in wake (Equation (72))
ν_T	Kinematic turbulent eddy viscosity
ρ	Density
τ_r, τ_z, τ_θ	Normalized turbulence intensities in the radial, axial, and tangential directions, respectively
	$(\sqrt{\overline{u'^2}}/W,\ \sqrt{\overline{w'^2}}/W,\ \sqrt{\overline{v'^2}}/W)$
τ_{sn}, τ_{sr}	Normalized streamwise and radial components of Reynolds stress, respectively
	$\overline{u'_s u'_n}/U_s^2$, $\overline{u'_r u'_n}/U_s^2$
ϕ	Flow coefficient ($W_1/\Omega r_{ms}$)
ψ_o	Stagnation pressure rise coefficient $[(Po_2 - Po_1)/(1/2\rho\Omega r_{ms})]$

ψ_s	Static pressure rise coefficient $[(P_2 - P_1)/(\rho Q_o^2/2)]$
Ω	Rotor speed of rotation (Figure 1)

Subscripts

a	In the absolute (stationary) frame of reference
c	At the wake centerline
d	Defect in wake velocity
e	Wake edge
L.S.	Leading surface of rotor blade
m	Maximum value in wake
ms	At mid-span of rotor
o	In free stream
T.S.	Trailing surface of rotor blade
t	At the tip
1, 2	Inlet and outlet to rotor, respectively

Superscripts

$\overline{\quad}$	Time average/passage average

Chapter 1

INTRODUCTION

1.1 Significance and Statement of the Problem

The study of the rotor or fan wakes is important for establishing improved aerodynamic design criteria, for predicting noise levels, and for determining the vibration characteristics of turbomachinery used in aircraft, naval, space, and land applications. Mixing of the rotor wake with the free stream represents a dissipation of energy and therefore a source of loss in efficiency. For these reasons, knowledge of rotor or fan wake characteristics is essential for building quieter and more efficient turbomachinery. The knowledge gained through such a study provides scientific information on the effects of rotation and curvature on the development and decay of turbulent shear flows.

A variety of parameters influence the characteristics of the rotor or fan wake. It is necessary to determine the effect of both rotor geometry and operating conditions on the wake. These two factors depend on a large number of parameters such as: radial, axial, and tangential pressure gradients, speed of rotation, lift coefficient, solidity, hub to tip ratio, blade spacing, inlet turbulence level, and distance from rotor blade trailing edge. These variables introduce many complications in the experimental and theoretical investigations of the rotor wake.

A highly three-dimensional flow, caused by centrifugal forces, Coriolis forces, and blade geometries, is characteristic of the rotor wake. This three-dimensionality introduces an additional complication to those mentioned above. These complications are evident in the typical rotor or fan wake illustrated in Figure 1. The three-dimensional nature of the flow exists in both the mean velocity and in the structure of

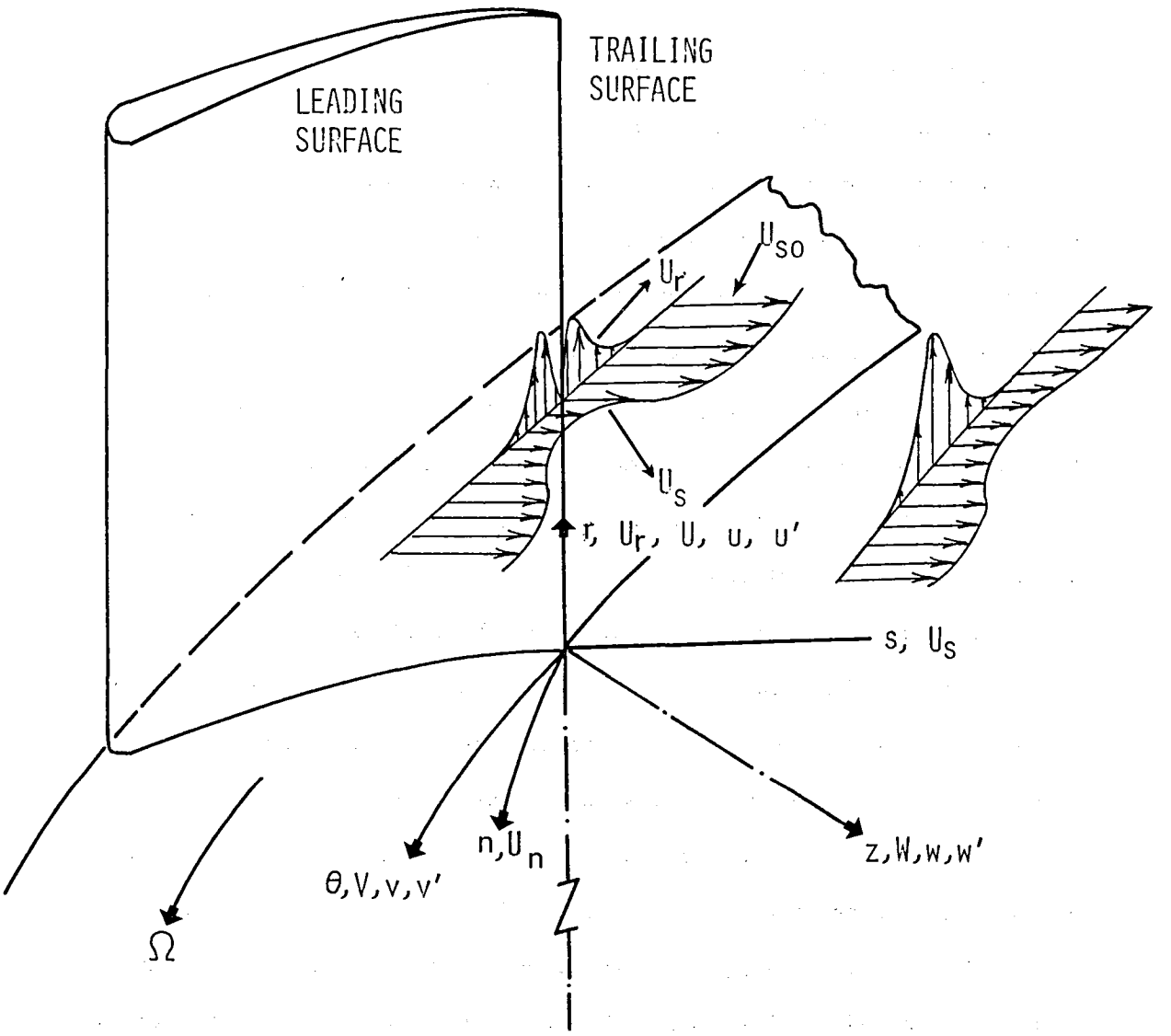

Figure 1. Characteristics of rotor wake and notations used

turbulence in the wake. Any theoretical analysis or experimental measurement technique becomes complex if it is to give accurate information of the rotor wake behavior.

It is advantageous to provide the turbomachinery aerodynamicist or acoustician with a means by which characteristics of the rotor wake may be determined. This information is essential in predicting the aerodynamic and acoustic properties of a turbomachine. The acoustician can more accurately predict the blade passing frequency and broadband noise levels and the aerodynamicist can minimize losses and optimize spacing of the rotor and stator. The information presented in this thesis is useful for obtaining a better understanding of the complex rotor wake flow.

1.2 Scope and Objective

The objective of this research was to study the properties of the rotor fan or compressor wake both theoretically and experimentally to understand the structure of the wake. This included a study of profile shape, decay characteristics, effects of rotation, and the effects of varying blade loading on the wake.

The research presented in this report is confined to a study of a low subsonic and incompressible wake flow downstream of a lightly loaded rotor. Theoretically, an analysis that could predict the gross, overall properties of the rotor wake was developed. Suitable assumptions were made to derive a solution for the three components of mean velocity and wake width in the far wake region, where wake defect is small compared to free stream velocity. Wake defect is defined as the difference between local velocity in the wake and free stream velocity. This analysis allowed the effects of varying blade loading on the three-dimensional wake characteristics to be studied. Experimentally the static pressure

and three-dimensional mean velocity and turbulence quantity (turbulence intensities and Reynolds stresses) variations across the rotor wake were measured. Measurements were made in the near and far wake regions for various downstream and spanwise locations at different rotor blade incidences. The near wake is defined as the region where wake defect is the same order of magnitude as free stream velocity. The experimental mean velocity and turbulence measurements are made using a tri-axial hot wire probe both rotating with the rotor and stationary behind the rotor. A conventional static pressure probe rotating with the rotor was used for all static pressure measurements.

This is the first attempt to measure systematically the wake of a rotor blade in the rotor frame of reference with a tri-axial hot wire probe. This is accomplished by rotating the probe at the same speed as the rotor and traversing it in the tangential direction with the aid of a specially designed traversing and control mechanism, while the rotor is in motion. This measurement technique is able to provide accurate information of the highly three-dimensional characteristics of mean velocity and turbulence in the near wake region behind the rotor.

1.3 Previous Investigations

Few experimental or theoretical investigations of the compressor or fan rotor wake have been undertaken to date. This is due to the many complexities involved in both analytical solutions of a highly turbulent, three-dimensional, and rotating flow and in experimental techniques capable of accurately measuring the characteristics of such complex rotor wake flow. The literature reviewed in this section represents the state of the art for experimental and theoretical studies of the rotor wake.

Investigations of the swirling wake or jet are also discussed due to the close similarity of this flow phenomena and rotor wake characteristics.

Of the limited number of rotor wake studies available, only a few provide any theoretical treatment of the rotor wake. Raj and Lakshminarayana (1976) and Lakshminarayana (1975) have theoretically determined the qualitative nature of the rotor wake for subsonic flow in the far wake region (far wake is approximately defined as the flow regime where the wake center streamwise mean velocity defect is an order of magnitude less than freestream mean velocity). A theoretical solution for a transonic compressor rotor is given by Chen and McCune (1975). The rotor wake is treated as a three-dimensional flow pheonomenon in all of the above theoretical studies.

Using the three-dimensional, nonlinear equations of mean motion in a streamwise orthogonal coordinate system, Raj and Lakshiminarayana (1976) developed an analytical solution valid only in the far wake. The effect of turbulence on the rotor wake is included in the analysis using the eddy viscosity concept to model stresses and assuming that the structure of the turbulent wake was homogeneous. In the far wake, the longitudinal radius of curvature was assumed to be large and constant and static pressure variations across the wake are neglected. This assumption is consistent with rotor wake measurements made in this investigation. Based on the assumption that similarity exists in the rotor wake, the resulting theoretical solution presented by Raj and Lakshminarayana (1976) indicates the dependency of the rotor wake characteristics on rotor geometry, turbulence quantities, operating conditions of the rotor, and radius of curvature of the flow. Agreement with measured quantities such as decay of mean velocities and turbulence quantities and the variation of wake width

downstream was found to be good. Additional empirical correlations were given for the decay of maximum turbulence intensity and shear stress.

Lakshminarayana (1976), using the three-dimensional equations of mean motion in cylindrical coordinates, solved for the variation of wake centerline defects in axial, tangential, and radial mean velocities and wake width downstream of the rotor. As in Raj and Lakshminarayana (1976), similarity and negligible static pressure variation in the far wake of a rotor was assumed. Neglecting turbulence effects and solving for a free-vortex design rotor, the momentum integral technique was used in order to derive a solution. Results for the analysis given by Lakshminaryana (1975) were similar to some of those of Raj and Lakshminarayana (1976); the rotor wake decays very slowly in the far wake and decay is faster than that for an isolated airfoil or cascade wake in the near wake region. Also, an interesting prediction from the theoretical solution was a variation of wake width with downstream location.

Chen and McCune (1975) solved for the flow pattern behind a transonic compressor rotor. This analysis models the rotor wake as a three-dimensional pitchwise perturbation flow. With this modeling, an inviscid, incompressible, and three-dimensional actuator disk flow theory is used to determine the outlet flow from a transonic rotor. The rotor blade row is replaced by lifting lines of bound vorticity with sheets of vorticity present downstream of the rotor. Comparison of theory and experiment for axial and pitchwise velocity variation across the wake shows reasonable agreement. It should be noted that a treatment of the transonic rotor wake as an incompressible, inviscid flow is questionable. Chen and McCune (1975) have indicated the limitations of the analysis due to that assumption.

A variety of experimental investigations of the rotor wake have been undertaken to date. Two general techniques have been used for making measurements of the rotor wake flow; placing a stationary probe behind the rotor or rotating the probe with the rotor. The former technique measures the periodic unsteadiness characteristics of the rotor wake in a stationary frame of reference while the latter technique enables the wake to be measured as a steady flow phenomenon. In order to determine accurately the rotor wake characteristics, both mean velocity and turbulence quantity variations across the wake should be determined.

Using the stationary probe technique developed by Whitfield et al. (1972), Schmidt and Okiishi (1977) and Wagner, et al. (1978) we were able to determine the three-dimensional mean velocity field behind the rotor using a single-sensor hot wire probe aligned in three coordinate directions. This experimental method did not allow the turbulent characteristics of the wake to be found. Evans (1975) made rotor wake measurements of mean velocity and turbulence quantities with a stationary x-sensor hot wire probe mounted behind the rotor. However, this procedure did not enable the large three-dimensional characteristics of the wake to be determined. Lakshiminarayana and Poncet (1974) have reported a procedure by which the three-dimensional mean velocity and turbulence quantity characteristics could be determined by mounting a tri-axial hot wire in the stationary frame (this experimental procedure has been used by Raj and Lakshminarayana (1976)). Since the technique given by Lakshminarayana and Poncet (1974) allowed measurements to be made of all desired wake flow properties, it was used for all stationary probe measurements reported in this investigation.

Rotating a probe with the rotor allows the rotor wake to be measured as a steady flow phenomenon. Klein (1974) and Gallus (1977) have traversed rotating pressure probes across the rotor wake. Their measurements allowed the stagnation pressure characteristics of the wake to be found. However, no turbulence or three-dimensional mean velocity information was determined. Gorton and Lakshiminarayana (1976) have measured the three-dimensional mean flow and turbulence variations inside an inducer passage using a tri-axial hot wire probe rotating with the blades. Using this technique, they measured mean velocity and turbulence variations across the rotor wake. For this reason, rotating probe wake measurements were made in the present investigation using the procedure given by Gorton and Lakshminarayana (1976).

The stationary and rotating probe experimental investigations described above have indicated the general characteristics peculiar to the rotor wake. The highly asymmetric nature of the rotor wake has been clearly seen in all investigations. The strong dependence of the mean velocity variation across the wake on upstream stator wake interference has been reported by Wagner et al. (1978). Evans (1975) has shown the strong effects of turbulence on rotor wake decay characteristics. Raj and Lakshminarayana (1976) measured the marked change of decay rates in mean velocity between the near and far wake flow regions. Illustrated by Lakshminarayana (1975) was the existence of similarity in axial velocity wake profiles and the turbulent characteristics of the rotor wake at varying axial locations downstream of the rotor.

In addition to the investigations discussed above, the rotor wake has also been studied by Bennett (1977), Kool, et al. (1978), Gallus (1977), Thompkins and Kerrebrock (1975), Muhlemann (1946), Muesmann

(1958), and Ufer (1968). Thompkins and Kerrebrock (1975) have made wake measurements in the stationary frame downstream of a transonic rotor using a fast response five-hole pressure probe. The wake flow measured by Thompkins and Kerrebrock (1975) was found to be very complex with large static pressure variations. Bennett (1977), using the stationary probe technique, was able to measure the far wake of a compressor rotor with a tri-axial hot film probe. Results from Bennett (1977) indicate the large three-dimensional nature of the flow. Bennett (1977) also shows larger radial velocities and a more rapid spreading of the rotor wake near the hub wall as compared to that found at mid-radius. Rotating a five hold pressure probe with the rotor Gallus (1977) has measured the marked effects of the inlet guide vane wakes through blade row interaction on the rotor wake. Gallus (1977) also indicates that a more rapid decay of the rotor wake can be expected for increased blade loading. This is consistent with results presented in the present investigation. Muesmann (1958) and Muhlemann (1946) both report the expected large asymmetric nature of the rotor wake. Muhlemann (1946) shows a strong dependence of the rotor wake on radial location with the largest mean velocity defects and wake widths near the hub and tip regions. Muhlemann (1946) also indicate a more rapid decay of the rotor wake with increased blade loading. Kool, et al. (1978), using the stationary single sensor hot wire probe measurement technique, shows the large asymmetric and three-dimensional nature of the rotor wake. While the results of Kool, et al. (1978) showed some unusual trends in rotor wake profile, this characteristic was not observed for the rotor investigated in the present investigation.

Ufer (1968) rotated a single-sensor hot wire probe to determine the blade to blade velocity distribution in the end wall region downstream

of a rotor blade row. The data due to Ufer (1968) clearly indicated a more rapid decay of the rotor wake for increased blade loading.

None of the above investigations have studied in depth the overall three-dimensional decay characteristics and changing structure of the mean velocity, turbulence, and static pressure variations across the wake downstream of the rotor blade in the near wake region. The results given by Gallus (1977), Kool, et al. (1978), Muesmann (1958), and Muhlemann (1946) do not supply information defining the turbulence characteristics of the wake. The measurements made in the present investigation and those due to Evans (1975) indicate that large turbulence levels can be expected in the rotor wake. As previously mentioned, it is essential for the theoretician and the turbomachinery aerodynamicist and acoustician to fully understand the nature of the turbulent wake if an accurate theoretical model is to be derived.

Since the swirling turbulent jet exhibits many of the characteristics seen in a rotor wake, the existence of self similarity in the former would suggest the same might be expected in the rotor wake. For the axial mean velocity in a swirling jet, Pratte and Keffer (1972) have measured self-similar profiles. The axial turbulence intensities did not become self-similar as quickly as mean velocity but did become similar far downstream from the jet origin. This indicates that the turbulence intensity profiles in the rotor wake may exhibit self similarity in the far wake region. Reynolds (1962) has also indicated that similarity exists in a swirling jet or wake in the region far downstream from the origin. Similarity of the rotor wake is an important characteristic for theoretical analysis and data correlation of the rotor wake.

The two-dimensional wake behind an isolated airfoil is representative of that found for a rotor blade without the effects of adjacent blades, rotation, the hub and end walls, and any stator or inlet guide vane wakes transported through the rotor blade row. For this reason, the rotor wake exhibits many of the same characteristics found for isolated airfoil or flat plate wakes. Airfoil wakes measured by Preston, et al. (1943), Preston, et al. (1945), Mendelsohn (1947), Silverstein, et al. (1939a), and Hah (1978) have all shown, as expected, that the streamwise mean velocity profile on the suction side of the wake is thicker than that on the pressure side. The above investigations have all reported a faster decay of streamwise mean velocity defect for increasing incidence. The rotor wake measurements in the present investigation have exhibited these same characterstics.

Only Hah (1978), using an x-sensor hot wire probe, has measured the turbulent characteristics of the airfoil wake. These results seem to show a rapid decay of the turbulence intensities and Reynolds stresses in the isolated airfoil wake in the near wake region. However, this decay was less rapid than that found for the mean velocities. Since the profile shape of the isolated airfoil investigated by Hah (1978) was identical to the rotor blade sections in the present investigation, these airfoil measurements have been compared to rotor wake measurements (reported in Chapter 5). The differences found result from the larger number of parameters controlling the rotor wake than for the corresponding isolated airfoil wake.

Silverstein, et al. (1939a) and Silverstein, et al. (1939b) have shown a good correlation of wake width and total velocity defect measurements using the drag coefficient. This correlation has been

examined in the present investigation for other airfoil data and seems to work well (reported in Chapter 5). Due to the similarities between the isolated airfoil, cascade, and rotor wakes, the correlation of Silverstein, et al. (1939a) and Silverstein, et al. (1939b) have also been used to study cascade and rotor wake data (reported in Chapter 5).

In addition to the literature reviewed above, Raj and Lakshminarayana (1975) have given a review of laminar wakes as well as some of the earlier work on the rotor wake. Ravindranath (1978) has reviewed cascade, inlet guide vane, and stator wakes.

Chapter 2

MOMENTUM INTEGRAL SOLUTION OF THE ROTOR WAKE

It is useful to have a theoretical analysis of the rotor wake which can predict the gross, overall properties of the wake flow. The analysis presented below is based on the momentum integral technique which has been commonly used in boundary layer theory. For the rotor wake, the equations of motion in a rotating cylindrical coordinate system were integrated across the wake. A set of four ordinary differential equations results. A solution of these equations gives the decay characteristics of semi-wake width, maximum radial velocities in the wake, and axial and tangential velocity defects at the wake centerline.

The following analysis modifies that given by Lakshminarayana (1976) in order to include the effects of turbulence, blade loading, shear stress, and static pressure on the rotor wake. Each of these effects is important in controlling the characteristics of the rotor wake.

2.1 Assumption and Simplification of the Equations of Motion

The equations of motion in cylindrical coordinates are given below for r, θ, and z, respectively (see Figure 1 for the coordinate system).

$$\frac{V}{r}\frac{\partial U}{\partial \theta} + U\frac{\partial U}{\partial r} + W\frac{\partial U}{\partial z} - \frac{1}{r}(V+\Omega r)^2 = -\frac{1}{\rho}\frac{\partial p}{\partial r} - \frac{\partial \overline{u'^2}}{\partial r} - \frac{\overline{u'^2}}{r} + \frac{\overline{v'^2}}{r} - \frac{\partial \overline{(u'v')}}{r\partial\theta} - \frac{\partial \overline{(u'w')}}{\partial z}, \qquad (1)$$

$$\frac{V}{r}\frac{\partial V}{\partial \theta} + U\frac{\partial V}{\partial r} + W\frac{\partial V}{\partial z} + \frac{UV}{r} + 2\Omega U = -\frac{1}{\rho r}\frac{\partial p}{\partial \theta} - \frac{1}{r}\frac{\partial \overline{(v'^2)}}{\partial \theta} - \frac{2\overline{(u'v')}}{r} - \frac{\partial \overline{(u'v')}}{\partial r} - \frac{\partial \overline{(v'w')}}{\partial z}, \qquad (2)$$

$$\frac{V}{r}\frac{\partial W}{\partial \theta}+U\frac{\partial W}{\partial r}+W\frac{\partial V}{\partial z}=-\frac{1}{\rho}\frac{\partial p}{\partial z}-\frac{\partial(\overline{w'^2})}{\partial z}-\frac{\partial(\overline{u'w'})}{\partial r}-\frac{(\overline{u'w'})}{r}-\frac{1}{r}\frac{\partial(\overline{v'w'})}{\partial \theta}\ , \qquad (3)$$

and continuity,

$$\frac{\partial V}{r\partial \theta}+\frac{\partial W}{\partial z}+\frac{\partial U}{\partial r}+\frac{U}{r}=0\ . \qquad (4)$$

In Equations (1) - (4) the wake flow is assumed to be steady relative to the rotor frame of reference and to be turbulent with negligible laminar stresses.

To integrate Equations (1) - (4) across the wake, the following assumptions are made.

1. The velocities V_o and W_o are large compared to the velocity defects u and w. In equation form this assumption is written as,

$$V = V_o(r) - v(\theta,z) \quad (V_o >> v) \qquad (5)$$

and

$$W = W_o(r) - w(\theta,z) \quad (w_o >> w)\ . \qquad (6)$$

2. The wake-edge radial velocity, U_o, is zero (no radial flows exist outside the wake). This assumption is based on mean velocity measurements made in the far wake region at rotor blade incidences of 10° and 15°, where radial velocities are found to be nearly zero in the free stream (reported in Section 5.3.3). Therefore, a free vortex flow exists in the free stream in the far wake region. This assumption is written as,

$$U = u(\theta,z) \quad (U_o = 0)\ . \qquad (7)$$

3. The static pressure varies as,

$$p = p(r,\theta,z)\ .$$

4. Similarity exists in the rotor wake mean velocity profiles.

5. Radial gradients of turbulence intensity are negligible.

Substituting Equations (5) - (7) into Equations (1) - (4) one finds,

$$\frac{V_o}{r}\frac{\partial u}{\partial \theta} + W_o \frac{\partial u}{\partial z} - \frac{1}{r}(V_o + \Omega r)^2 - \frac{1}{r}(-2vV_o - 2v\Omega r) = -\frac{1}{\rho}\frac{\partial p}{\partial r} - \frac{\overline{u'^2}}{r} + \frac{\overline{v'^2}}{r} - \frac{\partial(\overline{u'v'})}{r\partial\theta} - \frac{\partial(\overline{u'w'})}{\partial z} \quad , \tag{8}$$

$$-\frac{V_o}{r}\frac{\partial v}{\partial \theta} + u\frac{\partial V_o}{\partial r} - W_o\frac{\partial v}{\partial z} + 2\Omega u + \frac{uV_o}{r} = -\frac{1}{\rho}\frac{\partial p}{r\partial\theta} - \frac{1}{r}\frac{\partial(\overline{v'^2})}{\partial\theta} - \frac{2(\overline{u'v'})}{r} - \frac{(\overline{u'v'})}{\partial r} - \frac{(\overline{v'w'})}{\partial z} \quad , \tag{9}$$

$$-\frac{V_o}{r}\frac{\partial w}{\partial \theta} + u\frac{\partial W_o}{\partial r} - W_o\frac{\partial w}{\partial z} = -\frac{1}{\rho}\frac{\partial p}{\partial z} - \frac{\partial(\overline{w'^2})}{\partial z} - \frac{\partial(\overline{u'w'})}{\partial r} - \frac{\partial(\overline{u'w'})}{r} - \frac{1}{r}\frac{\partial(\overline{v'w'})}{\partial\theta} \quad , \tag{10}$$

and

$$-\frac{1}{r}\frac{\partial v}{\partial\theta} - \frac{\partial w}{\partial z} + \frac{u}{r} = 0 \quad . \tag{11}$$

2.2 Momentum Integral Equations

Integrations across the wake of the inertial terms in Equation (8) - (11) are given by Lakshminarayana (1976). The integrations of the turbulence intensity terms, shear stress terms, and static pressure terms are given below.

Integration of any quantity q across the wake is given as (Lakshminarayana, 1976),

$$\int_{\theta_c}^{\theta_o} \frac{\partial q}{\partial \theta}\, d\theta = -q_c \tag{12}$$

and

$$\int_{\theta_c}^{\theta_o} \frac{\partial(q(z,\theta))}{\partial z}\, d\theta = \frac{d}{dz}\left[\int_{\theta_c}^{\theta_o} q(z,\theta)d\theta\right] + q_c \frac{\partial \theta_c}{\partial z} - q_o \frac{\partial \theta_o}{\partial z} \quad . \tag{13}$$

If similarity in the rotor wake exists,

$$q = q_c(z)q(\eta) \quad . \tag{14}$$

Using Equation (14), one can write Equation (13) as,

$$\int_{\theta_c}^{\theta_o} \frac{\partial(q(z,\theta))}{\partial z}\, d\theta = \frac{d(q_c\delta)}{rdz} \int_o^1 q(\eta)d\eta + \frac{q_c}{r}\left(\frac{V_o - v_c}{W_o - w_c}\right) \quad . \tag{15}$$

From Equation (13) one also knows that,

$$\int_{\theta_c}^{\theta_o} q d\theta = \frac{\delta q_c}{r} \int_o^1 q(\eta)d\eta \quad . \tag{16}$$

Using Equations (12), (15), and (16), one integrates the turbulence intensity terms in Equations (8) - (10) across the wake by assuming similarity in their profile shapes. These integrations are given as follows:

$$\int_{\theta_c}^{\theta_o} \left(-\frac{\overline{u'^2}}{r} + \frac{\overline{v'^2}}{r}\right)d\theta = -\frac{\delta \overline{u_c'^2}}{r^2} \int_o^1 \overline{u'^2}(\eta)d\eta + \frac{\delta \overline{v_c'^2}}{r^2} \int_o^1 \overline{v'^2}(\eta)d\eta \quad , \tag{17}$$

$$\int_{\theta_c}^{\theta_o} \left(-\frac{\partial(\overline{v'^2})}{r\partial\theta}\right)d\theta = -\frac{\overline{v_c'^2}}{r} \quad , \tag{18}$$

and

$$\int_{\theta_c}^{\theta_o} \left(-\frac{\partial(\overline{w'^2})}{\partial z}\right)d\theta = -\frac{d(\overline{w_c'^2}\delta)}{rdz} \int_o^1 \overline{w_c'^2}(\eta)d\eta - \frac{\overline{w_c'^2}}{r}\left(\frac{V_o - v_c}{W_o - w_c}\right) \quad . \tag{19}$$

The shear stress terms in Equation (8) are integrated across the wake as follows. First, it is known that,

$$\int_{\theta_c}^{\theta_o} \frac{\partial(\overline{u'w'})}{r\partial\theta}\, d\theta = \int_{\theta_c}^{\theta_o} \frac{\partial(\overline{u'v'})}{r\partial\theta}\, d\theta = 0 \tag{20}$$

since correlations are zero outside the wake as well as at the centerline of the wake. The remaining shear stress terms in Equation (8) are evaluated using the eddy viscosity concept,

$$\overline{u'w'} = -\nu_T\left(\frac{\partial u}{\partial z} + \frac{\partial w}{\partial r}\right) \quad . \tag{21}$$

Neglecting radial gradients one gets,

$$\overline{u'w'} = -\nu_T\left(\frac{\partial u}{\partial z}\right) \quad . \tag{22}$$

Hence, it is known that,

$$-\frac{d}{dz}\int_{\theta_c}^{\theta_o}(\overline{u'w'})d\theta = \nu_T\frac{d}{dz}\int_{\theta_c}^{\theta_o}\frac{\partial u}{\partial z}\,d\theta \quad . \tag{23}$$

Using Equation (13) and Equation (23), we have,

$$-\int_{\theta_c}^{\theta_o}\frac{\partial}{\partial z}(\overline{u'w'})d\theta = \nu_T\frac{\partial}{\partial z}\left[\frac{d}{dz}\int_{\theta_c}^{\theta_o} u\,d\theta + u_m\frac{\partial\theta_c}{\partial z}\right] \tag{24}$$

$$= \nu_T\frac{\partial}{\partial z}\left[\frac{H}{r}\frac{d}{dz}(\delta u_m) + \frac{u_m}{r}\left(\frac{V_o - v_c}{W_o - w_c}\right)\right] \tag{25}$$

$$= \nu_T\frac{H}{r}\frac{d^2}{dz^2}(\delta u_m) - \frac{\nu_T}{r}\frac{d}{dz}\left[\frac{V_o u_m}{W_o}\right.$$

$$\left. -\frac{v_c u_m}{W_o} + \frac{V_o w_c u_m}{W_o^2}\right] \quad . \tag{26}$$

Neglecting second order terms in Equation (26) one finds,

$$-\int_{\theta_c}^{\theta_o}\frac{\partial}{\partial z}(\overline{u'w'})d\theta = \frac{\nu_T}{r}\left[H\frac{d^2}{dz^2}(\delta u_m) + \frac{V_o}{W_o}\frac{d(u_m)}{dz}\right] \tag{27}$$

where H is defined in Equation (44). Using a similar procedure the shear stress term in the tangential momentum equation can be proved to be,

$$\int_{\theta_c}^{\theta_o}\frac{\partial}{\partial z}(v'w')d\theta = -\frac{\nu_T}{r}\left[G\frac{d^2}{dz^2}(\delta v_c) + \frac{V_o}{w_o}\frac{d(v_c)}{dz}\right] \tag{28}$$

where G is defined in Equation (43). The radial gradients of shear stress are assumed to be negligible.

The static pressure terms in Equation (8) - (10) are integrated across the wake in the following manner. For Equation (9) one gets,

$$\int_{\theta_c}^{\theta_o} \frac{1}{r} \frac{\partial p}{\partial \theta} d\theta = \frac{1}{r}(p_e - p_c) \quad . \tag{29}$$

Integration of the pressure term in Equation (8) is given as,

$$\int_{\theta_c}^{\theta_o} \frac{\partial p}{\partial r} d\theta = \frac{\partial[\bar{p}(\delta/r)]}{\partial r} + p_c \frac{\partial \theta_c}{\partial r} - p_e \frac{\partial \theta_o}{\partial r} \tag{30}$$

where passage averaged static pressure is defined as,

$$\bar{p} = \frac{\delta}{r} \int_o^1 p d\eta \quad . \tag{31}$$

It is known that,

$$r(\theta_c - \theta_o) = -\delta \quad . \tag{32}$$

Differentiating Equation (32) one finds,

$$r \frac{\partial \theta_o}{\partial r} = -\frac{\delta}{r} + \frac{\partial \delta}{\partial r} + r \frac{\partial \theta_c}{\partial r} \quad . \tag{33}$$

Substituting Equation (33) into Equation (30) one gets,

$$\int_{\theta_c}^{\theta_o} \frac{\partial p}{\partial r} d\theta = \frac{\partial(\bar{p}\delta/r)}{\partial r} + (p_c - p_e)\frac{\partial \theta_c}{\partial r} - p_e\left(-\frac{\delta}{r^2} + \frac{\partial \delta}{r \partial r}\right) \quad . \tag{34}$$

Integration of the static pressure term in Equation (10) is given as,

$$\int_{\theta_c}^{\theta_o} \frac{\partial p}{\partial z} d\theta = \frac{\partial(\bar{p}\delta/r)}{\partial z} + p_c \frac{\partial \theta_c}{\partial z} - p_e \frac{\partial \theta_o}{\partial z} \tag{35}$$

where

$$\frac{\partial \theta_c}{\partial z} = \frac{1}{r}\left(\frac{V}{W}\right)_c = \frac{1}{r}\left(\frac{V_o - v_c}{W_o - w_c}\right) \tag{36}$$

and

$$\frac{\partial \theta_o}{\partial z} = \frac{\partial \theta_c}{\partial z} + \frac{1}{r}\frac{\partial \delta}{\partial z} \quad . \tag{37}$$

Substituting Equations (36) and (37) into Equation (35) one gets,

$$\int_{\theta_c}^{\theta_o} \frac{\partial p}{\partial z}\, d\theta = \frac{\partial(\bar{p}\delta/r)}{\partial z} + \frac{p_c}{r}\left(\frac{V_o - v_c}{W_o - w_c}\right) - p_e\left[\frac{1}{r}\left(\frac{V_o - v_c}{W_o - w_c}\right) + \frac{1}{r}\frac{\partial \delta}{\partial z}\right] \quad . \tag{38}$$

Using Equations (12), (15), and (16) one can integrate the remaining terms in Equations (8) - (11) across the wake (Lakshminarayana (1976)), The radial, tangential, and axial momentum equations are now written as follows:

$$\frac{H}{r} S \frac{d(u_m \delta)}{dz} - \frac{(V_o + \Omega r)^2 \delta S}{r^2 W_o^2} + \frac{2\delta G (V_o + \Omega r) v_c S}{W_o r^2}$$

$$= -\frac{1}{\rho}\frac{\partial(\bar{p}\delta/r)}{\partial r}\frac{S}{W_o^2} - \frac{1}{\rho W_o^2} S \frac{\partial \theta_c}{\partial r}(p_c - p_e) + \frac{S p_e}{W_o^2}\left(\frac{-\delta}{r^2} + \frac{d\delta}{r dr}\right)$$

$$- \frac{S\delta}{W_o^2 r^2}\overline{u_c'^2}\, I + \frac{S\delta}{W_o^2 r^2}\overline{v_c'^2}\, J + \frac{S\nu_T}{W_o r}\left[H \frac{d^2}{dz^2}(\delta u_m) + \frac{V_o}{W_o}\frac{du_m}{dz}\right] , \tag{39}$$

$$S \frac{\delta u_m}{W_o r}\left[H \frac{dV_o}{dr} + \frac{V_o}{r} + 2\Omega\right] - \frac{GS}{r}\frac{d}{dz}(v_c \delta) = -\frac{S}{W_o^2}\frac{\overline{v_c'^2}}{r} - \frac{1}{r W_o^2 \rho} S(p_e - p_c)$$

$$- \frac{S\nu_T}{W_o r}\left[G \frac{d^2}{dz^2}(\delta v_c) + \frac{V_o}{W_o}\frac{dv_c}{dz}\right] , \tag{40}$$

$$\frac{dW_o}{dr} S \frac{\delta u_m H}{W_o r} - \frac{S}{r}\frac{d(w_c \delta)}{dz} F = -\frac{S}{W_o^2}\frac{d(\overline{w_c'^2}\delta)}{r dz} K - \frac{1}{W_o^2 \rho} S \frac{\partial(\bar{p}\delta/r)}{\partial z}$$

$$+ \frac{1}{\rho r} S(p_c - p_e)\frac{V_o}{W_o^3} + \frac{p_e S}{W_o^2 r}\frac{d\delta}{dz} - \frac{S\overline{w_c'^2}}{r}\frac{V_o}{W_o} \quad , \tag{41}$$

and continuity becomes,

$$\frac{Sv_c}{r} - \frac{SF}{r}\frac{d(\delta w_c)}{dz} + \frac{S\delta u_m H}{r^2} - \frac{Sw_c V_o}{rW_o} = 0 \qquad (42)$$

where w_c, v_c, and u_m are nondimensional and from Lakshminarayana (1975),

$$G = \int_o^1 g(\eta)d\eta \ , \quad \frac{v}{v_c(z)W_o} = g(\eta) \ , \qquad (43)$$

$$H = \int_o^1 h(\eta)d\eta \ , \quad \frac{u}{u_m(z)W_o} = h(\eta) \ , \qquad (44)$$

and

$$F = \int_o^1 f(\eta)d\eta \ , \quad \frac{w}{w_c(z)W_o} = f(\eta) \ . \qquad (45)$$

In addition to the functions of wake profile F, G, and H defined by Lakshminarayana (1976), the following functions have been used in Equation (39) and (41):

$$I = \int_o^1 \frac{\overline{u'^2}(\eta)}{\overline{u_c'^2}} d\eta \ , \qquad (46)$$

$$J = \int_o^1 \frac{\overline{v'^2}(\eta)}{\overline{u_c'^2}} d\eta \ , \qquad (47)$$

and

$$K = \int_o^1 \frac{\overline{w'^2}(\eta)}{\overline{w_c'^2}} d\eta \ . \qquad (48)$$

2.3 Method of Solution

Equations (39), (40), (41), and (42) provide a set of four equations (continuity and r, θ, and z momentum) which can be employed in solving for the unknowns δ, u_m, v_c, and w_c. From wake measurements made in this investigation behind a lightly loaded rotor, turbulence intensity terms, shear stress terms, and static pressure variations across the wake are

found to have only a second order effect in the far wake region. Neglecting these terms in Equations (39), (40), and (41) one finds,

$$\frac{H}{r} S \frac{d(u_m \delta)}{dz} + \frac{2SG(V_o + \Omega r)v_c \delta}{W_o r^2} \equiv 0 \tag{49}$$

$$GS \frac{d(v_c \delta)}{dz} = \frac{SH\delta u_m}{W_o r}\left[\frac{dV_o}{dr} + \frac{V_o}{r} + 2\Omega\right] , \tag{50}$$

and

$$\frac{SF}{r} \frac{d(w_c \delta)}{dz} = \frac{dW_o}{dr} S \frac{\delta u_m H}{W_o r} , \tag{51}$$

where radial gradients of static pressure are controlled by external pressure gradients. Equations (49), (50), (51), and (42) can now be employed to derive an analytical solution for δ, u_m, v_c, and w_c.

First, Equation (51) is rearranged to give,

$$\delta u_m = \frac{F}{H} \frac{d(w_c \delta)}{dz} \frac{W_o}{dW_o/dr} . \tag{52}$$

Substituting Equation (52) into Equation (50) one gets,

$$GS \frac{d(v_c \delta)}{dz} = \frac{SF}{r} \frac{1}{dW_o/dr}\left[\frac{dV_o}{dr} + \frac{V_o}{r} + 2\Omega\right]\frac{d(w_c \delta)}{dz} . \tag{53}$$

A solution using the functional dependence,

$$w_c \delta = C_1 z^{m1} \tag{54}$$

had been assumed for an analytical solution for δ, u_m, v_c, and w_c. However, the relation given by Equation (54) did not provide any meaningful results in a three-dimensional solution where u_m is finite. Therefore, a functional dependence of the form,

$$w_c = C_2 z^{m2} + C_3 z^{m3} \tag{55}$$

is assumed for the axial component of the mean velocity defect. This function dependence has shown good agreement with the near and far wake data reported later. Furthermore, since the momentum integral solution is only valid in the far wake region, experimental measurements indicate that $C_3 = 0.0$ and Equation (55) is written as,

$$w_c = C_2 z^{m_2} \quad . \tag{56}$$

Using Equation (56) and Equation (53), one finds that the following relationship can be derived,

$$v_c = K_1(r) C_2 z^{m_2} + C_4/\delta \tag{57}$$

where

$$K_1(r) = \frac{F}{G}\left[\frac{dV_o}{dr} + \frac{V_o}{r} + 2\Omega\right]\frac{1}{r(dW_o/dr)} \quad , \tag{58}$$

and C_4 is a constant of integration. The constant C_4 will be zero if the curvature of the wake centerline is zero. Substitution of Equation (51) and elimination of v_c and w_c in Equation (42) gives,

$$\frac{d\delta}{dz} + \delta m_2 z^{-1} + \frac{1}{F}\frac{C_4}{C_2} K_2(r) \frac{z^{-m_2}}{\delta} = \frac{K_2(r)}{F}\left[\frac{V_o}{W_o} - K_1(r)\right] \tag{59}$$

where

$$K_2(r) = \left[\frac{W_o}{r dW_o/dr} - 1\right]^{-1} \quad . \tag{60}$$

From wake measurements made behind the lightly rotor studied in this investigation the radius of curvature of the wake centerline can be expected to be negligibly small in the far wake region (reported later). Hence, the constant C_4 is assumed equal to zero and the solution of Equation (59) is given as

$$\delta = \frac{K_2(r)}{F(m_2 + 1)}\left[\frac{V_o}{W_o} - K_1(r)\right] z + C_5 z^{-m_2} \tag{61}$$

where C_5 is a constant of integration. One finds that Equation (57) can now be written as

$$v_c = K_1(r)C_2 z^{m2} \quad . \tag{62}$$

Substituting Equations (56) and (61) into Equation (52) gives the solution for u_m as

$$u_m = z^{m2} \frac{K_2(r)}{H} \frac{W_o}{dW_o/dr}\left[\frac{V_o}{W_o} - K_1(r)\right] \cdot \left\{\frac{K_2(r)}{F(m_2+1)}\left[\frac{V_o}{W_o} - K_1(r)\right]z + C_5 z^{-m2}\right\}^{-1} \quad . \tag{63}$$

Equations (56), (61), (62), and (63) provide analytic solutions for the dependent variables w_c, δ, v_c, and u_m, respectively. Inclusive with the boundary conditions, the solutions must include a virtual origin. This requires that z be replaced by $z + z_o$, where z_o represents the virtual or apparent origin. Equations (56), (61), (62), and (63) are therefore written as follows:

$$w_c = C_2(z + z_o)^{m2} \quad , \tag{64}$$

$$\delta = \frac{K_2(r)}{F(m_2+1)}\left[\frac{V_o}{W_o} - K_1(r)\right](z + z_o) + C_5(z + z_o)^{-m2} \quad , \tag{65}$$

and

$$v_c = K_1(r)C_2(z + z_o)^{m2} \quad , \tag{66}$$

$$u_m = (z + z_o)^{m2} \frac{K_2(r)}{H} \frac{W_o}{dW_o/dr}\left[\frac{V_o}{W_o} - K_1(r)\right] \cdot \left\{\frac{K_2(r)}{F(m_2+1)}\left[\frac{V_o}{W_o} - K_1(r)\right](z + z_o) + C_5(z + z_o)^{-m2}\right\}^{-1} \quad . \tag{67}$$

It should be noted that since a functional dependence for w_c on z was assumed (Equation (55)) only the axial and tangential momentum equations and the continuity equation are used to derive solutions for v_c, δ, and u_m.

Lakshminarayna (1976) and Raj and Lakshminarayana (1976) have derived solutions for the gross, overall properties of the far wake of a rotor operating with zero blade loading. Lakshminarayana (1976) has given polynomial expressions for the decays in the initial far wake region for axial and tangential velocity defects at the wake center and maximum radial velocities in the wake. For axial and tangential velocity defects these solutions are of the same form as that given by Equations (64) and (66). However, the solution given by Equation (67) shows a more complex behavior of maximum radial velocity in the wake with the inclusion of blade loading than that given by Lakshminarayana (1976). For the region far downstream from the rotor Lakshminarayana (1976) derives an exponential decay rate for axial and tangential mean velocity defects at the wake center and maximum radial velocity in the wake. An exponential functional dependence with downstream distance was also found by Raj and Lakshminarayana (1976) for the far wake decay of defect in total relative velocity at the wake center and maximum radial velocities in the wake. An exponential decay rate is not given in the present investigation for any of the solutions.

Lakshminarayana (1976) and Raj and Lakshminarayana (1976) have given polynomial expressions for the increase in semi-wake width downstream of the rotor in the far wake region. These expressions are of the same form as that given by Equation (65) with the first term on the right hand side removed. The first term on the right hand side shows the additional effects of blade loading on wake width as compared to that given by Lakshminaryana (1976) and Raj and Lakshminarayana (1976) for the zero blade loading case.

Chapter 3

EXPERIMENTAL EQUIPMENT AND PROCEDURE

Two measurement techniques were employed to determine experimentally the variation of mean velocity and turbulence quantities across the rotor wake. By rotating a tri-axial hot wire probe with the rotor, wake measurements were made in the relative or rotating frame of reference using the technique developed by Gorton and Lakshminarayana (1976). This technique used a rotating traverse gear, described in Section 3.3.1, which allowed the probe to be traversed across the rotor wake measuring it as a steady flow. Mean velocity and turbulence quantity variations across the rotor wake were also measured in the stationary frame of reference using the technique developed by Lakshminarayana and Poncet (1974) and modified by Raj and Lakshminarayana (1976). The periodic, unsteady flow sensed by a stationary probe could be recorded due to the fast response of the tri-axial hot wire probe used in this investigation. Ensemble averaging of the recorded periodic flow enabled the desired measurement quantities to be determined. Together, the rotating and stationary tri-axial probe experimental programs provided the rotor wake characteristics in the near and far wake regions.

3.1 Description of the Facility

The Axial Flow Research Fan Facility at the Applied Research Laboratory of The Pennsylvania State University was used for all rotor wake measurements made in this investigation. The facility is schematically illustrated in Figure 2. All measurements were made downstream of the rotor test blades. At a fixed rotor speed of rotation, operating conditions were varied by changing the operating conditions of the

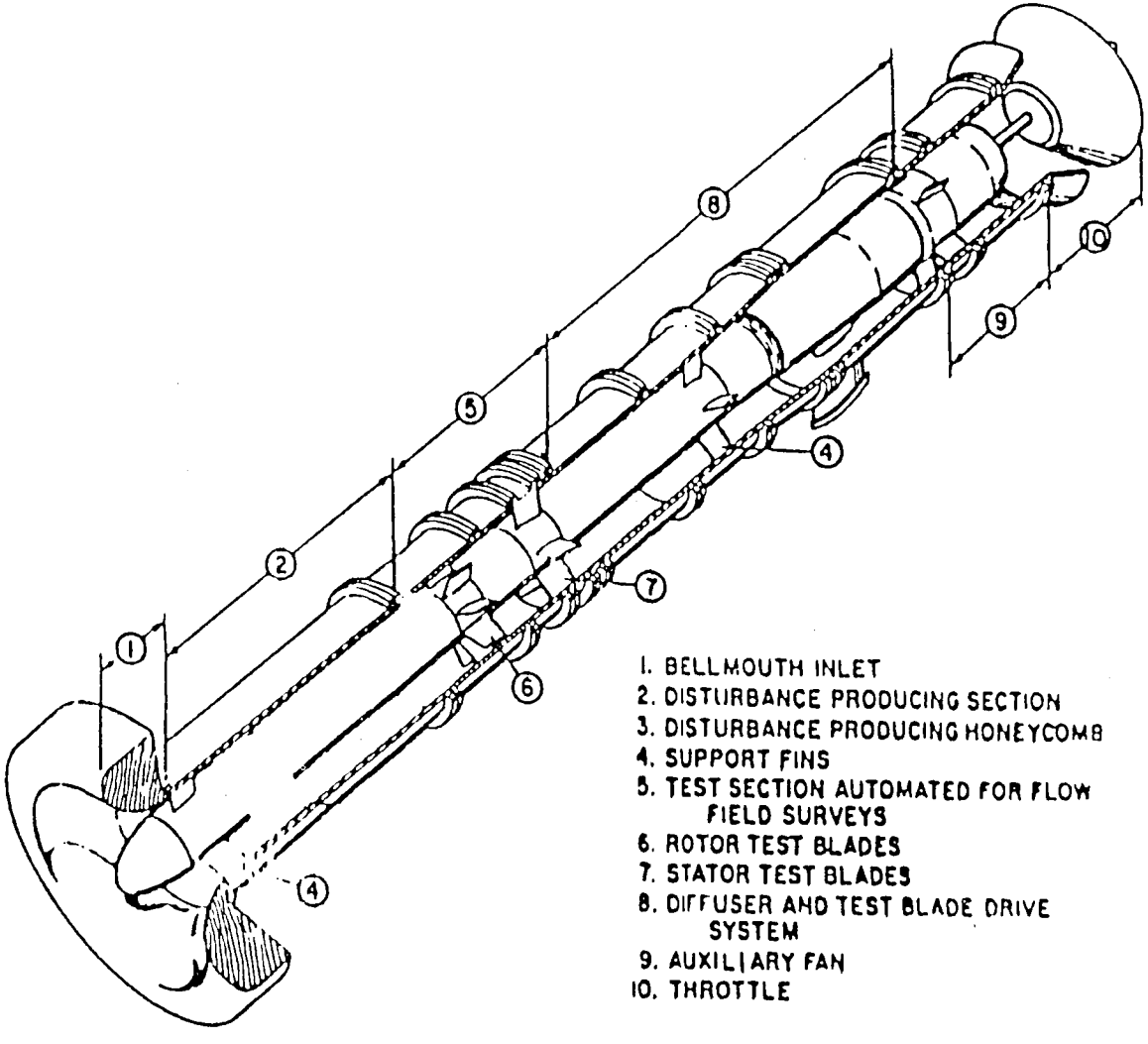

Figure 2. Axial Flow Research Fan Facility of the Applied Research Laboratory

auxiliary fan in the facility. To remove foreign particles from the flow measured by the tri-axial hot wire probe, a large dust screen was placed around the bellmouth inlet (not illustrated in the figure).

The Axial Flow Research Fan has the following physical dimensions and specifications:

Overall length = 5.99 meters

Inner cylindrical casing diameter = 0.546 meters

Hub diameter = 0.241 meters

Rotor motor power (enclosed in hub) = 749.0 Kg.-calories/min.

Rotor revolutions per minute or cycles per second are measured by a photocell attached to the rotor shaft. A detailed description of the facility is given by Bruce (1974).

A twelve-bladed uncambered rotor was used for all wake measurements made in this investigation. The rotor blade row is installed at location number six in Figure 2. Each rotor blade section was a British C1 profile with the rotor designed as a free vortex type. The twelve-bladed rotor has the following specifications:

Tip diameter = 54.6 cm

Hub diameter = 24.1 cm

Blade chord = 15.2 cm

Tip clearance = 0.64 cm

s/c (mid-span) = 0.68

Stagger angle (mid-span) = 45.0°.

The stator blades were removed when the rotor was installed for this investigation. Operating conditions used were:

Rotor speed of rotation = 1010 rpm

Incidence at mid span = 0°, 5°, 10°, 15°.

The location on the stagnation pressure rise coefficient, ψ_{s_o}, vs. flow coefficient, ϕ, is given in Figure 3 for each of the rotor blade incidences tested. Detailed blade element performance data for this rotor is given by Bruce (1974).

3.2 Description of the Probes

A tri-axial hot wire probe was used for all velocity measurements made in this investigation. The probe could accurately measure the three-dimensional mean velocity and turbulence characteristics of the rotor wake when used in either the rotating or stationary probe experimental programs. The probe (manufactured by Disa Electronics) is shown in Figure 4. Direction cosines for each wire were measured with respect to the probe coordinate system in the figure. These direction cosines are given in Table 1. Each wire was made from tungston and had a length/diameter ratio of 300.

A typical set of calibration curves for the tri-axial probe are shown in Figure 5. The relationship between voltage and velocity for each hot wire is given by King's law,

$$E^2 - E_o^2 = B_c V^{n_c} \tag{68}$$

where B_c and n_c are determined for each calibration curve. Resistance of each wire was between 4.5 and 6.0 ohms and the resistance of each probe lead was 1.0 ohm. Variations in the calibration curve due to wire aging and ambient temperature changes were found by measuring voltage at zero velocity, E_o, at the beginning and end of each experiment. Errors in addition to E_o variation are discussed by Anand (1976). Rotation of the probe has negligible effect on the heat transfer properties of the hot wires as given by Hah and Lakshminarayana (1978).

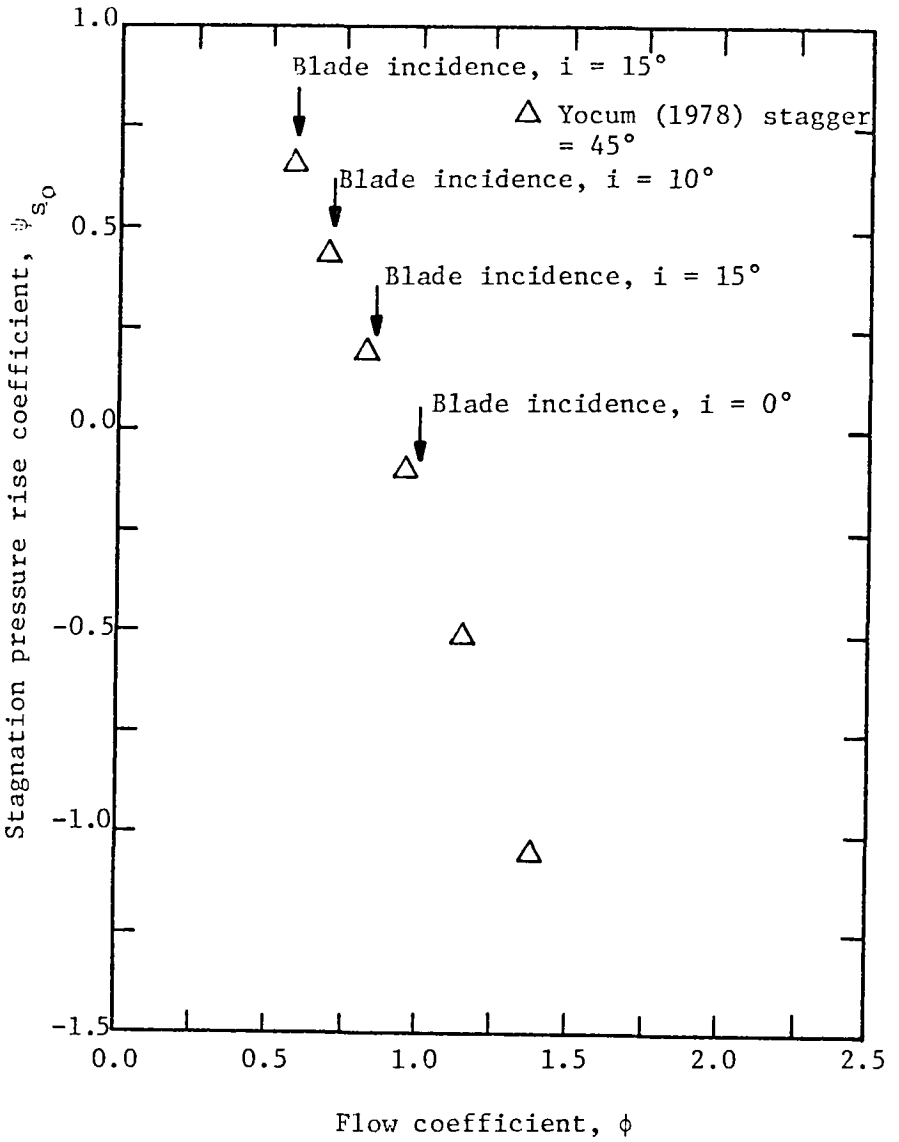

Figure 3. Twelve bladed rotor performance measurements at midradius

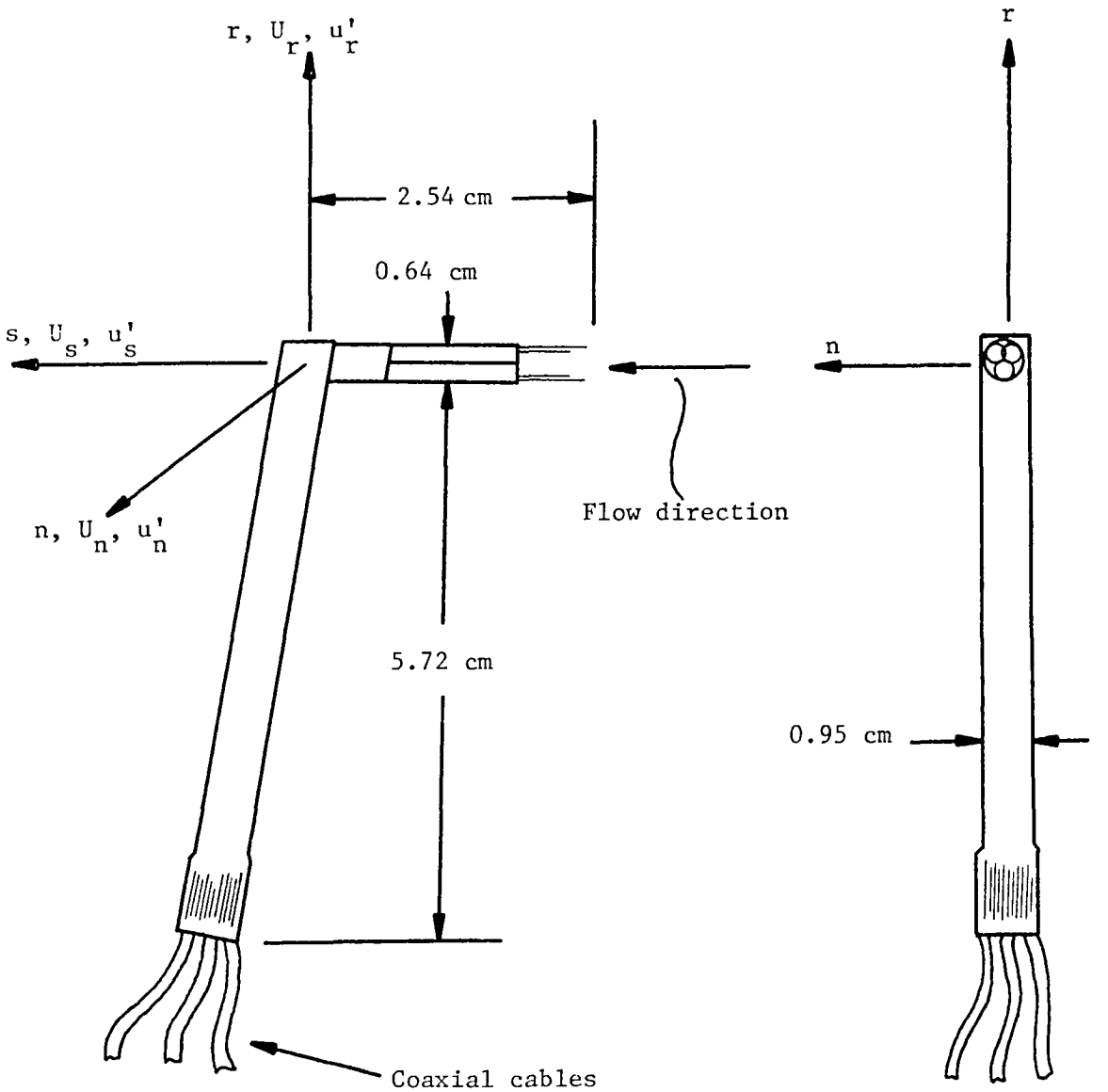

Figure 4. Tri-axial hot wire probe and experimental s, n, r coordinate system

a_{ij}		j		
		1	2	3
i	s	.5803	.6582	.5205
	n	.8404	-.4544	-.1808
	r	-.1014	.5697	-.8089

i represents coordinate direction in experimental s, n, r system

j represents one of the three tri-axial probe sensors

Table 1. Direction cosines for tri-axial probe sensors with respect to the coordinate system shown in Figure 3

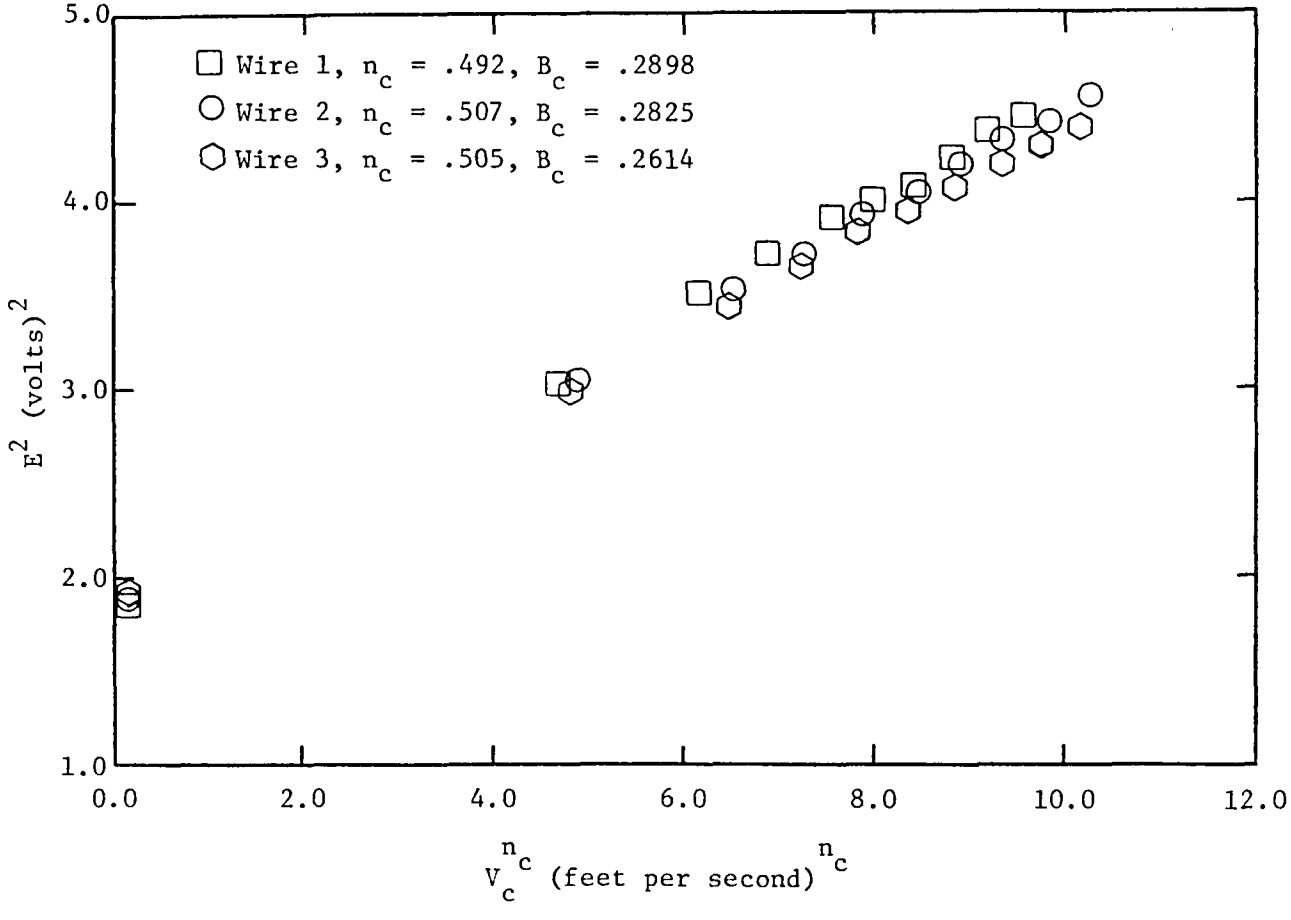

Figure 5. Typical set of calibration curves for tri-axial probe

A spherical head static pressure probe (made by Datametrics) was rotated with the traversing mechanism described in Section 3.3.1 to measure the static pressure distribution in the wake. The probe consists of a .318 cm sphere with trips mounted to stablize the probe wake region. The probe measures this wake region which is correlated to the actual static pressure in the flow using the relation,

$$p = p_{probe} + \frac{K_p}{2} \rho U_s^2 + \frac{1}{2} \rho (\Omega r)^2 \quad . \tag{69}$$

The constant K_p in Equation (69) was found to be .502 through calibration of the probe and a centrifugal force correction is applied with the third term on the right hand side. The third term on the right hand side is zero if no centrifugal force correction is applied (the probe is not rotated). This probe was insensitive to large pitch and yaw angles which are encountered in the three-dimensional wake flow being measured.

3.3 Rotating Probe Experiment

3.3.1 Rotating traverse mechanism

A rotating probe traverse mechanism was designed and built both to rotate the probe with the rotor and to enable the probe to be traversed across the wake in the tangential direction while the rotor is in motion. All electrical signals from the tri-axial hot wire were transferred to the stationary frame of reference through a mercury slip ring unit.

Figure 6 shows the important features of the probe traverse mechanism built for use in the Axial Flow Research Fan. As shown in the figure, it is located immediately downstream of the rotor test blades. Two major functions were performed by the mechanism; to allow the probe to be traversed across the wake at a variety of axial and radial locations and

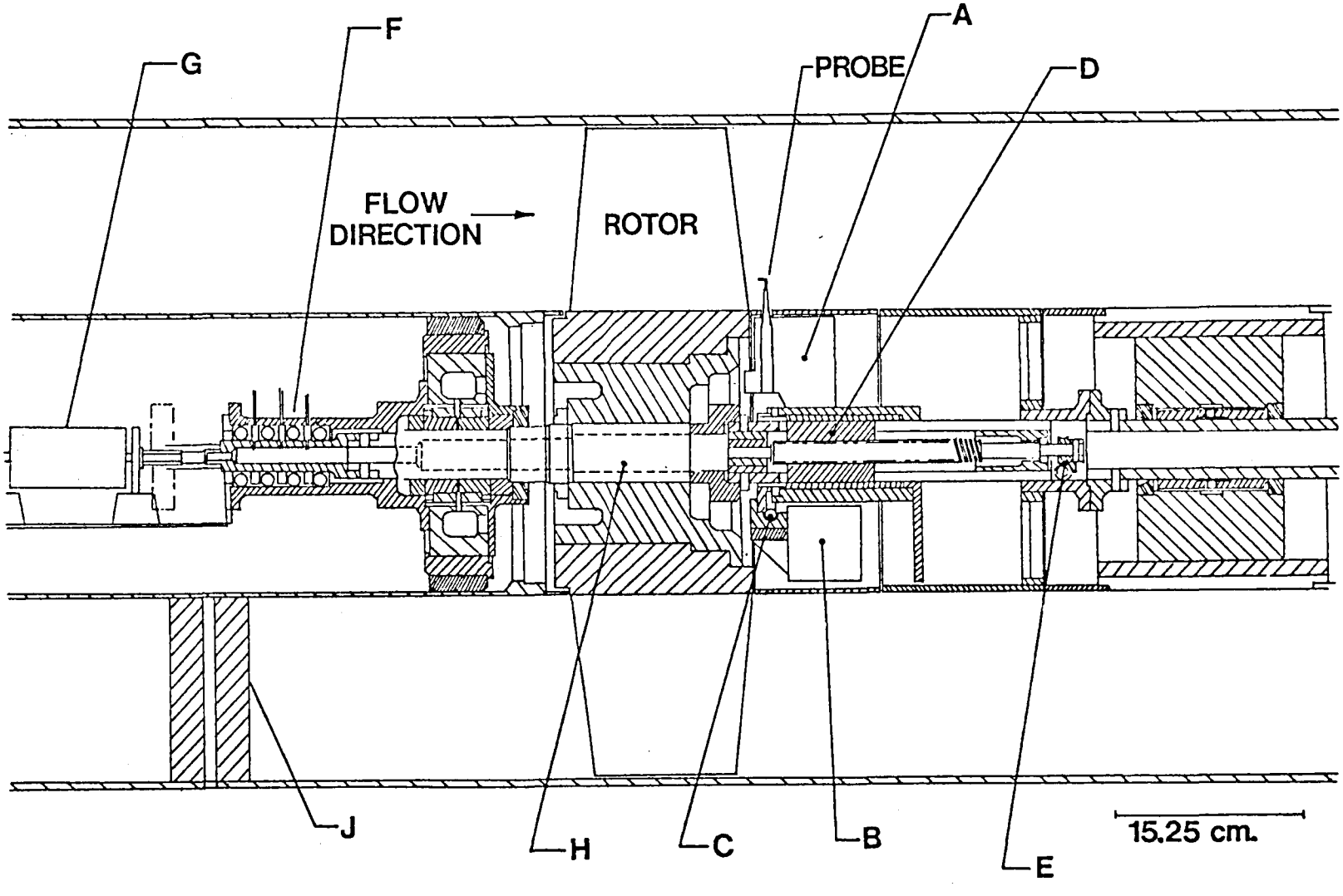

Figure 6. Rotating traverse mechanism

to allow probe signals to be transferred to the stationary frame of reference through the data transmission system illustrated in Figure 6.

As shown in Figure 6, the probe is mounted in the probe traverse assembly A downstream of the rotor test blades within the rotating hub section. With the probe traverse device and the step motor B fixed to the cylindrical section D, tangential motion of the probe is performed. The cylindrical section D is stepped tangentially with a gearing assembly at C between the rotor fixed frame of reference and that of the step motor assembly B. The step motor is actuated by a slow-syn preset indexer through a set of brush contacts as indicated in Figure 6. Tangential steps small enough, .0192 degrees/step, were achieved to allow an accurate measurement of the rotor wake.

The axial position of the probe is adjusted by turning a worm gear at E as shown in Figure 6. Turning of the worm gear at E moves the entire traversing mechanism in the axial direction. The probe is manually moved in the radial direction. The traversing mechanism was statically and dynamically balanced for all of the probe positions used.

Pressure or electrical signals from a probe are transmitted to the stationary frame of reference with a pneumatic transfer device at location F (Figure 6) and with a mercury slipring unit at location G, respectively. Pressure and electrical connections between the mercury slipring or pneumatic transfer device and the probe are located within the rotating shaft designated as H. Three pressure signals can be simultaneously transmitted to the stationary frame. A ten channel mercury slipring was installed for the experiments reported in this investigation, of which only six channels were needed with the tri-axial hot wire probe. Triple distilled mercury is used in each slipring channel to give a negligible

noise to signal ratio necessary for the hot wire signal. Pressure and electrical lines in the stationary frame located within the stationary hub section upstream of the rotor are transferred out of the hub through the strut shown at location J.

3.3.2 Instrumentation

Instrumentation used with the tri-axial hot wire probe is illustrated in Figure 7. The instrumentation shown in the figure enabled raw data to be in a form such that mean velocity, turbulence intensity, and Reynolds stress variation across the wake could be determined from the data processing described in Section 4.1.

As illustrated in Figure 7, each of the three sensors on the tri-axial probe was connected to one of the constant temperature anemometers. The three anemometers, DO1 series manufactured by Disa Electronics, were operated with the following settings:

Gain setting	= 5
Overheat ratio	= 1.5
High frequency filter setting	= 2
Cable length to probe	= 5.0 meters.

With these characteristics the frequency response of the probe was set to exceed any of the frequencies of turbulent fluctuations sensed by the probe.

Figure 7 illustrates how the instantaneous signal output from each of the anemometers ($E_1 + e_1$, $E_2 + e_2$, $E_3 + e_3$) was analyzed. The experimental setup of the instrumentation used is shown in Figure 8. The electronic signal processing gave the following quantities to be recorded at each measurement location: E_1, E_2, E_3, $\sqrt{\overline{e_1^2}}$, $\sqrt{\overline{e_2^2}}$, $\sqrt{\overline{e_3^2}}$, $\sqrt{\overline{(e_1 \pm e_2)^2}}$, $\sqrt{\overline{(e_2 \pm e_3)^2}}$, $\sqrt{\overline{(e_1 \pm e_3)^2}}$. Also, a spectrum analyzer was

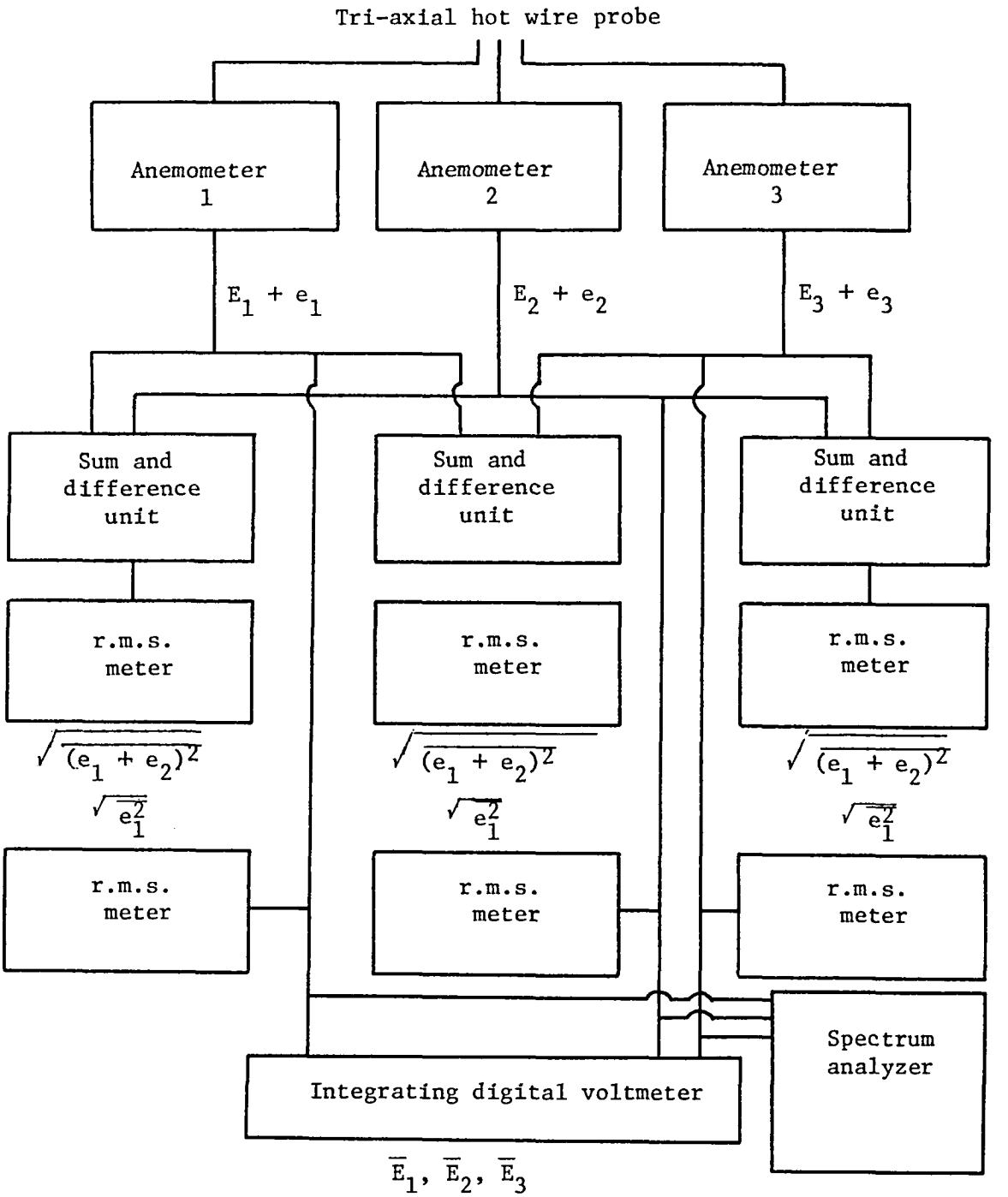

Figure 7. Instrumentation used for rotating tri-axial probe experimentation

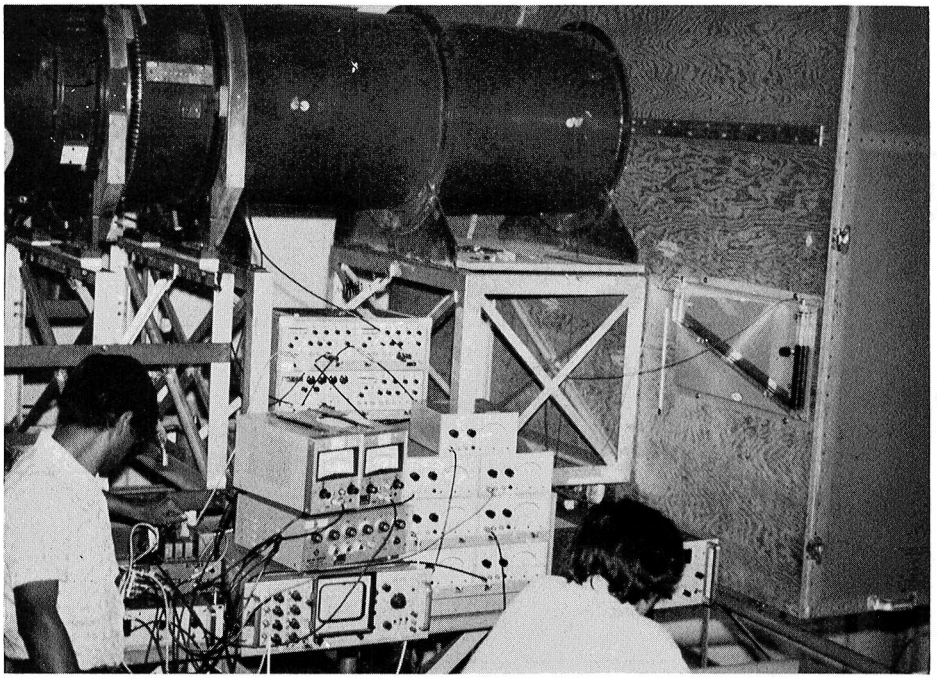

Figure 8. Equipment set-up used in the rotating tri-axial probe experimental program

used to determine turbulent energy spectra for each of the three sensors of the tri-axial probe.

3.3.3 Measurement stations

The rotating probe experimental program made rotor wake measurements at each of the stations given in Table 2. Included in the table are the operating conditions at which each of the wakes were measured. The measurements provided rotor wake data in both the near and far wake flow regions. The measurements at 0° incidence at midradius were taken by Raj (unpublished).

3.4 Stationary Probe Experiment

3.4.1 Instrumentation

The experimental instrumentation used to record signals from the tri-axial hot wire probe mounted in the stationary frame of reference is illustrated in Figure 9. The tri-axial hot wire probe sensors were connected to the three constant temperature anemometers described in Section 3.3.2. The frequency response of each anemometer was adjusted to be high enough so that the periodic and random unsteadiness sensed by the probe would be accurately measured. As illustrated in Figure 9, after removal of the d.c. component (E_1, E_2, and E_3), the measured fluctuating components of voltage (e_1, e_2, and e_3) were recorded on the first three channels of a seven track analog tape recorder. A one pulse per revolution signal was simultaneously recorded on the fourth channel while measurements were being made. The tape recorded was run in the FM mode with a tape speed of 15 i.p.s. The frequency response of the analog tape recorder was 10.0 kHz. The signal output from each anemometer was also taken to a digital voltmeter where the mean d.c. voltage was noted.

r/r_t	z/c	i
0.721	0.021	10°
0.721	0.042	10°
0.721	0.083	10°
0.721	0.167	10°
0.721	0.271	10°
0.721	0.007	0°
0.721	0.021	0°
0.721	0.032	0°
0.721	0.064	0°
0.721	0.072	0°
0.721	0.083	0°
0.860	0.021	10°
0.860	0.042	10°
0.860	0.083	10°
0.860	0.167	10°
0.860	0.271	10°
0.860	0.021	0°
0.860	0.083	0°
0.860	0.271	0°

Table 2. Measurement stations for rotating tri-axial probe experimental program

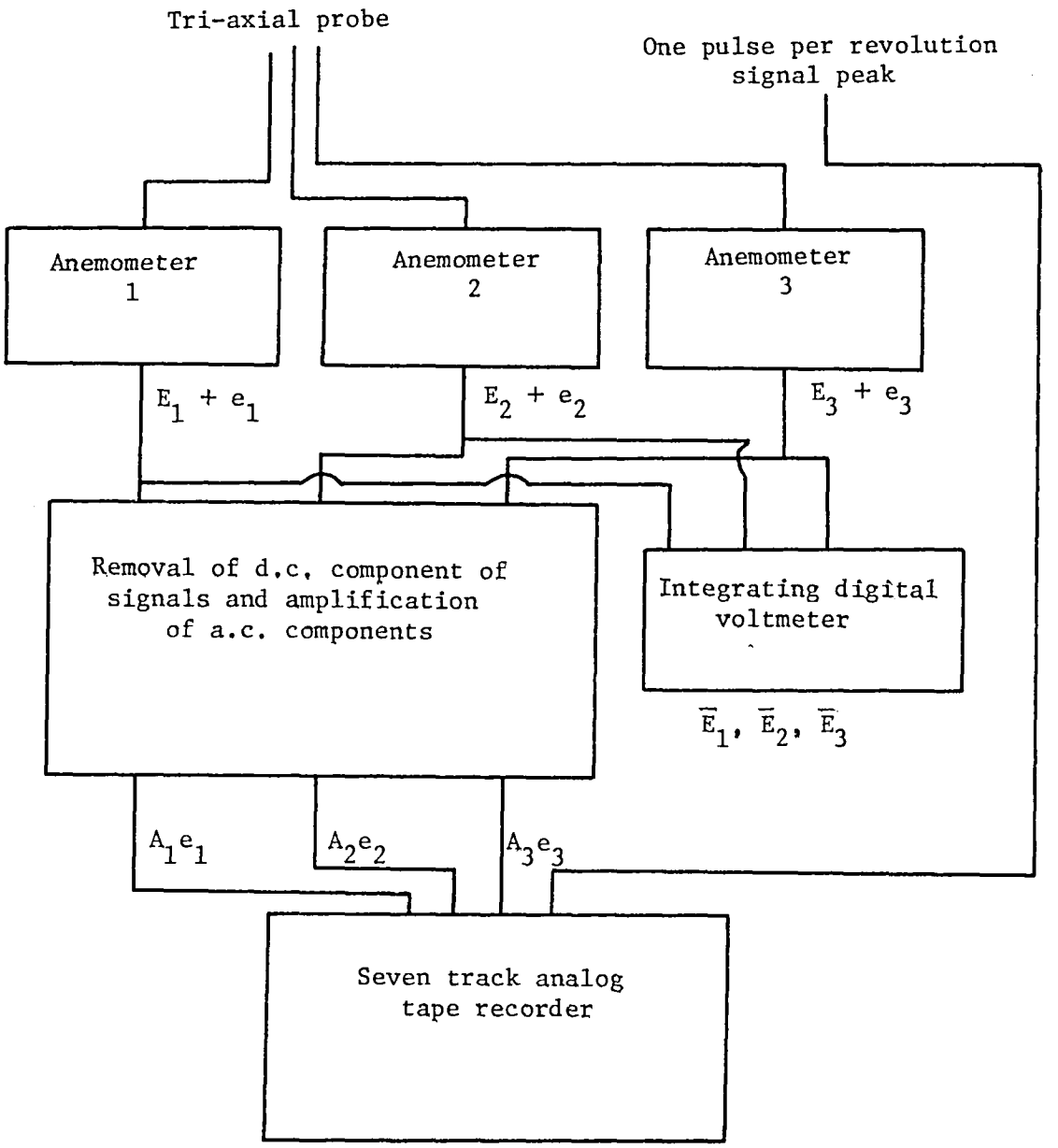

Figure 9. Instrumentation used for stationary tri-axial probe experimentation

3.4.2 Measurement stations

Stationary probe rotor wake data was recorded at each of the measurement stations given in Table 3. At each mid-radius station, the blade loading was varied such that the rotor operated at an incidence of 5°, 10°, and 15°. This resulted in the measurement of 95 rotor wakes using this experimental procedure.

i = 10°, 15°	Twelve bladed rotor								
Station	9	8	7	6	5	4	3	2	1
r/r_t	z/c								
0.465	——	0.134	0.592	0.759	0.926	1.092	1.259	1.426	1.592
0.535	——	0.154	0.612	0.779	0.945	1.112	1.279	1.445	1.612
0.628	——	0.180	0.638	0.805	0.971	1.138	1.305	1.471	1.638
0.721*	0.039	0.206	0.664	0.831	0.998	1.164	1.331	1.498	1.664
0.814	0.066	0.232	0.691	0.857	1.024	1.191	1.358	1.524	1.691
0.907	0.092	0.259	0.717	0.884	1.050	1.217	1.384	1.550	1.717

*Measurements were made at i = 5° for all stations at this radius

Table 3. Measurement stations for stationary tri-axial probe experiment

Chapter 4

DATA PROCESSING

Data processing involved reduction of two types of raw data: rotating and stationary tri-axial probe data. Both types of data processing will be discussed.

4.1 Rotating Tri-Axial Probe Data Processing

Since the rotor wake was measured as a steady flow by the tri-axial probe rotating with the rotor, the data reduction computer program given by Gorton and Lakshminarayanana (1976) was used. The program was well suited for use with the raw data generated by the experimental procedure described in Section 3.3. Output of the computer program gives mean velocity and turbulence quantity variations across the rotor wake.

Mean and fluctuating components of voltage were required input to the computer program at each measurement location. The d.c. components of measured ovltage (E_1, E_2, and E_3) are used to determine the mean velocities in the wake. The measured a.c. components ($\sqrt{\overline{e_1^2}}$, $\sqrt{\overline{e_2^2}}$, $\sqrt{\overline{e_3^2}}$, $\sqrt{\overline{(e_1 \pm e_2)^2}}$, $\sqrt{\overline{(e_2 \pm e_3)^2}}$, $\sqrt{\overline{(e_1 \pm e_3)^2}}$) were used for the calculation of turbulence intensities and Reynolds stress variations. Calculation of the mean velocity and turbulence quantities using the data processing described above involved the solution of a nine by nine matrix as reported by Gorton and Lakshminarayana (1976).

Consistent with assumptions made in the data processing of Gorton and Lakshminarayana (1976) ($U_s > U_r > U_n$), the rotor wake was measured in an approximate streamwise coordinate system. This was accomplished by aligning the axis of the tri-axial probe with the surface of the rotor blade at the trailing edge. The approximate s, n, r coordinate system

with respect to the tri-axial probe is shown in Figure 4. Mean velocities and turbulence quantities in the experimental streamwise coordinate system were then transformed to the r, θ, a coordinate system. Final output from the rotating probe data processing described above gave the variation of the following quantities across the rotor wake; mean velocities W, V, and U, turbulence intensities $\overline{w'^2}$, $\overline{v'^2}$, $\overline{u'^2}$, and Reynolds stresses $\overline{w'v'}$, $\overline{v'u'}$, and $\overline{w'u'}$.

As discussed in Section 3.2, variations of the hot wire calibration curves due to wire aging and temperature changes were found by measuring E_o at the beginning and end of each experiment. The computer program given by Gorton and Lakshminarayana (1976) was modified at each point to allow for continuous variation of E_o with time in the probe hot wire calibrations. A sample result of this correction when applied to the wake measurements made is shown in Figure 10. Before the correction is made, measurements at the beginning and end of the experiment at the same location on the trailing surface side of the wake show poor agreement. After correcting for the changes in the calibration characteristics, measurements made at the beginning and end of the experiment on the trailing surface side of the wake show good agreement. Only half of the wakes measured with the tri-axial probe were corrected. Wakes that had been measured in a short period of time did not show any appreciable E_o variations.

4.2 Stationary Tri-Axial Probe Data Processing

The data processing used for this type of data analyzed the periodic and random unsteady flow characteristic of the rotor wake in the stationary frame of reference. The computational scheme used for stationary probe data processing is illustrated in Figure 11. The four major steps in data

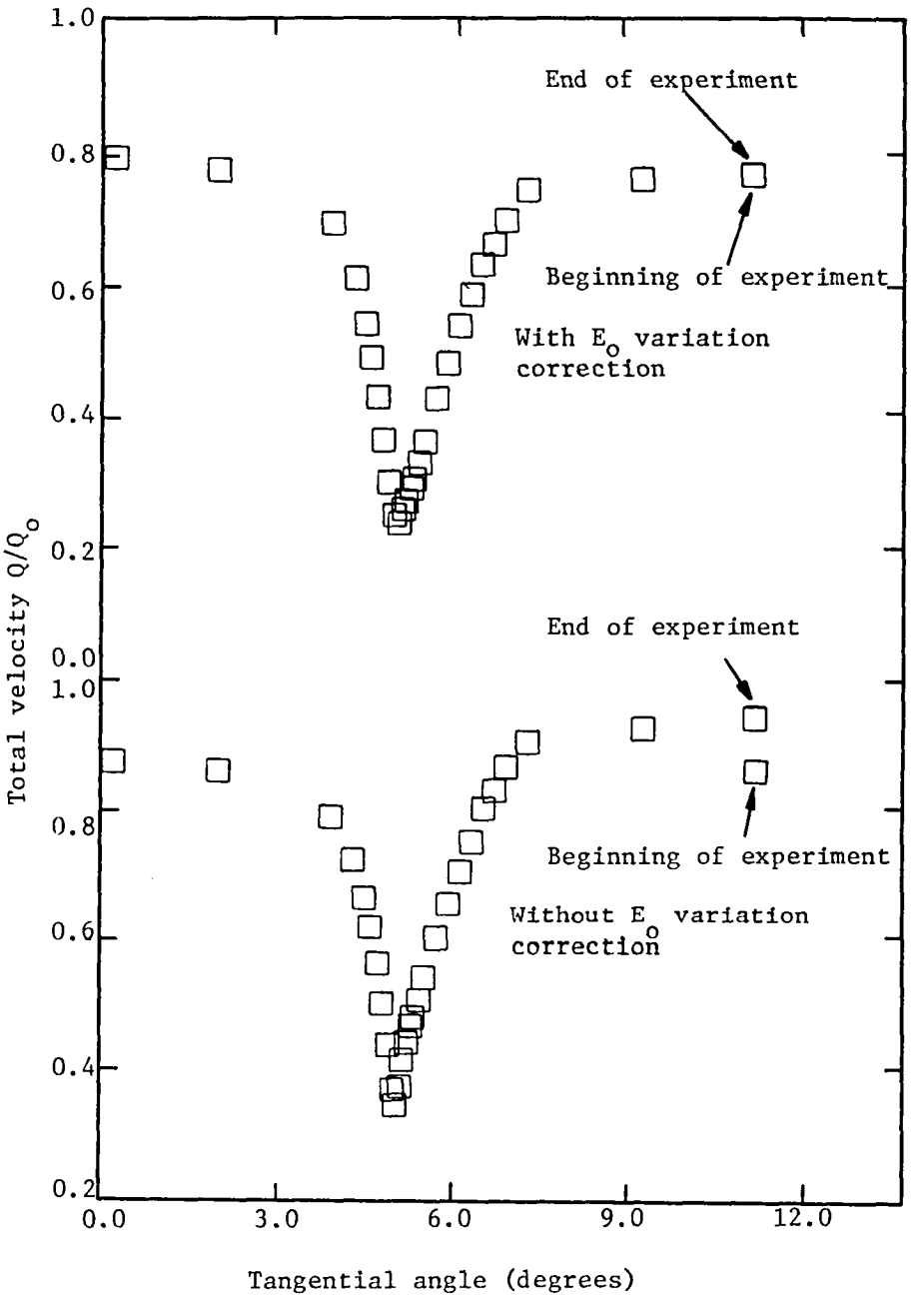

Figure 10. Correction applied to rotating probe wake measurements for E_o variation

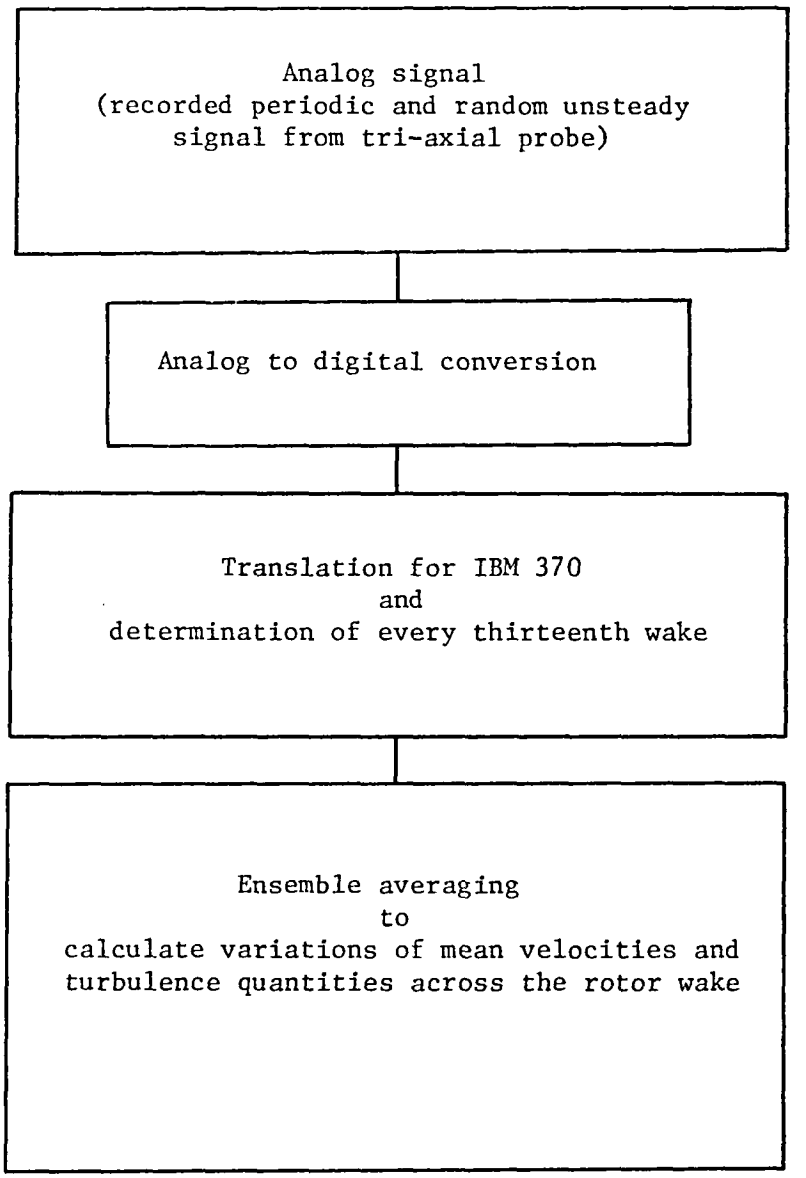

Figure 11. Data processing for stationary tri-axial probe investigation

processing were; analog to digital conversion, translation for IBM 370, determination of every thirteenth wake, and ensemble averaging of digital data. This technique is described by Lakshminarayana and Poncet (1974) and Raj and Lakshminarayana (1976).

4.2.1 Analog to digital conversion and translation for IBM 370

So that all data processing could be done on the IBM 370 computer at The Pennsylvania State University, the recorded analog signals from the stationary probe experiment were converted to digital form. This required simultaneous digitizing of four channels of analog data; three channels of tri-axial probe signals and a one spike per revolution signal peak.

An analog to digital converter manufactured by Datel was used for this phase of data processing. The digitizing unit could convert data at a maximum rate of 2465 samples per second for each of the simultaneously digitized channels. Thus, a real time analog to digital conversion was not possible. So that approximately 388 digital points would represent the blade to blade variation in measured quantities, the analog signal was digitized at a tape speed 1/30 of real time. The one spike per revolution signal peak was used as an accurate measure of one rotor revolution in any time base.

Since all subsequent data processing was performed on the IBM 370 computer, digitized data from the analog to digital conversion was translated to a form compatible with the IBM 370. Digitized data was in a form where each coded word contained a four bit channel number, a six bit identification number, a four bit synchronization nibble, and a ten bit integer data value. The ten bit integer data value ranged from -512 to +511. The coded data was translated to a form accessible to standard IBM and Fortran language conventions. On the IBM 370 the data values were

in a positive integer form where the two lowest order bits in the digitized data were dropped so that the values could be stored in single bites. The converted data ranged from 0 to 255. The four channels of data were stored in four bytes in channel sequence.

4.2.2 Ensemble averaging

To adjust the digitized data to represent the characteristics across the wake of one rotor blade, only every thirteenth wake was saved. The stationary data reduction procedure given by Raj and Lakshminarayana (1976) was modified for use in this phase of data reduction. The modification made use of the one spike per revolution signal peak to determine every thirteenth wake.

A sample input to this phase of data processing is shown in Figure 12. So that the wake characteristics downstream of only one rotor blade could be studied, only the first wake past each signal peak was saved. Figure 12 also illustrates the stationary probe data in the every thirteenth wake form. For this investigation, 120 rotor wakes in the thirteenth wake form were saved to be used in ensemble averaging of the data.

With data in the thirteenth wake form, ensemble averaging was performed using the computer program given by Raj and Lakshminarayana (1976). This ensemble averaging technique used was developed by Lakshminarayana and Poncet (1974). The computer program of Raj and Lakshminarayana (1976) was modified to allow a tri-axial probe of any geometry to be used and to allow for variations in the hot wire calibrations due to wire aging and temperature changes. As previously mentioned the change in calibration characteristics was determined by measuring voltage at zero velocity before and after each experimental run. Output from this phase of data processing gave the three-dimensional

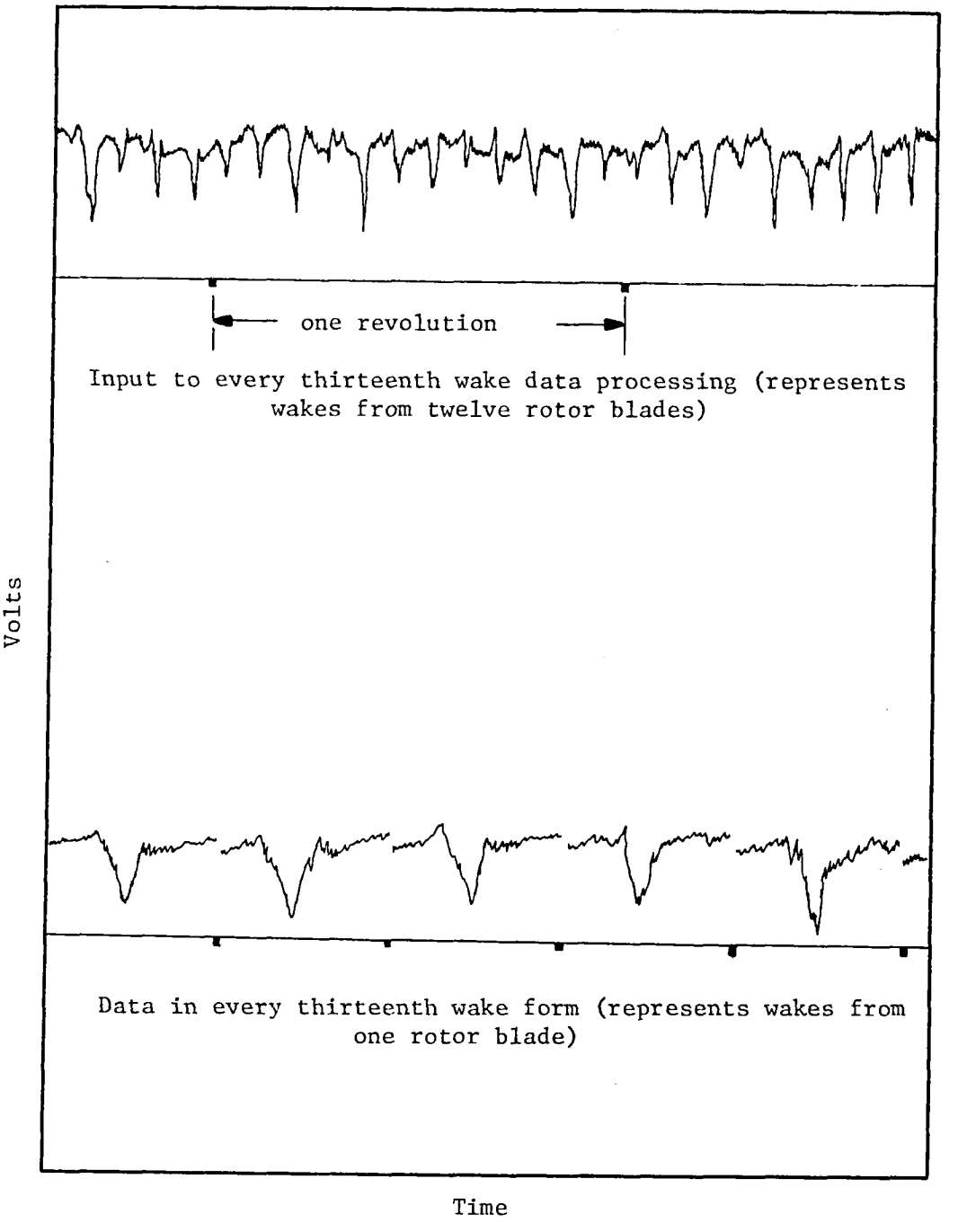

Figure 12. Conversion of stationary tri-axial probe data to every thirteenth wake form

variations of mean velocities, turbulent intensities, and Reynolds stress across the rotor wake in the r, θ, z coordinate system. Reynolds stress data was then transformed to the relative streamwise coordinate system (Figure 1).

Chapter 5

EXPERIMENTAL RESULTS, CORRELATION, AND COMPARISON WITH THEORY

5.1 Comparison of Mean Velocity Measurement Techniques

Three types of experimental techniques have been used to make three-dimensional mean velocity measurements in the Axial Flow Research Fan Facility; stationary tri-axial hot wire probe, rotating tri-axial hot wire probe, and a five hole pitot probe (Yocum, 1978). Hub to tip variations of streamwise and radial mean velocities are compared for data from the stationary tri-axial and stationary five-hole probes. Wake measurements made using the rotating and stationary tri-axial probe techniques are also compared.

5.1.1 Stationary tri-axial hot wire and five hole pressure probes

Measured hub to tip variations of total and radial mean velocities from the stationary tri-axial and stationary five hole probes are shown in Figure 13. Measurements are compared for the rotor blades operating with 10° incidence at mid-span (R = .721). Good agreement is shown for the total velocity distribution measured by both probes. As expected, total velocity increases with radius in the region between the hub and end wall boundary layers. Appreciable discrepancies between the two measurement methods is seen in the radial velocity distribution. The five hole pressure probe shows an almost constant, nearly zero radial velocity profile from hub to tip where the tri-axial probe shows an increase of radial velocities. An increase of radial velocities may be expected from a transfer of momentum and energy in the wake (reported later) towards the end wall region. For the case shown in Figure 13, the tri-axial probe seems to have measured more accurately the hub to tip

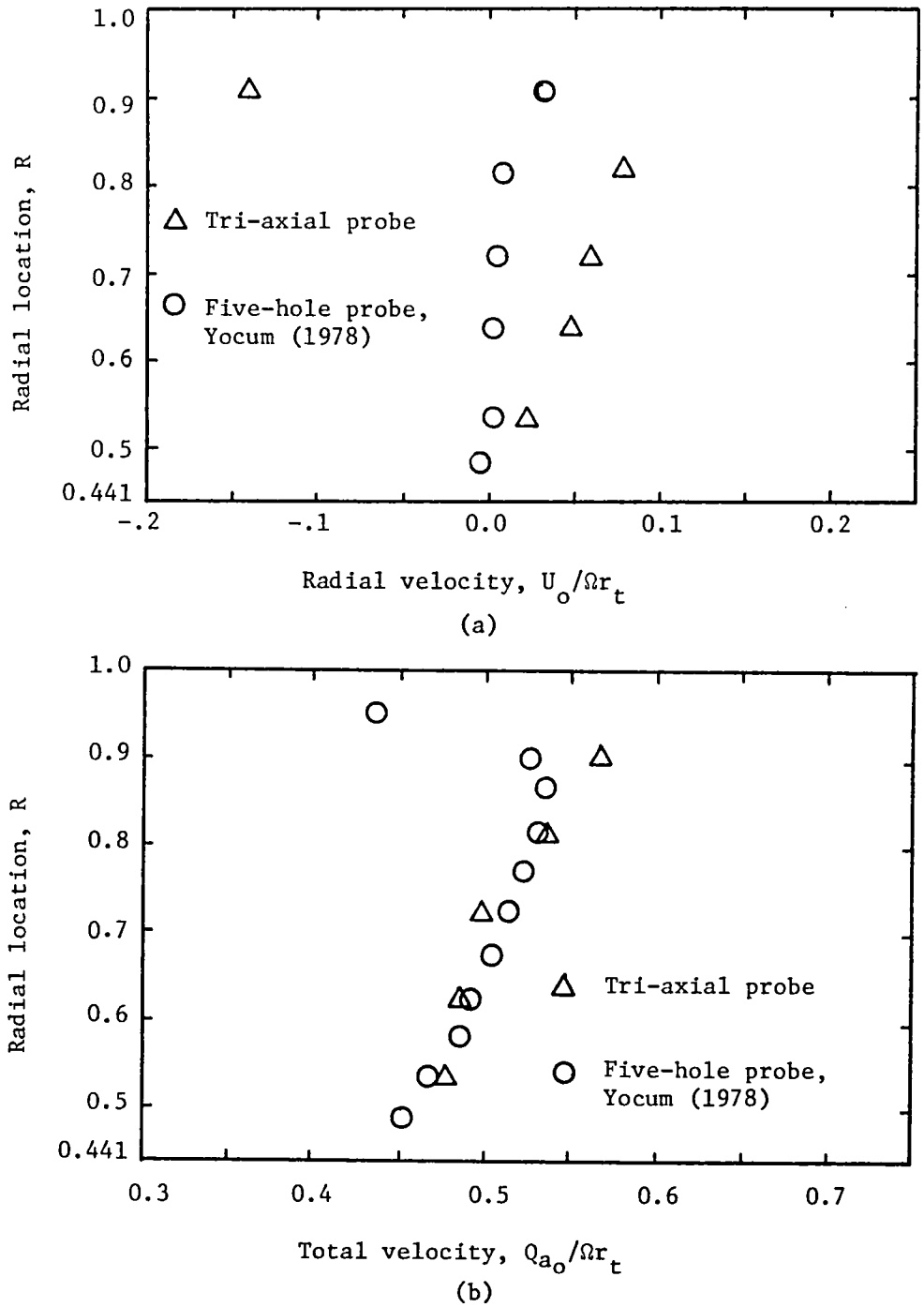

Figure 13. Hub to tip variations of radial and total mean velocities downstream of the test rotor in the stationary frame

variations of radial velocity. However, both probes show the same total velocity distribution, indicating no differences in the measurement of this quantity using either probe.

5.1.2 Stationary and rotating tri-axial probes

Mean velocities and turbulence quantities have been compared for rotor wake measurements made using both the rotating and stationary tri-axial probe techniques.

A comparison of the axial and tangential components of mean velocity measured in both the near and the far wake regions is shown in Figures 14 and 15. As shown in Figure 14, the axial component of velocity in the near wake shows a difference of approximately 20 percent at the wake centerline, and the discrepancy is vanishingly small everywhere else. The axial velocity stationary probe results in the near wake do not show the sharp profile shape at the wake centerline as measured by the rotating probe. The axial components of mean velocity agree in the far wake for $Z > .2$. Poor agreement is found for the tangential components of mean velocity in the near wake region as shown in Figure 15. Here, the difference is approximately 60 percent and the profile shapes are distinctly different. This difference is not as pronounced in the far wake region for $Z > .2$ where it is fourteen percent.

Errors due to the ensemble averaging technique result in some of the discrepancies shown in Figures 14 and 15. These errors are discussed by Lakshminarayana and Poncet (1974). Small sample theory gives a maximum error of approximately one percent near the wake center for both the axial and tangential components of mean velocity. Negligibly small errors exist for the ensemble averaging of the free stream stationary probe data. In addition to the errors given by small sample theory, an error in the

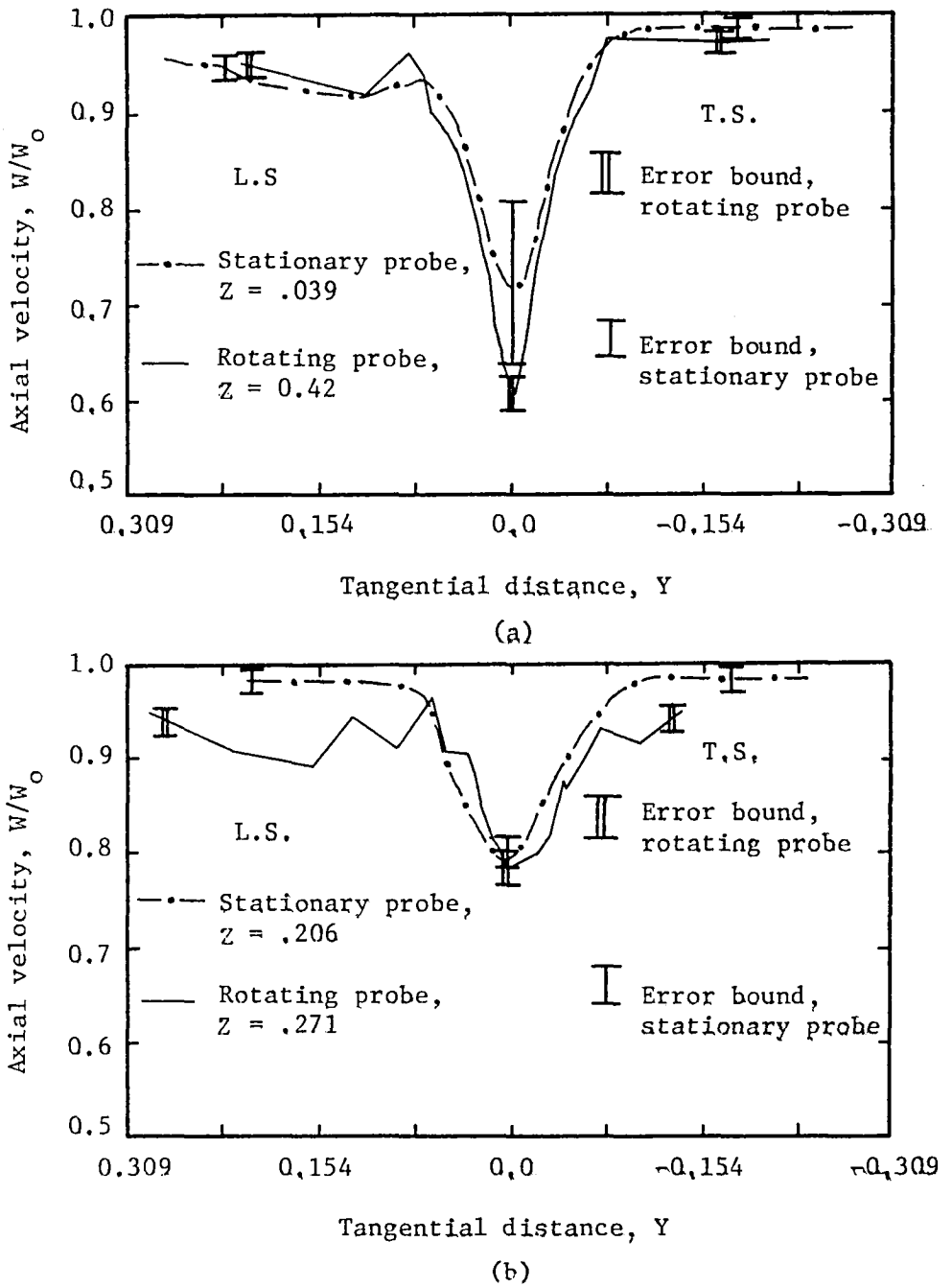

Figure 14. Comparison of rotating and stationary tri-axial probe wake measurements for axial mean velocity, i = 10° and R = .721

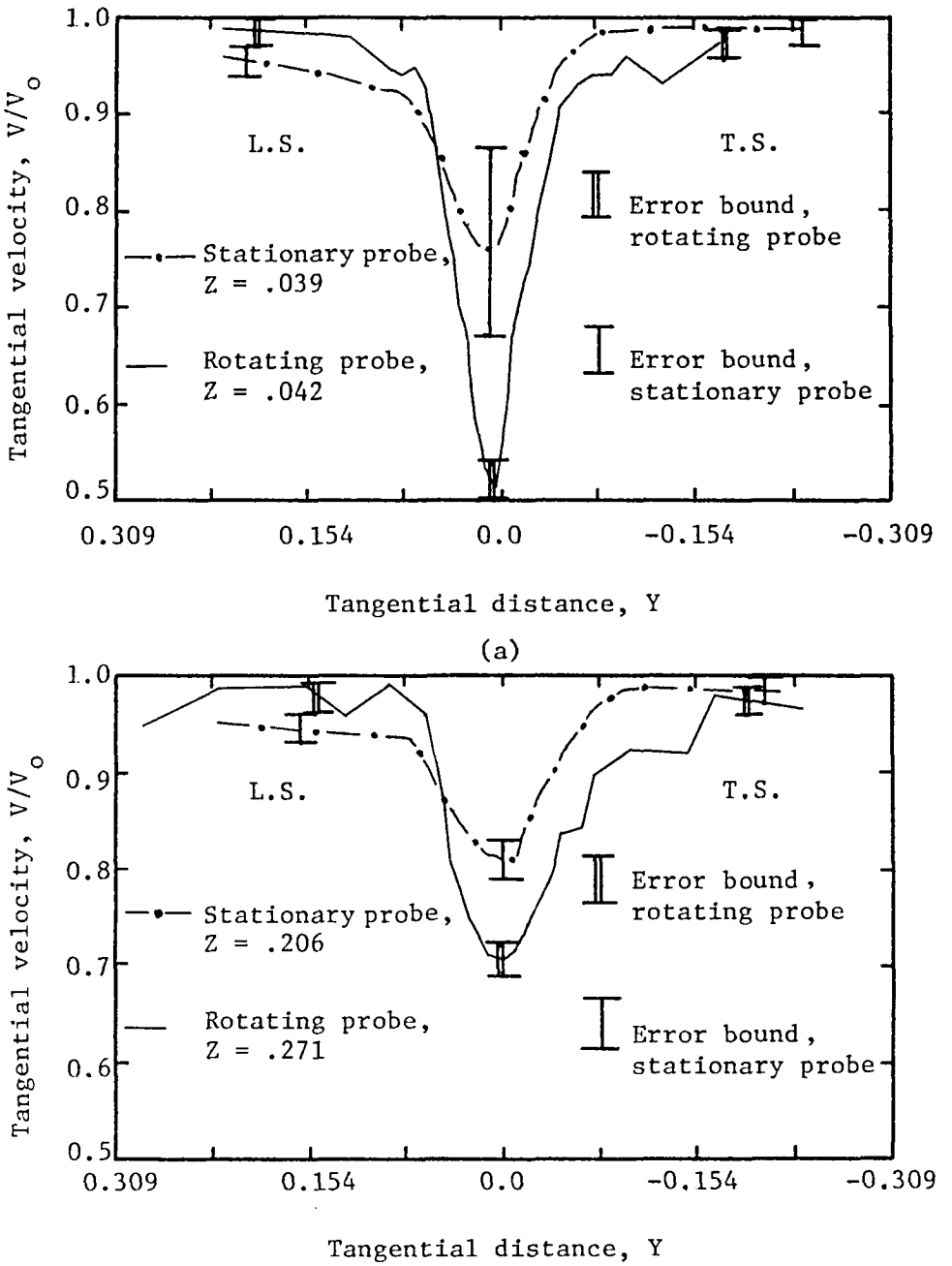

Figure 15. Comparison of rotating and stationary tri-axial probe wake measurements for tangential mean velocity, i = 10° and R = .721

stationary probe data processing results from any unsteadiness of the wake location in the rotating frame of reference with respect to the rotor blade. Also, in the analog to digital conversion of the data an error results from only a discrete number of points being digitized in one blade spacing. These two effects give a maximum anticipated error that may be of the order of ten percent in the near wake region where the shear gradients are large. In the far wake region and in the free stream these errors are negligibly small since the shear gradients are small. These errors are only applicable to the stationary probe data processing used in this investigation.

For the rotating and stationary probe investigations, errors in the axial and tangential mean velocity measurements due to the tri-axial probe are given by Anand (1976). The major errors present for the tri-axial probe used in this investigation are (hot wire probe errors for turbulence intensity and Reynolds stress measurements are also discussed below since a comparison of the stationary and rotating probe results for these quantities are discussed later in this section):

1. Changes in the effective cooling velocity on the hot wire, resulting in a deviation from cosine law. A correction is applied in both the rotating and stationary probe data processing to eliminate any errors from this effect.
2. A change in the heat transfer characteristics of the hot wire and interference to the flow due to the prongs and probe body. Errors due to this effect are negligible for the probe used in this investigation and are included in the hot wire calibration.

3. Errors resulting from the minimum spacial resolution of the probe. This characteristic of the tri-axial probe gives an anticipated error for large shear gradients (near wake) of approximately $\pm$ two percent and $\pm$ four percent for the mean velocity and turbulence intensity data, respectively. Since the detailed structure of the turbulence (length scales and eddy structure) is not known, no detailed estimate of the errors in stress correlation due to the spacial resolution of the probe is given.
4. Errors due to the thermal inertia of the hot wires. This effect is negligible for the fluctuating velocity levels present in the rotor wake investigated.
5. Changes in the hot wire calibration due to wire aging, oxidation, and contamination. Errors due to these effects are corrected for in the data processing.
6. Changes in the hot wire calibration due to ambient temperature drifts. Errors due to this effect are eliminated in the data processing.
7. Finite sampling times for the r.m.s. (root mean square) meter and integrating digital voltmeter. Errors due to this effect are negligibly small.
8. Measurement of the hot wire angles with respect to the tri-axial probe coordinate system. The maximum anticipated errors are $\pm$ .6% for the mean velocity, turbulence intensity, and Reynolds stress measurements made in this investigation.

The maximum anticipated errors in the measured axial and tangential components of mean velocity at the wake center are shown as errors bounds in Figures 14 and 15. In the near wake region the differences in the axial velocity profiles for the rotating and stationary probe data at the wake center is almost within the limits of that expected from the anticipated errors. Axial mean velocity profiles show almost identical results in the far wake region for $Z > .2$. However, for the tangential velocity profiles in the near and far wake regions, the maximum anticipated errors do not account for all of the discrepancies shown. For this reason, the tangential mean velocity data presented later in this chapter must be viewed with caution.

Axial, tangential, and radial components of turbulence intensities have been compared for the two experimental techniques as shown in Figure 16. Data has been compared in the near wake region at mid-radius where agreement is fair for all of the components of turbulence intensities shown. Error bounds for the maximum anticipated errors in the stationary and rotating probe turbulence intensity data are shown in Figure 16. The discrepancies in axial, tangential, and radial turbulence intensity measurements are found to be well within the expected error limits.

A comparison of the streamwise and radial components of stress are shown in Figure 17. The measurements shown are in the near wake at mid-radius ($R = .721$) at a rotor blade incidence of 10°. The streamwise component of stress show good agreement and the discrepancies shown for the radial component of stress are small. Error bounds for the streamwise and radial Reynolds stress profiles are not shown in Figure 17 since the detailed structure of turbulence (length scales and eddy structure) is not known. Knowledge of the structure of turbulence is essential if an

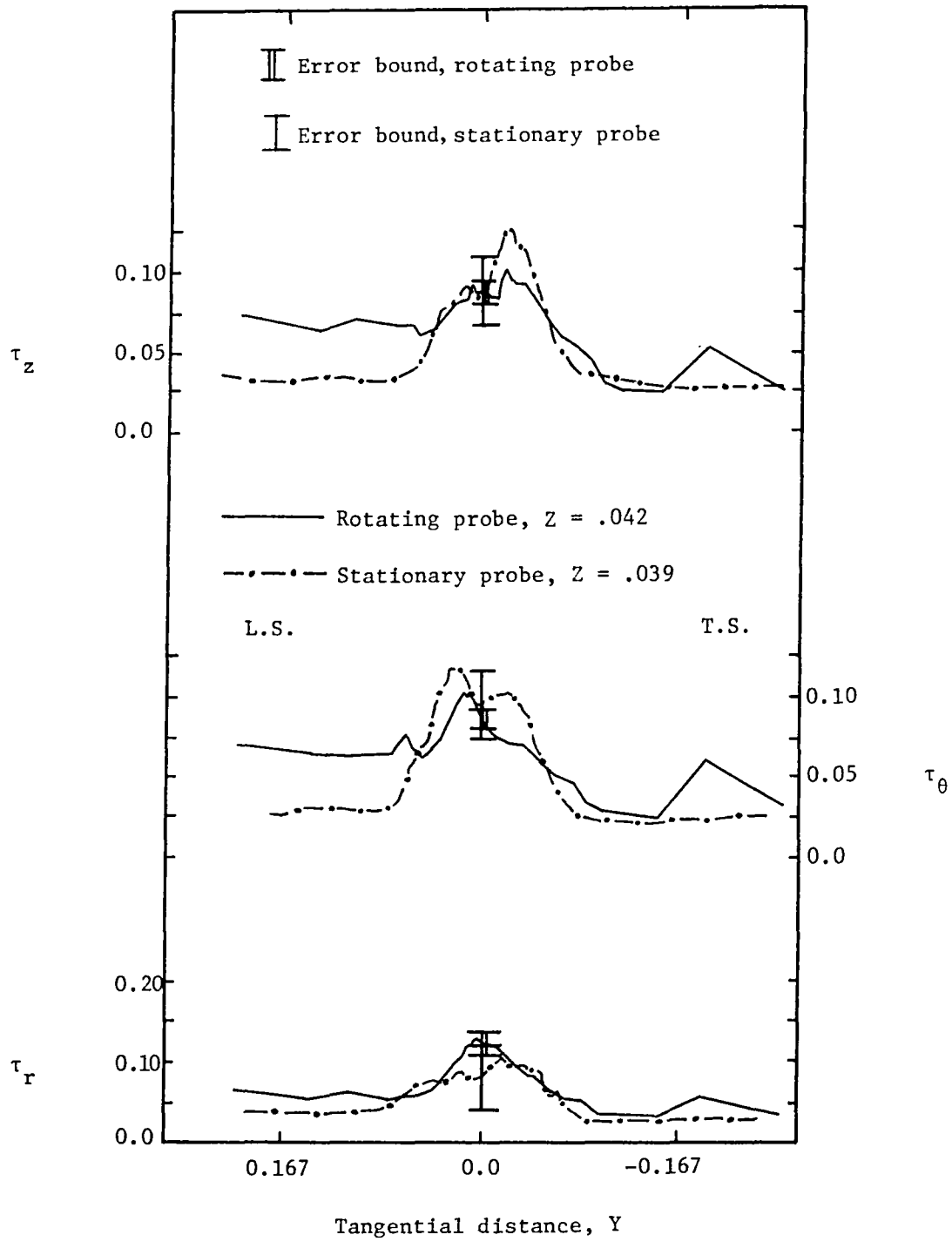

Figure 16. Comparison of rotating and stationary tri-axial probe wake measurements for axial, tangential, and radial turbulence intensities, i = 10° and R = .721

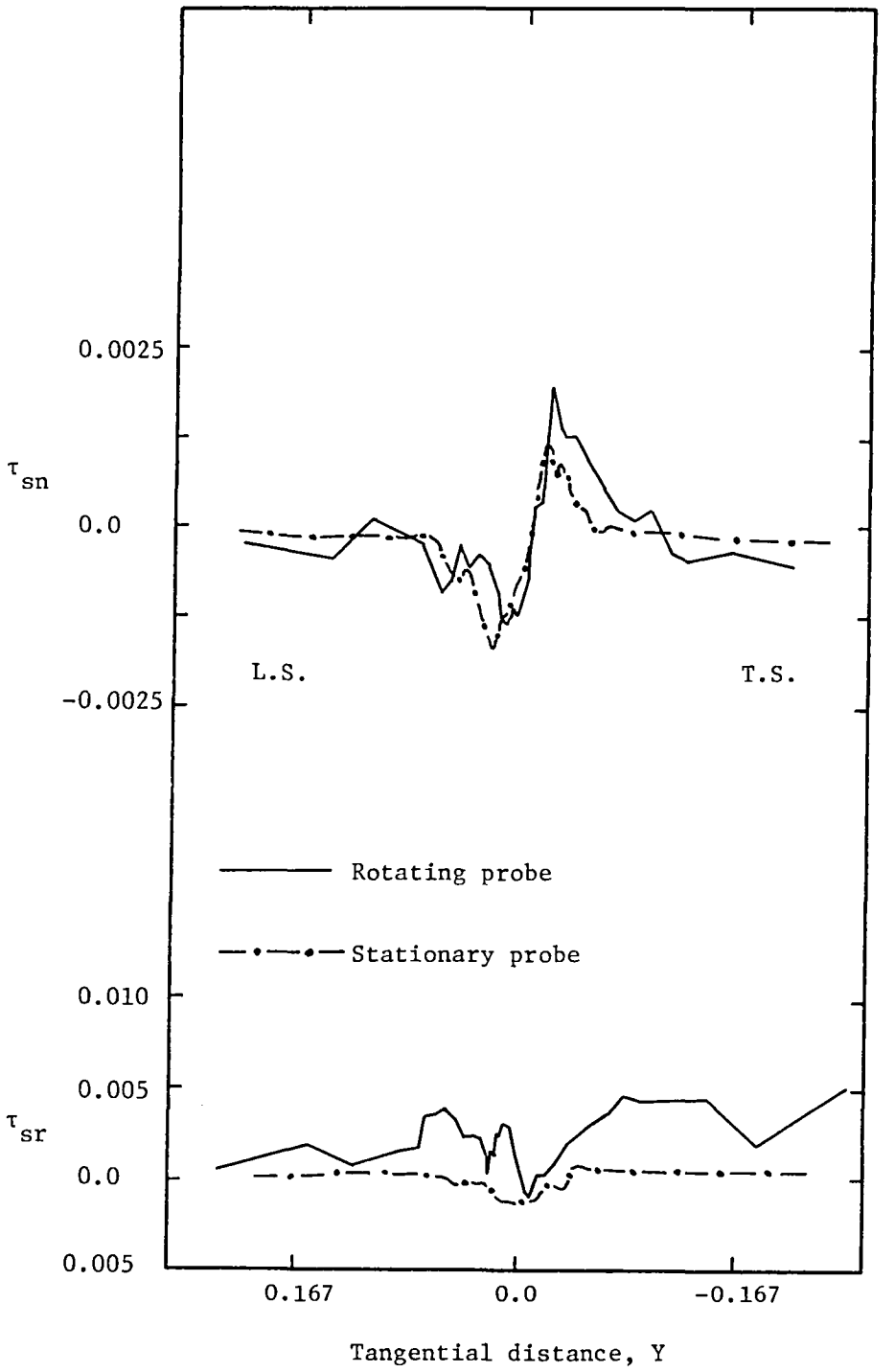

Figure 17. Comparison of rotating and stationary tri-axial probe wake measurements for streamwise and radial Reynolds stress, i = 10° and R = .721

accurate estimation of the errors resulting from the spacial resolution of the probe (a major error in stress correlations) is to be found.

5.2 Rotor Inlet Conditions

Mean velocity and turbulence intensity profiles upstream of the rotor blade row were measured since the flow conditions in this region will affect the characteristics of the rotor wake. Figure 18 shows the axial mean velocity and turbulence intensity wake profiles resulting from one of the two adjacent struts upstream of the rotor. The free stream region shown outside of the wake represents the inlet conditions at all other circumferential locations. The measurements shown were made with a single-sensor hot wire probe.

The axial mean velocity profile in Figure 18 shows that the strut wakes have decayed considerably before reaching the rotor. The defect in axial mean velocity is shown to be less than ten percent. However, the strut wakes are still of sufficient magnitude to show distinct peaks in turbulent energy spectra measured in the rotating frame of reference downstream of the rotor (reported in Section 5.10.2). It should be noted that in the rotating frame of reference the strut wake is sensed as an unsteady flow condition therefore resulting in its effect on the turbulence energy spectrum.

Axial turbulence intensity upstream of the rotor is also shown in Figure 18. Turbulence intensity outside of the strut wake is about two percent with an increase to four percent measured near the wake center. The increase in the strut wake will contribute to the mean velocity profile in forming the distinct peaks of energy measured in the rotating frame of reference behind the rotor. The free stream turbulence intensity

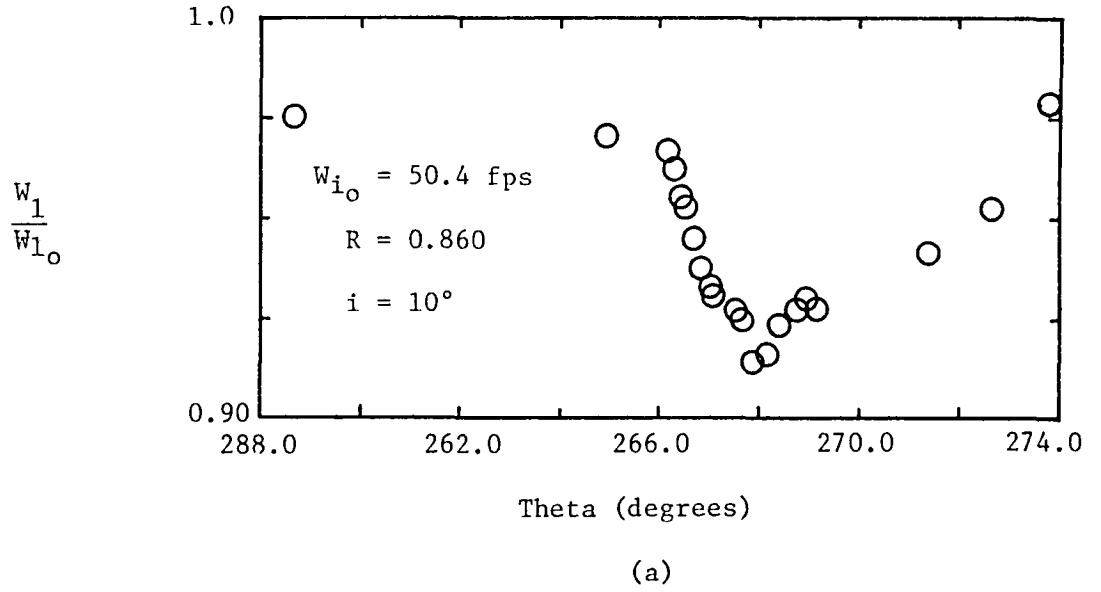

(a)

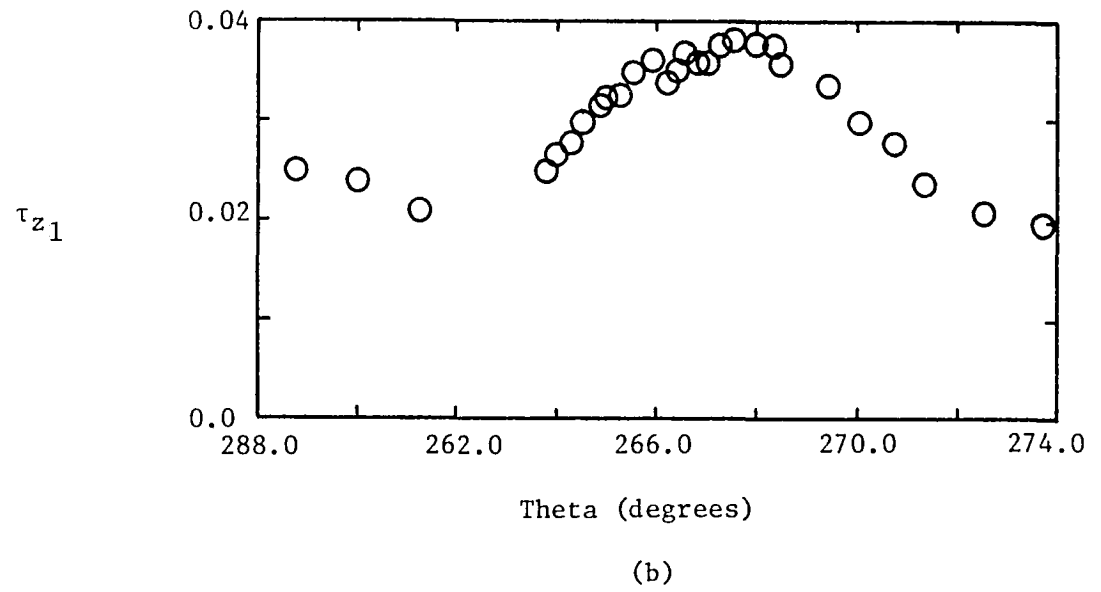

(b)

Figure 18. Inlet mean velocity and turbulence intensity profiles

effects the structure of turbulence within the blade row and downstream of the rotor.

5.3 Wake Profiles

Rotating and stationary tri-axial hot wire probe measurements have been used to study the characteristics of the rotor wake in both the near and far wake regions. The near wake is defined as the region where the mean velocity defects are of the same order of magnitude as the free stream velocity. In the far wake, the defects are small compared to free stream velocity. Axial, tangential, and radial profiles of mean velocity and turbulence intensity and profiles of streamwise and normal components of Reynolds stress are studies in this section, including the effects of blade loading on the wake profile. The static pressure variations across the rotor wake in the near wake region are also given. All of the velocity data presented in this section are in the relative or rotating frame of reference.

5.3.1 Axial mean velocity

Variation of axial mean velocity profiles (normalized by free stream axial velocity) in the rotor wake at mid-radius (R = .721) at the rotor blade incidences of 0°, 5°, 10°, and 15° are illustrated in Figures 19, 20, 21, and 22, respectively. The abscissa in the figures represents tangential distance as a function of blade spacing with Y equal to zero at the wake centerline.

The wake profiles are clearly asymmetric about the wake centerline in the near wake region for rotor blade incidences of 5°, 10°, and 15°. This indicates that the rotor blade suction surface boundary layer is thicker than the pressure surface boundary layer. At the positive

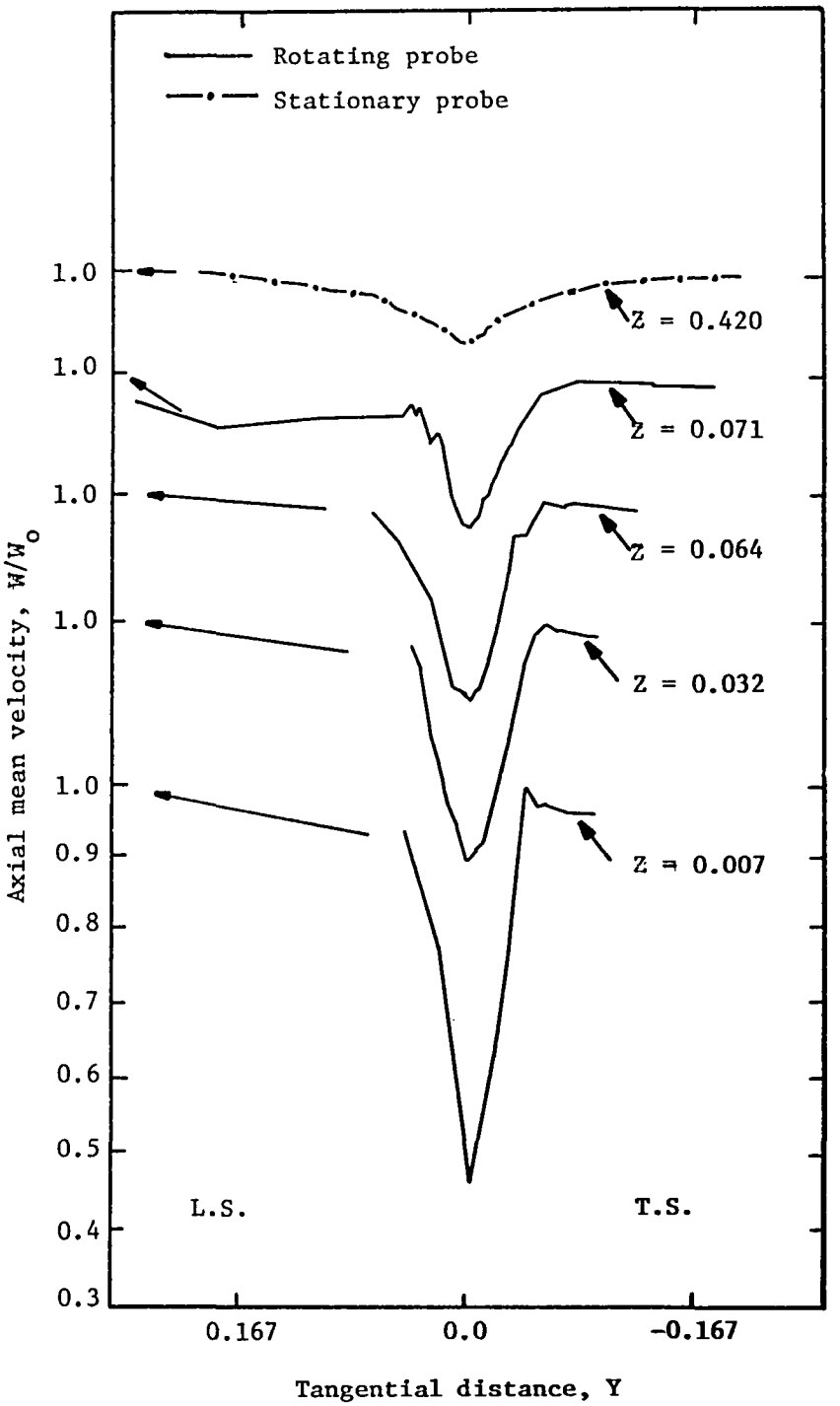

Figure 19. Axial mean velocity profiles for i = 0° and R = .721

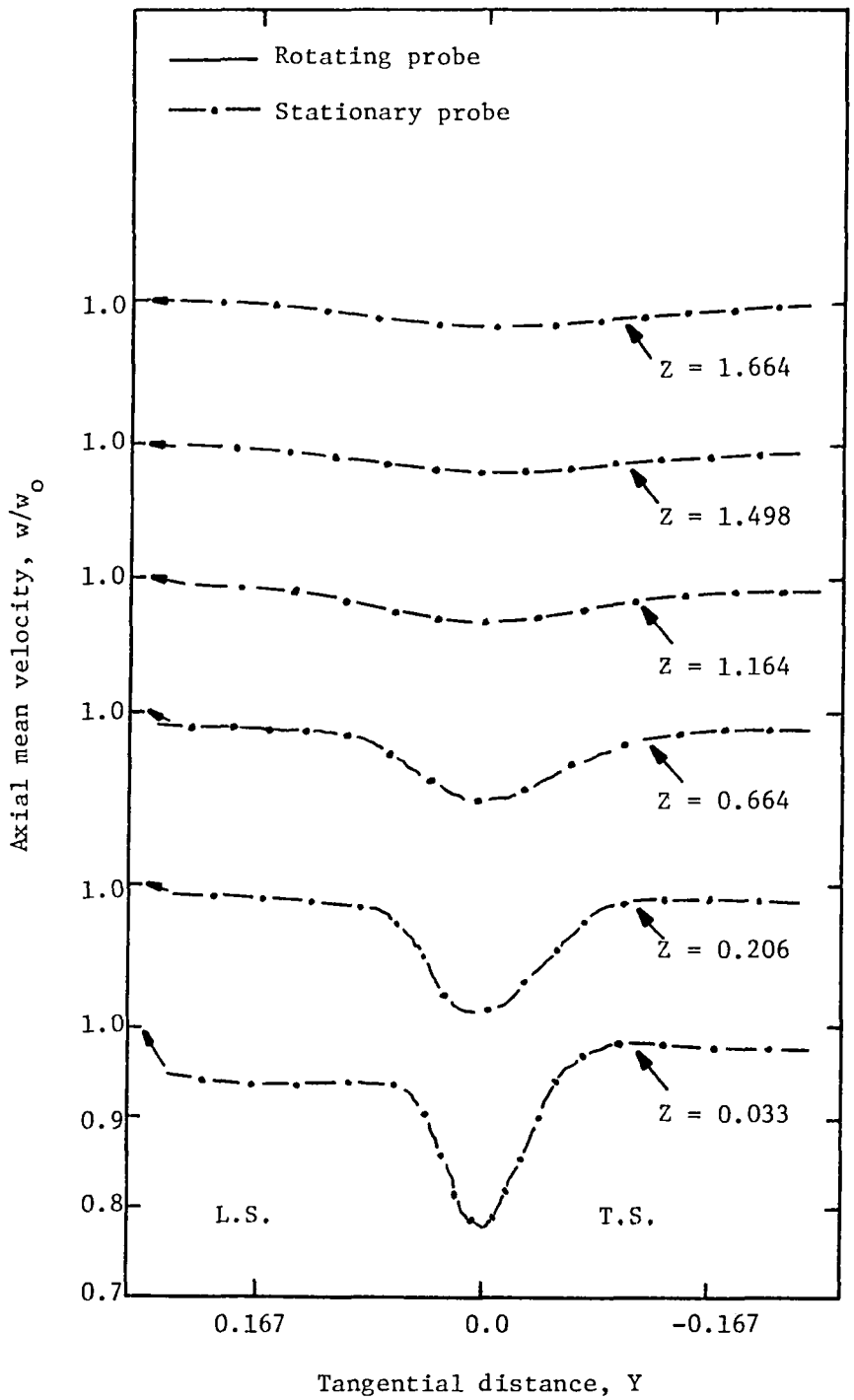

Figure 20. Axial mean velocity profiles for i = 5° and R = .721

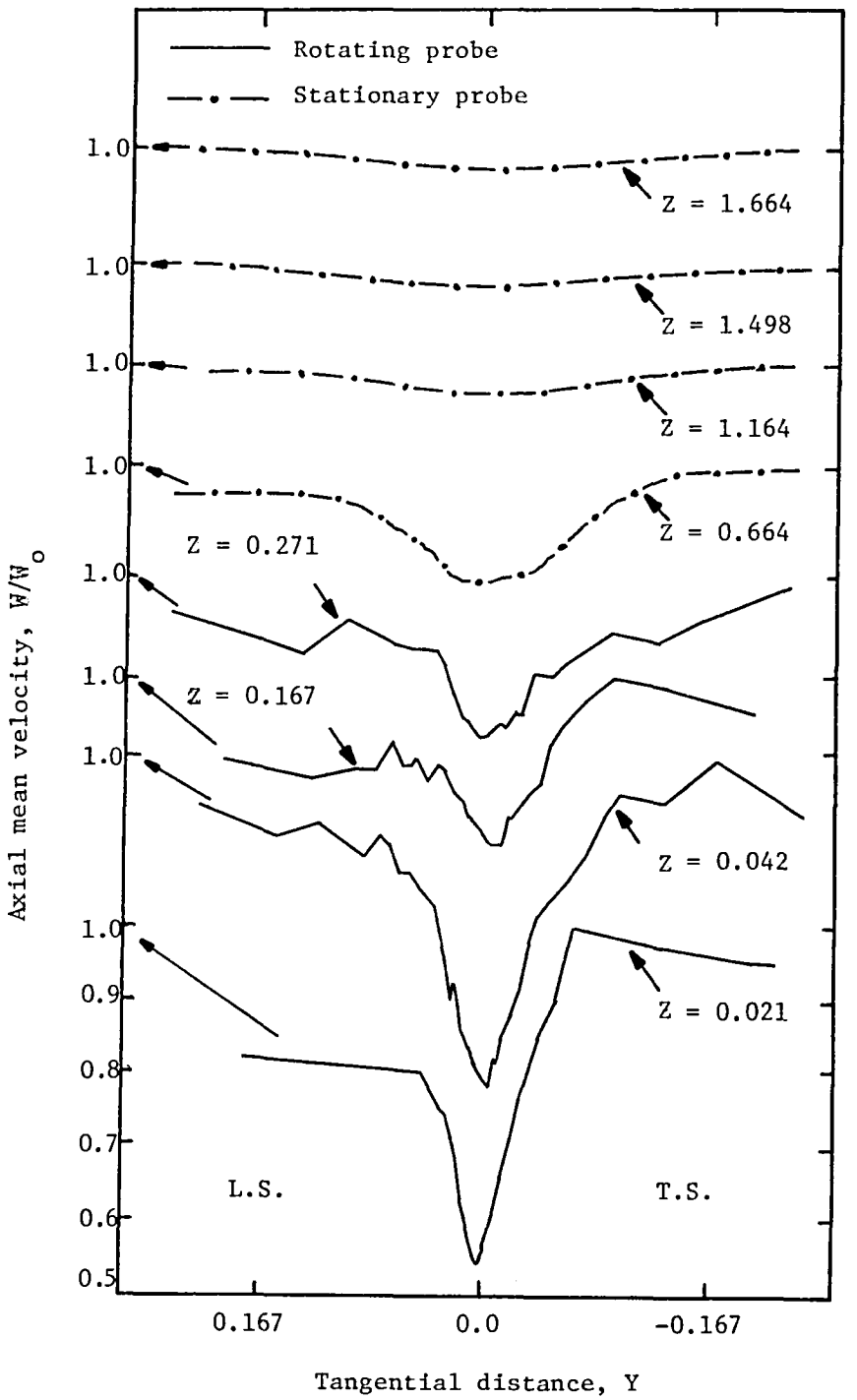

Figure 21. Axial mean velocity profiles for i = 10° and R = .721

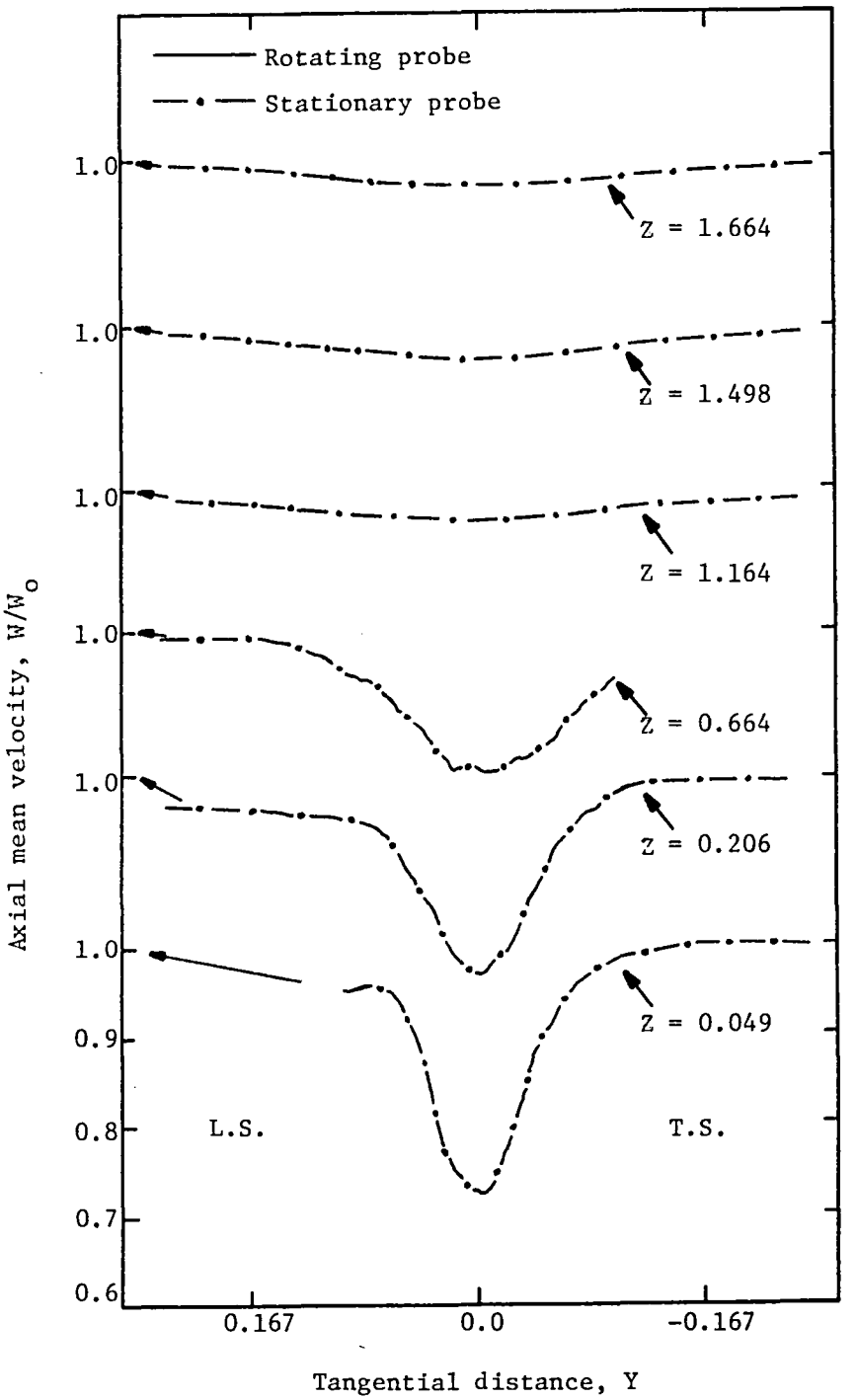

Figure 22. Axial mean velocity profiles for i = 15° and R = .721

incidence operating conditions, the trailing surface becomes the suction side of the uncambered rotor blade while the leading surface is the pressure side. Asymmetry of the wake profiles is discernible even at the far wake stations for Z > .2 at 5°, 10°, and 15° incidences but has become much less pronounced. At the far downstream stations, Z > 1.0, the rotor wake has become symmetric about its centerline. Symmetry in the rotor wake results from wake spreading and mixing with the free stream as well as interchange of momentum and energy between each side of the wake.

The wake profiles shown in Figure 19 for the 0° operating condition do not exhibit the asymmetry measured for the 5°, 10°, and 15° operating conditions. This is expected since the leading and trailing surface boundary layers should be the same for an uncambered rotor blade operating at nearly 0° incidence. It should be noted that at the 0° incidence operating condition the blade row investigated was operating as a weak turbine, resulting in the slightly asymmetry seen in the profiles. No asymmetry is seen in the wake profile at the far downstream station for Z = .420.

At 5°, 10°, and 15° incidence operating conditions, the axial mean velocity profiles show a lower value of the free stream velocity on the pressure side and higher value on the suction side. This is a consequence of the existence of pressure gradients (inviscid effect) across the passage immediately downstream of the trailing edge. This effect is most pronounced at 10° incidence at Z = .021 and has disappeared for Z > .2 for both 5° and 10° incidences. At the 15° incidence operating condition the effect is still discernible for Z >.2. However, for the far downstream

stations (Z > 1.0) this inviscid effect disappears for all of the rotor blade incidences tested.

The variation of the tangential gradients of axial mean velocity in the wake indicate the pronounced change in profile shape downstream of the rotor. At Z stations in the near wake region at the 0°, 5°, 10°, and 15° operating conditions (Figures 19, 20, 21, and 22, respectively) the gradients are large. This characteristic results from the development of the flow as it moved through the rotor blade row and in transition from boundary layer to wake. Spreading of the wake and mixing with the free stream results in the milder velocity gradients shown in the far wake region. The steep gradients of velocity in the near wake, especially near the wake center, represent a very unstable flow condition.

5.3.2 Tangential mean velocity

The relative tangential velocities, normalized by axial velocity in the free stream, W_o, are shown in Figures 23, 24, 25, and 26 for various distances downstream of the blade trailing edge for R = .721 at 0°, 5°, 10°, and 15° incidences, respectively. The tangential velocity profiles at the 5° and 15° operating conditions in the near wake should be viewed with caution. Large discrepancies between the rotating and stationary tri-axial probe results were found for tangential velocities measured in this region as discussed in Section 5.1.2.

For the rotating tri-axial probe data shown in the near wake for 0° and 10° incidences (Figures 23 and 24), the maximum tangential velocity defect is slightly larger than the axial velocity defect for both operating conditions. Comparison of tangential and axial velocity profiles for all rotor blade incidences tested show a rapid decay of the defect from the

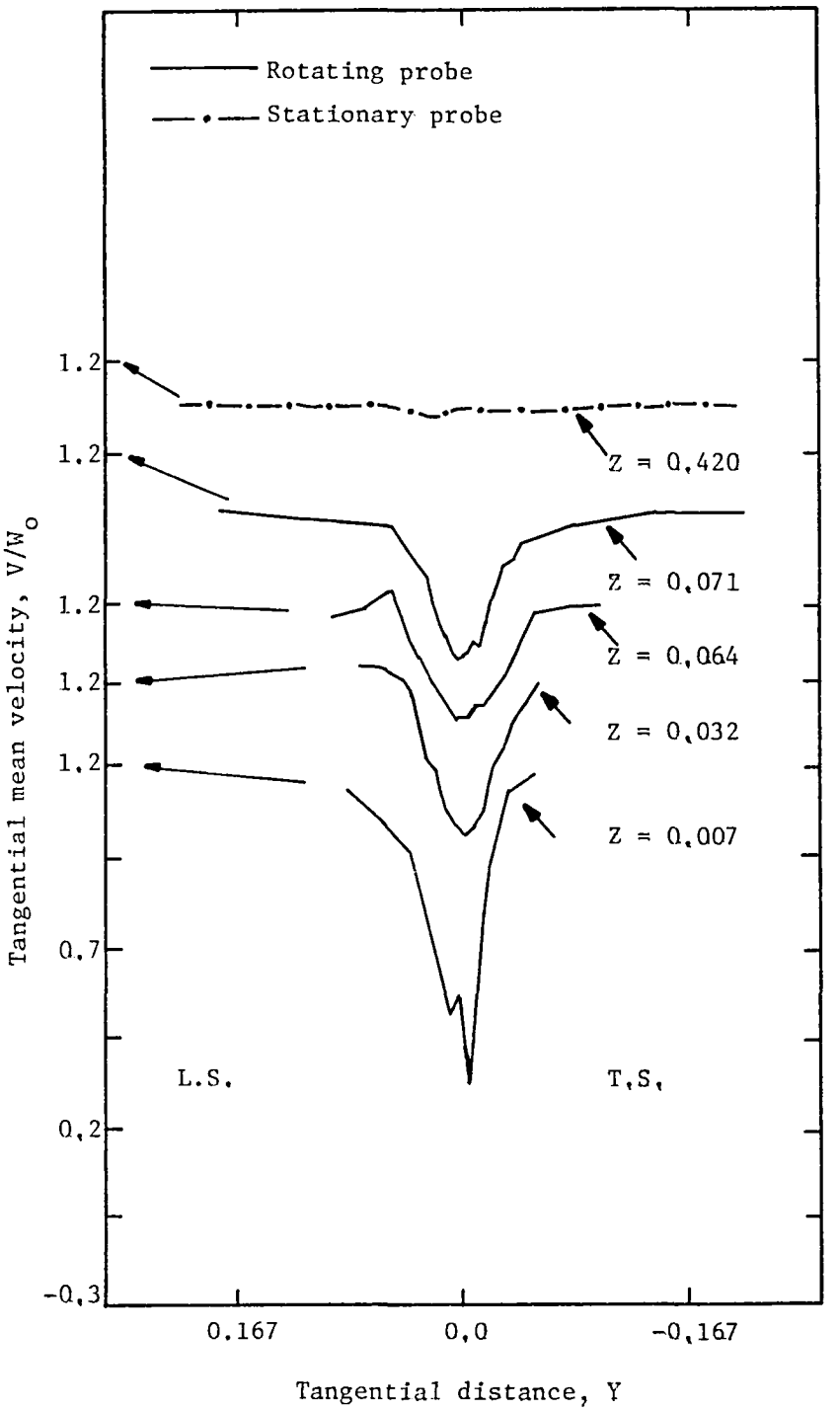

Figure 23. Tangential mean velocity profiles for i = 0° and R = .721

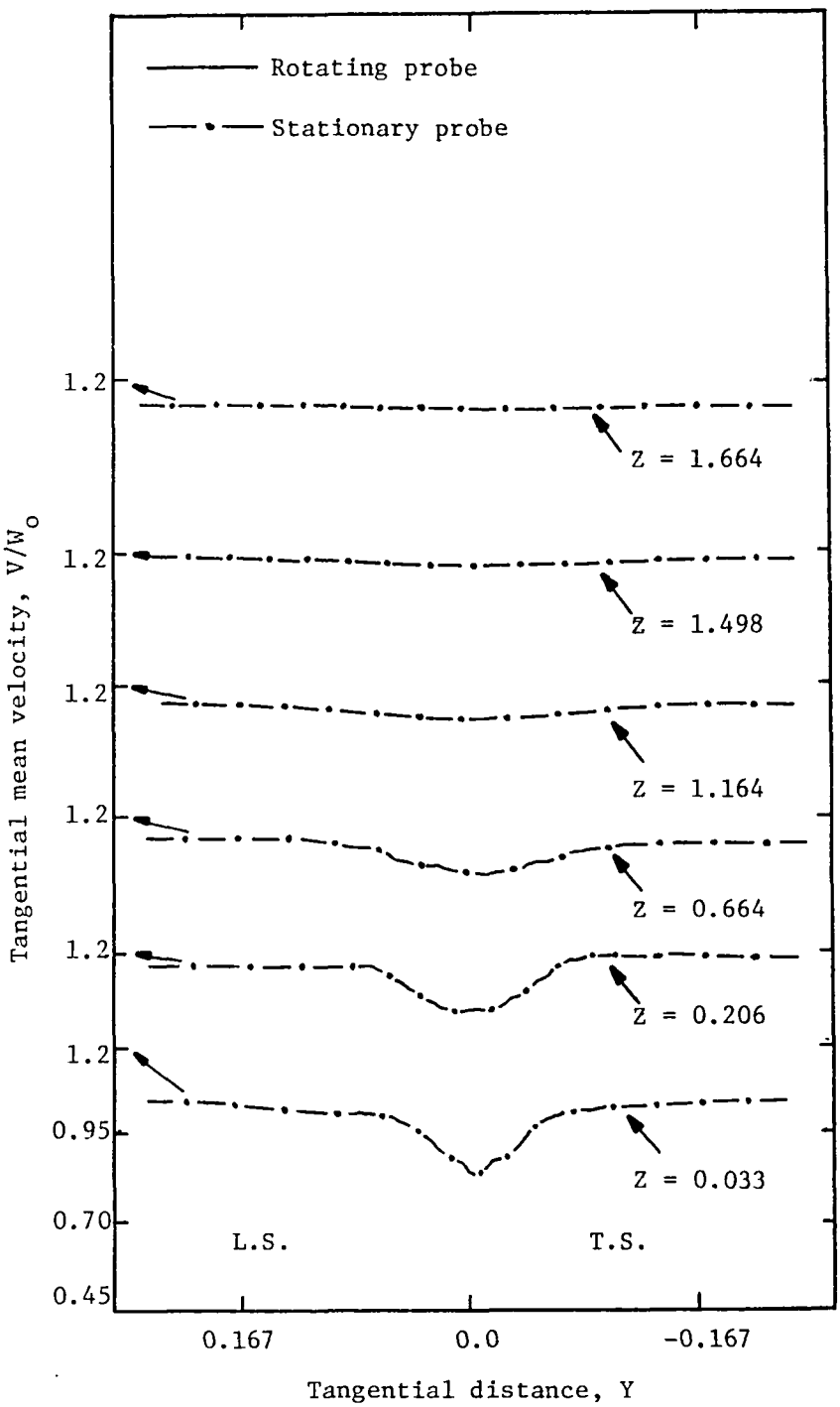

Figure 24. Tangential mean velocity profiles for i = 5° and R = .721

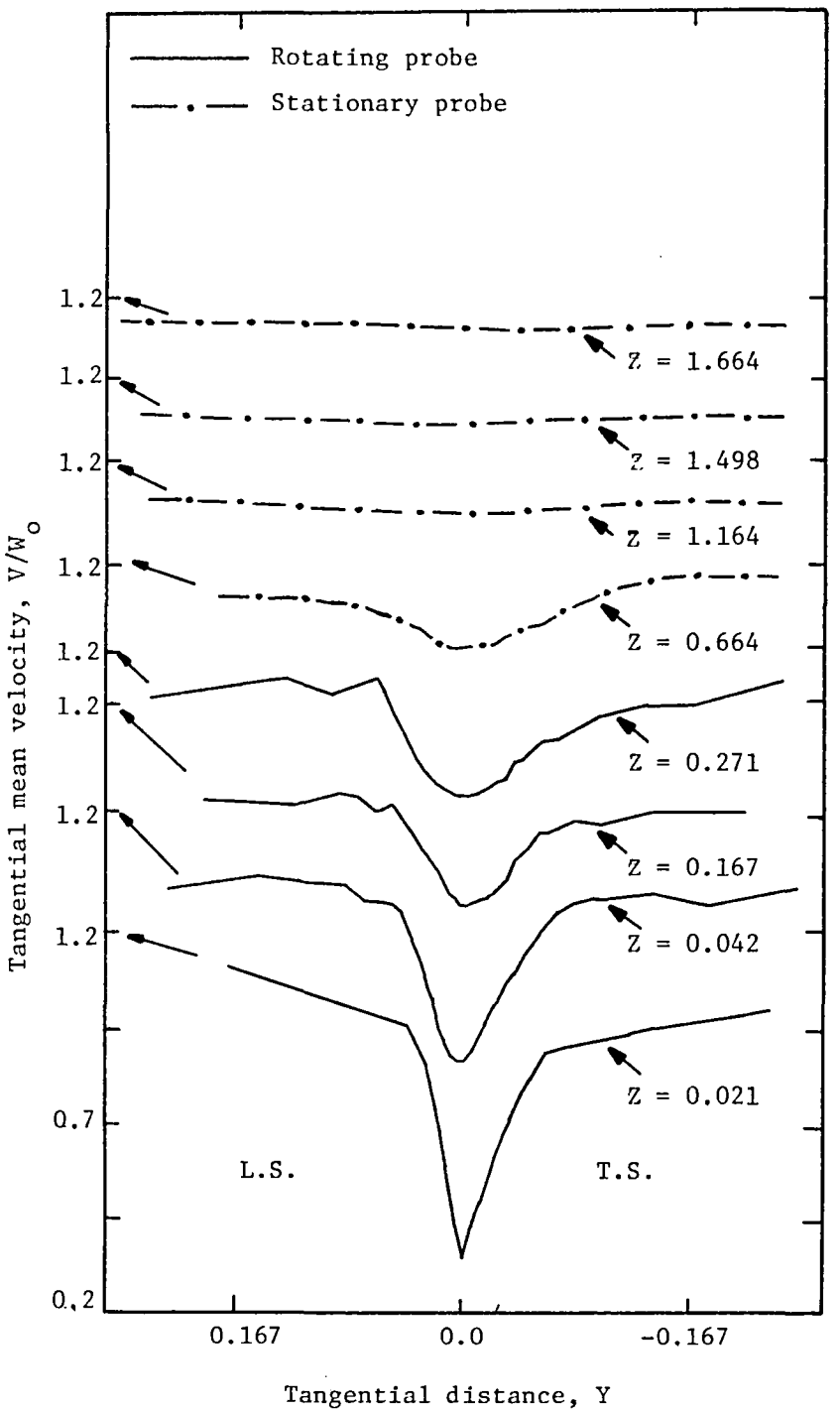

Figure 25. Tangential mean velocity profiles for i = 10° and R = .721

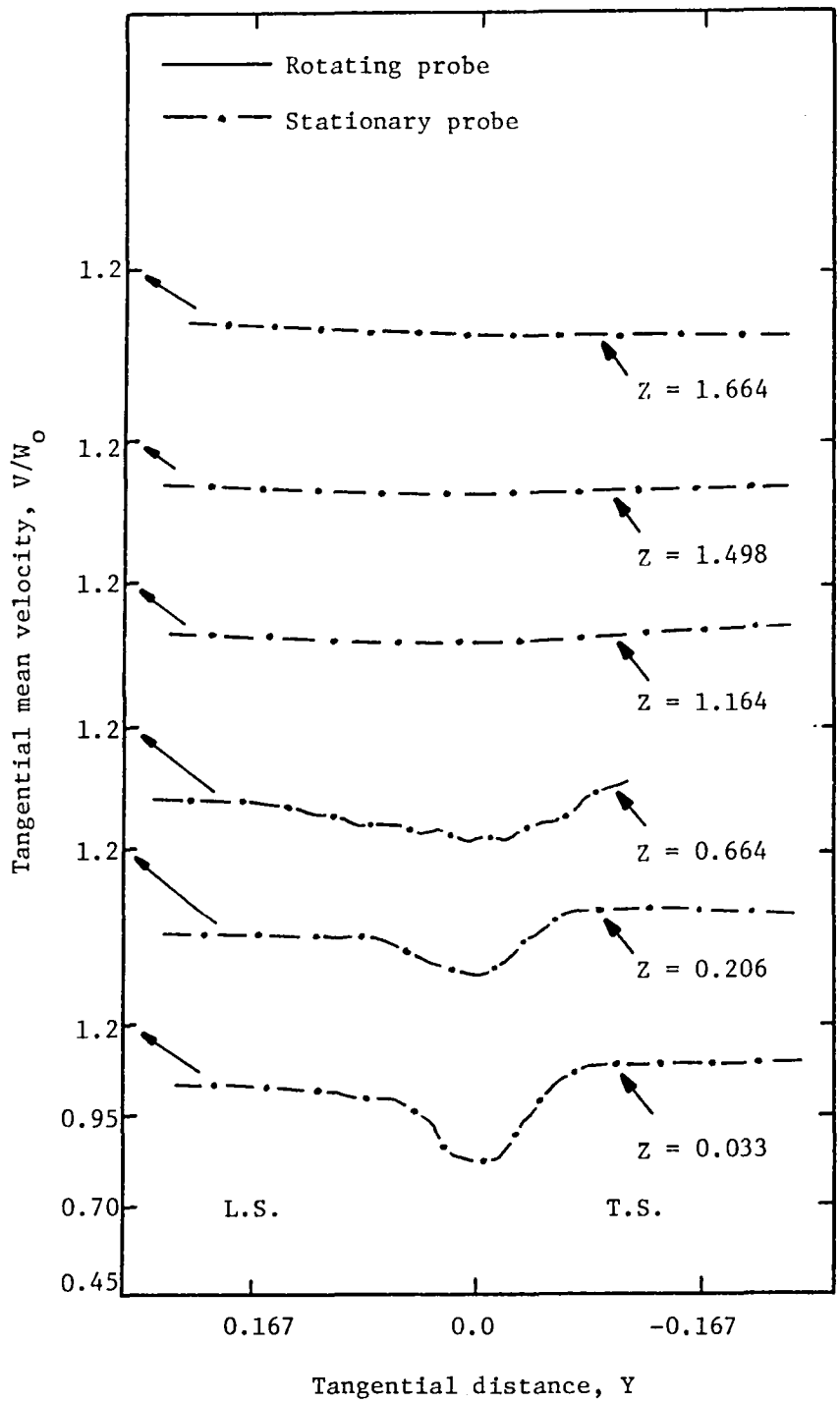

Figure 26. Tangential mean velocity profiles for i = 15° and R = .721

trailing edge to stations at Z > .2, becoming less than twenty percent of the free stream value.

In the near wake region, tangential mean velocity profiles in Figures 24, 25, and 26 (rotor blade incidences of 5°, 10°, and 15°, respectively) are shown to be asymmetric about the wake centerline. At the 0° incidence operating condition shown in Figure 23 the wake profile is approximately symmetric about its centerline. As previously discussed (Section 5.3.1), this characteristic results from boundary layer developments on the leading and trailing surfaces of the rotor blade. However, unlike the axial mean velocity profiles, asymmetry in tangential mean velocity profiles is still clearly discernible at Z > .2 for the 10° and 15° operating conditions. At the far downstream stations (Z > 1.0) tangential mean velocity profiles have become symmetric about the wake centerline.

Similar to axial mean velocity profiles in the near wake region, steep gradients of tangential mean velocity were measured for the 0° and 10° operating conditions. However, at the far downstream stations, Z = 1.164 for i = 10° and Z = 0.420 for i = 0°, the gradients of tangential velocity have become very small. This indicates a more rapid decay of the relative tangential mean velocity defect than that for the axial mean velocity defect in the far wake region. It is possible that the rapid decay of tangential velocity in the far wake region results from an exchange of energy and momentum in the radial direction due to radial velocities in the wake. The radial velocities partially result from an imbalance between radial pressure gradients and centrifugal forces in the rotor wake. It is through this mechanism in which the energy and momentum exchange may take place between tangential and radial velocities in the wake.

5.3.3 Radial mean velocity

Radial mean velocity profiles at R = .721 (mid-radius) with rotor blade incidences of 0°, 5°, 10°, and 15° are shown in Figures 27, 28, 29, and 30, respectively.

At rotor blade incidences of 5°, 10°, and 15°, radially outward velocities near the wake centerline were found to be characteristic of the rotor wake flow. Comparison of Figures 28, 29, and 30 shows an increase in the radial velocities in the outer layer of the rotor wake on the pressure side for increasing blade loading. At i = 15° the largest difference in radial mean velocities between the pressure and suction surface outer layers of the wake is seen. Physically at either surface of the rotor blade trailing edge radial velocities must be zero with a radial velocity distribution such as that found in the outer layer of the wake occuring slightly away from the blade surface. This profile shape may appear as shown in Figure 1. Immediately downstream of the trailing edge, a large redistribution of energy and momentum causes the radial velocity wake profiles shown for i = 5°, 10°, and 15° in the near wake region to result.

In the far wake region for Z > 1.0 the radial velocity difference between the wake and free stream has decayed considerably for the 5°, 10°, and 15° operating conditions. However, for increasing rotor blade incidence the maximum difference between the wake and free stream is shown to increase in the far wake region.

A very complex flow pattern is evident in the radial mean velocity profiles as shown in Figure 27 for the 0° incidence operating condition. Since the rotor was operating weakly as a turbine for i = 0°, the profile shape is reversed from that shown in Figure 28 for i = 5°. A very

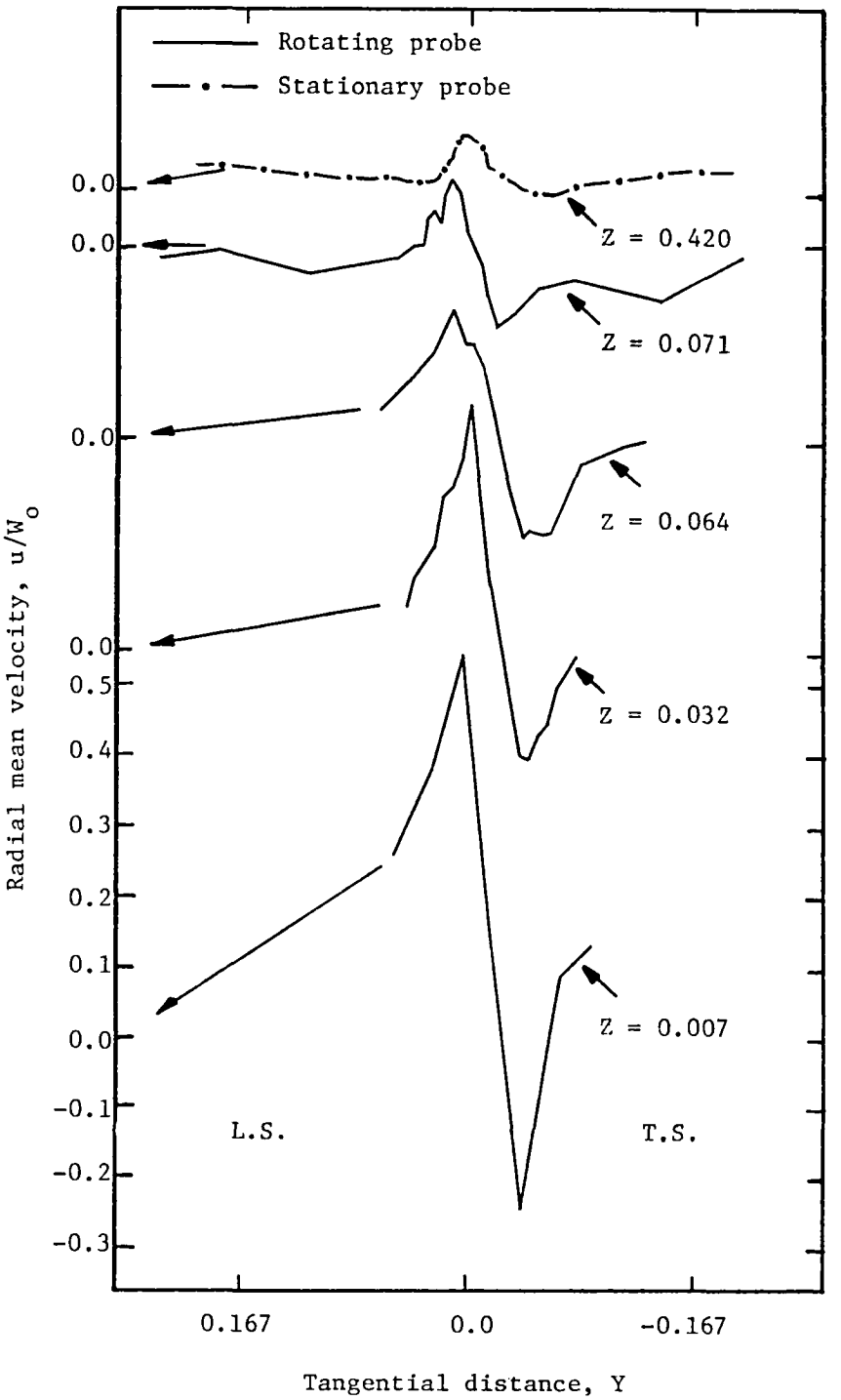

Figure 27. Radial mean velocity profiles for i = 0° and R = .721

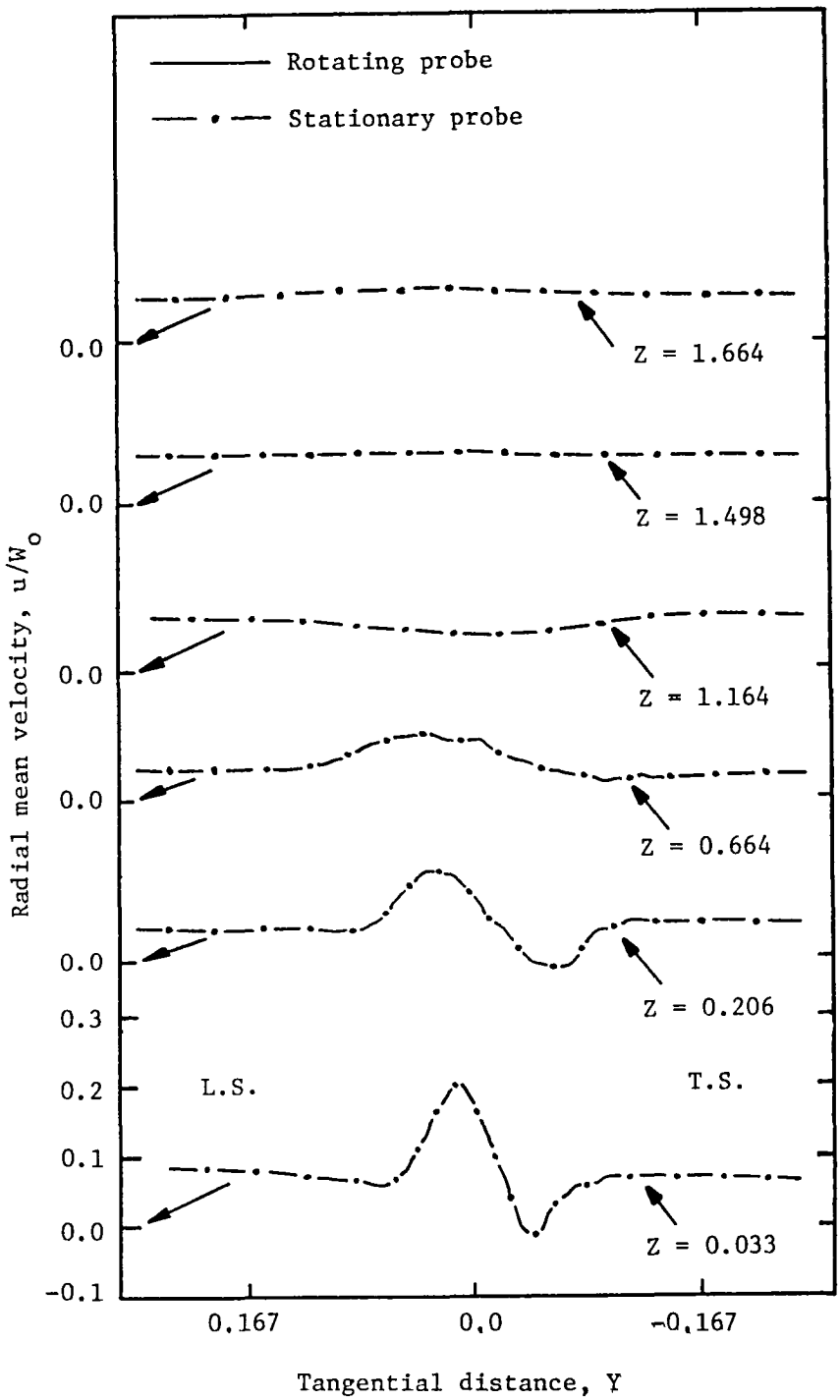

Figure 28. Radial mean velocity profiles for i = 5° and R = .721

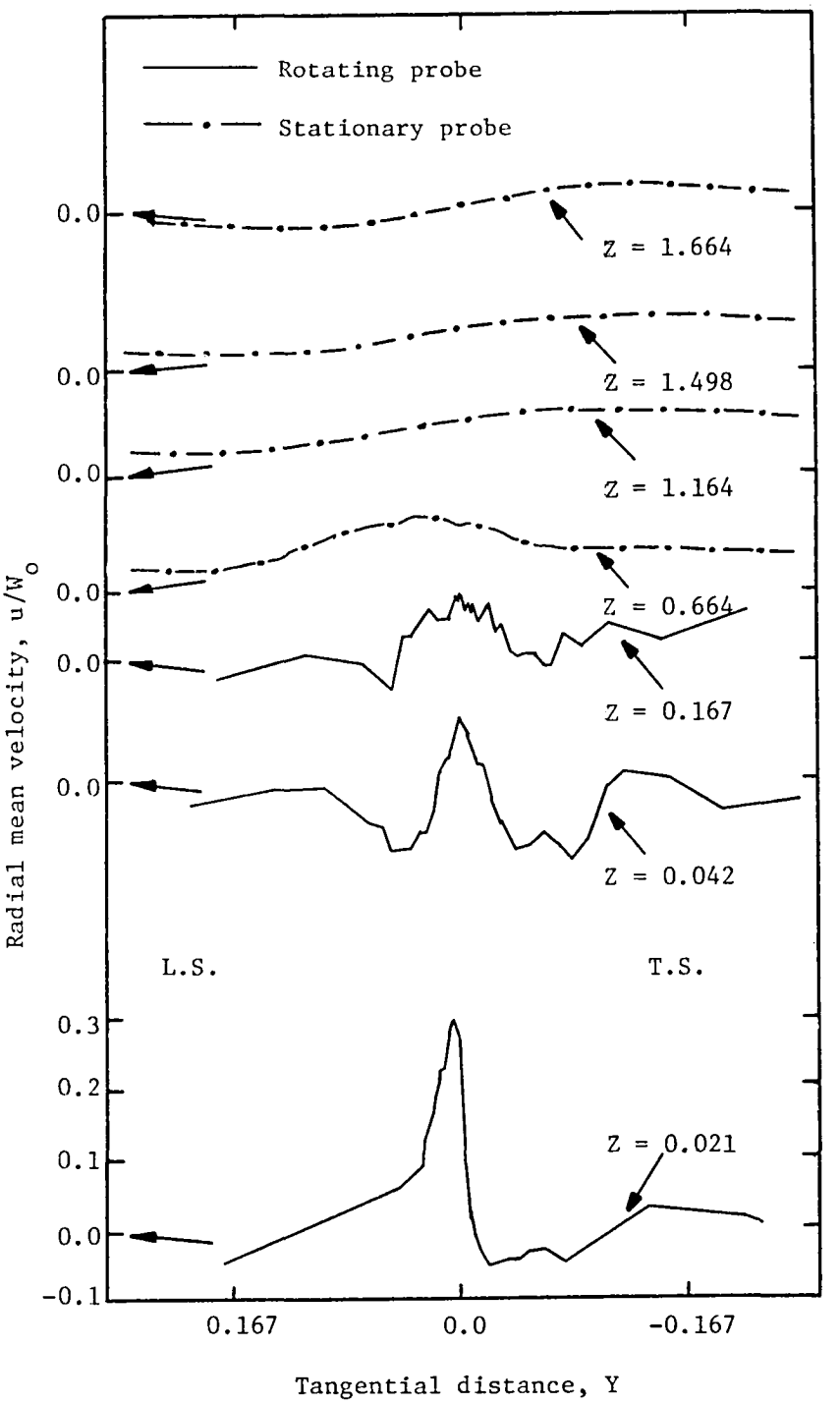

Figure 29. Radial mean velocity profiles for i = 10° and R = .721

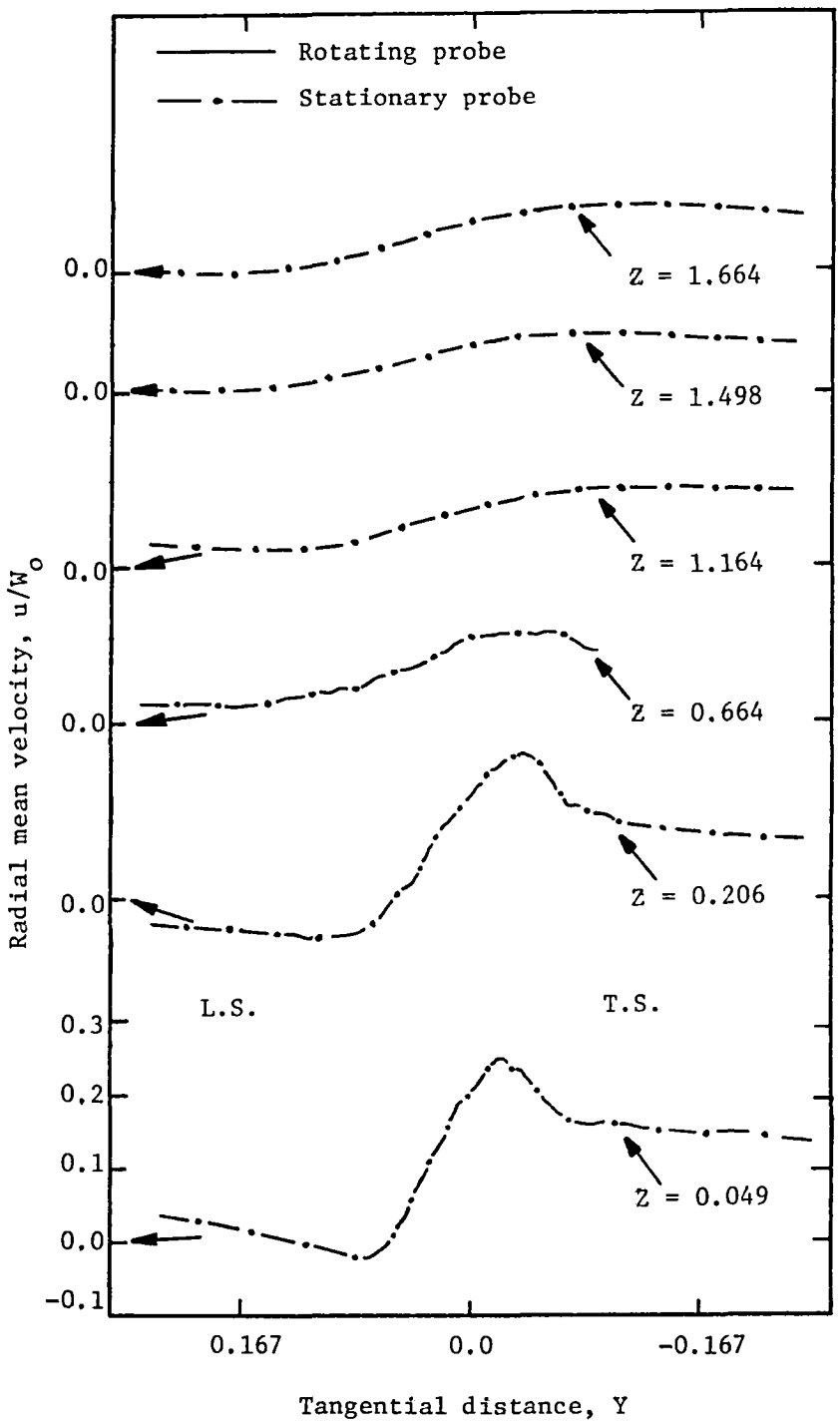

Figure 30. Radial mean velocity profiles for i = 15° and R = .721

unconventional flow pattern at i = 0° results from velocity triangles in the free stream representative of a turbine while those at the wake centerline will be characteristic of a compressor. For this reason no physical explanation of the radial mean velocity profiles at i = 0° is given.

In Figures 27-30 the large radial components of mean velocity in the near wake region indicate the highly three-dimensional nature of the rotor or fan wake. Radially inward or outward flow in the wake will result in an increased dissipation of energy in the rotor wake as compared to a corresponding two-dimensional wake. At positive blade incidences of 5°, 10°, and 15°, a radially outward transport of flow momentum and energy indicates that a complex wake behavior can be expected with increasing radius. This may also account for a large decay of the defect in streamwise mean velocity with no corresponding increase in wake width (discussed later) at this radius (R = .721).

5.3.4 Static pressure

The static pressure distribution across the rotor wake at mid-radius and at an incidence of 10° is shown in Figure 31. In the figure, static pressure coefficient, ψ_s, is shown as a function of tangential position. The static pressure data shows an appreciable variation of static pressures inside the wake as well as in the inviscid free stream. A description of the mechanisms causing the static pressure variations found in the rotor wake is given in Appendix A. The profiles seem to show low pressures at the wake center which then increase gradually to higher values than the free stream near the outer edge of the wake. Thompkins and Kerrebrock (1975) have also reported twenty to 25 percent variations in static pressure at ten percent of the axial chord downstream of a transonic

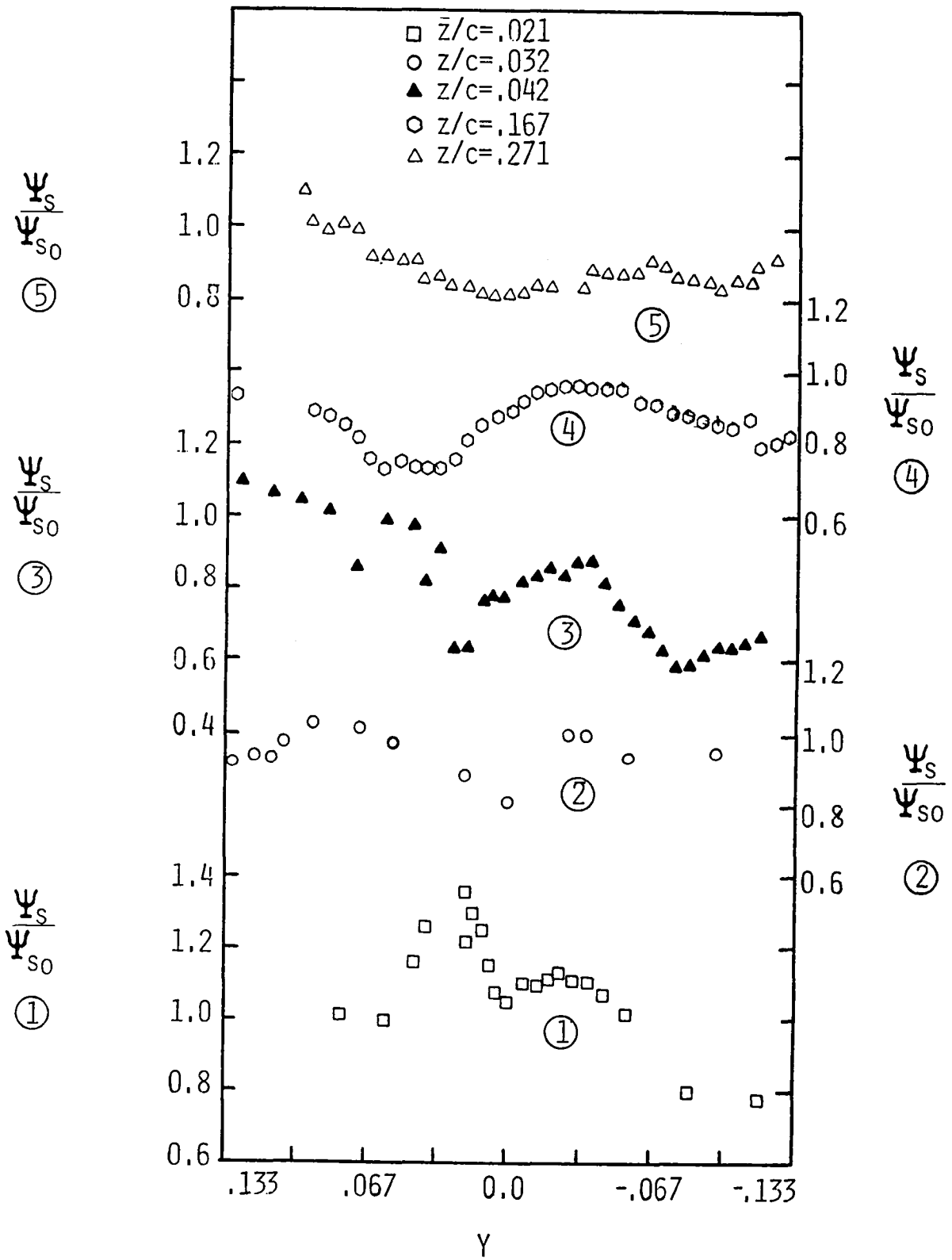

Figure 31. Static pressure variation in rotor wake for i = 10° and R = .721

rotor. Their data seems to confirm the trends described above for the present investigation.

At Z = .021 the static pressure variation in the wake is about 25 percent. Further downstream, the variation of static pressure in the wake is reduced substantially at about 1/4 chord (Z = .271). This characteristic of the static pressure profiles seems to justify some of the assumptions made in Section 2.1. However, one must view the static pressure data with caution. There are spacial errors (finite diameter of probe in a large shear layer) as well as large turbulence intensities measured in the wake flow and these factors may introduce errors in the data.

5.3.5 Axial turbulence intensity

Axial turbulence intensity profiles at mid-radius (R = .721) at rotor blade incidences of 0°, 5°, 10°, and 15° are shown in Figures 32, 33, 34, and 35, respectively. Turbulence intensity has been non-dimensionalized by local mean velocity since turbulence is dependent on local flow conditions.

The axial turbulence intensity profiles in the near wake region are seen to be asymmetric at all of the operating conditions tested. This characteristic results from the difference in the development of turbulence on the leading and trailing surfaces of the rotor blade. Symmetry in the axial intensity profiles is found only at the far downstream stations (Z > 1.0).

All of the axial turbulence intensity profiles in the near wake region show a "dip" at the wake centerline (except at a 5° incidence). The "dip" at the wake centelrine is expected since turbulence intensities in this region are zero at the wake centerline on the surface of the

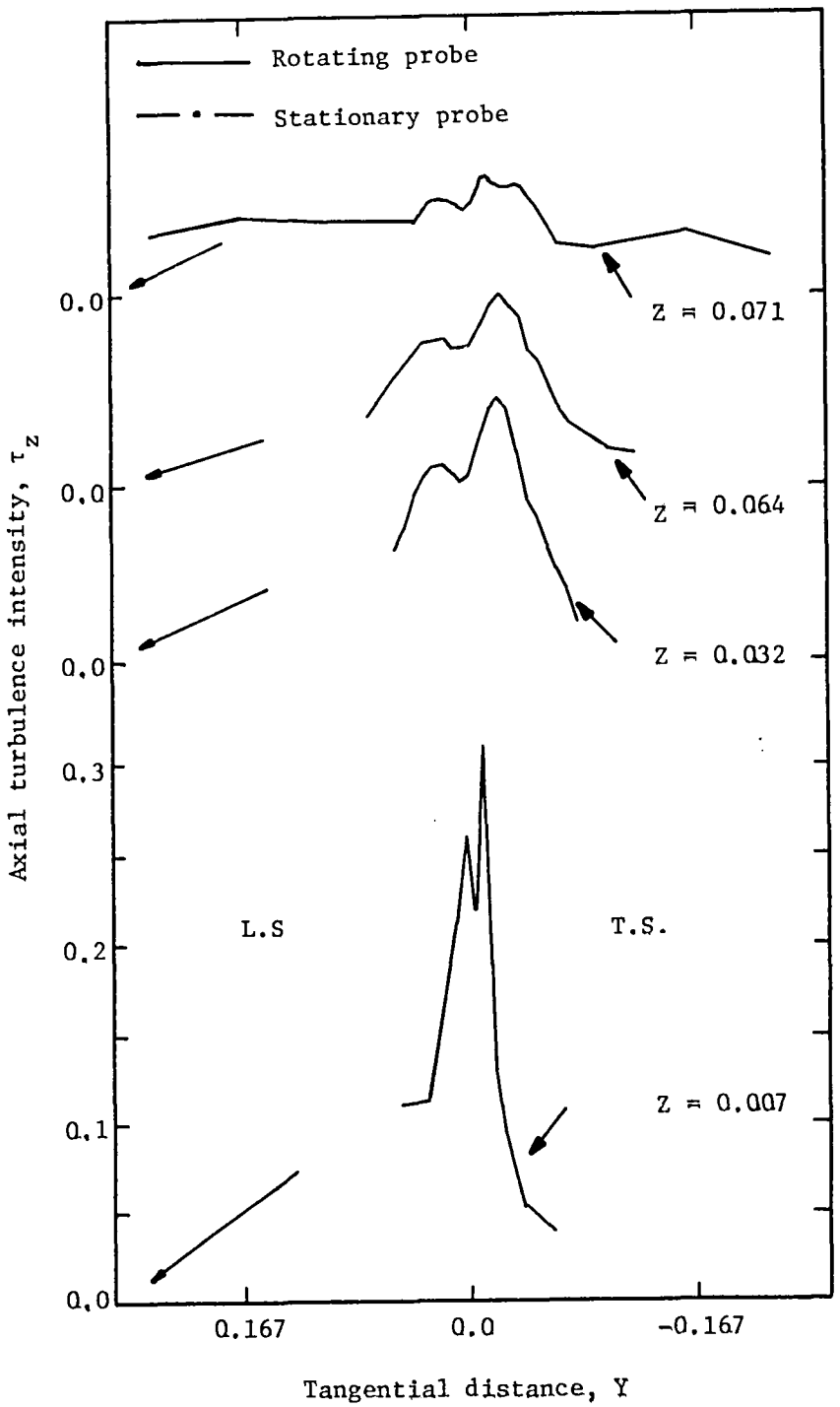

Figure 32. Axial turbulence intensity profiles for i = 0° and R = .721

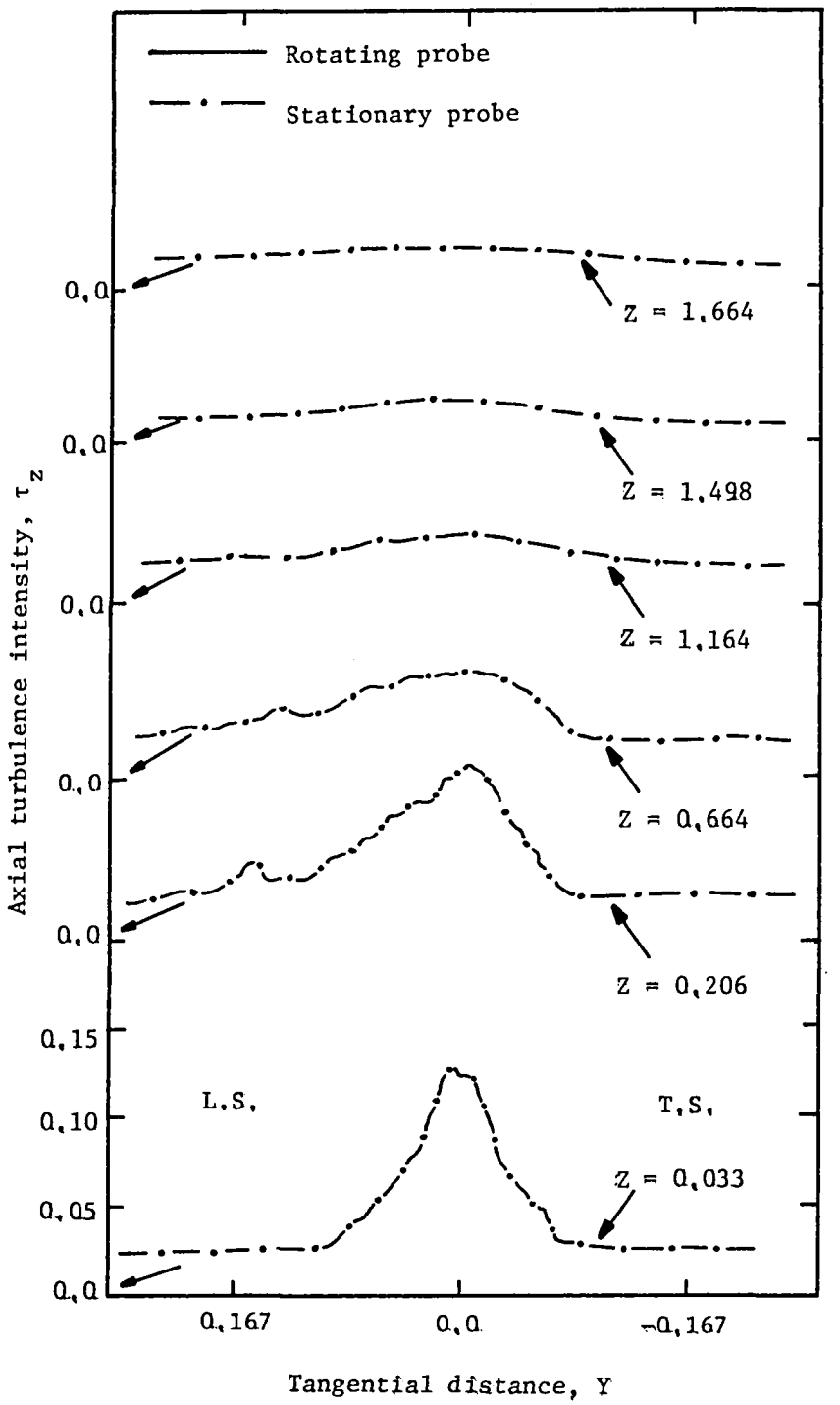

Figure 33. Axial turbulence intensity profiles for i = 5° and R = .721

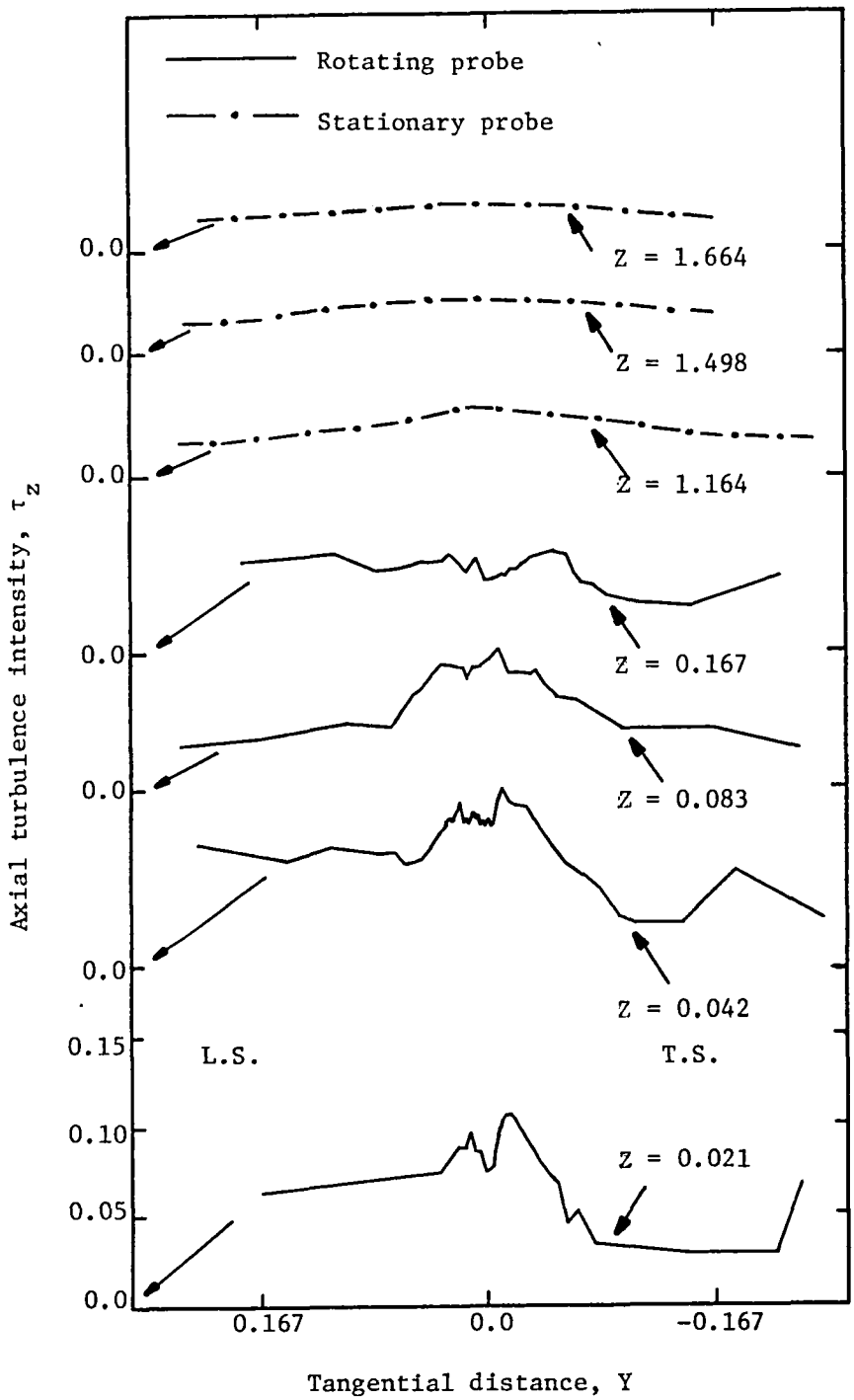

Figure 34. Axial turbulence intensity profiles for i = 10° and R = .721

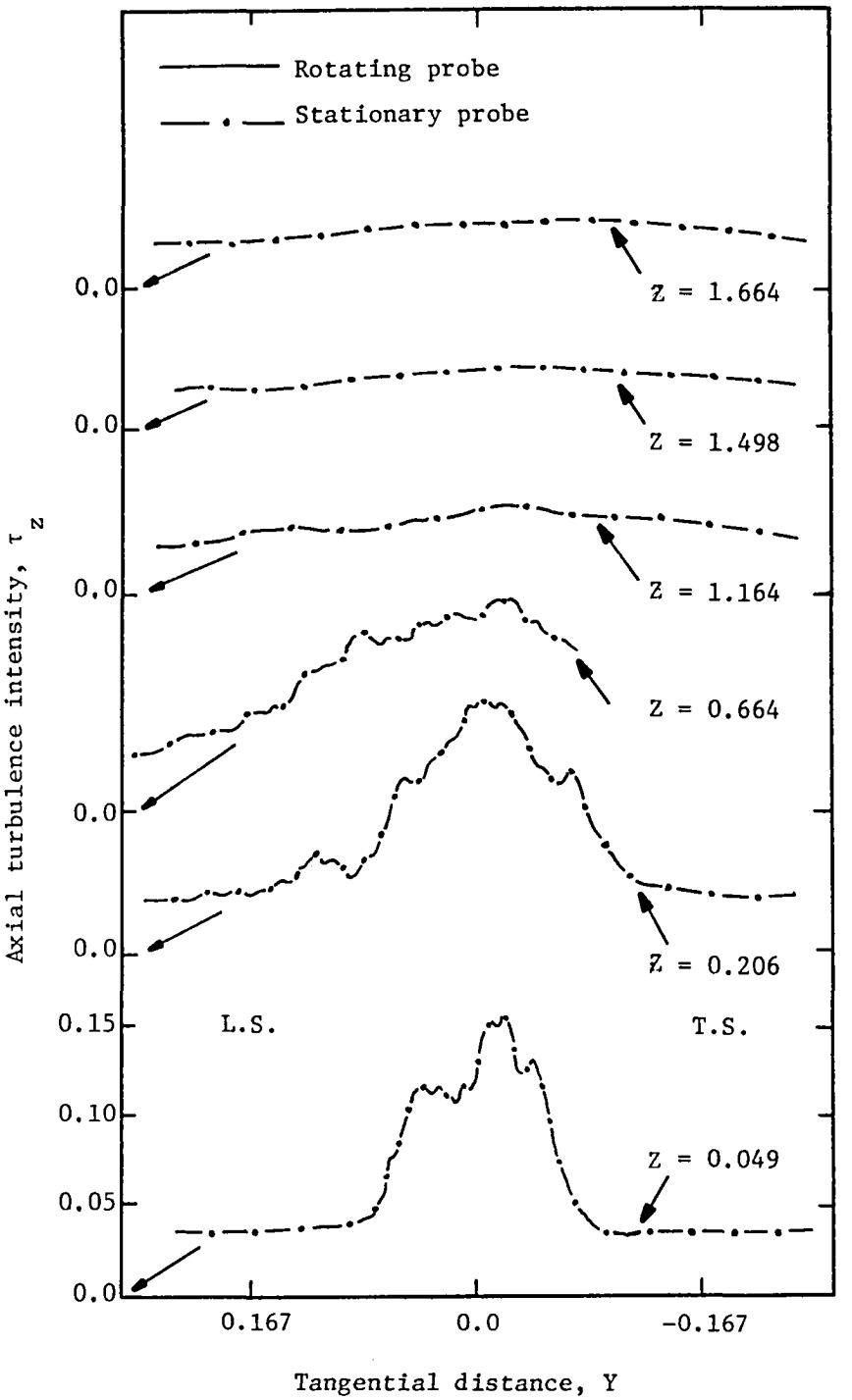

Figure 35. Axial turbulence intensity profiles for i = 15° and R = .721

rotor blade trailing edge. Maximum intensities will occur slightly away from each surface. The intensity peaks in the near wake region show a larger value on the suction side (trailing surface) for positive blade incidences of 10° and 15°. This characteristic is also found for i = 0° where (as previously discussed) velocity triangles near the wake center at this operating condition represent those for a compressor. No "dip" is shown in the near wake region for data at a blade incidence of 5°. At this operating condition the "dip" may have existed, but in a region too narrow to measure accurately. The i = 5° profile shape may also indicate a more rapid redistribution of energy and momentum than that found for i = 10° and i = 15° in the near wake region.

Free stream axial turbulence intensities shown in Figures 32, 33, 34, and 35 result from the inlet flow conditions (discussed in Section 5.2) to the rotor. An inlet turbulence of approximately two percent does not show any appreciable amplification after moving through the rotor blade row. Free stream axial turbulence intensity downstream of the rotor is at a level of approximately 2.5 percent.

Stationary probe axial turbulence intensity data shown in Figures 33 and 35 for rotor blade incidences of 5° and 15°, respectively, show a significantly larger turbulence intensity at Z = .206 and Z = .664 than was measured by the rotating tri-axial probe in these regions (Figure 34). The large turbulence intensities in the wake measured by the stationary probe at these stations do not exhibit an expected monotonically decaying characteristic in this region. No physical explanation of what mechanisms may cause this phenomena is presently offered and the data should be viewed with caution at these stations.

5.3.6 Tangential turbulence intensity

Tangential turbulence intensity profiles are shown in Figures 36, 37, 38, and 39 at mid-radius for rotor blade incidences of 0°, 5°, 10°, and 15°, respectively. As with the axial intensity profiles, tangential turbulence intensities have been non-dimensionalized by local axial mean velocities.

Asymmetries in tangential intensity profiles are clearly seen for measurements made at all rotor blade incidences in the near wake region. This characteristic is similar to that found for axial turbulence intensity profiles in the near wake region, with different boundary layers developing on the pressure and suction surfaces of the rotor blade. At $i = 0°$ the velocity triangles in the boundary layers near the blade surfaces and near the wake center are like that for a compressor, resulting in the asymmetry found for these profiles. Symmetry is obtained only far downstream of the rotor ($Z > 1.0$) where tangential intensities have decayed to a level only slightly greater than free stream.

Unlike the axial component of turbulence intensity, no "dip" is found at the wake centerline for the tangential intensity profiles at all rotor blade incidences. This indicates that in the inner layer of the wake a larger redistribution of energy and momentum occurs for tangential intensities near the rotor blade trailing edge than that for the axial intensities. However, tangential intensities in the inner layer still show distinctly different profiles on the pressure and suction sides of the wake for the 0°, 10°, and 15° operating conditions. At 10° and 15° maximum intensities are found on the pressure side of the wake which is opposite to that found for the axial component of intensity. The turbulence structure is shown here to differ greatly between the axial

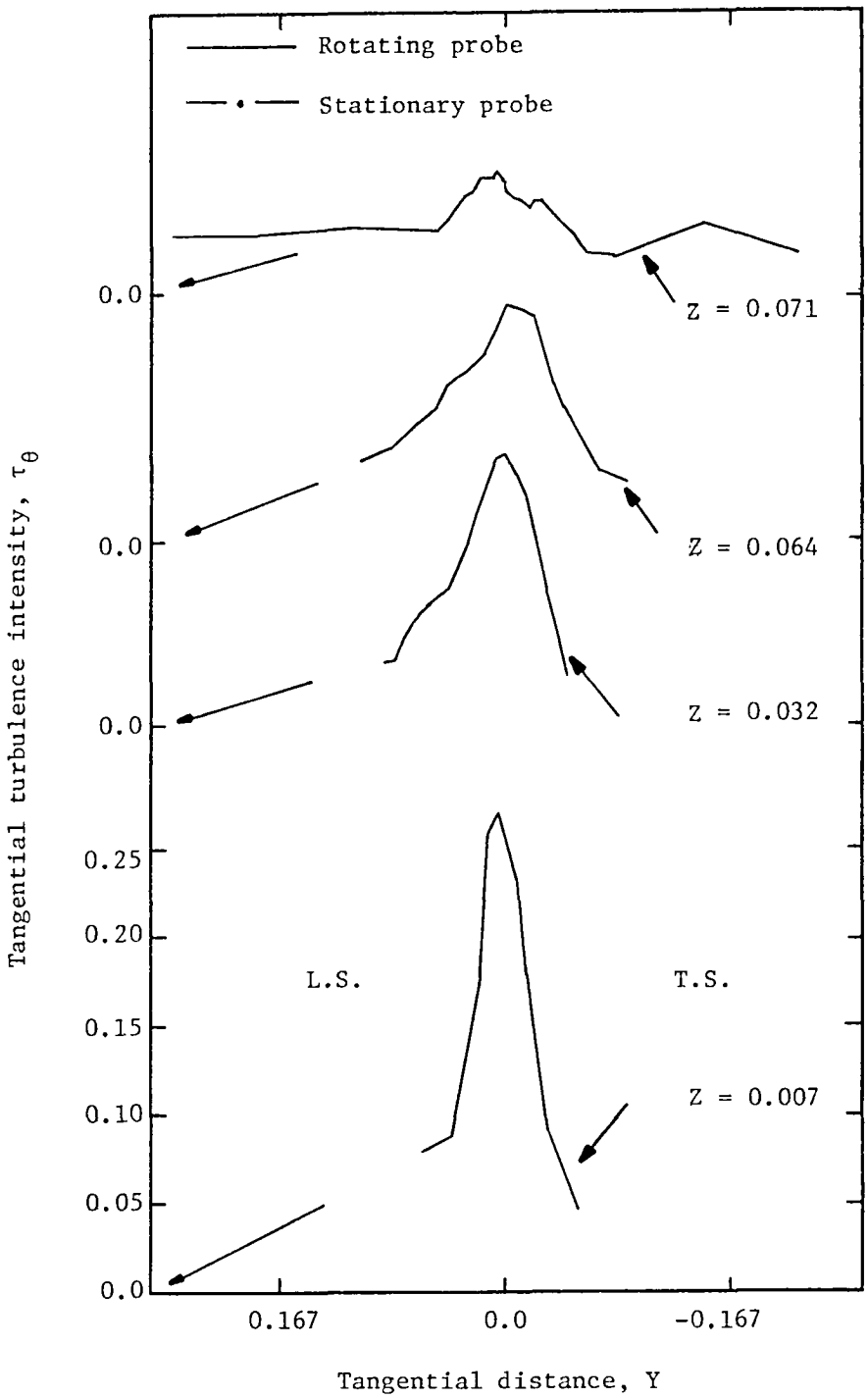

Figure 36. Tangential turbulence intensity profiles for i = 0° and R = .721

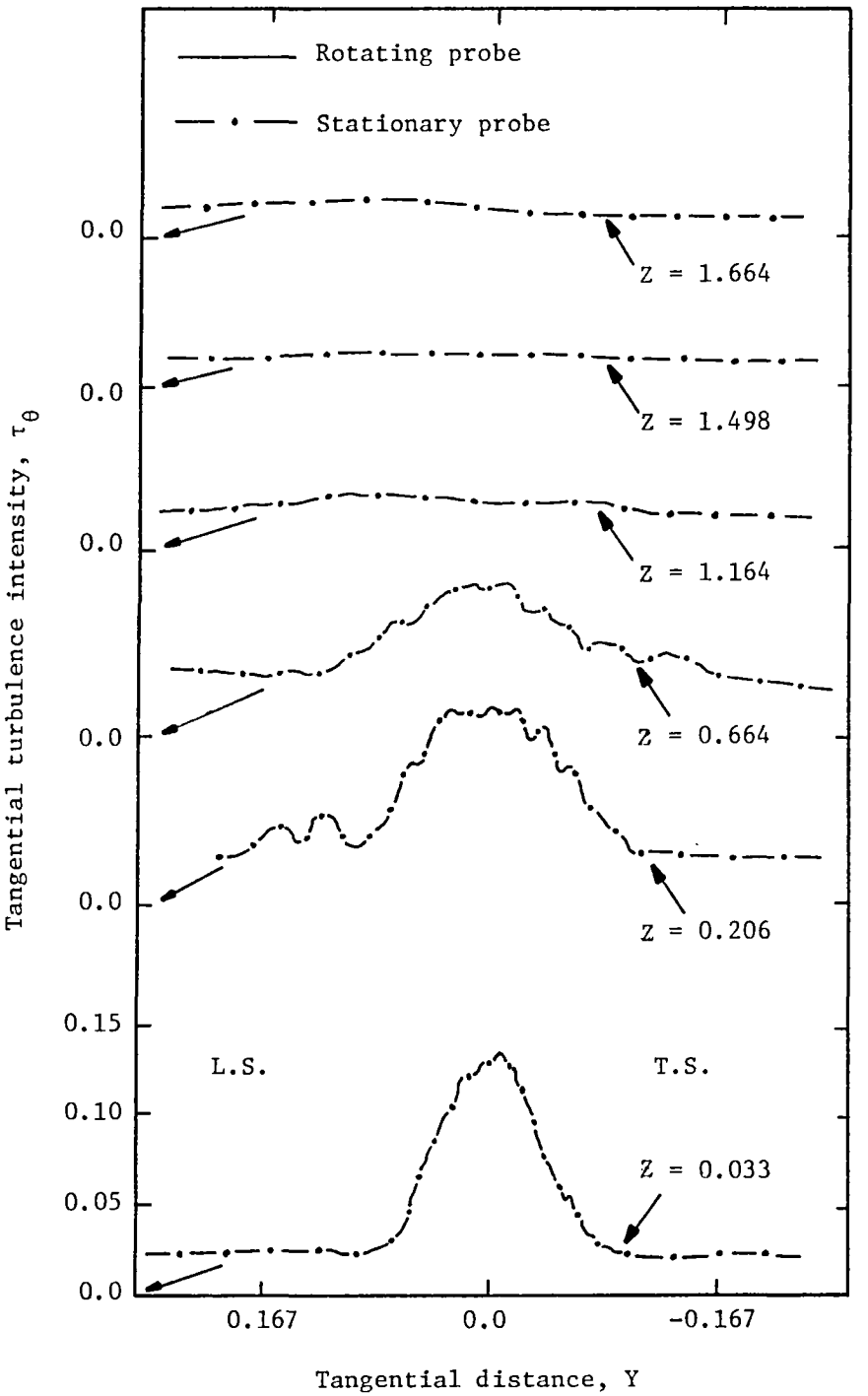

Figure 37. Tangential turbulence intensity profiles for i = 5° and R = .721

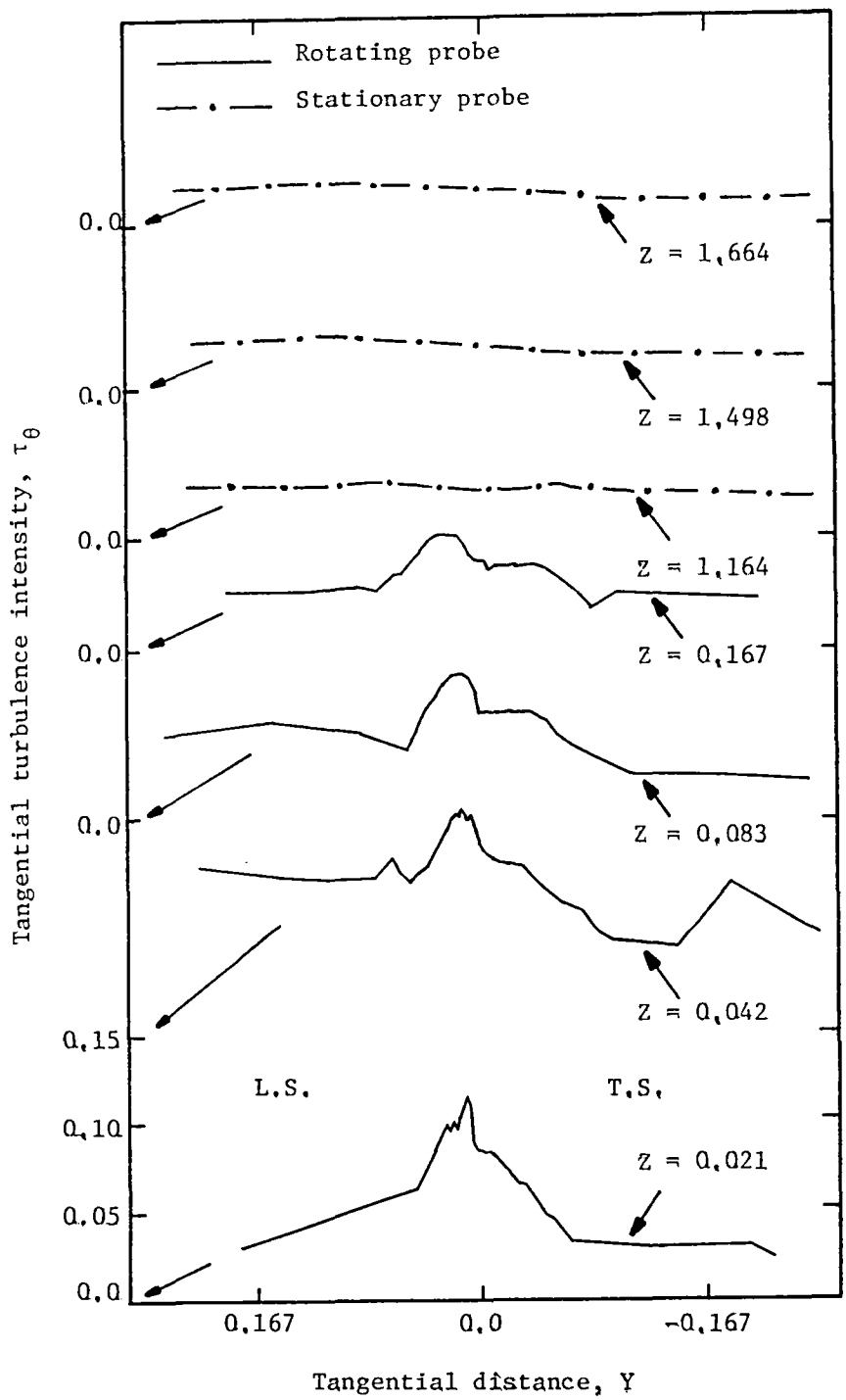

Figure 38. Tangential turbulence intensity profiles for i = 10° and R = ,721

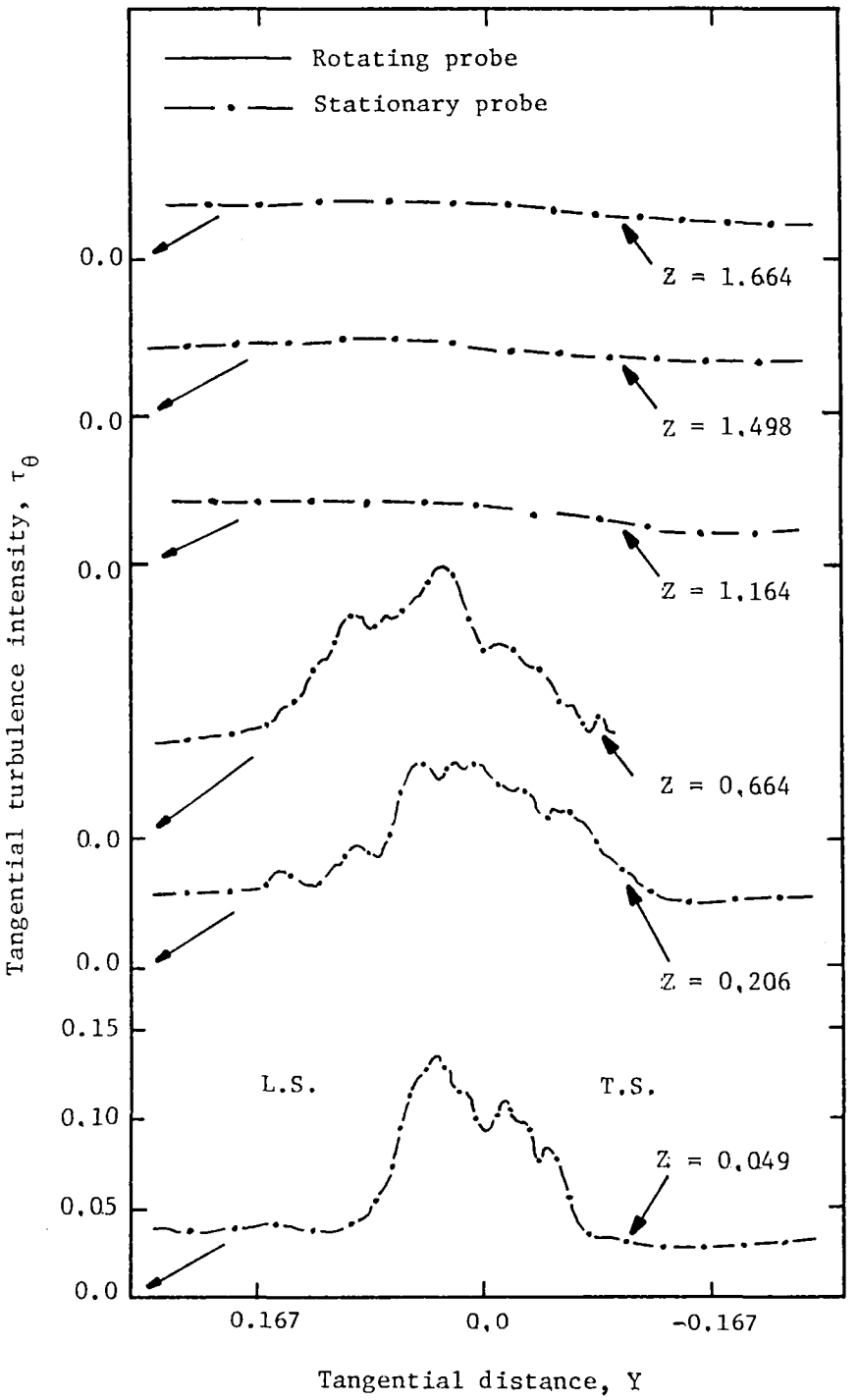

Figure 39. Tangential turbulence intensity profiles for i = 15° and R = .721

and tangential components of intensity. This turbulence property is not evident for the tangential intensity profiles at 5° incidence. As previously discussed, a larger redistribution of energy and momentum might occur near the trailing edge at this operating condition. The above characteristics are not found for the far downstream stations (Z > 1.0). Comparison of the magnitudes of axial and tangential components of turbulence intensity in the wake indicates that they are of the same order for all rotor blade incidences tested. This characteristic is evident in both the near and far wake regions.

5.3.7 Radial turbulence intensity

Radial turbulence intensity profiles at rotor blade incidences of 0°, 5°, 10°, and 15° are shown in Figures 40, 41, 42, and 43, respectively. In all of the above figures radial turbulence intensity has been non-dimensionalized by local axial mean velocity.

Radial intensity profiles are asymmetric in the near wake region for all rotor blade incidences as was found for the axial and tangential components. Symmetry is shown only at the far downstream stations (Z > 1.0) at all operating conditions.

An intensity "dip" at the wake centerline was not found at any of the near wake measurement stations at rotor blade incidences of 5°, 10°, and 15°. The intensity "dip" characteristic is observed only at the 0° incidence operating condition at Z = .007. This indicates that the redistribution of energy and momentum for the radial turbulence intensities is more rapid than that for the axial intensities. The large redistribution seems to be comparable to that found for the tangential components of turbulence intensity. While no intensity "dip" is exhibited in the wake profiles, a large maximum intensity is shown on the pressure (leading

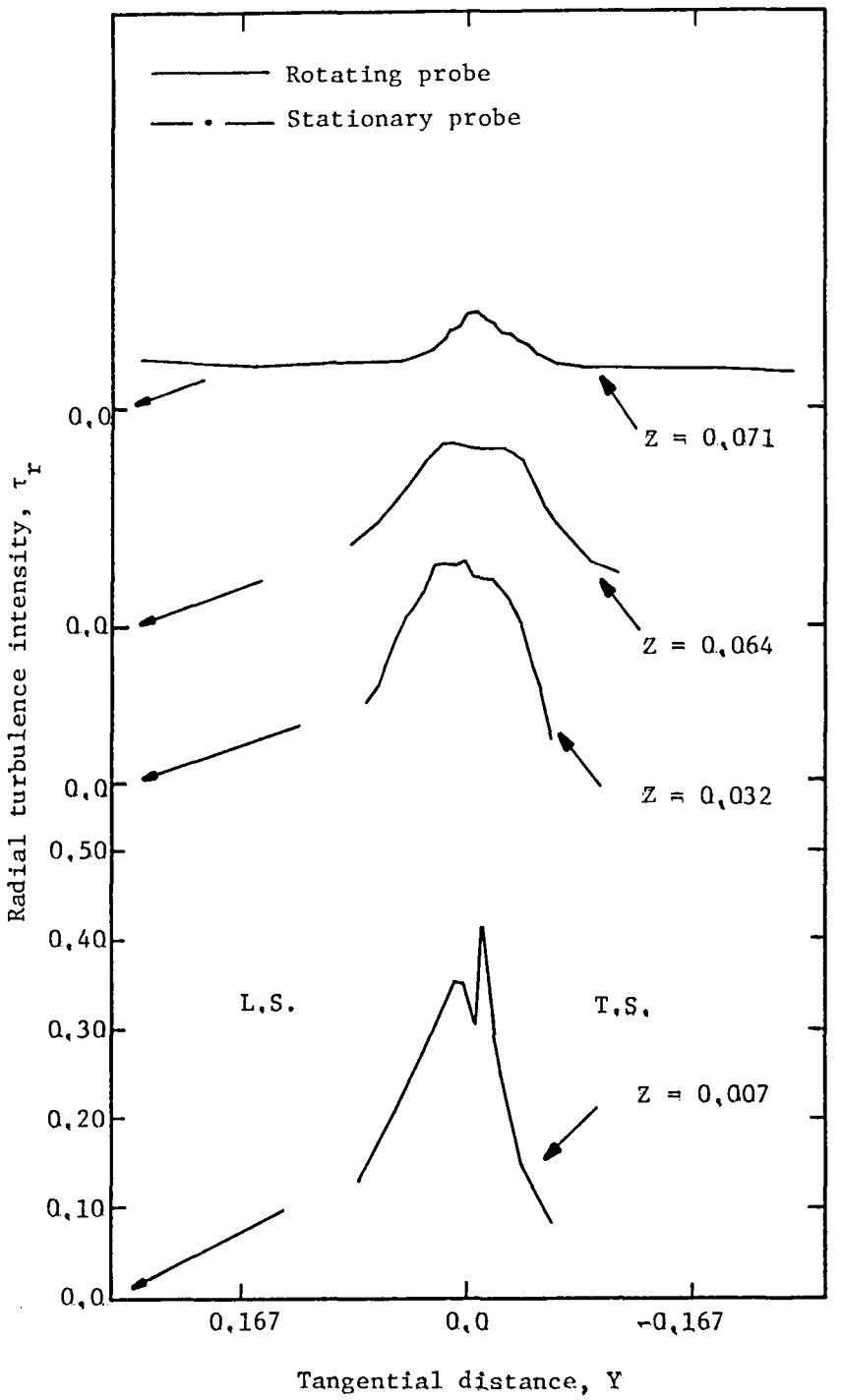

Figure 40. Radial turbulence intensity profiles for i = 0° and R = ,721

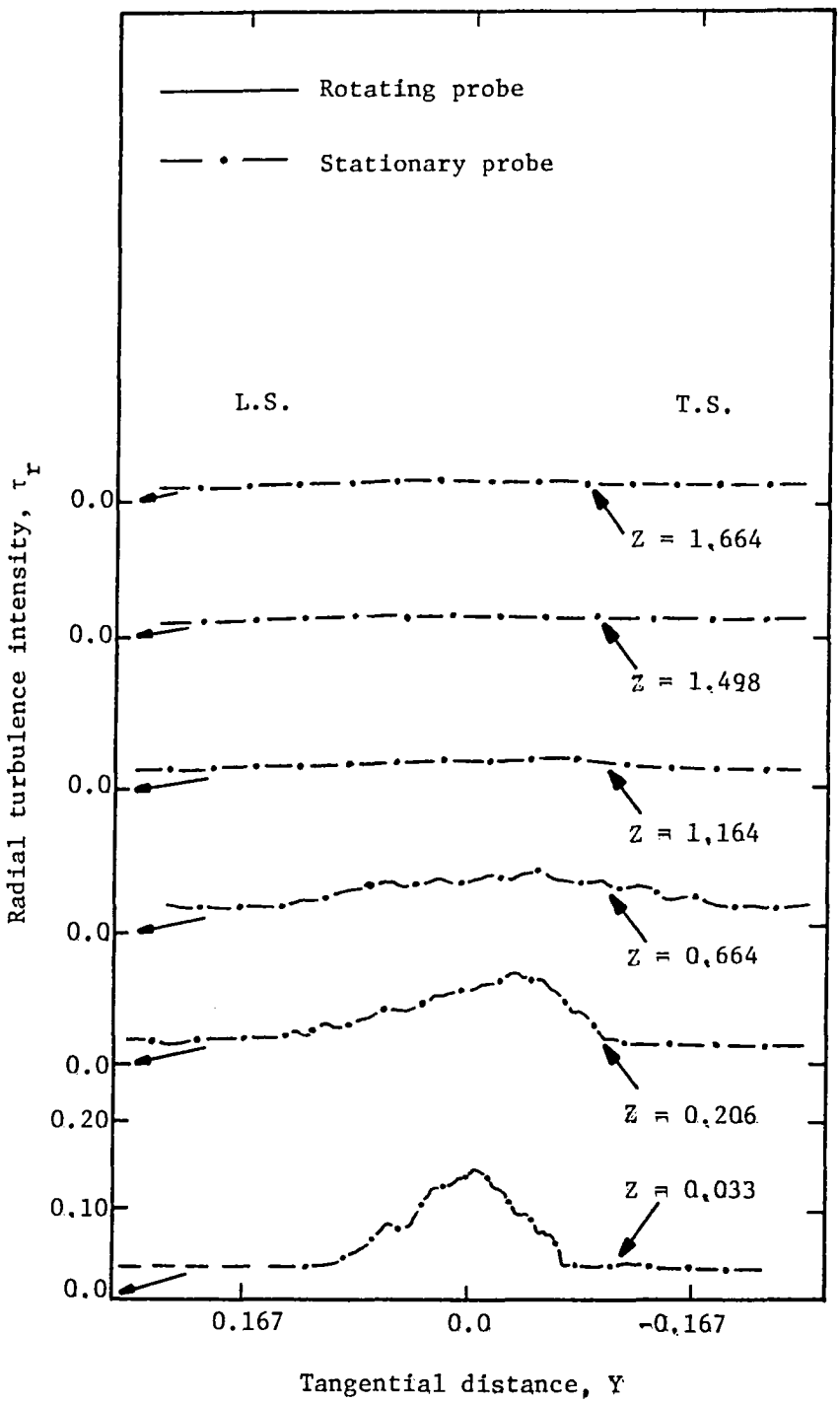

Figure 41. Radial turbulence intensity profiles for i = 5° and R = .721

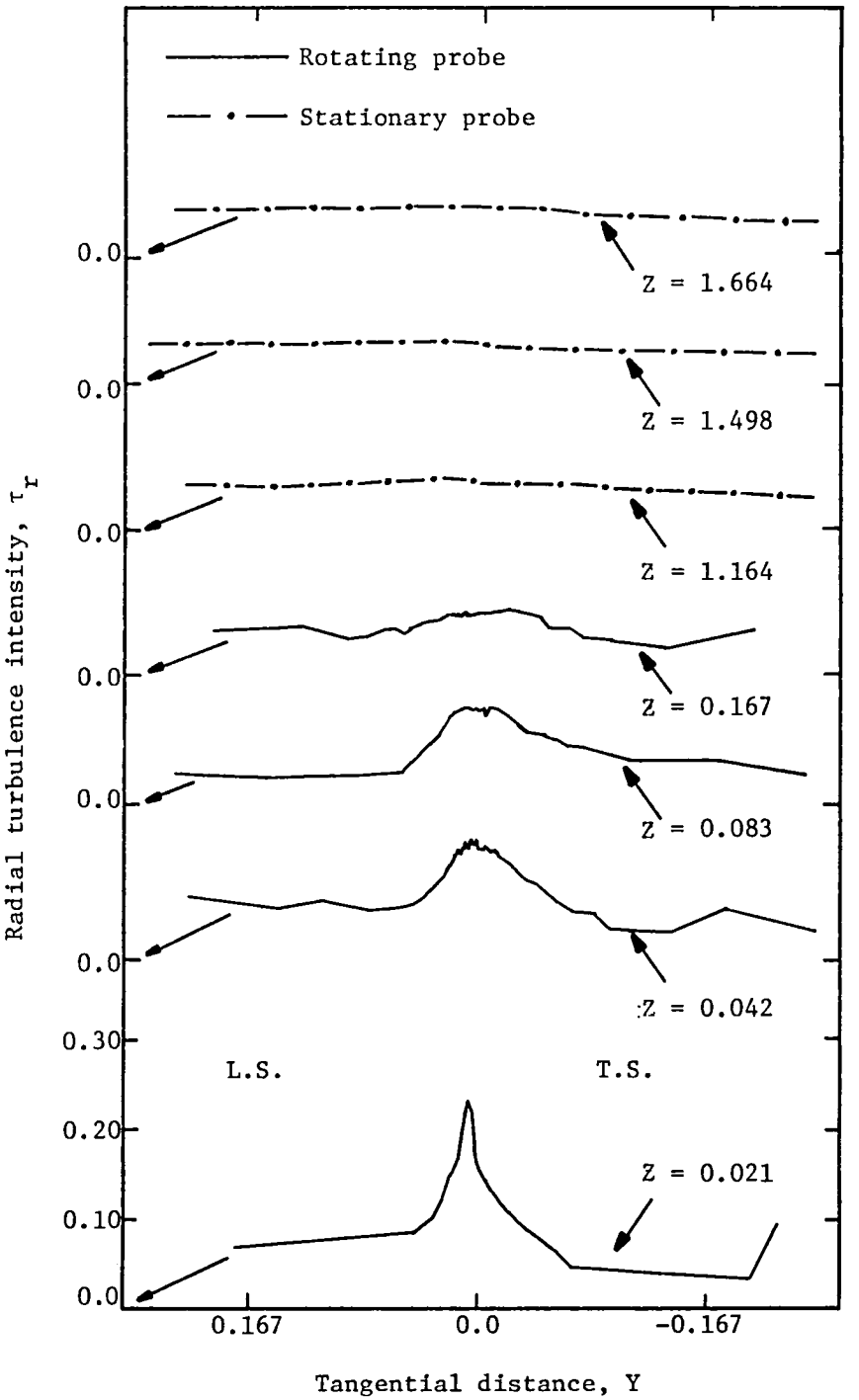

Figure 42. Radial turbulence intensity profiles for i = 10° and R = .721

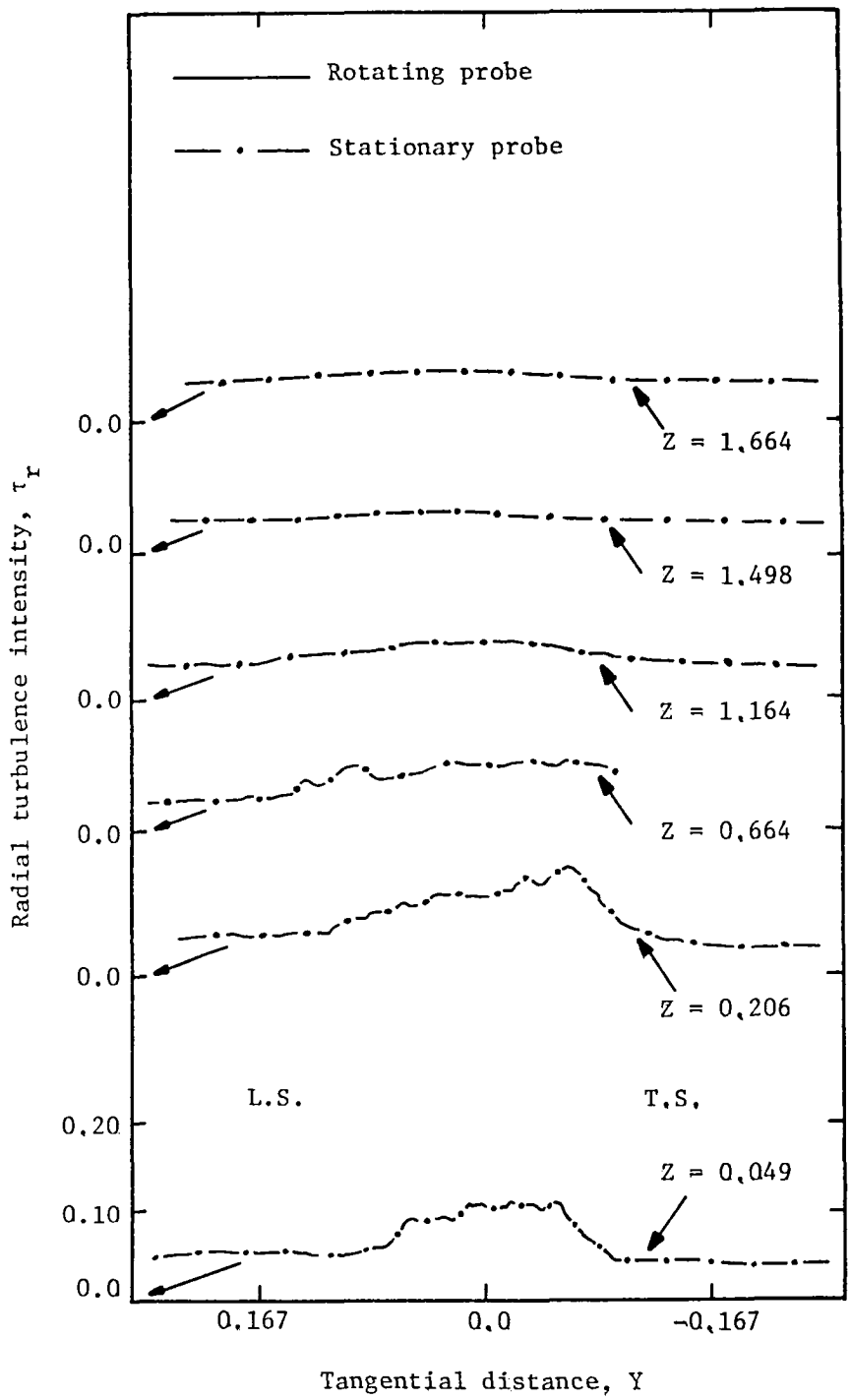

Figure 43. Radial turbulence intensity profiles for i = 15° and R = .721

surface) side for the near wake profile at $i = 10°$, $Z = .021$. This characteristic is not found for the near wake station at $i = 10°$, $Z = .042$. Data at all other blade incidences do not exhibit any large intensity peaks away from the wake centerline for measurement stations shown in the near wake region.

Radial intensities in the free stream are found to be approximately three to four percent for all rotor blade incidences tested. This is slightly larger than that found for the axial and tangential components.

The existence of the large radial components of intensities exhibits the three-dimensional nature of the rotor or fan wake flow. Large radial intensities result from centrifugal and Coriolis force effects on the rotor blade boundary layers and on the wake flow. This is evident from the boundary layer measurements on a rotor blade reported by Anand and Lakshminarayana (1978) where the radial component was dominant. Rotation effects are significant in the turbulence intensity structure of the rotor wake and show a marked change for varying blade loading.

5.3.8 Streamwise and radial components of Reynolds stress

Variations of streamwise and radial Reynolds stresses of rotor blade incidences of 5°, 10°, and 15° are shown in Figures 44 and 45, 46 and 47, and 48 and 49, respectively. Reynolds stress was non-dimensionalized in all of the above figures by local dynamic pressure based on streamwise velocity.

Figures 44, 46, and 48 show the expected positive, negative streamwise Reynolds stress distribution about the wake centerline. The positive, negative stress distribution results from opposite gradients of streamwise mean velocity in the normal direction ($\partial Q/\partial n$) about the centerline. However, the location of zero streamwise Reynolds stress is

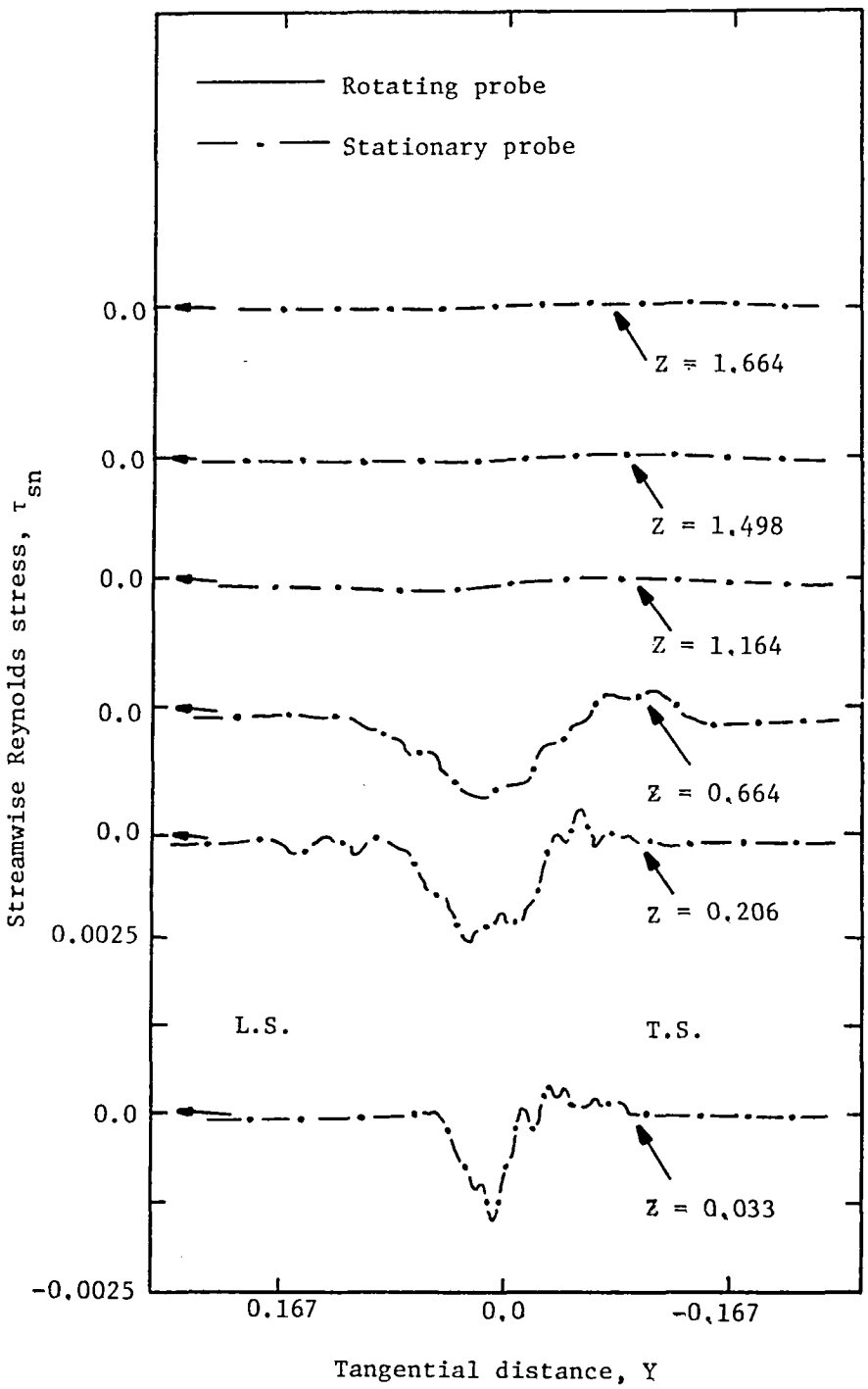

Figure 44. Streamwise Reynolds stress distribution for i = 5° and R = .721

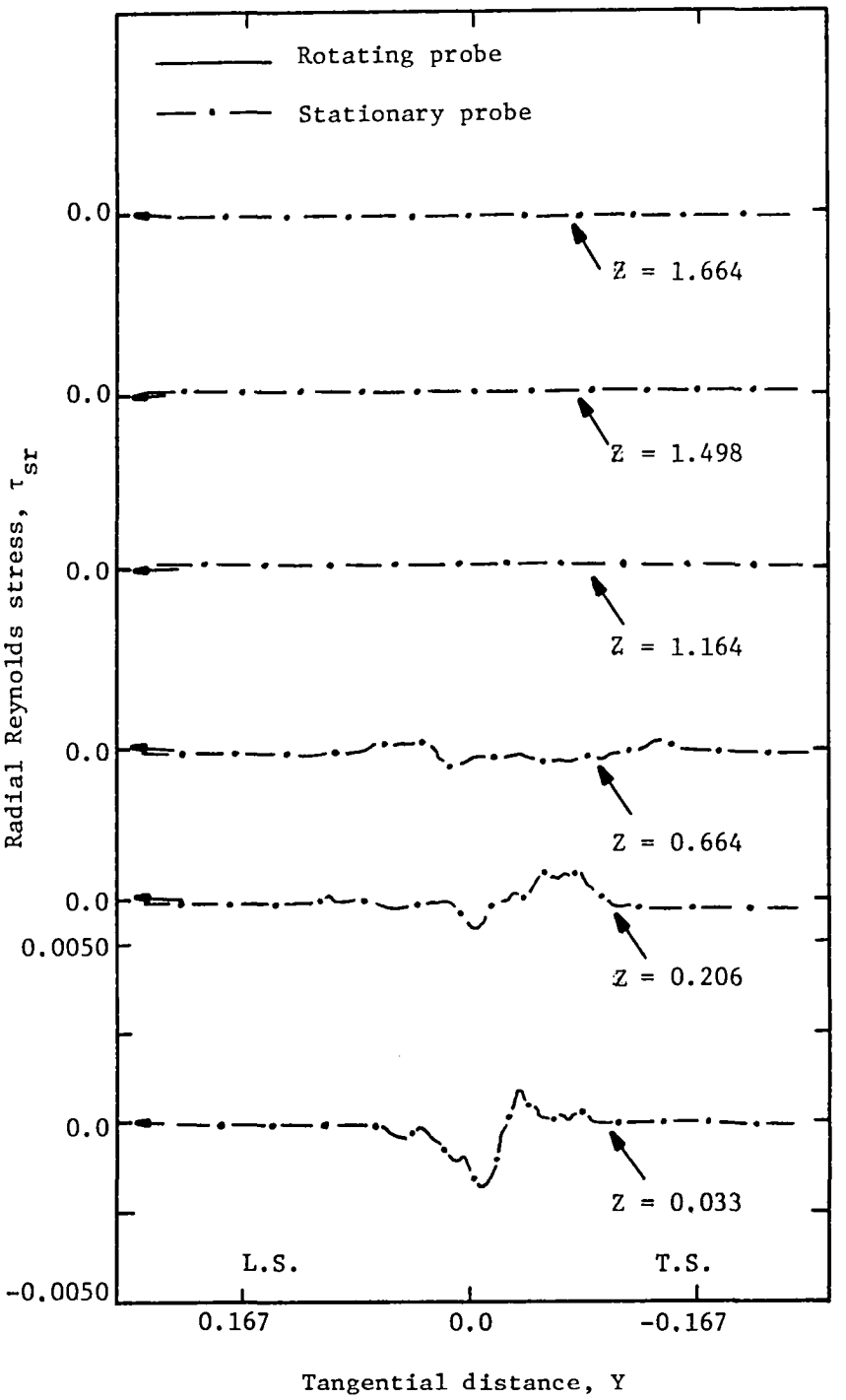

Figure 45. Radial Reynolds stress distribution for i = 5° and R = .721

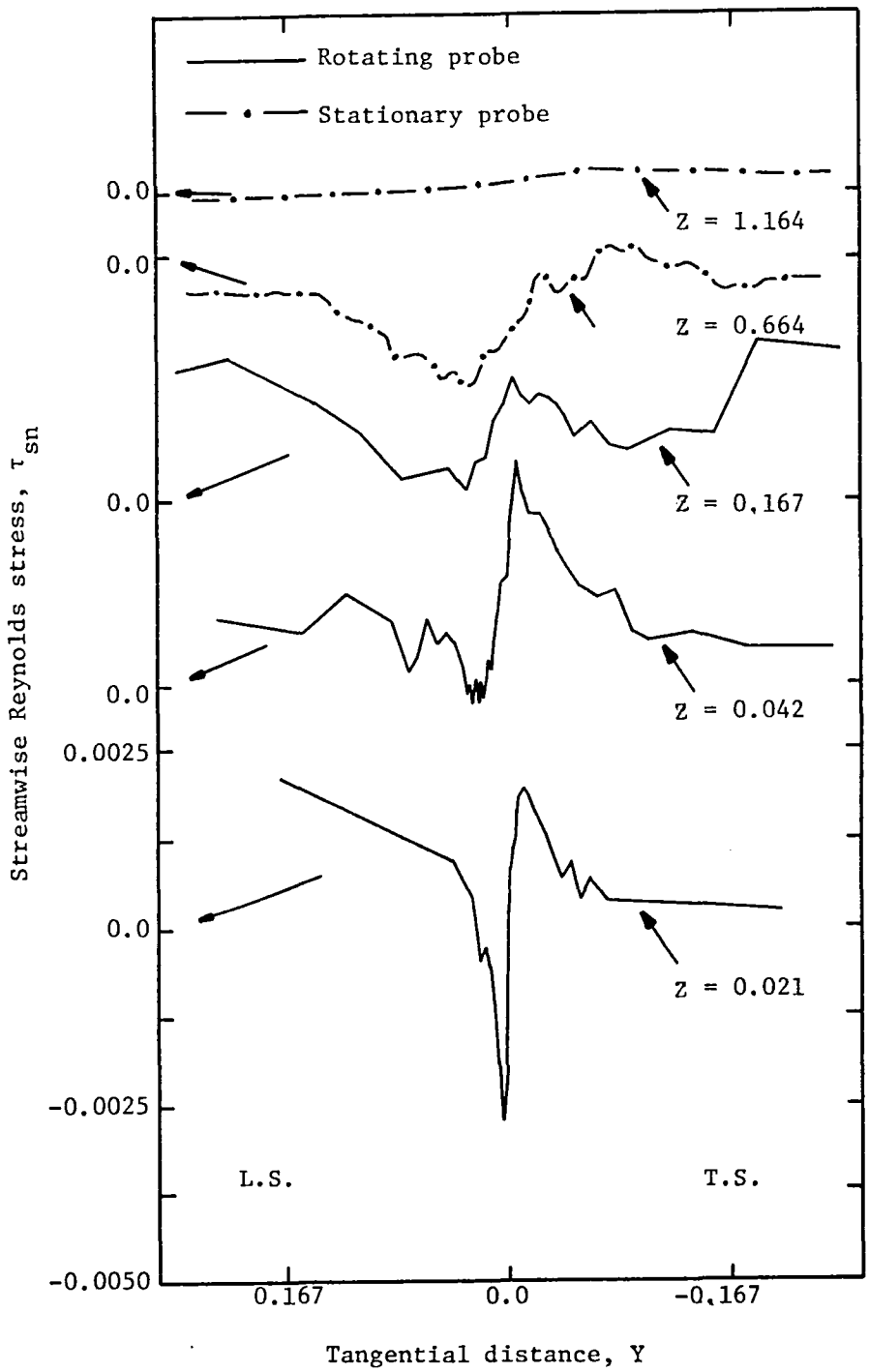

Figure 46. Streamwise Reynolds stress distribution for i = 10° and R = .721

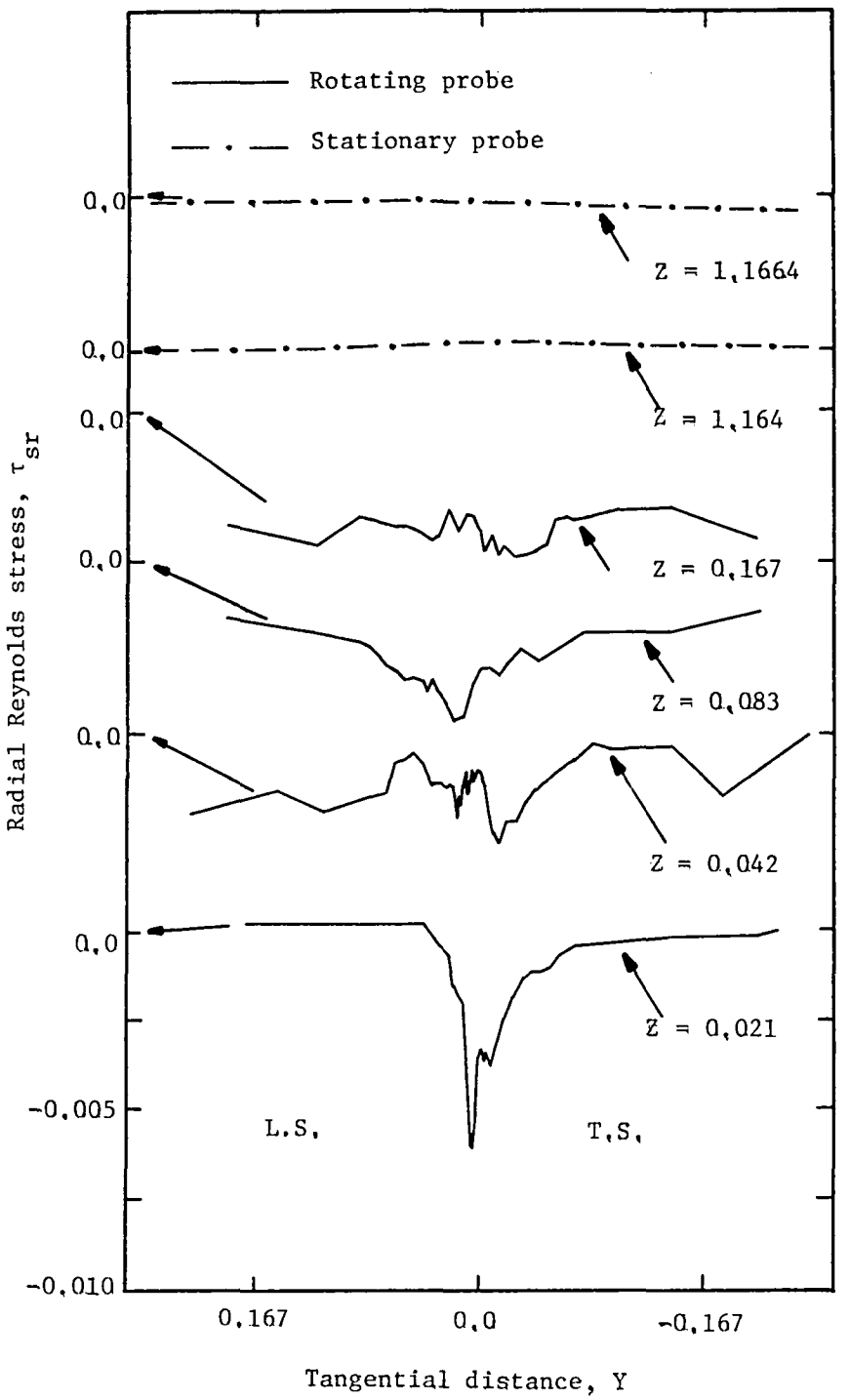

Figure 47. Radial Reynolds stress distribution for i = 10° and R = .721

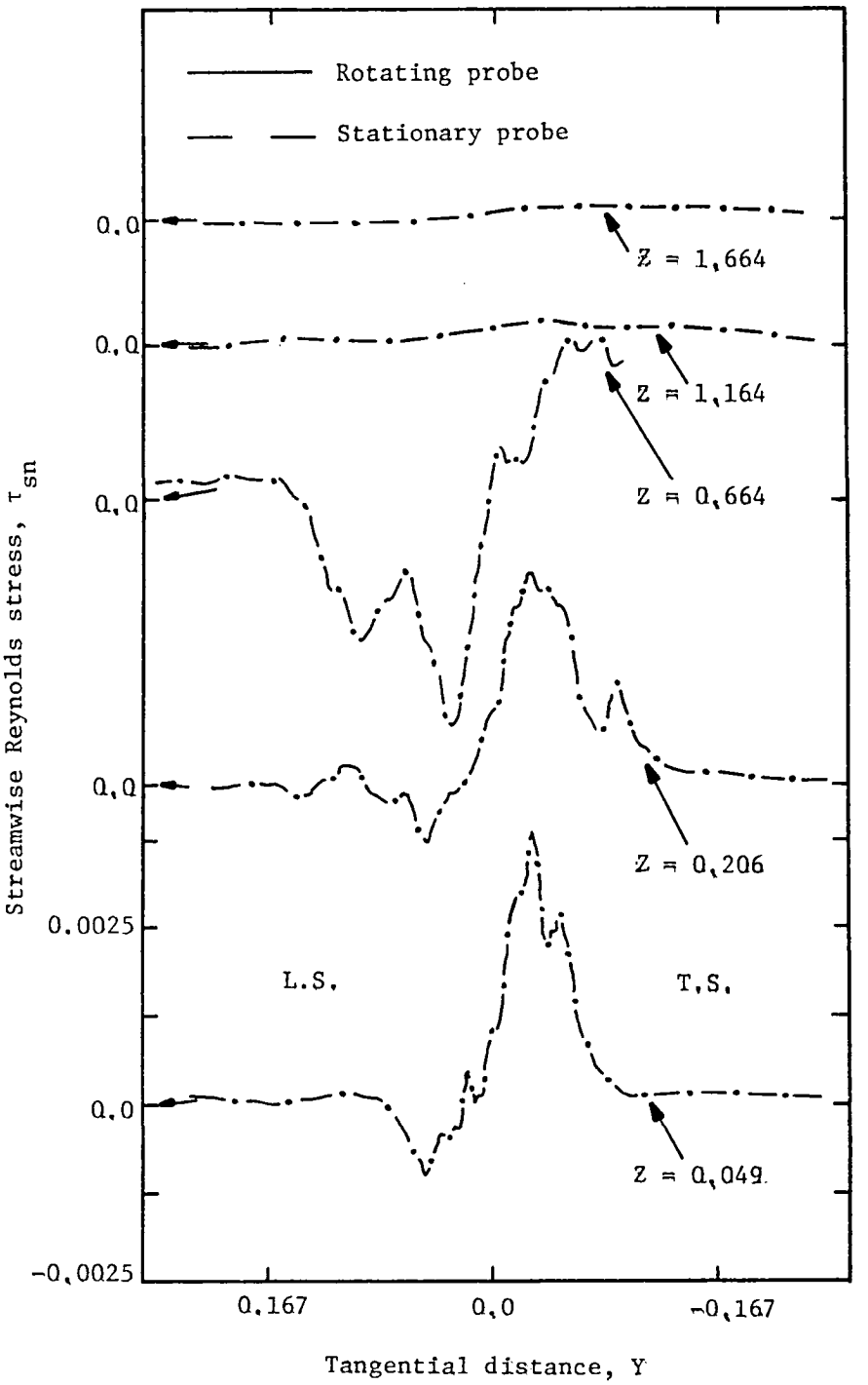

Figure 48. Streamwise Reynolds stress distribution for $i = 15°$ and $R = ,721$

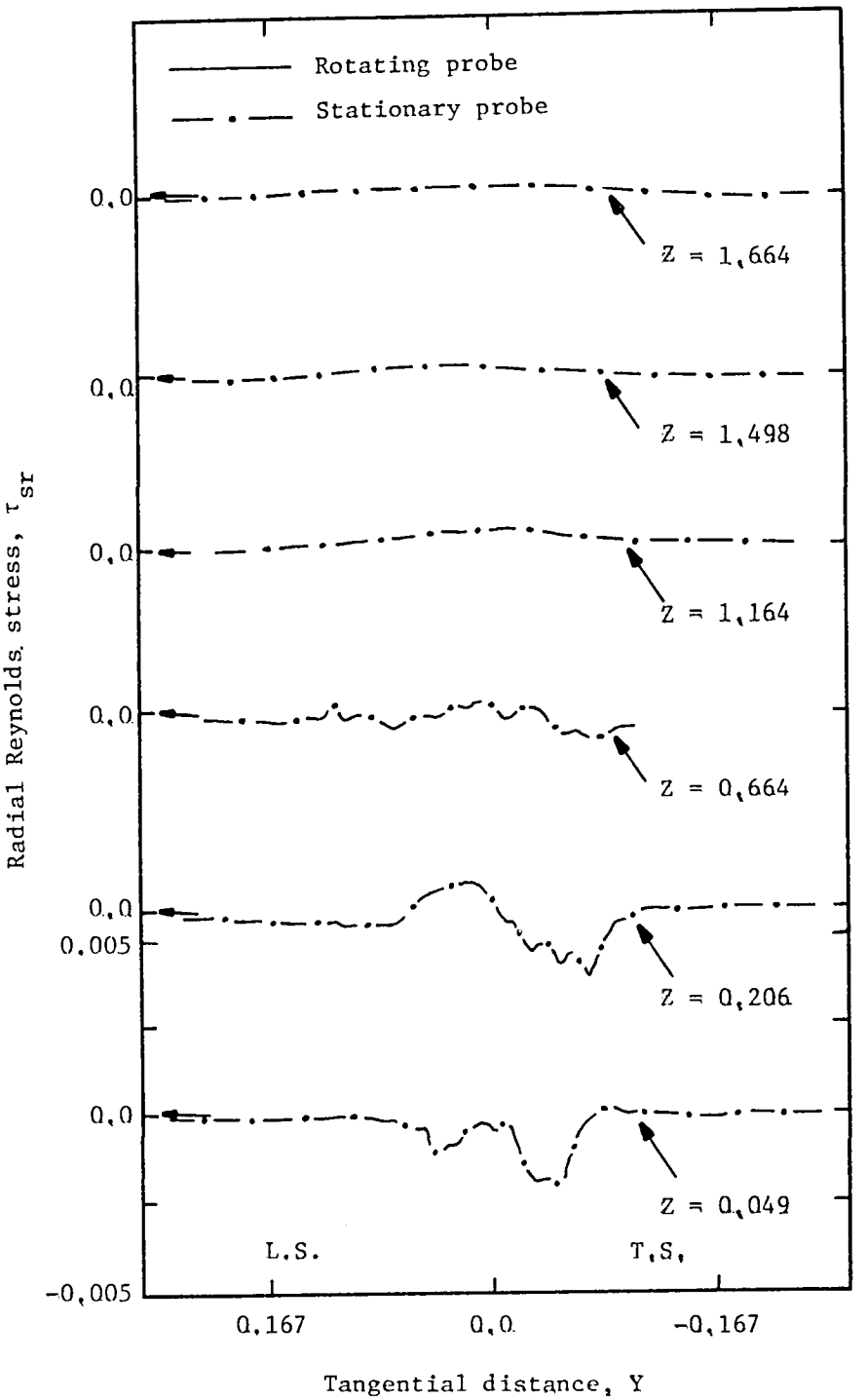

Figure 49. Radial Reynolds stress distribution for i = 15° and R = ,721

not found at the wake centerline where $\partial Q/\partial n = 0$. This same characteristic has been measured by Raj and Lakshminarayana (1973) for the wake behind a cascade of airfoils.

Radial Reynolds stress shows a very complex structure in Figure 45, 47, and 49 for all rotor blade incidences tested. Radial stress profiles in the near wake region for i = 10° and i = 15° show a lower value of correlation (less negative) near the wake centerline.

The component of streamwise Reynolds stress is shown to be larger than the radial component of stress. This characteristic is most pronounced at a rotor blade incidence of 15°. In the near wake region the ratio of τ_{rn}/τ_{sn} is approximately 1.13, 1.0, and .53 for the 5°, 10°, and 15° operating conditions. These ratios represent deviation of the total stress vector from the streamwise direction. This vector is at 48.5, 45.0, and 27.9 degrees from the streamwise mean velocity vector at 5°, 10°, and 15° incidences, respectively. The effect of increased blade loading on the total stress vector was clearly shown. At the far downstream measurement stations both components of Reynolds stress have nearly decayed to the free stream value.

The existence of radial Reynolds stresses and the deviation of the stress vector from the streamwise direction shows the large three-dimensional nature of the rotor wake. The existence of streamwise and radial stresses also represents the complex structure of turbulence in the rotor wake.

The streamwise and radial Reynolds stresses shown in the freestream for the rotating probe data at i = 10° represent the effects of the upstream strut wakes. This correlation is not found for the stationary

probe data since the upstream struts were located 180° circumferentially from the probe location.

The Reynolds stress data shown in Figures 44-49 must be studied with caution. The results shown are only qualitative since spacial errors may exist when using a tri-axial hot wire probe to measure stress correlations. Each of the three wires are physically at different locations and, therefore, measure flow properties at different locations in the wake. For the large gradients of stress measured in the rotor wake this error may be significant. The contribution to stress from eddies larger than the distance between the tri-axial probe sensors is measured accurately.

5.4 Similarity Rule

Experimental evidence has shown that similarity in streamwise mean velocity profiles for the wakes behind flat plates, circular cylinders, and isolated airfoils exists, prompting a search for the similarity in the rotor wake. Below, the similarity rule is examined for the rotor wake mean velocity measurements reported in Section 5.3. Similarity in the outer layer of the turbulence intensity profiles reported in Section 5.3 is also discussed.

5.4.1 Mean velocity

The maximum velocity difference in the rotor wake was used as a non-dimensionalizing velocity scale for all mean velocity profiles. The distance from the wake centerline to the location where the velocity defect is one-half was used as a characteristic length scale ($L_{T.S.}$ and $L_{L.S.}$). These characteristic velocity and length scales are defined in Figure 50. Using this technique, one finds similarity for the axial and tangential components of mean velocity.

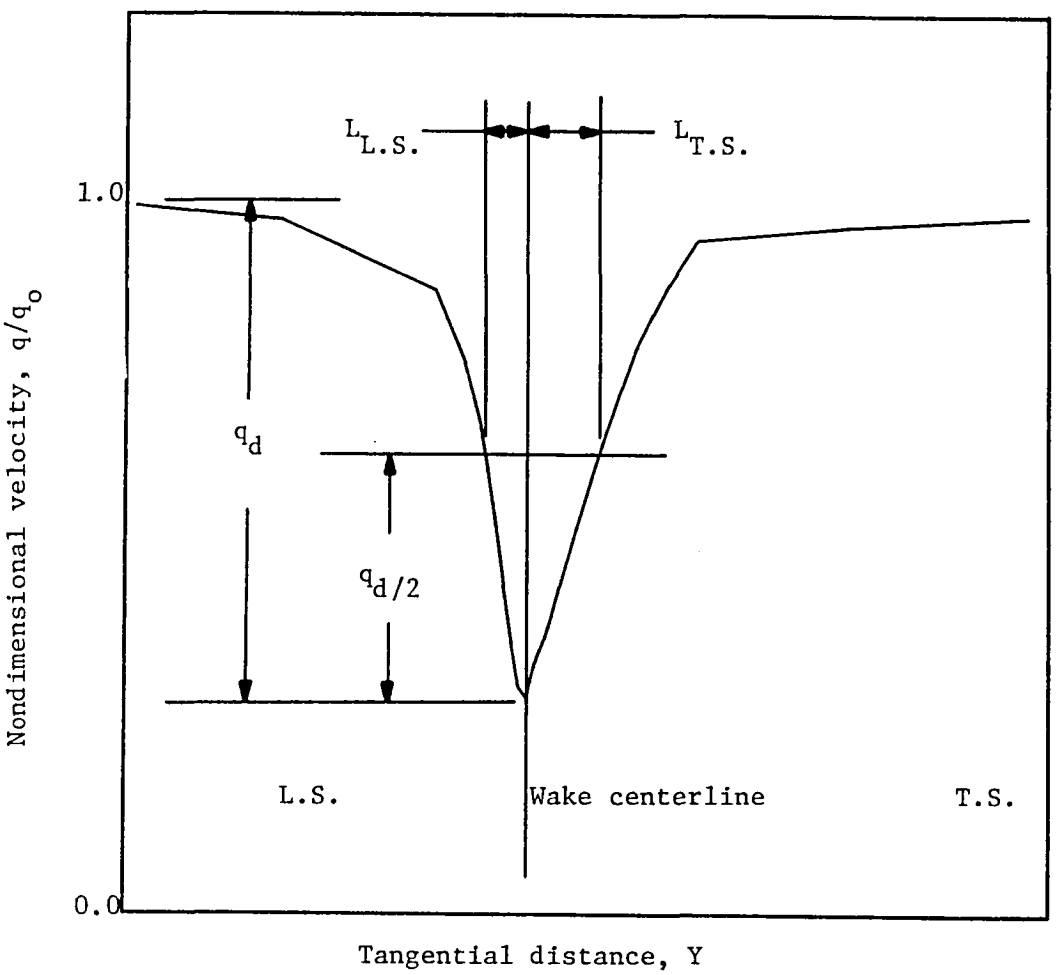

Figure 50. Definition of characteristic velocity and length scales used in the rotor wake

The axial and tangential components of mean velocity similarity profiles in the near wake region at mid-radius (R = .721) are shown in Figures 51 and 52 for rotor blade incidences of 10° and 0°, 5°, and 15°, respectively. As expected, the similarity rule is also valid in the far wake region as shown in Figure 51 for 10° incidence. All of the similarity profiles seem to follow the Gauss' function ($e^{-\eta^2.693}$). The Gaussian distribution has been derived theoretically (Schlicting, 1968)) for the two-dimensional far wake profile from a flat plate. A similarity rule has not been found that is valid at all of the rotor blade incidences tested for the complex radial mean velocity profiles.

The above similarity analysis is useful for predicting the rotor wake using a theoretically or experimentally derived correlation, such as,

$$q[Z,\theta(\text{or } \eta)] = f_s(Z)e^{-.693\eta^2} \tag{70}$$

where the function q represents a mean velocity component in the rotor wake. Attempts are made later (Section 5.8) to use Equation (70) to determine the function $f(Z)_s$ for correlated streamwise mean velocity.

5.4.2 Turbulence intensity

The similarity rule has been examined for the axial, tangential, and radial components of turbulence intensity in the outer layer of the wake profiles. Turbulence intensities were normalized with respect to an extrapolated peak intensity near the wake center. The corresponding value in the free stream was subtracted off. The distance from the wake centerline to the location where the extrapolated maximum intensity is half was used as a characteristic length scale on the pressure and suction sides ($L_{T.S.}$ and $L_{L.S.}$). Thus, one plots the intensities as,

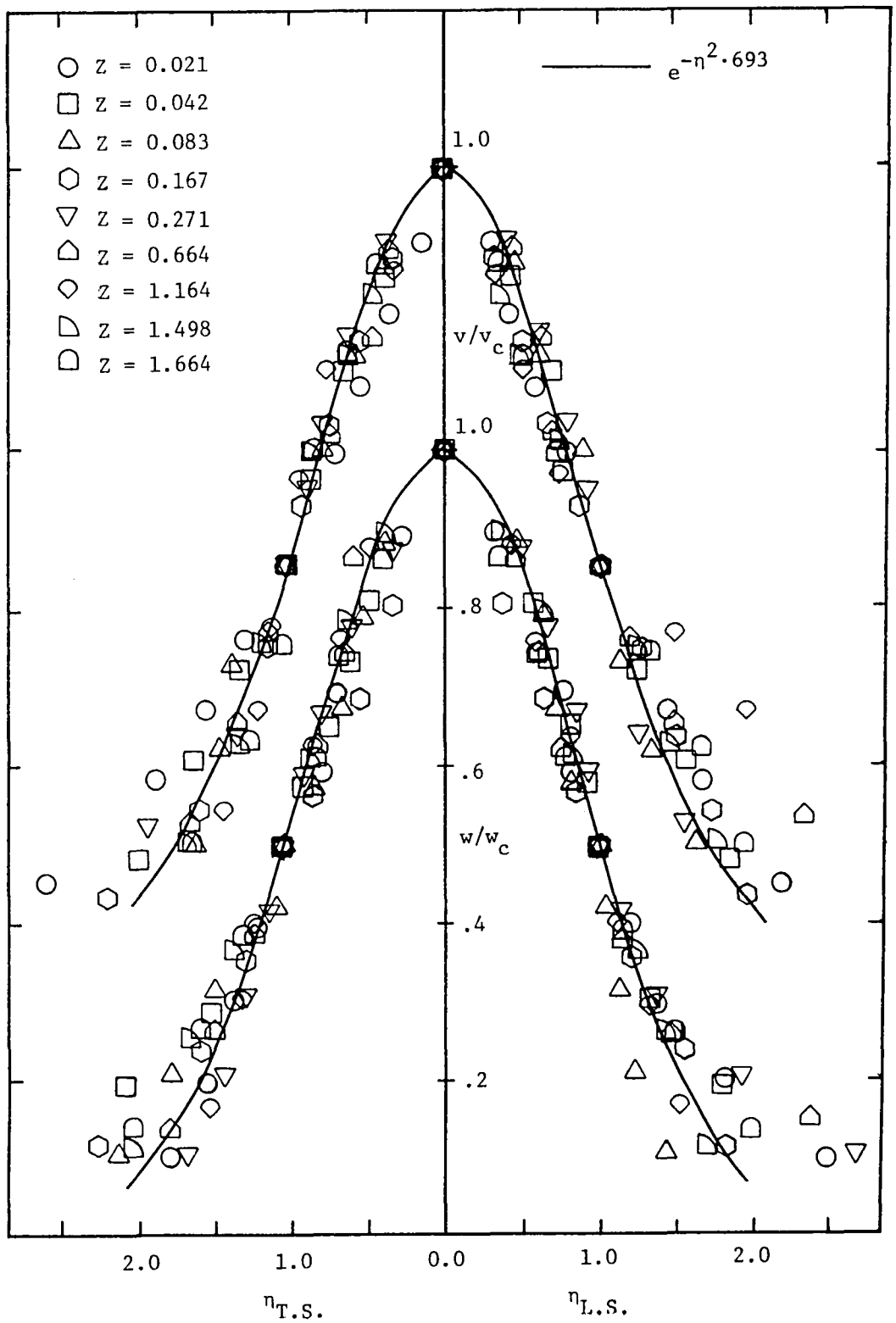

Figure 51. Similarity for axial and tangential mean velocity profiles for i = 10° and R = .721

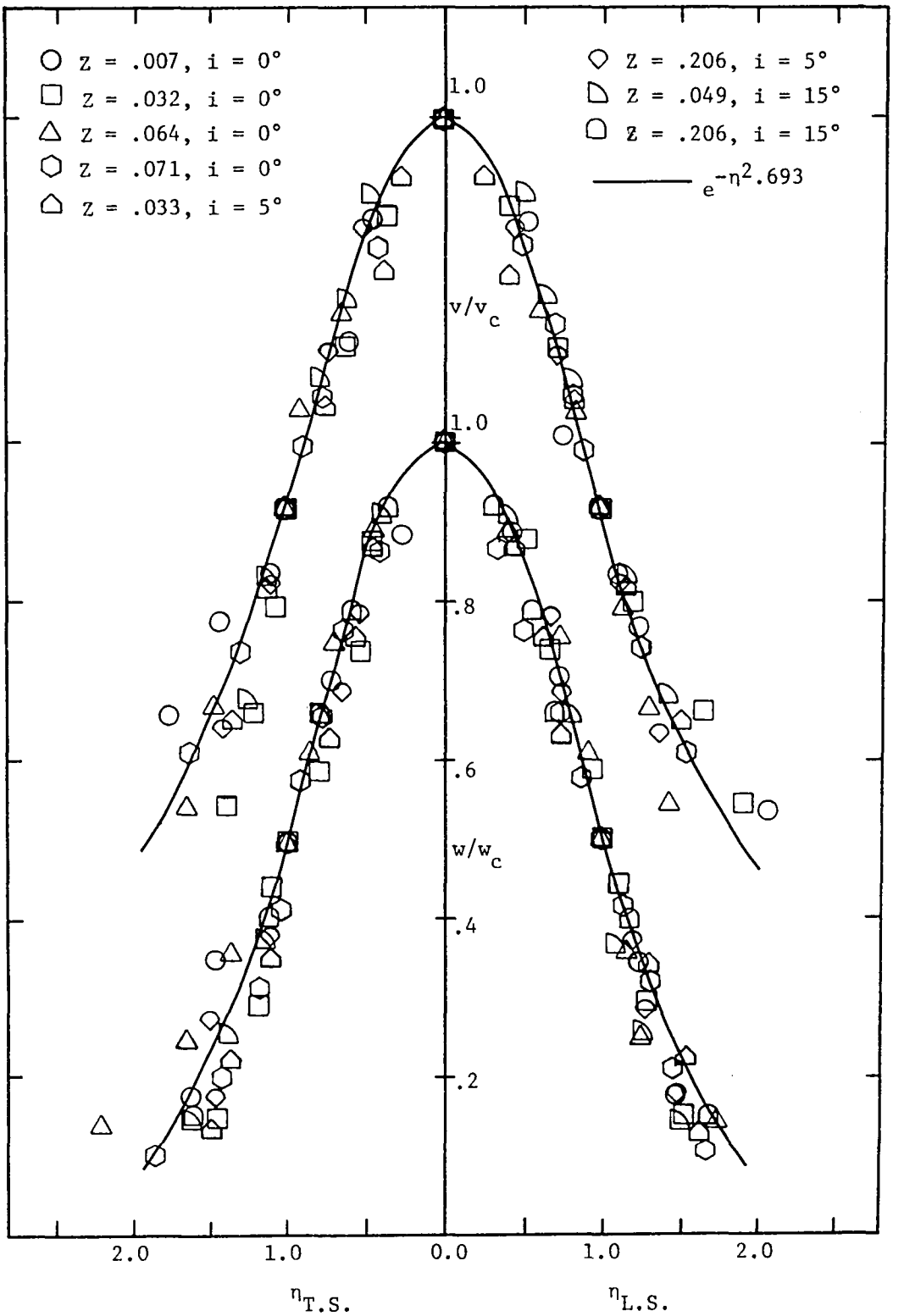

Figure 52. Similarity for axial and tangential mean velocity profiles for i = 0°, 5°, and 15° and R = .721

$$\sqrt{\overline{q'^2}}/\sqrt{\overline{q'^2_c}} - \sqrt{\overline{q'^2_e}}/\sqrt{\overline{q'^2_c}} \quad \text{vs.} \quad \eta_{T.S.} \text{ or } \eta_{L.S.} \tag{71}$$

where q' represents a fluctuating component of velocity.

Similarity in the outer layer in the near wake region for axial, tangential, and radial components of turbulence intensity are shown in Figures 53, 54, and 55, respectively. As expected, similarity was found in the far wake region for all components of turbulence intensity (shown for the 10° incidence operating condition). All intensity profiles in the outer layer of the wake seem to follow the Gauss' function.

5.5 Wake Curvature

Curvature of the rotor wake centerline (location of maximum streamwise velocity defect) is shown in Figure 56 for the 10° incidence operating condition at R = .721 and R = .860. The wake centerline positions are shown in the rotor relative frame of reference. Curvature of the rotor wake is found to be small in the near and far wake regions at both radial measurement stations. In the near wake region the path of the wake centerline is approximately coincident with the rotor blade stagger angles at each radius. The radius of curvature of the wake centerline is shown to be slightly smaller at R = .860 than at mid-radius (R = .721). These radius of curvatures (non-dimensionalized by chord length) are .733 and .814 at R = .860 and R = .721, respectively. The path of the wake centerline is shown to be deflected away from the blade stagger towards the trailing surface of the rotor blade in the far wake region at about 25 percent of the chord for R = .860. From momentum and continuity considerations this can be expected as given by Speidel and Scholz (1957). The deflection of the wake from the blade stagger is appreciable for R = .860.

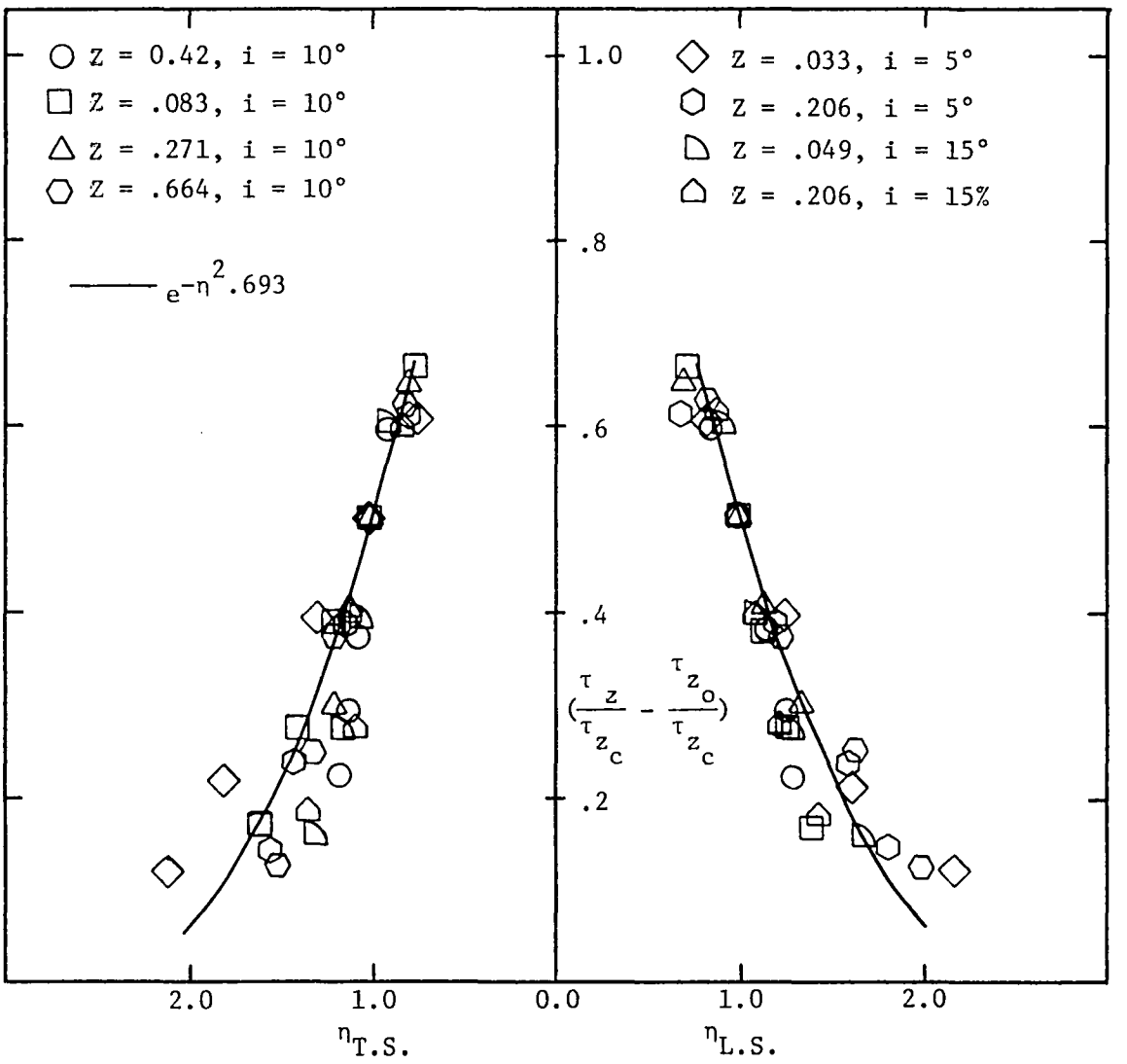

Figure 53. Similarity in the outer layer in the near and far wake regions for axial turbulence intensity profiles for i = 5°, 10°, and 15° and R = .721

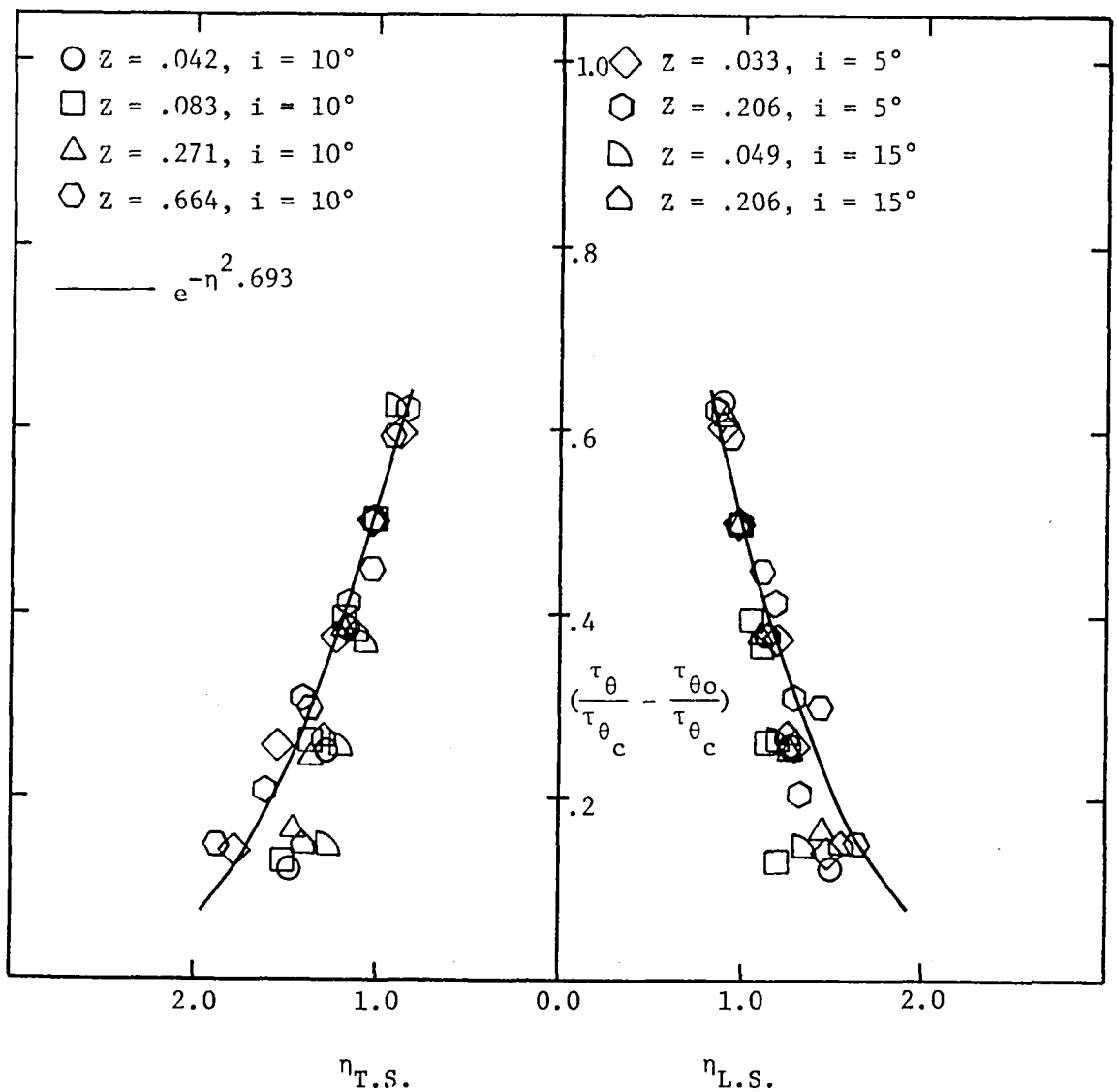

Figure 54. Similarity in the outer layer in the near and far wake regions for tangential turbulence intensity profiles for i = 5°, 10°, and 15° and R = .721

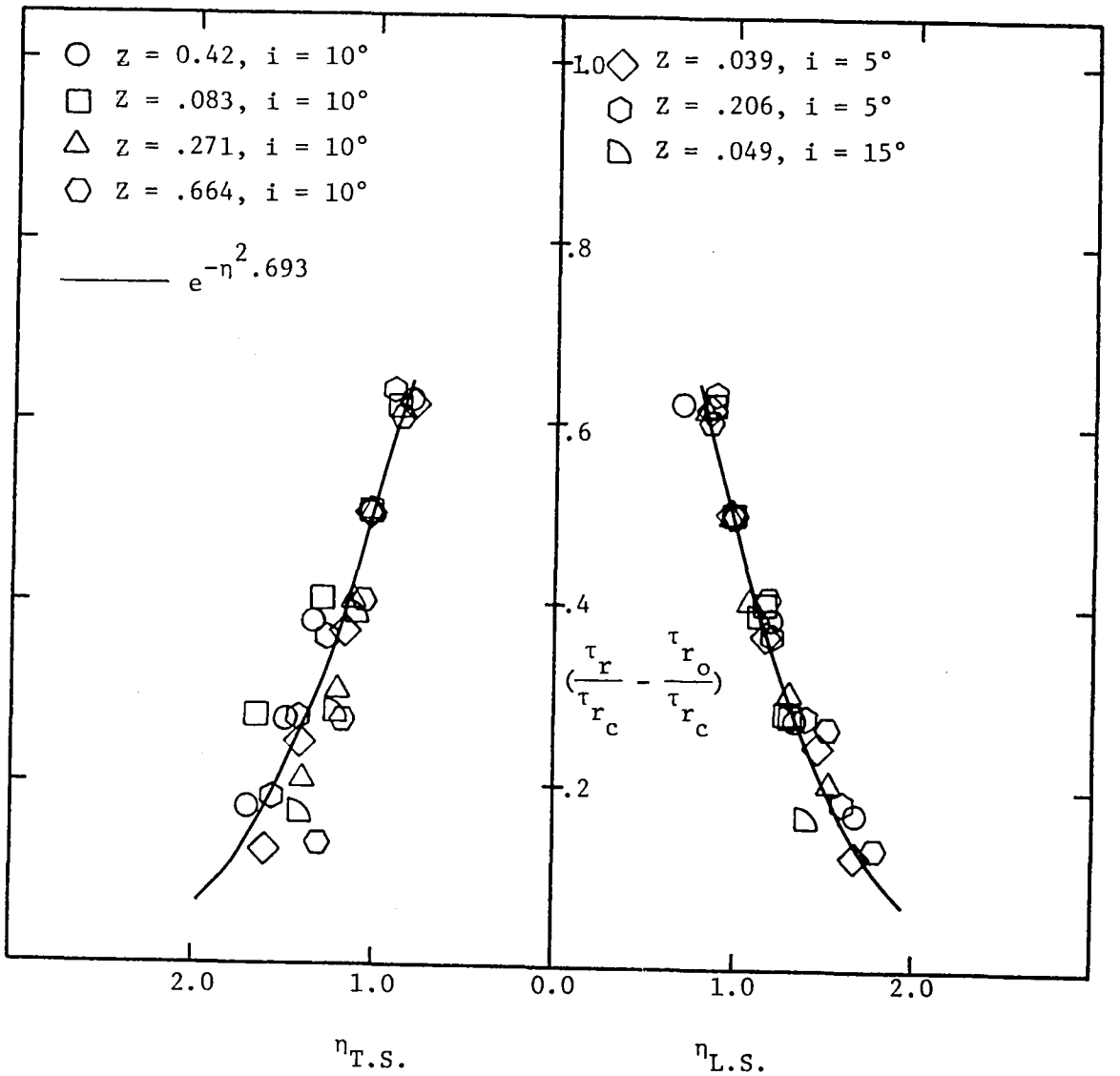

Figure 55. Similarity in the outer layer in the near and far wake regions for radial turbulence intensity profiles for i = 5°, 10°, and 15° and R = .721

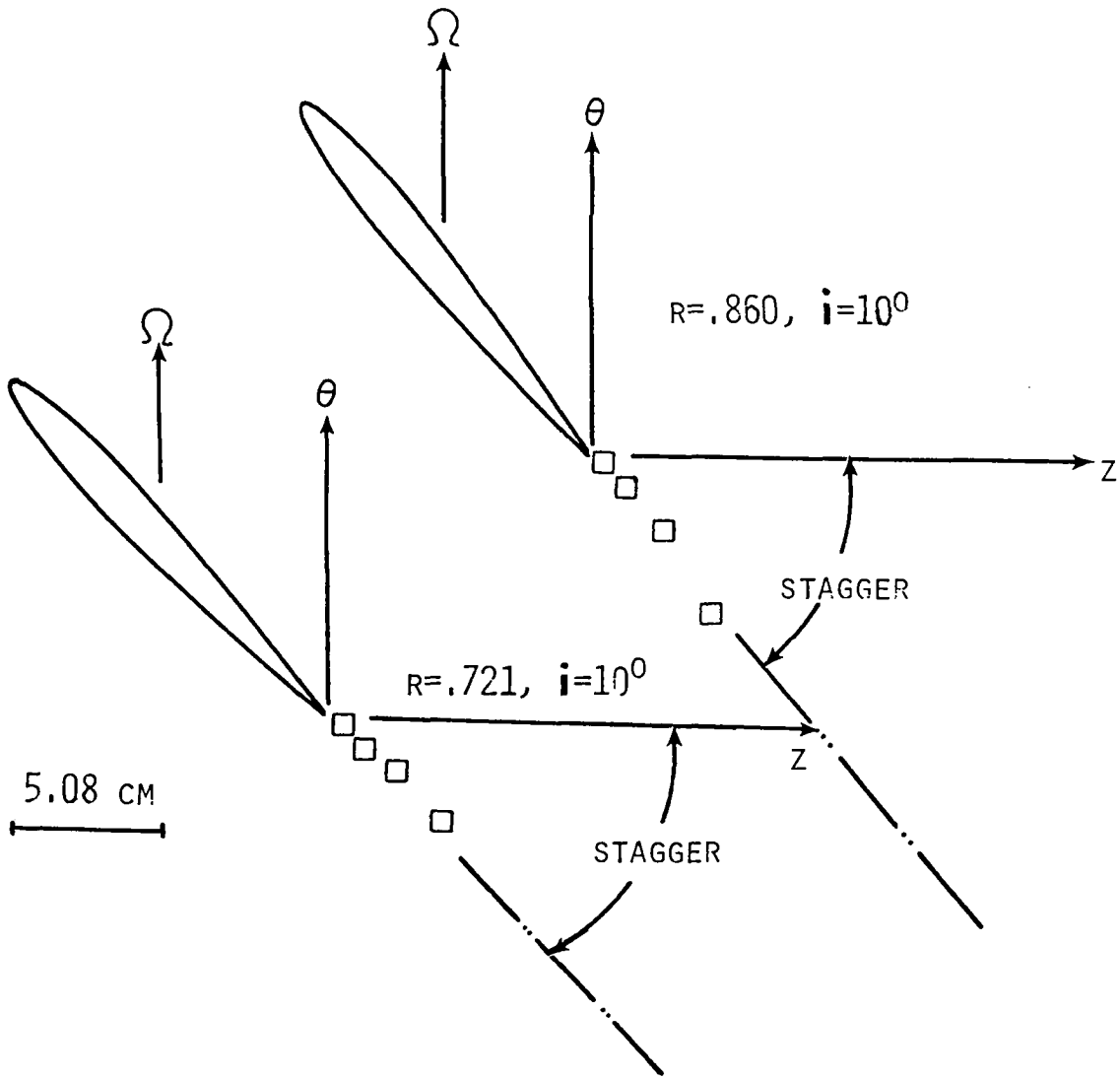

Figure 56. Curvature of the rotor wake centerline for i = 10°, R = .721 and i = 10°, R = .860

5.6 Decay Characteristics

5.6.1 Mean velocity

Decay of defects in axial and tangential mean velocities at the wake centerline are shown in Figure 57 at R = .721 for all rotor blade incidences tested. Also shown in Figure 57 are the maximum differences in radial velocity in the wake at 5°, 10°, and 15° rotor blade incidences.

A very rapid decay is indicated in the trialing edge region for both axial and tangential velocity defects at 0° and 10° incidences. For the measurements made at both blade incidences the tangential velocity defect is shown to decay less rapidly than axial defect in this region. This results in larger tangential than axial components of mean velocity defect in the near wake region for both incidences. Axial and tangential velocity defects for 5° and 10° incidences are not shown in the near wake. These measurements were made with the stationary tri-axial probe which was shown to have large inherent errors in this region. These errors are discussed in Section 5.1.2.

At the far downstream measurement stations, Z = .42 for 0° incidence and Z > 1.0 for 5°, 10°, and 15° incidences, axial and tangential velocity defects have become very small and are decaying very slowly. However, in these regions, defects in tangential velocity are significantly smaller than the axial defects. This indicates a more rapid decay of tangential defect in the far wake than for axial defect. This characteristic is consistent with the results from Lakshminarayana (1975).

Comparison of the near wake axial and tangential velocity defects for 0° and 10° incidence data clearly indicates the effects of blade loading. As shown in Figure 57, an increase in blade loading increases the defects of both axial and tangential velocities. Although the

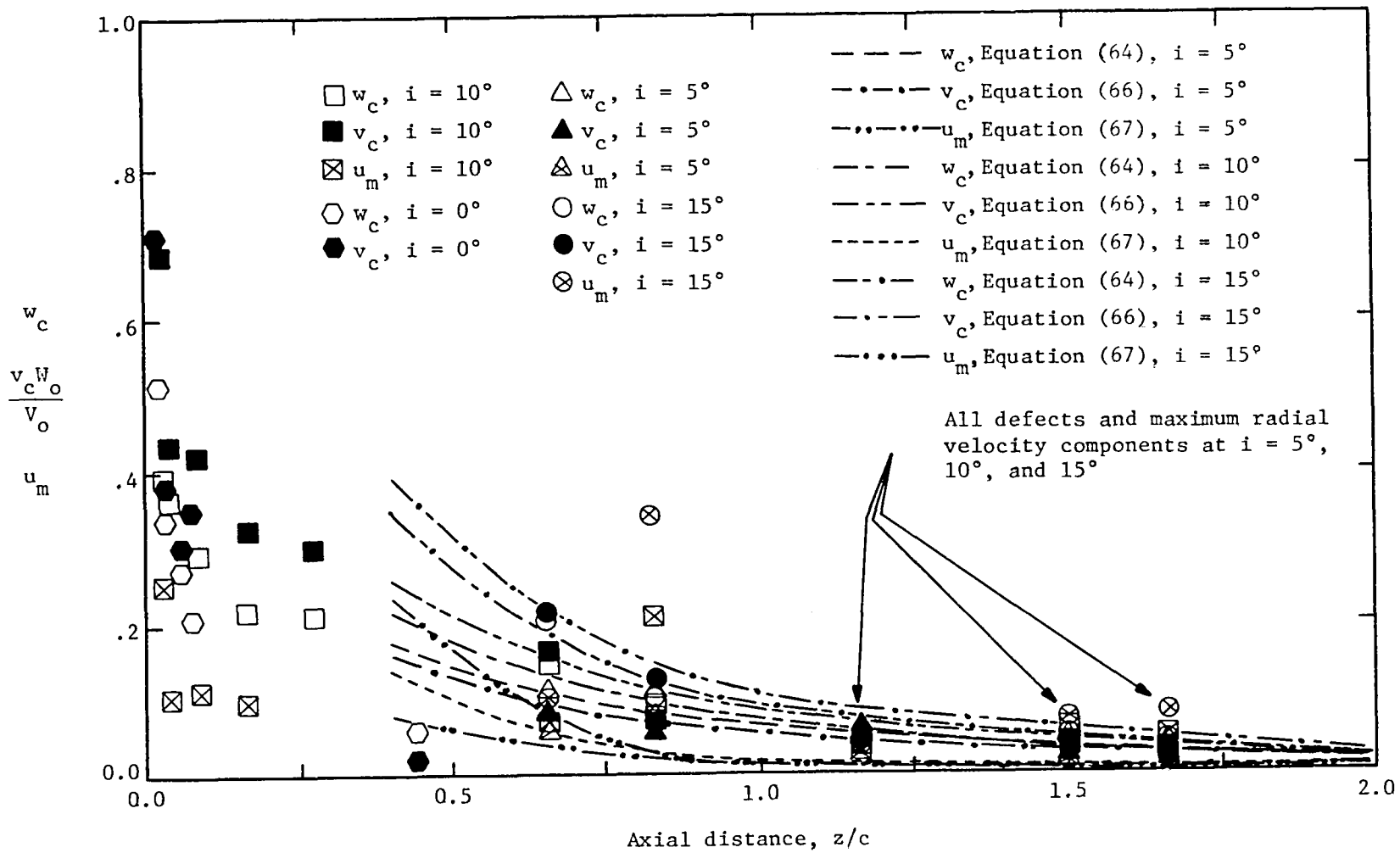

Figure 57. Decay of radial velocity and defects in axial and tangential velocity at R = .721

tangential velocity defect decays slower than the axial component in the trailing edge region at both blade incidences, this characteristic seems to be most pronounced at 10° incidence. Increased blade loading is therefore shown to have a greater effect on tangential velocity defects, more so than for the axial velocity defects.

With the rotor operating at an incidence of 10°, a very rapid decay of maximum radial velocity difference is shown in the trailing edge region. This decay rate slows considerably in the near wake region. The far wake region shows a smaller decay rate than that found in the near wake. Maximum radial velocity difference in the wake at the far downstream measurement stations ($Z > 1.0$) still shows significant radial velocities. Radial velocities in this region are found to increase for increased blade loading. These trends indicate a large radial migration of flow in the rotor wake.

The decay of total mean velocity (resultant relative velocity) defect is shown in Figure 58 for measurements made at mid-radius ($R = .721$) at the 0°, 5°, 10°, and 15° incidence operating conditions. Also shown in Figure 58 is data due to Hah (1978) for measurements made behind an isolated airfoil. The isolated airfoil had a thickness distribution corresponding to the rotor blade sections tested in the present investigation. The effect of increased blade loading is clearly seen for both the isolated airfoil and rotor wakes shown in Figure 52. Increasing incidence is found to slow the decay of total mean velocity. This effect is still discernible for all wake data shown in the far wake region.

The isolated airfoil wake is shown to decay slower than the rotor wake in the trialing edge region. Data should be compared for the isolated airfoil and rotor wakes between 0° and 10° or between 3° and 10°,

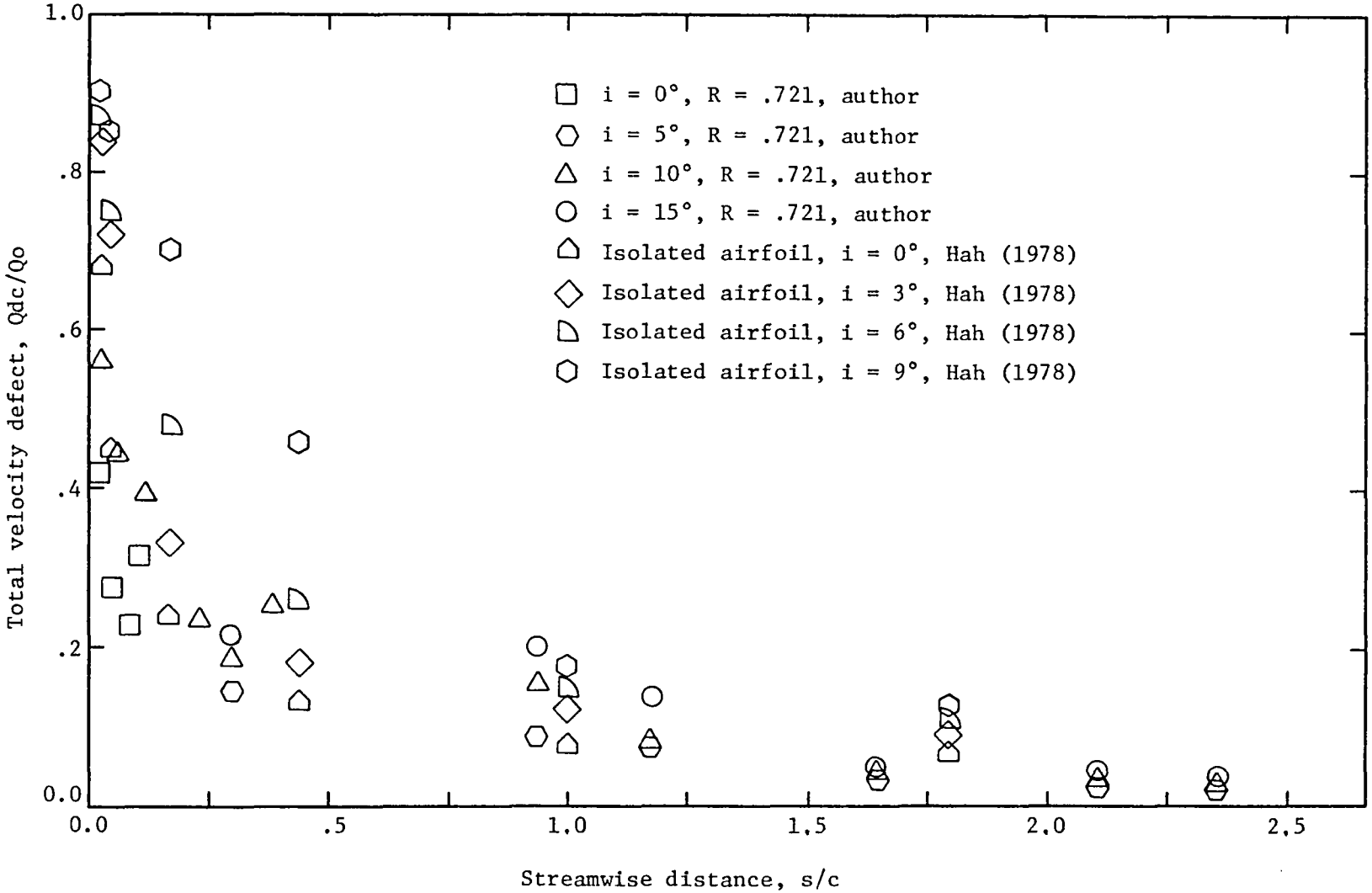

Figure 58. Decay of defect in total mean velocity (resultant relative velocity) in streamwise direction at wake centerline

respectively. The isolated airfoil and rotor blades had identical lift coefficients (C_{ℓ} = .30) at the 3° and 10° incidences, respectively. In the near wake region the isolated airfoil and rotor wakes show similar total velocity defects and decay rates. For measurements in the far wake region the rotor wake initially shows a faster decay than the isolated airfoil between s/c = 1.0 to s/c = 1.5. Beyond s/c = 1.5 the rotor wake shows an extremely small decay rate. This may result due to constraints on the rotor wake from adjoining blade wakes. The effect of rotation and centrifugal forces may result in the faster decay rate for the rotor wake in the trailing edge region than that for the isolated airfoil wake.

5.6.2 Comparison of mean velocity experimental results with theory

Theoretical predictions from the momentum integral analysis given in Chapter 2 are shown in Figure 57 in the far wake region for maximum radial velocity and defects in axial and tangential mean velocities in the wake. Predictions are shown for the 5°, 10°, and 15° operating conditions at mid-radius (R = .721). To evaluate the constants in Equations (64) and (65) the experimentally measured axial velocity defects and semi-wake widths were specified at Z > .75. These constants are given in Table 4 at each of the operating conditions for which a theoretical solution is shown. The blade loading parameters in Equations (65), (66), and (67) were determined from experimental measurements.

The virtual or apparent origin, z_o, was determined from experimental results for semi-wake width at the 5°, 10°, and 15° incidence operating conditions. The virtual origin for each rotor blade incidence is given in Table 4.

The theoretical predictions shown in Figure 57 clearly indicate the effects of blade loading for Z < 1.0. Increased blade loading shows an

Rotor blade incidence	C_2	C_5	m_2	z_o
5°	.0360	.1746	-1.441	.1300
10°	.0357	.2029	-1.634	.1326
15°	.0428	.3039	-2.155	.1767

Table 4. Constants and virtual origins used in momentum integral solution of rotor wake

increase in axial and tangential wake center defects and maximum radial velocities in the wake. Far downstream for Z > 1.0 all of the theoretically determined axial and tangential velocity defects have decayed to approximately the same level for the 5°, 10°, and 15° operating conditions. Maximum radial velocities in the wake have decayed to a very small level, less than for the axial and tangential velocity defects for Z > 1.0. For the initial decay rate shown at Z > .4, the maximum radial velocities are greater than the corresponding axial and tangential velocity defects. The decay rate for maximum radial velocities and axial and tangential velocity defects is shown to increase for increased blade loading. For Z < .4 the theoretical curves for axial and tangential velocity defects and maximum radial velocity in the wake overpredicts the experimentally measured values. This overprediction is large enough such that the theoretical far wake assumptions made in Chapter 2 are no longer valid. For this reason, no theoretical results are shown for Z < .4 in Figure 57.

It should be noted that Equations (65), (66), and (67) become indeterminant at the 0° incidence operating condition. For this free vortex, zero blade loading operating condition, Equations (42), (49), (50), and (51) must be used to derive a simplified solution where the blade loading terms are neglected. This solution is given by Lakshminarayana (1976) and will not be discussed.

5.6.3 Turbulence intensity

Decay of maximum axial, tangential, and radial intensities in the rotor wake are shown in Figure 59 for all operating conditions tested at mid-radius (R = .721).

Axial, tangential, and radial components of turbulence intensity are found to be very large in the near wake region for all rotor blade

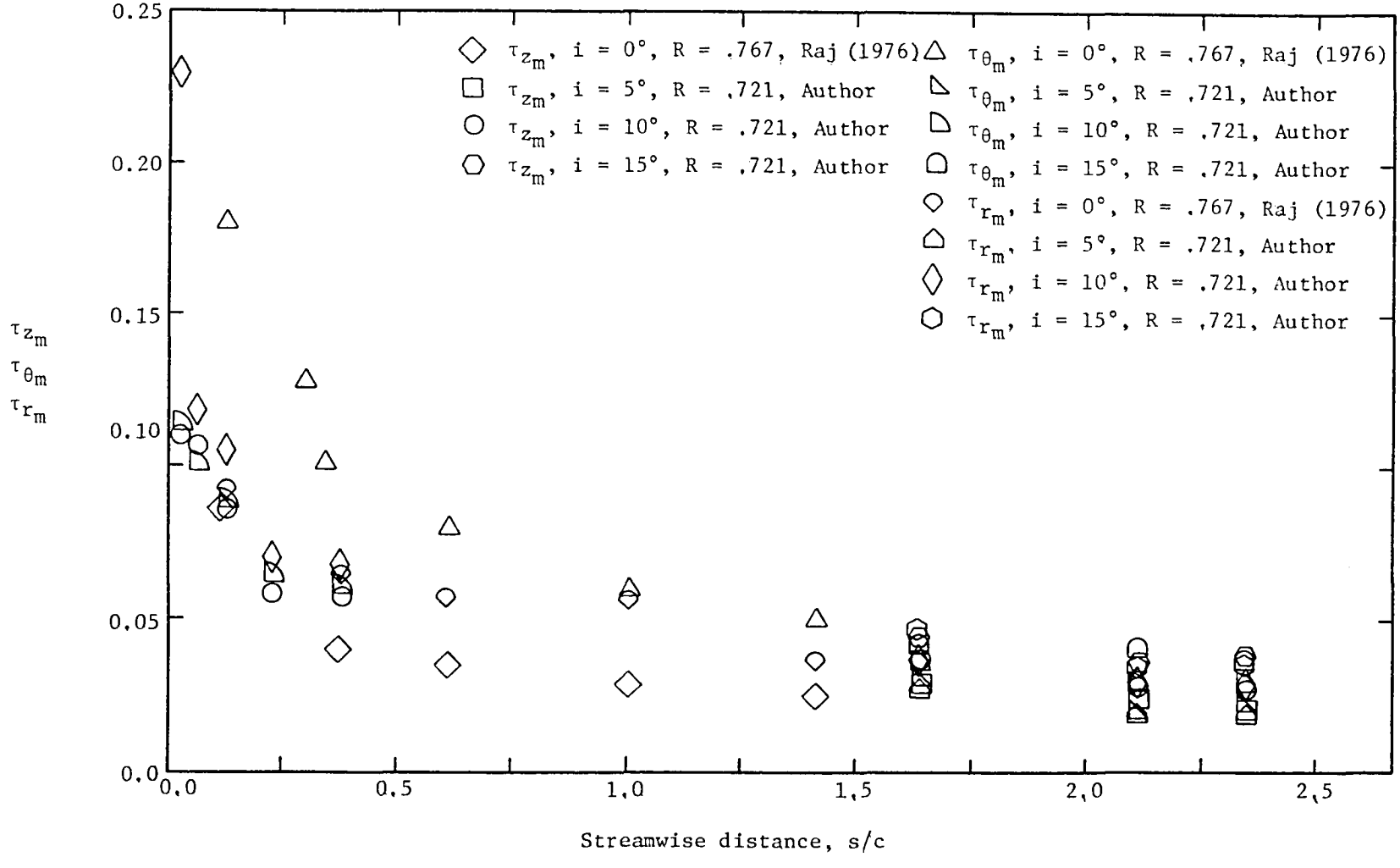

Figure 59. Decay of maximum axial, tangential, and radial turbulence intensities

incidences. While all three quantities are large, radial intensities were found to be significantly larger than the axial and tangential intensities at s/c = .030 for i = 10°. However, all components have decayed to approximately the same level for s/c > .4. In the far wake region for s/c > 1.5 the maximum axial, tangential and radial components of intensity have decayed to levels near their free stream values. Axial and tangential intensities are found to be slightly greater than radial intensities in this region. The effect of varying blade loading is clearly discernible in the far wake region for s/c > 1.5. Larger blade loading shows increased maximum axial, tangential, and radial turbulence intensities in the wake.

The measurement locations at Z = .206 and Z = .664 are not shown in Figure 59. The unconventional behavior of the turbulence intensity data at these stations is discussed in Section 5.3.5.

5.7 Wake Width, Momentum Thickness, and Shape Factor

The variation of semi-wake width is shown in Figure 60 for measurements made at mid-radius (R = .721) with rotor blade incidences of 0°, 5°, 10°, and 15°. Semi-wake width is defined as the width of the wake where the total relative velocity defect is one-half.

At 10° incidence near trailing edge region, the semi-wake width grows rapidly between s/c = .030 and s/c = .059. Wake width seems to increase at a rate proportional to s/c in this region. In the near wake region from s/c = .059 to s/c = .236 the wake width is shown to be nearly constant. Wake width is then found to increase again beyond s/c = .236. The variation of semi-wake width at 0° incidence shows a similar trend except for some scatter in the data at s/c = .099. This behavior is contrary to those observed for an isolated airfoil (Preston, et al.

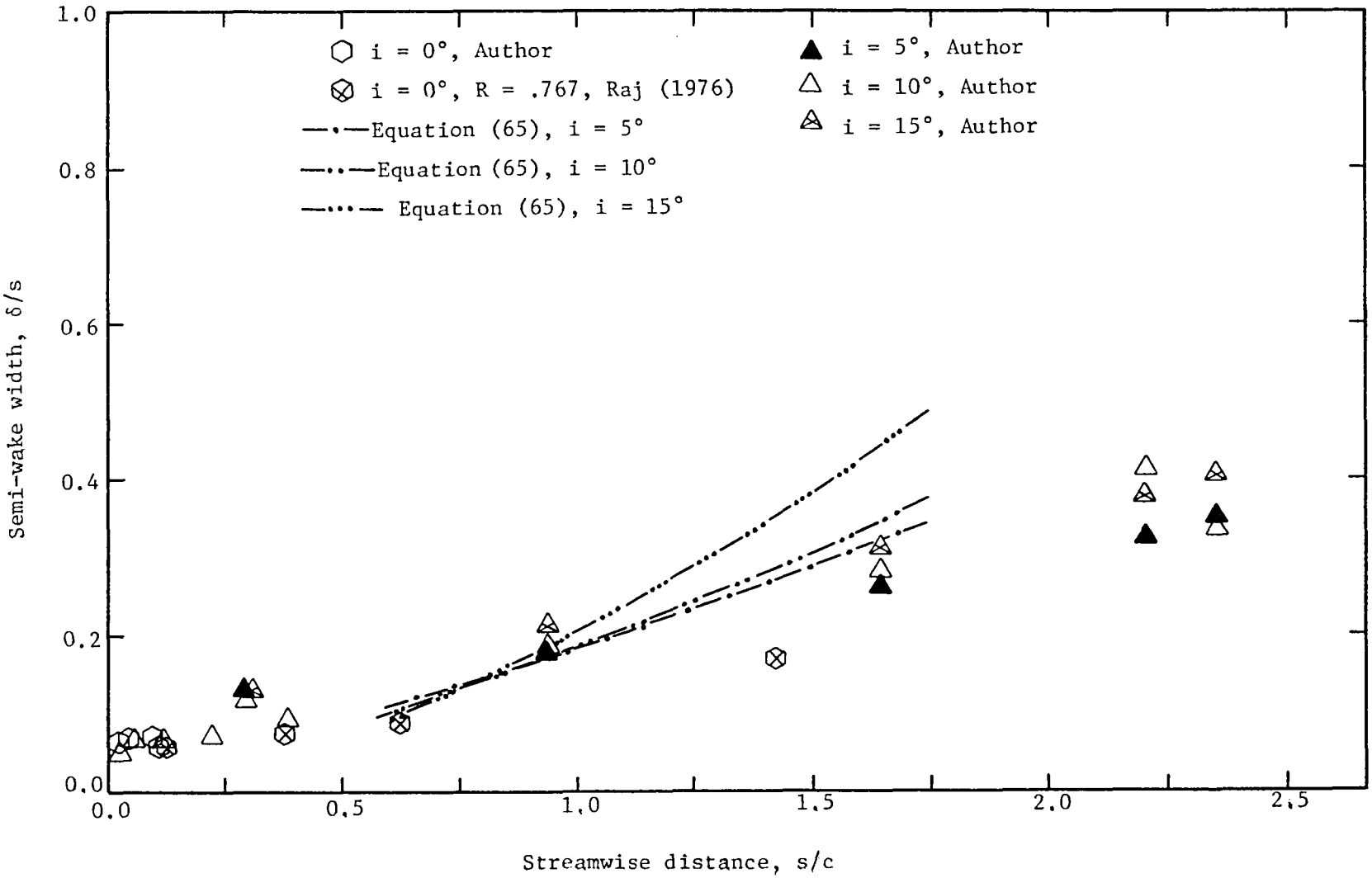

Figure 60, Semi-wake width variation downstream of the rotor at R = .721

(1945), Mendelsohn (1947), and Silverstein, et al. (1939a)) and for a flat plate (Chevray and Kovasznay (1969)). The effect of three-dimensional flow on the wake can clearly be seen here. The radial transport of mass, momentum, and energy may be responsible for the near constant wake width at mid-radius, even though the wake defect is decaying rapidly.

Semi-wake width is shown in Figure 60 for 5°, 10°, and 15° incidences in the far wake region. Here, semi-wake width seems to increase at a rate given by $\sqrt{s/c}$. The effect of increased blade loading is found to increase the wake width in the far wake region for all measurement stations shown. Wake width at the 15° incidence operating condition grows slightly faster than for 5° or 10° incidences.

The trends observed for the rotor wake near the trailing edge region for $s/c < .059$ and in the far wake region for $s/c > .236$ seem to be consistent with the results from a single airfoil. In these regions the functional dependence of semi-wake width with s/c was found to be proportional to s/c and $\sqrt{s/c}$ for the trailing edge and far wake regions, respectively.

A theoretical prediction for semi-wake width from Equation (65) is shown in Figure 60 for the 5°, 10°, and 15° operating conditions in the far wake at mid-radius (R = .721). The constant C_5 in Equation (65) was determined used experimentally measured values of wake width at s/c = 1.13 for each of the operating conditions. Values of C_5 determined for the 5°, 10°, and 15° operating conditions are given in Table 4.

Agreement between theoretical predictions and experimental measurements is shown to be good for $s/c > .55$. The theoretical predictions clearly shows the effects of blade loading on wake width. Increased blade loading is shown to increase semi-wake width growth, consistent with the experimentally measured trend. However, the

theoretical predictions for s/c > 1.25 overpredict the experimentally measured rate of wake spreading. This overprediction is shown to be largest for the 15° incidence operating condition. Since the effects of adjacent wakes on the wake spreading characteristics is not included in the theoretical analysis, the predictions are not shown for s/c > 1.75 where the semi-wake widths are approaching mid-passage values.

The wake momentum thickness and shape factor variations downstream of the rotor are shown in Figures 61 and 62, respectively. Rotor wake data for the 5°, 10°, and 15° operating conditions are shown for measurements made at mid-radius (R = .721) in both the near and far wake regions. Also shown in Figures 61 and 62 are isolated airfoil data due to Preston, et al. (1945), cascade data from Raj and Lakshminarayana (1973), and flat plate data from Chevray and Kovasznay (1969).

Momentum thickness for the rotor wake was determined using the equation,

$$\theta^* = \frac{1}{S} \int_o^S \frac{Q}{Q_o}\left(1 - \frac{Q}{Q_o}\right) r d\theta \tag{72}$$

where integration was performed in the tangential direction across one blade spacing. Shape factor in the wake was found using the expression,

$$H_1 = \frac{\delta^*}{\theta^*} \tag{73}$$

where δ^* represents the displacement thickness. Displacement thickness was determined using the equation,

$$\delta^* = \frac{1}{S} \int_o^S \left(1 - \frac{Q}{Q_o}\right) r d\theta \tag{74}$$

where integration was performed across one blade spacing in the tangential direction.

The variation of momentum thickness for the flat plate, isolated airfoil, cascade, and rotor wakes are shown in Figure 61. The momentum

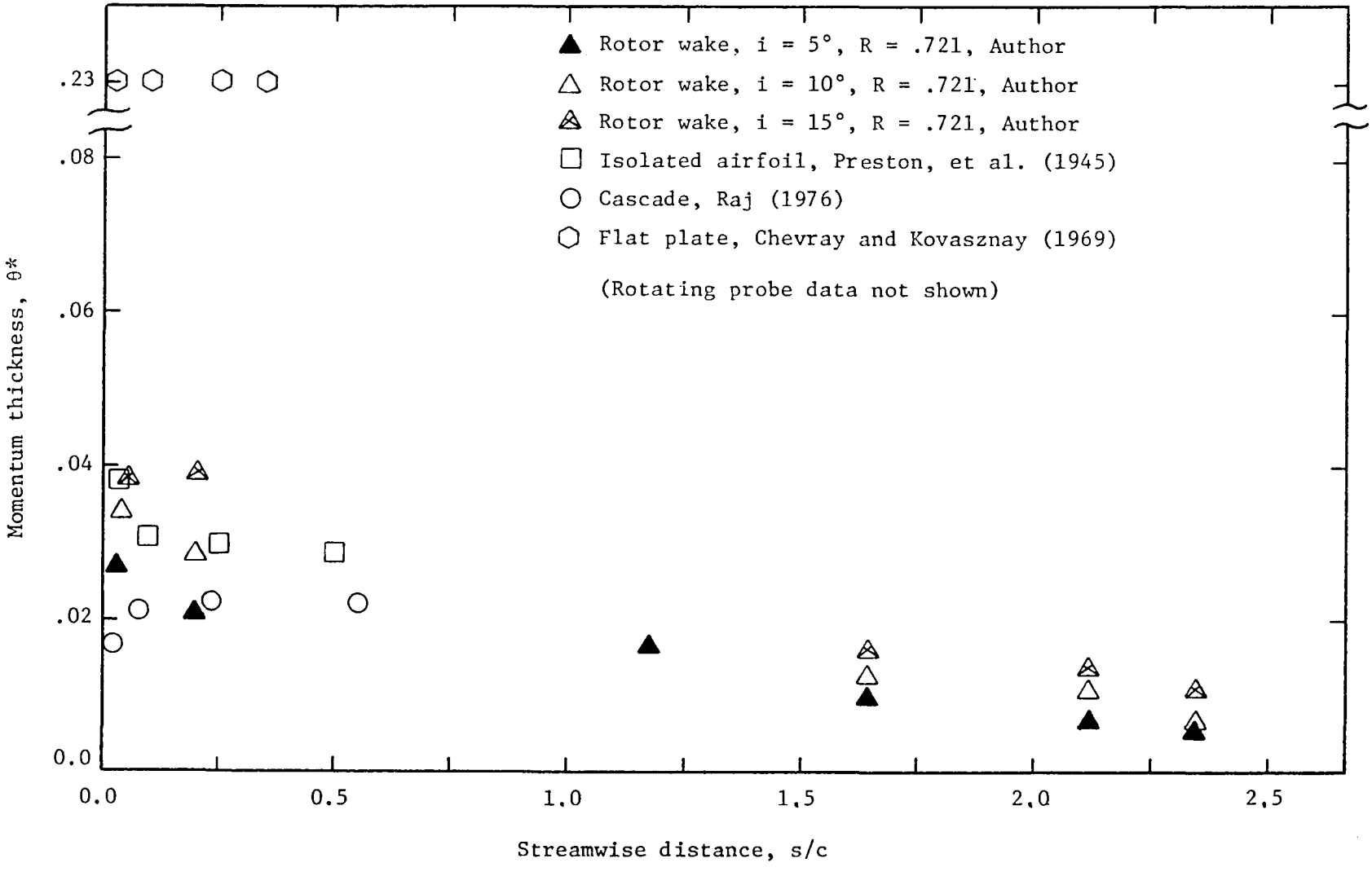

Figure 61. Momentum thickness in isolated airfoil, cascade, and rotor wakes

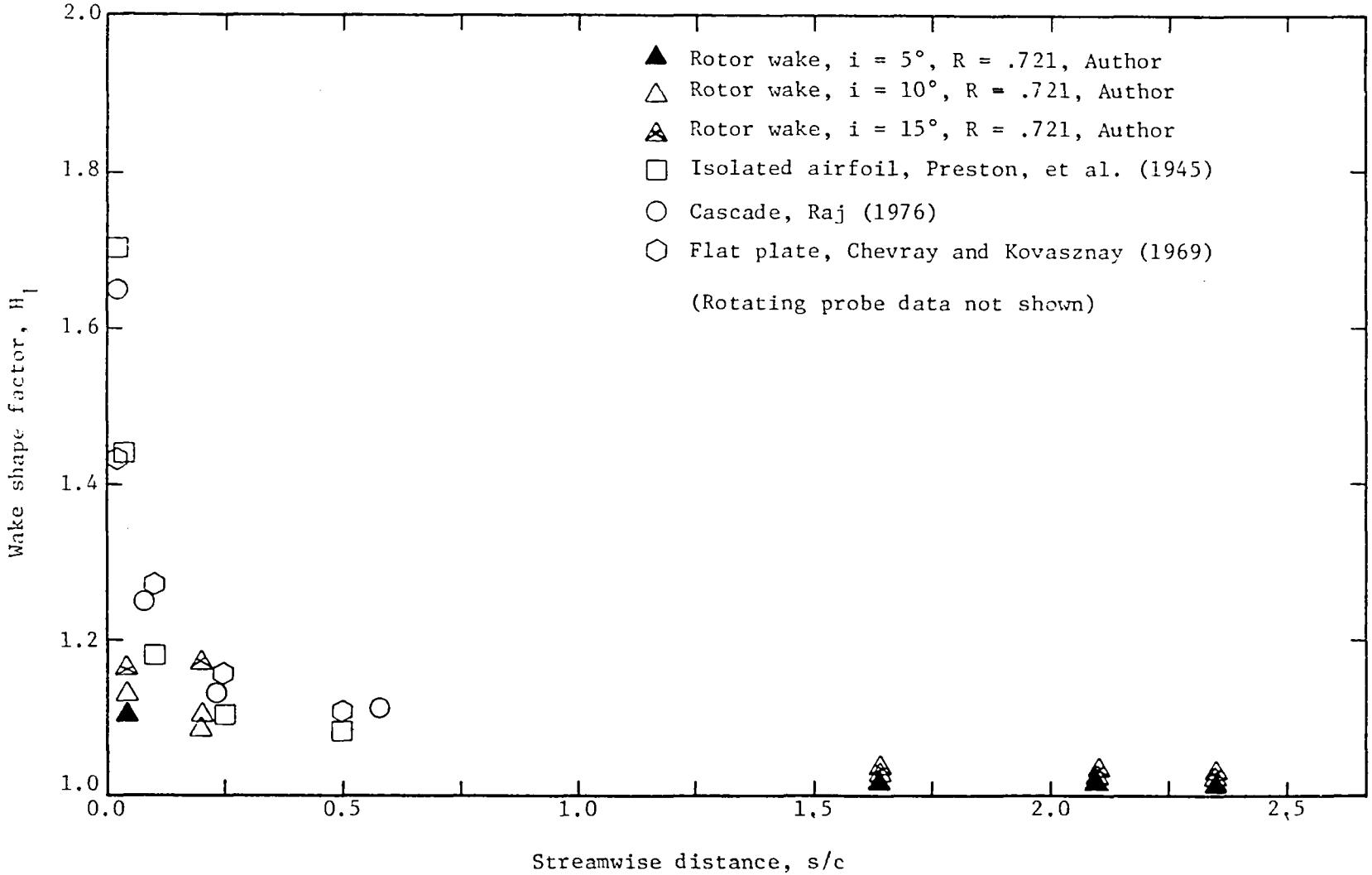

Figure 62. Shape factor in isolated airfoil, cascade, and rotor wakes

thickness for the flat plate is shown to be constant for all s/c locations. The isolated airfoil and cascade momentum thicknesses are shown to decrease and increase respectively in the near wake region and then to approach nearly constant values in the far wake. These trends are explained for the flat plate, isolated airfoil, and cascade wake by Raj and Lakshminarayana (1973).

The momentum thickness for the rotor wake at mid-radius for 5° and 10° incidences is shown to decrease initially and then to approach nearly constant values at the far downstream stations. At i = 15° the momentum thickness is found to increase slightly in the near wake and then to decrease to a nearly constant value at the far downstream locations. For all of the rotor wake measurements at mid-radius, increased blade loading is shown to result in larger momentum thicknesses. This indicates that a larger momentum deficit exists in the rotor wake for increased blade loading. A larger momentum deficit may result from an increased radial transport of momentum.

Equation (41) can be used to explain the decrease in momentum thickness for increasing distance from the rotor. Assuming semi-wake width is given by,

$$\delta = L_1 \theta^* \tag{75}$$

where L_1 is constant, one may write Equation (41) as,

$$\underbrace{\frac{1}{\theta^*}\frac{d\theta^*}{dz}\left(\frac{SFw_c}{r}+\frac{P_e S}{W_o^2 \rho r}+\frac{SK\overline{w'^2_c}}{W_o^2 r}\right)}_{(1)\ (2)\ (3)} + \underbrace{\frac{1}{\theta^*}\frac{\partial\theta^*}{\partial z}\frac{\bar{p}S}{W_o^2\rho r}}_{(4)} + \underbrace{\frac{S\overline{w'^2_c}}{L_1\theta^*}}_{(5)} = \underbrace{-\frac{SF}{r}\frac{dw_c}{dz}}_{(6)}$$

$$\underbrace{-\frac{SK}{W_o^2 r}\frac{\overline{dw'^2_c}}{dz}}_{(7)} + \underbrace{\frac{dW_o}{dr}\frac{Su_m H}{W_o r}}_{(8)} + \underbrace{\frac{1}{\rho r}S(P_c - P_e)\frac{V_o}{W_o^3}}_{(9)} + \underbrace{\frac{-S}{W_o^2\rho r}\frac{\partial\bar{P}}{\partial z}}_{(10)}, \tag{76}$$

Since terms (1) - (4) are positive, the right hand side of Equation (74) must be negative for momentum thickness to decrease for increasing z. Terms (5) - (8), representing turbulence intensity, blade loading, and radial velocity effects, are positive for the rotor tested. Therefore, decreasing momentum thickness in the near wake region may be attributed to static pressure variations as given by terms (9) and (10) which are negative. In the far wake region the static pressure variations are small (reported in Section 5.3.4) as will be terms (9) and (10), resulting in the nearly constant momentum thickness measured in this region.

The variation of wake shape factor, H_1, is shown in Figure 62 for flat plate, isolated airfoil, cascade, and rotor wake measurements. Wake shape factor for all of the data in Figure 62 is shown to decrease in the near wake region except at i = 15° for the rotor wake. However, the decrease in shape factor is less pronounced for the rotor wake data. In the far wake region all of the measurements shown in Figure 62 have obtained nearly constant but slowly decaying values. From its definition, shape factor will approach zero for s/c becoming very large. The effect of blade loading on the rotor wake shape factor is clearly seen in Figure 62, larger values of shape factor are measured for increased blade loading.

The trends for the flat plate, isolated airfoil, and cascade wake shape factors is discussed by Raj and Lakshminarayana (1973) using an expression for shape factor given by Spence (1952). This expression is not valid for the rotor wake due to the large three-dimensional nature of flow. This three-dimensionality may have resulted in the lower values of shape factor found in the near wake for the rotor wake when compared to flat plate, isolated airfoil, and cascade measurements.

5.8 Isolated Airfoil, Cascade, and Rotor Wake Correlations

Correlation of the far wake data behind a body was determined theoretically (Schlicting, 1968) using the drag coefficient, c_d, to collapse mean velocity data from different configurations into a single curve. Schlichting's (1968) analysis of the two-dimensional turbulent far wake indicate a dependency of the type,

$$\frac{Qd_c}{Q_o} = c_d^{1/2} f_1(s/c) \quad . \tag{77}$$

However, Silverstein, et al. (1939a) and Silverstein, et al. (1939b) show a good correlation for measurements made behind an isolated airfoil using a different functional dependence for c_d than that given in Equation (77). This functional dependence was given as,

$$\frac{Qd_c}{Q_o} = c_d^{1/4} f_2(s/c) \quad . \tag{78}$$

Correlated wake defect data was examined using the relationships given by Equations (77) and (78). The correlation given by Equation (78) has been determined to give the better correlation. Hence, correlated isolated airfoil, cascade, and rotor wake data is presented using the relationship given by Equation (78).

A correlation of isolated airfoil wake data from Mendelshon (1947) and Preston, et al. (1945) is shown in Figure 63 using the functional dependence given by Equation (78). The correlation seems to work well in the far wake region ($s/c > .25$). Even in the near wake region the correlation is quite good. However, in the trailing edge region the correlation shows a significant degree of scatter. The decay rate in the near wake region for the isolated airfoil correlation shown in Figure 63 is found to agree well with the equation given by,

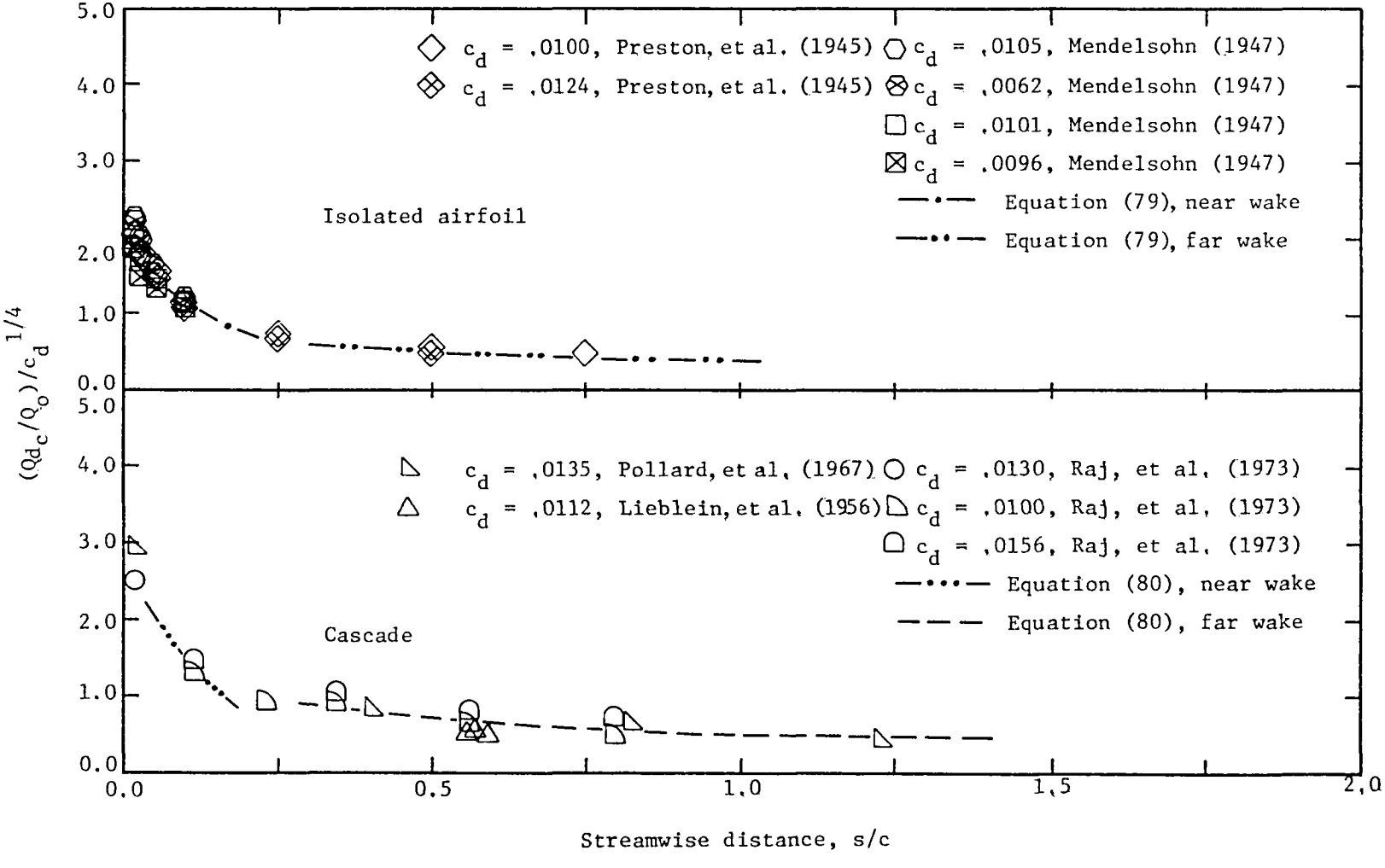

Figure 63. Isolated airfoil and cascade wake total velocity correlation

$$\frac{Q_{d_c}}{Q_o} = c_d^{1/4}\left[B_1\left(\frac{s}{c} - \frac{s_o}{c}\right)^{-1/2} + B_2\left(\frac{s}{c} - \frac{s_o}{c}\right)^{-1}\right] \tag{79}$$

where s_o/c represents the virtual origin. The functional relation in Equation (79) is given by Goldstein (1953) for a flat plate laminar wake. This relation is used since no analytical expressions are presently available from a near wake solution of a turbulent wake. The constants B_1 and B_2 and the virtual origin, determined for the curve shown in Figure 63, are given in Table 5. The decay rate in the far wake region agrees well with the curve given by Equation (79) with $B_2 = 0.0$. This curve is shown in Figure 63 and the constants and virtual origins are given in Table 5.

A cascade wake correlation is shown in Figure 63 using the data from Pollard and Gostelow (1967), Lieblein and Roudebush (1956), and Raj and Lakshminarayana (1973). A good correlation is shown in both the near and far wake regions using the correlation given by Equation (78). The functional dependence with s/c is shown in the near and far wake regions using the relationship,

$$\frac{Q_{d_c}}{Q_o} = c_d^{1/4}\left[B_3\left(\frac{s}{c} - \frac{s_o}{c}\right)^{-1/2} + B_4\left(\frac{s}{c} - \frac{s_o}{c}\right)^{-1}\right] \tag{80}$$

where $B_4 = 0.0$ in the far wake region. As in Equation (79) s_o/c represents the virtual origin. The virtual origins and constants B_3 and B_4 are given in Table 5 for each curve.

A rotor wake correlation is shown in Figure 64 using data from the present investigation and from Schmidt and Okkishi (1977). The correlation using $c_d^{1/4}$ is seen to be good for both the near and far wake regions. However, a large scatter is shown than for the isolated airfoil or cascade

Equation	Region	Virtual origin	Constants
(79)	Near wake	-.193	$B_1 = -.578$, $B_2 = .650$
(79)	Far wake	-.182	$B_1 = .495$, $B_2 = 0.0$
(80)	Near wake	-.141	$B_3 = -.706$, $B_4 = .681$
(80)	Far wake	-.060	$B_3 = .540$, $B_4 = 0.0$
(81)	Near wake	-.160	$B_5 = -.361$, $B_6 = .463$
(81)	Far wake	-.360	$B_5 = .271$, $B_6 = 0.0$
(83)	Near wake	-.530	$D_1 = -.096$, $D_2 = .229$
(83)	Far wake	-.225	$D_1 = .070$, $D_2 = 0.0$
(84)	Far wake	-.143	$D_3 = .391$, $D_4 = 0.0$
(85)	Near wake	-.400	$D_5 = -.306$, $D_6 = .845$
(85)	Far wake	.258	$D_5 = .735$, $D_6 = 0.0$

Table 5. Constants and virtual origins in Equations (79), (80), (81), (83), (84), and (85)

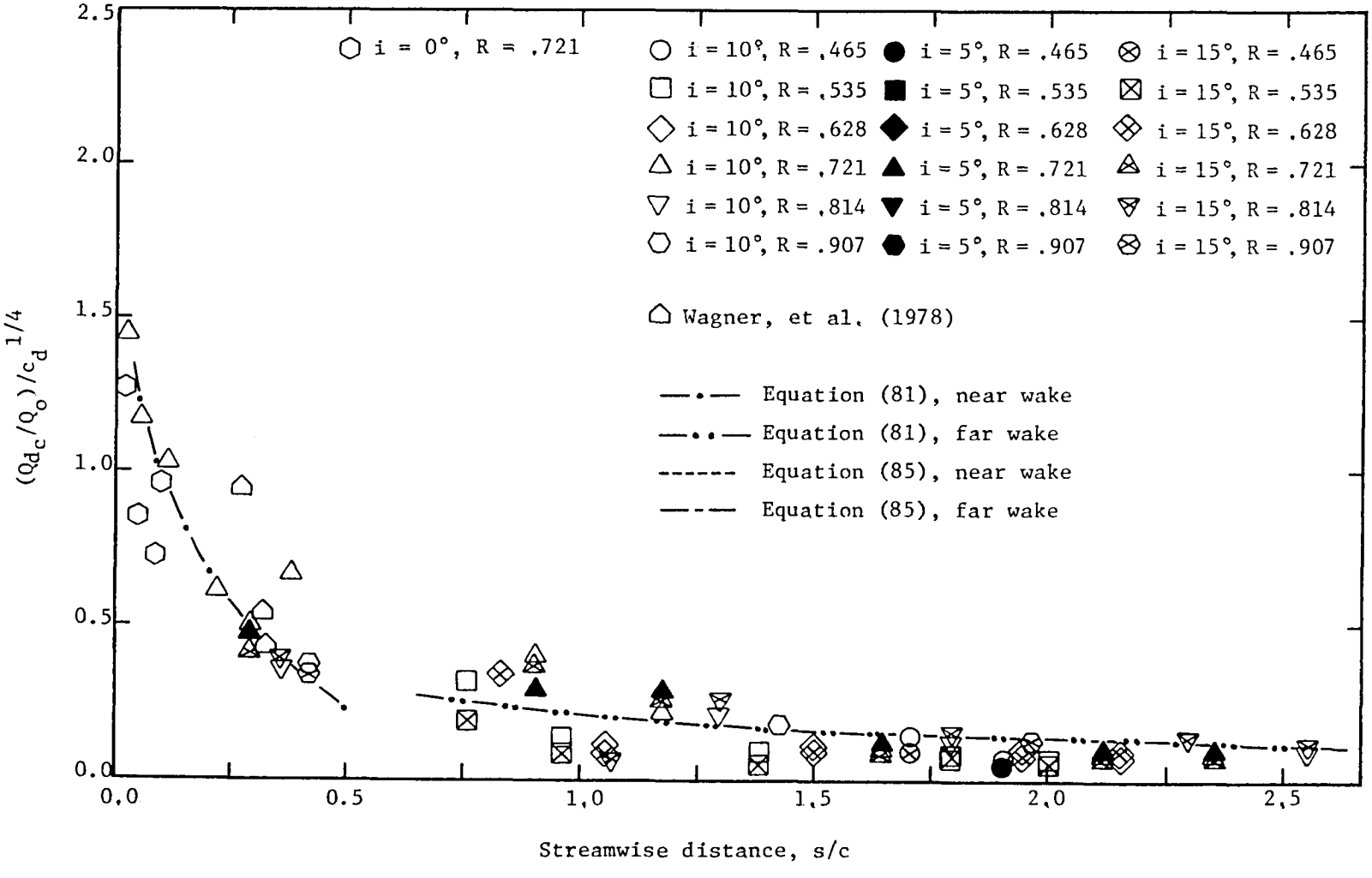

Figure 64. Rotor wake total velocity correlation with $c_d^{1/4}$

wake correlations. The correlated data show reasonable agreement with the equation,

$$\frac{Qd_c}{Q_o} = c_d^{1/4}[B_5(\frac{s}{c} - \frac{s_o}{c})^{-1/2} + B_6(\frac{s}{c} - \frac{s_o}{c})^{-1}] \quad (81)$$

in both the near and far wake regions. The functional dependence with s/c is shown in the far wake region for $B_6 = 0.0$. Constants B_5 and B_6 and virtual origins for each curve are given in Table 5.

The correlation of wake data using $c_d^{1/2}$ had previously been reported by Reynolds, et al. (1978) to give better results for the rotor wake than that found with $c_d^{1/4}$. For the measurements presented in this thesis the correlation of rotor wake data using $c_d^{1/2}$ is shown in Figure 65. The correlation with $c_d^{1/4}$ shown in Figure 64 is clearly an improvement over that shown in Figure 65 with $c_d^{1/2}$. Therefore, all wake measurements reported in this investigation are correlated with $c_d^{1/4}$.

Semi-wake width has been correlated with $c_d^{1/4}$ for isolated airfoil, cascade, and rotor wake data. This correlation is given as,

$$\frac{\delta}{S} = c_d^{1/4} f_3(\frac{s}{c}) \quad . \quad (82)$$

A correlation of semi-wake data from Mendelshon (1947) and Preston, et al. (1945) is shown in Figure 66. Semi-wake width correlation in the trailing edge and near wake regions show significant scatter. However, in the far wake region the correlation is found to be quite good. The near and far wake semi-wake width correlation is shown to agree well with a functional dependence of s/c given by,

$$\frac{\delta}{C} = c_d^{1/4}[D_1(\frac{s}{c} - \frac{s_o}{c})^{1/2} + D_2(\frac{s}{c} - \frac{s_o}{c})] \quad (83)$$

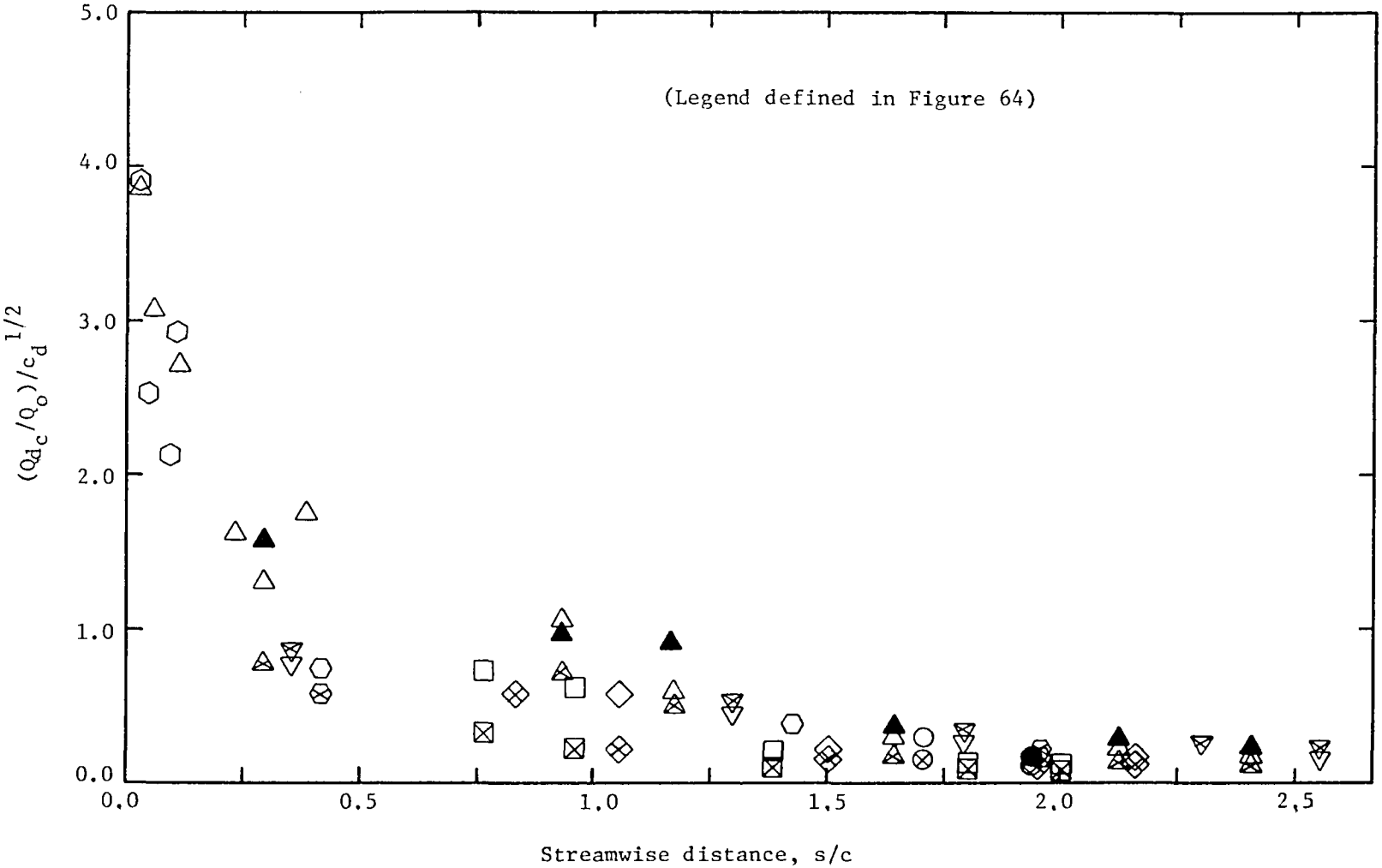

Figure 65. Rotor wake total velocity correlation with $c_d^{1/2}$

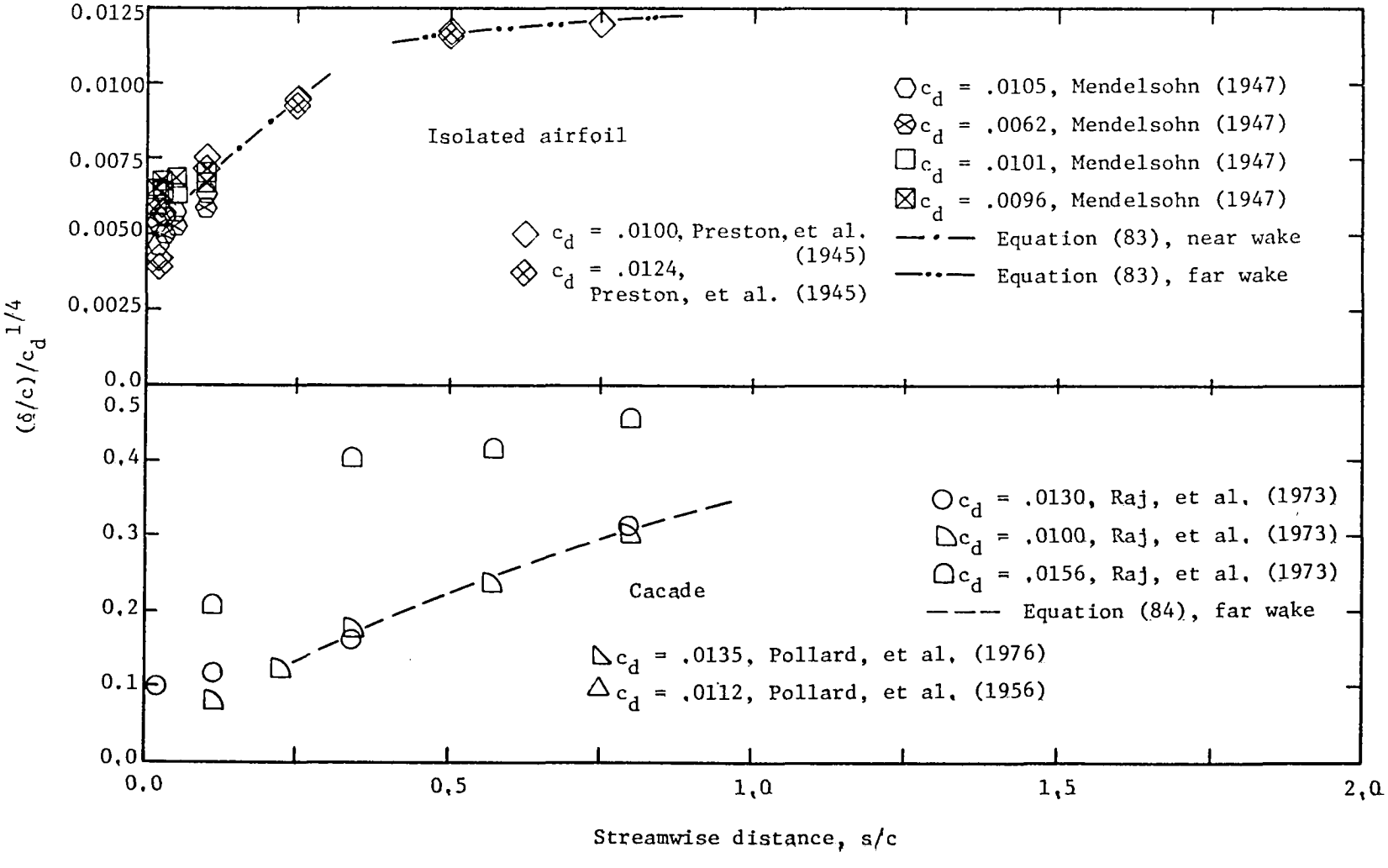

Figure 66. Isolated airfoil and cascade wake semi-wake width correlation

with $D_2 = 0.0$ in the far wake region. The virtual origin is represented by s_o/c. The constants D_1, D_2, and s_o/c, determined for each curve shown in Figure 66, are given in Table 5.

A semi-wake width correlation for the cascade wake data due to Raj and Lakshminarayana (1973) is shown in Figure 66. The correlation of semi-wake width shows a large degree of scatter in both the near and far wake regions. However, two of the operating conditions tested by Raj and Lakshminarayana (1973) do show a good correlation. The correlated semi-wake width in the far wake seems to agree with the expression given by,

$$\frac{\delta}{c} = c_d^{1/4}[D_3(\frac{s}{c} - \frac{s_o}{c})^{1/2} + D_4(\frac{s}{c} - \frac{s_o}{c})] \qquad (84)$$

where $D_4 = 0.0$ in the far wake and s_o/c represents the virtual origin. The virtual origins and constants D_3 and D_4 are given in Table 5.

Correlation of the rotor wake semi-wake width data from the present investigation using Equation (82) is shown in Figure 67. The correlation is found to work well in both the near and far wake regions. Some scatter in the data may be due to the effect on the width from radial velocities in the wake. The correlated semi-wake width is shown to agree well for a functional dependence of s/c given by,

$$\frac{\delta}{S} = c_d^{1/4}[D_5(\frac{s}{c} - \frac{s_o}{c})^{1/2} + D_6(\frac{s}{c} - \frac{s_o}{c})d \qquad (85)$$

where s_o/c represents the virtual origin in the wake and in the far wake region $D_6 = 0.0$. The constants D_5 and D_6 and the virtual origins, determined for each curve shown in Figure 67 are given in Table 5.

5.9 Wake Property Variation with Radius

5.9.1 Mean velocity

Radial variations of axial and tangential mean velocity defects and maximum radial mean velocity difference in the rotor wake is shown in

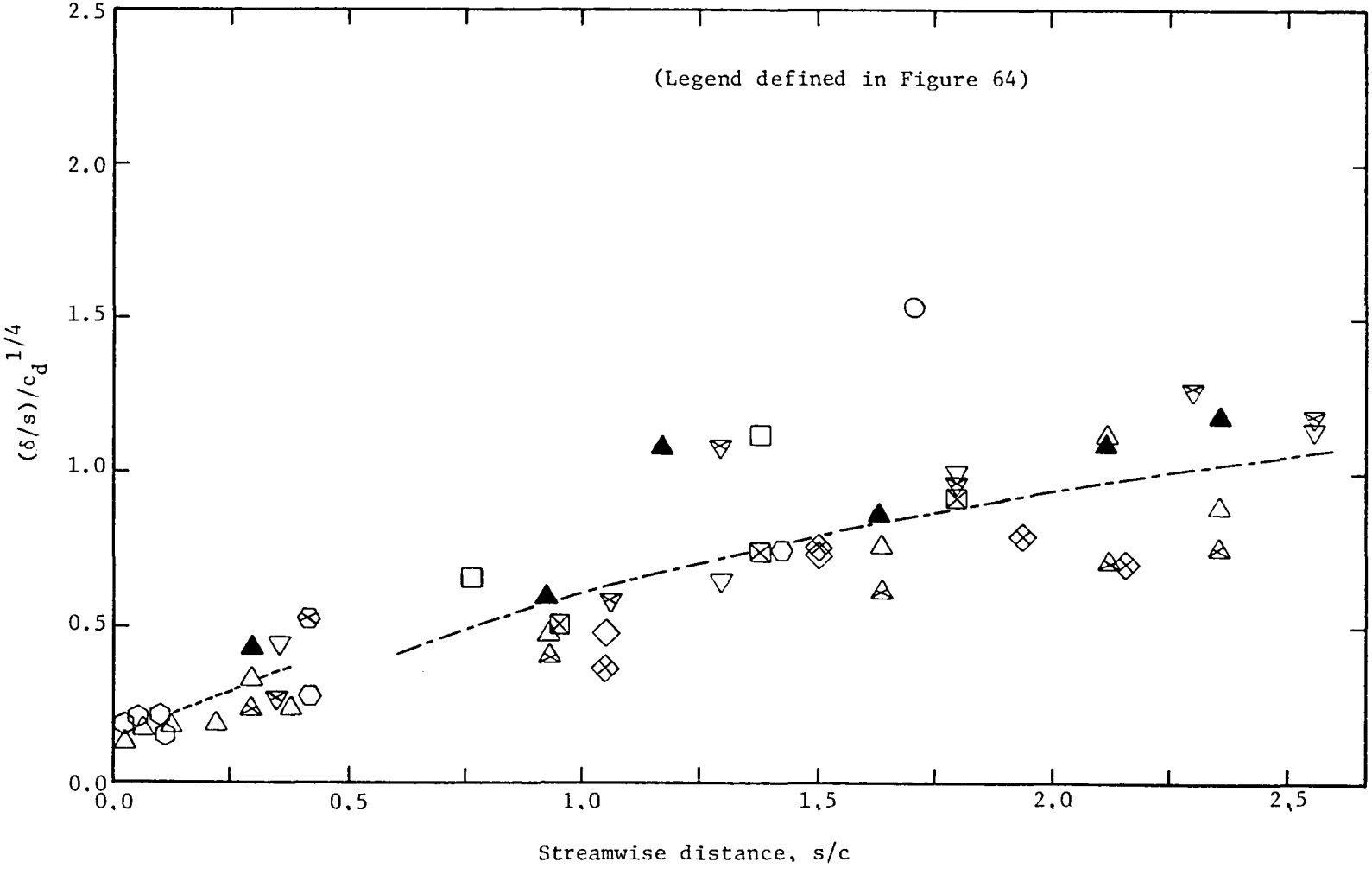

Figure 67. Rotor wake semi-wake width correlation

Figure 68, 69, and 70, respectively. Data is shown for measurement stations 1, 4, and 6 (defined in Table 3) for rotor blade incidences of 10° and 15°.

Axial mean velocity defect variation with radius is shown in Figure 68. Data at station 6 for both rotor blade incidences (10° and 15°) shows a decrease in axial velocity defect for increasing radius except between R = .628 and R = .721 where the defect is approximately constant. This trend is as expected since streamwise distance downstream of the rotor in the relative frame of reference increases for increasing radius. Since the wake decays along the relative streamlines, measurements at larger radial positions is in fact at larger s/c locations. However, axial mean velocity defect is significantly larger for R = .535 than for other radial locations for station 6. This may result from the effects of the hub wall boundary layer on the wake decay characteristics.

The axial velocity defects for stations 1 and 4 in Figure 68 show relatively small changes for varying radius. Measurements made at these stations are sufficiently far downstream so that the axial velocity defect is small for all radial locations. The data shown for stations 1 and 4 does show slightly larger axial velocity defects towards the hub and end wall boundary layers. Axial defect for R > .721 would be expected to decrease for increasing radius since streamwise distance from the rotor is larger. This increase in axial velocity defect indicates the effects of radial transport of mass and momentum and end wall flows on the rotor wake.

The effect of increasing rotor blade incidence on axial velocity defect is small for the far wake measurement stations shown in Figure 68. Axial velocity defect is found to be slightly larger for the 15° operating

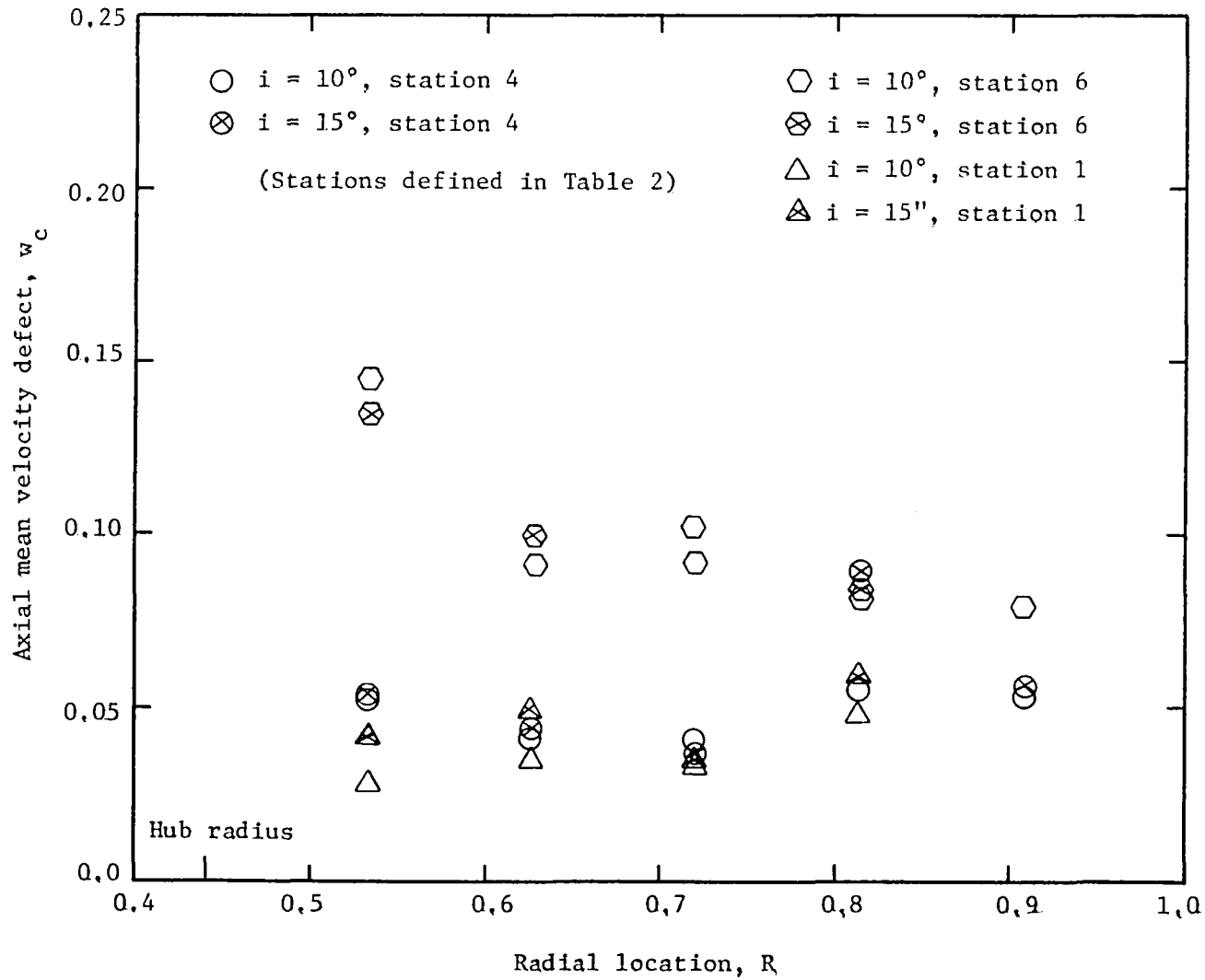

Figure 68. Radial variation of axial mean velocity defect at the wake centerline for i = 10° and 15°

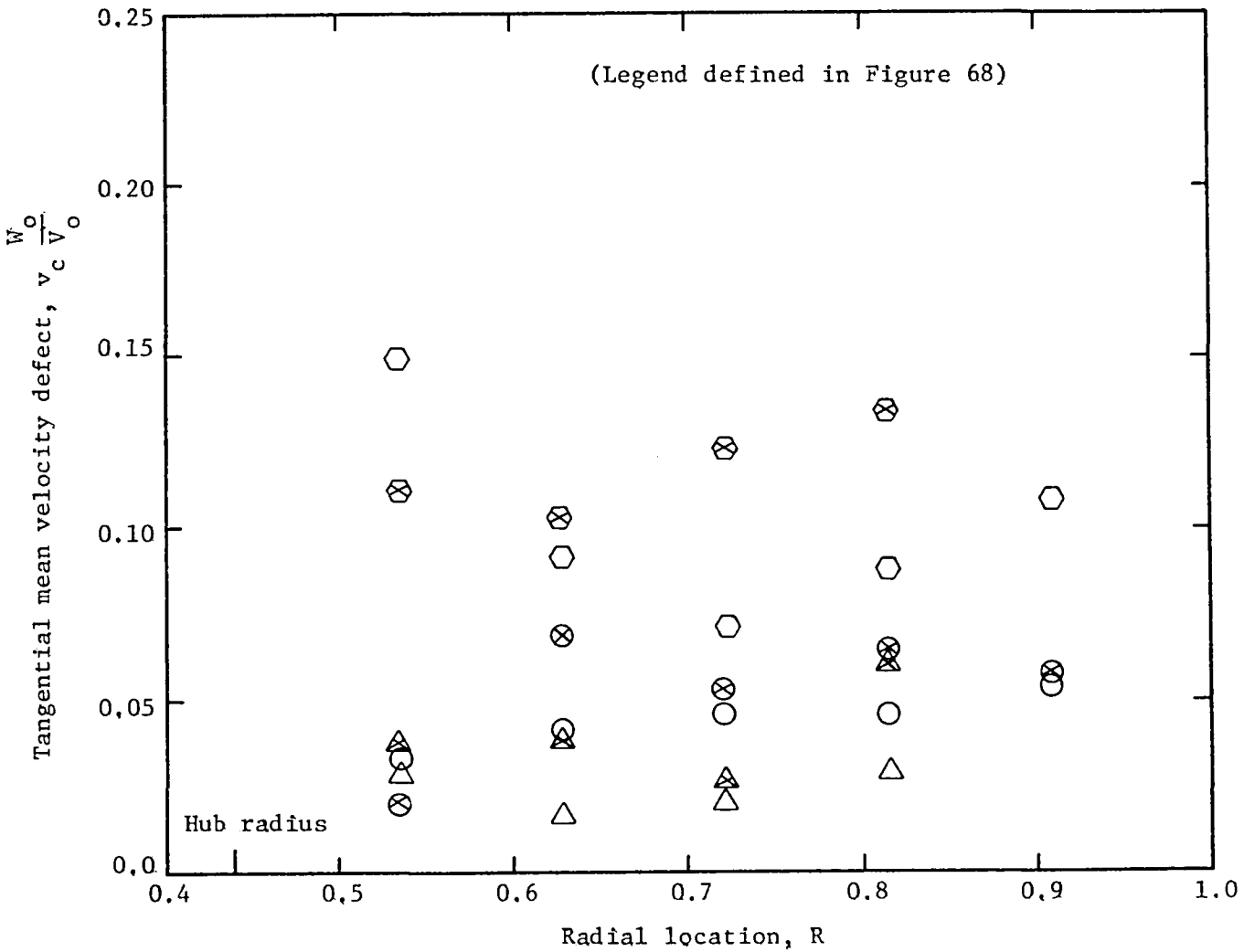

Figure 69. Radial variation of tangential mean velocity defect at the wake centerline for $i = 10°$ and $15°$

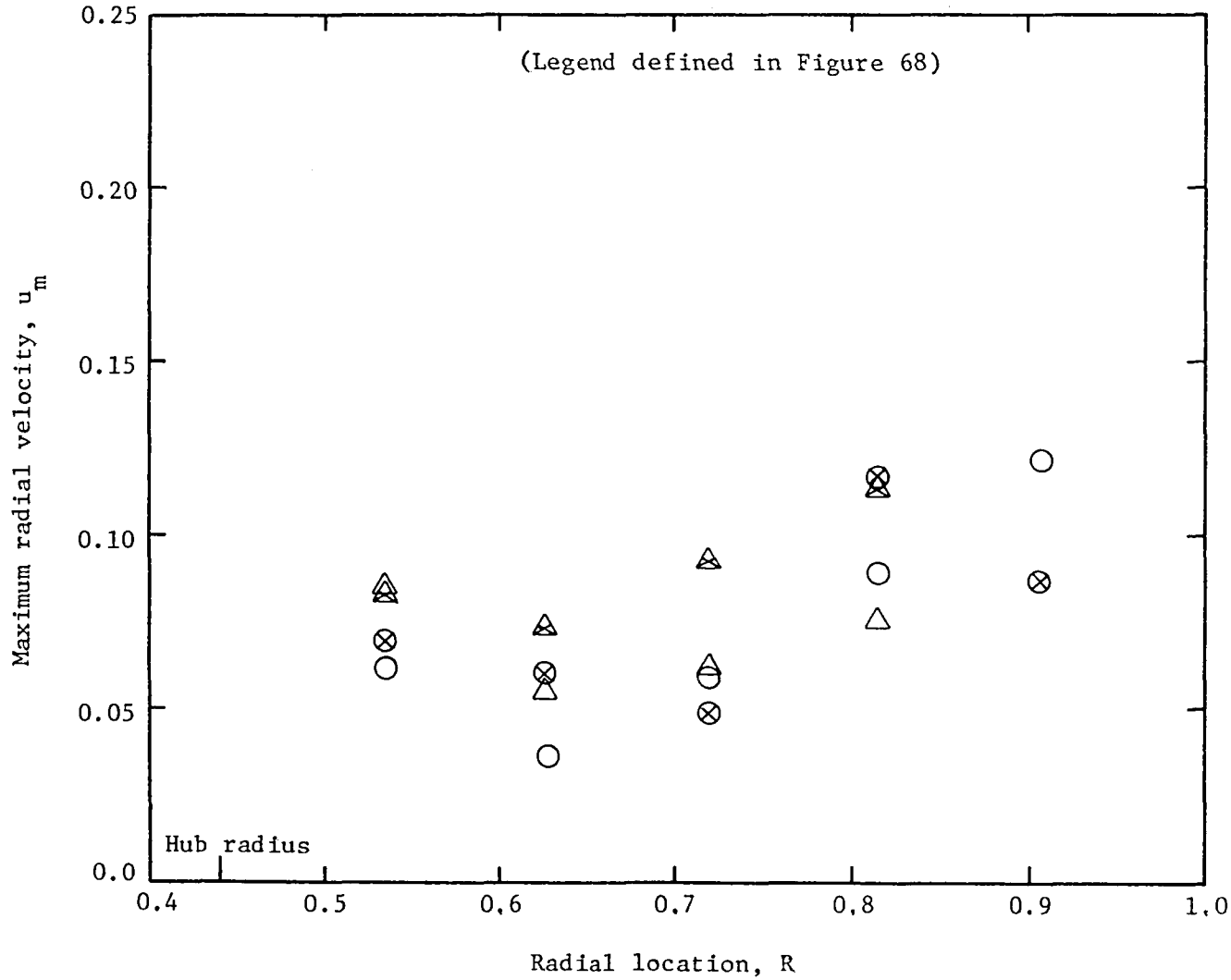

Figure 70. Radial variation of maximum radial velocity difference in the wake for i = 10° and 15°

condition than for the 10° operating condition for almost all of the data shown.

Variation of tangential velocity defect with radius is shown in Figure 69. For the measurements at 10° incidence shown for station 6 the tangential velocity defect is found to increase with radius for R > .721. For the 15° operating condition, the tangential velocity defect increases for R > .628. At both 10° and 15° rotor blade incidences at station 6 the defect also increases towards the hub wall as indicated by the data at R = .535. Defect in tangential velocity defect is expected to decrease for increasing radius since larger s/c locations are found at larger radial positions. This clearly indicates the three-dimensional effects on the rotor wake flow. Secondary flows near the hub wall may result for the increase in tangential velocity defect in this region. Strong end wall flow effects, either tip vortex or secondary flows, result in the increased tangential velocity defects found for increasing radius beyond mid-span. The radial transport of mass and momentum may also account for the increased tangential velocity defects.

At stations 1 and 4 in Figure 69 the tangential velocity defects show the same trends as that found at station 6. The effects of the hub and end wall flows are shown to be weaker at these stations since they are farther downstream from the rotor.

The effects of varying blade loading on the tangential velocity defect is clearly shown in Figure 69. Tangential velocity defect is found to increase for increased blade loading except for some scatter in the data at station 6 for R = .535. The increase in tangential velocity defects in Figure 69 are more pronounced than for corresponding axial velocity defects shown in Figure 68. This is consistent with the rotor

wake characteristics found at all Z locations at mid-radius (R = .721) as discussed in Section 5.7.1.

The effects of varying radius on the maximum radial velocity differences in the rotor wake at stations 1 and 4 are shown in Figure 70. Radial velocities in the wake are shown to still be significant at rotor blade incidences of 10° and 15° for both of the far wake stations. This indicates that the rotor wake is highly three-dimensional with a large radial transport of mass, momentum, and energy in the far wake region. This radial transport will result in small defects in axial and tangential mean velocities as shown in Figures 68 and 69, respectively. An increase in maximum radial velocity difference in the wake is clearly shown for increasing radius past mid-span (R = .721). This increase in radial velocities in the wake shows the effects of strong radial pressure gradients and end wall flows. The increase of maximum radial velocity difference towards the hub may indicate the effects of secondary flows near the hub wall.

5.9.2 Turbulence intensities

The radial variation of wake maximum axial, tangential, and radial turbulence intensities are shown in Figures 71, 72, and 73, respectively. Measurements are shown for rotor blade incidences of 10° and 15° at stations 1, 2, and 4 (defined in Table 3). At all the measurement stations shown in Figures 71, 72, and 73 the wake maximum axial, tangential, and radial turbulence intensities show the lowest values near mid-radius at R = .628 and R = .721. All components of maximum intensities show similar increases towards the hub and end wall radii. This trend is still very pronounced at the farthest downstream station (station 1). The hub and end wall flows are therefore found to alter substantially

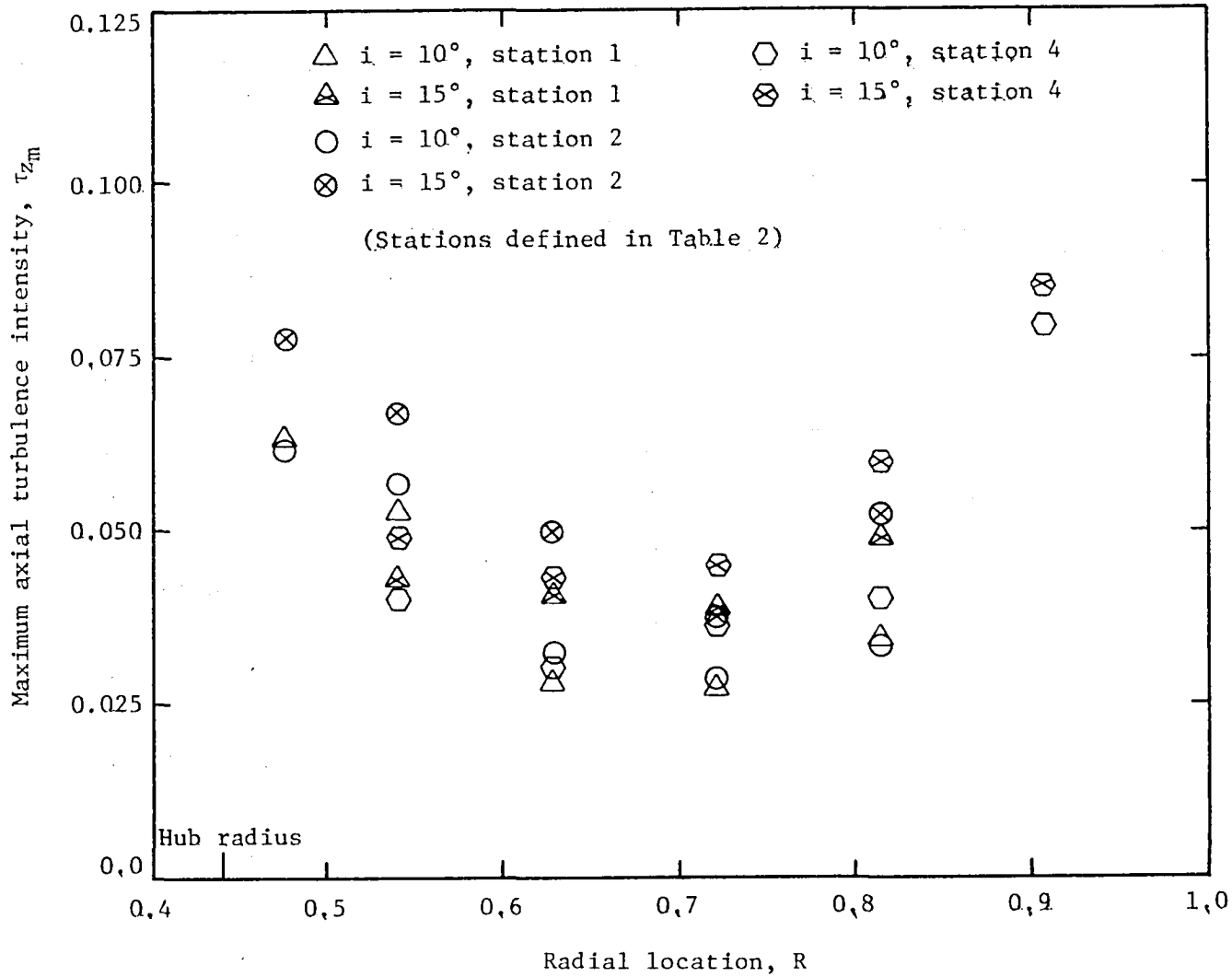

Figure 71. Radial variation of maximum axial turbulence intensity in the wake for i = 10° and 15°

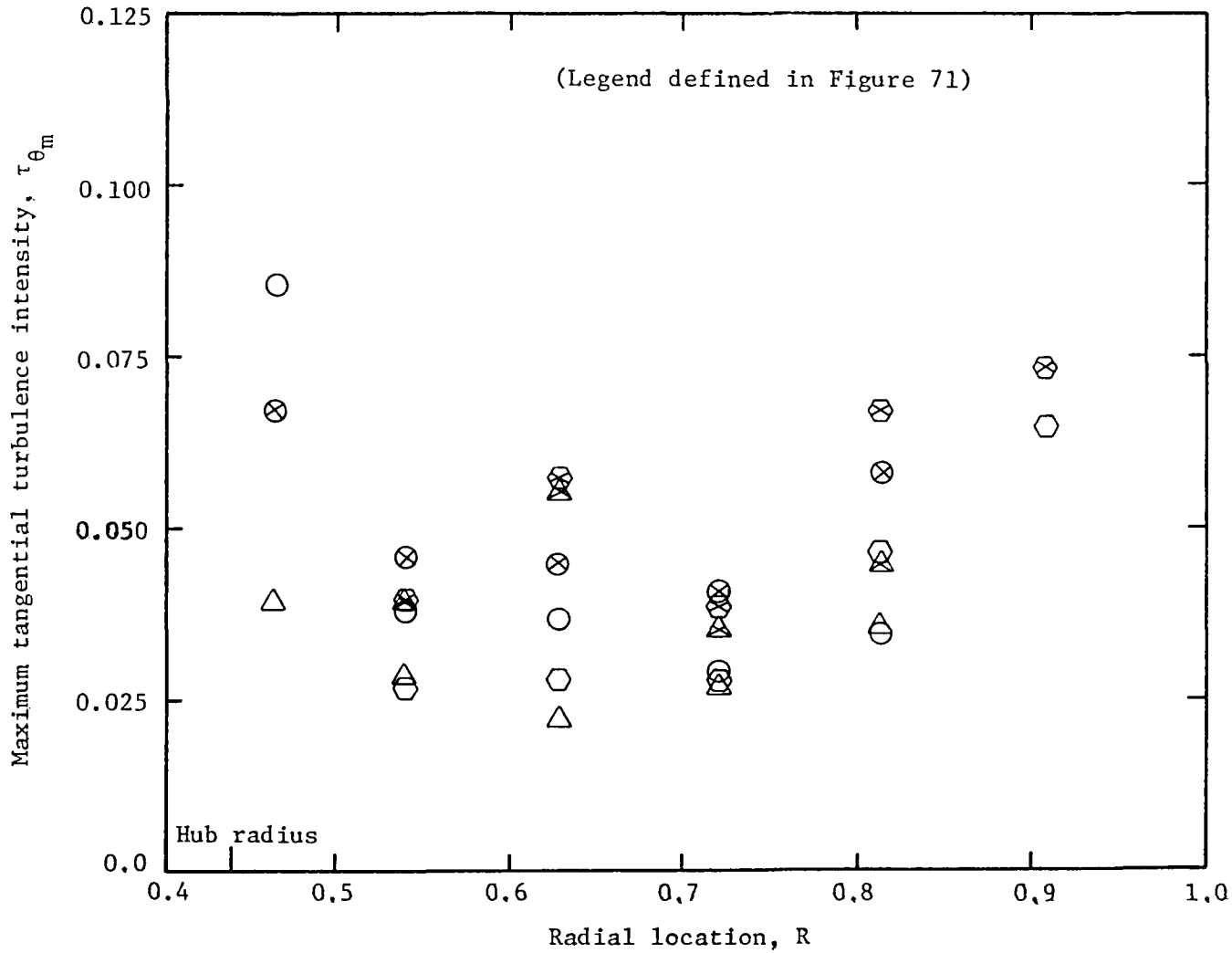

Figure 72. Radial variation of maximum tangential turbulence intensity in the wake for i = 10° and 15°

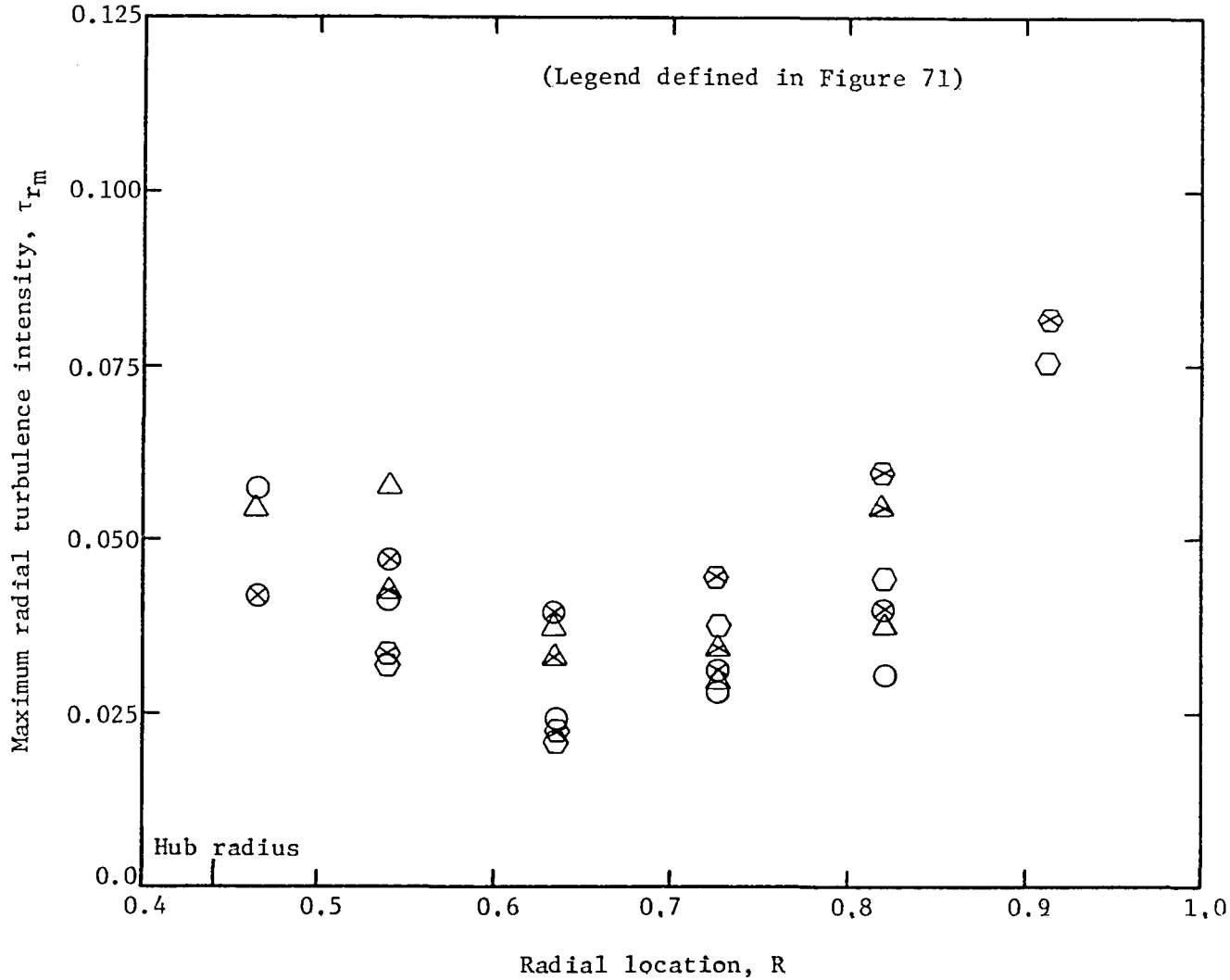

Fiugre 73. Radial variation of maximum radial turbulent intensity in the wake for i = 10° and 15°

the axial, tangential, and radial intensities in the rotor wake. Hence, the resulting periodic and unsteady inlet conditions to a subsequent blade row due to the rotor wake would not be radially uniform for turbulence intensities. It is shown to be uniform near mid-radius for only approximately twenty percent of the radius.

The presence of maximum radial intensities of the same order of magnitude as the axial and tangential components in the rotor wake indicates the three-dimensional structure of the turbulence. This characteristic is present at all radial locations for both rotor blade incidences (10° and 15°) even for measurements far downstream at station 1.

Free stream axial, tangential, and radial intensities are shown in Figures 74, 75, and 76, respectively. The data is shown for the 10° and 15° operating conditions at stations 1, 2, and 4 (defined in Table 3). While this data does not indicate any rotor wake characteristics it is useful to the turbomachine acoustician or aerodynamicist. The measurements show a free stream structure of turbulence that will be present at the inlet to a subsequent blade row. All components of free stream turbulence intensities are found to be constant over a large percent of the radius (approximately 50 percent). The increase of all components of intensity near the hub and end walls indicates the presence of the hub and end wall boundary layers. The data shows a three-dimensional structure of turbulence in the free stream with axial, tangential, and radial intensities of the same order of magnitude.

5.9.3 Semi-wake width

The variation of semi-wake width with radius is shown in Figure 77 for measurements made at stations 1 and 4 (defined in Table 3) with rotor blade incidences of 10° and 15°. For all measurements shown in Figure 77,

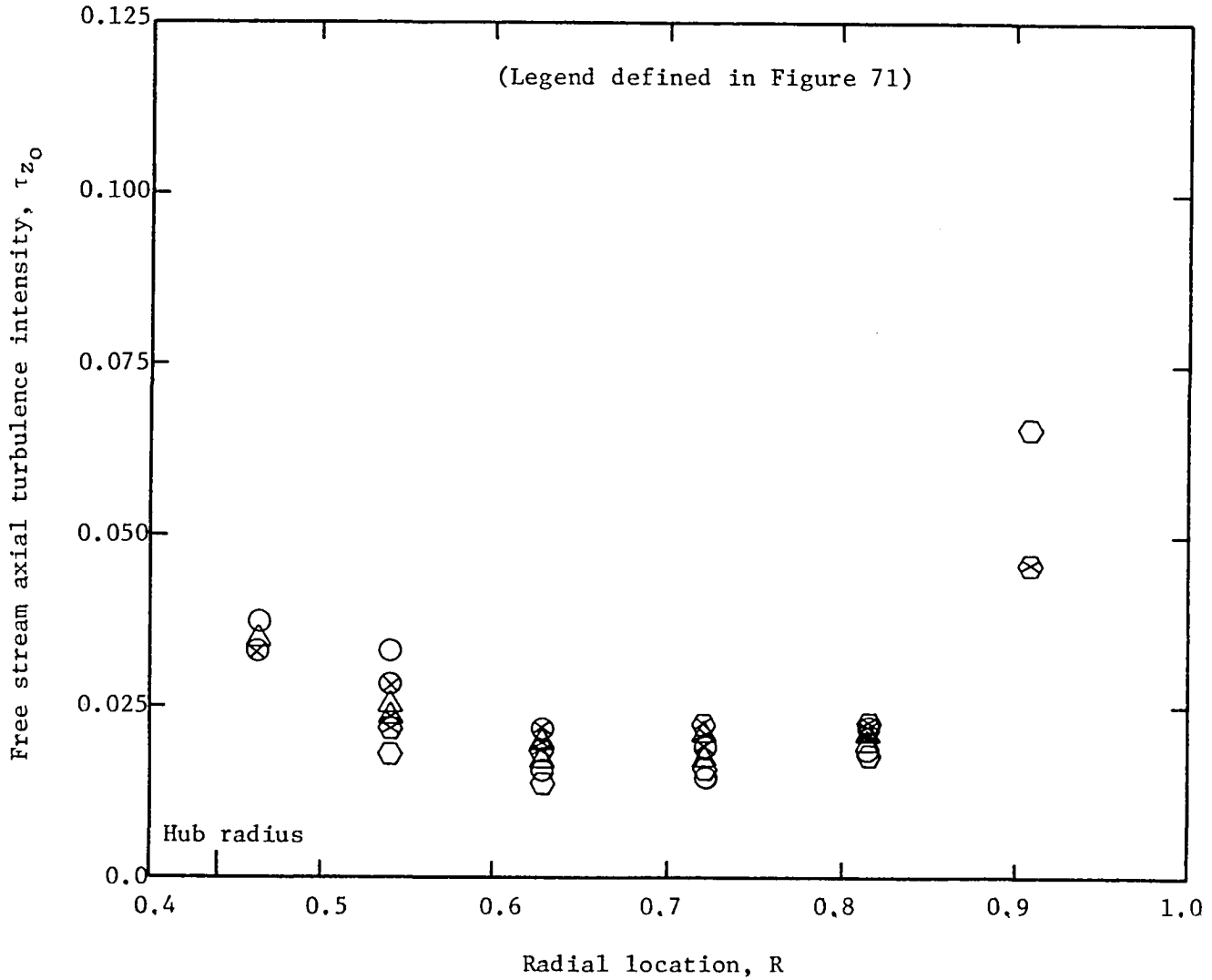

Figure 74. Radial variation of free stream axial turbulence intensity for i = 10° and 15°

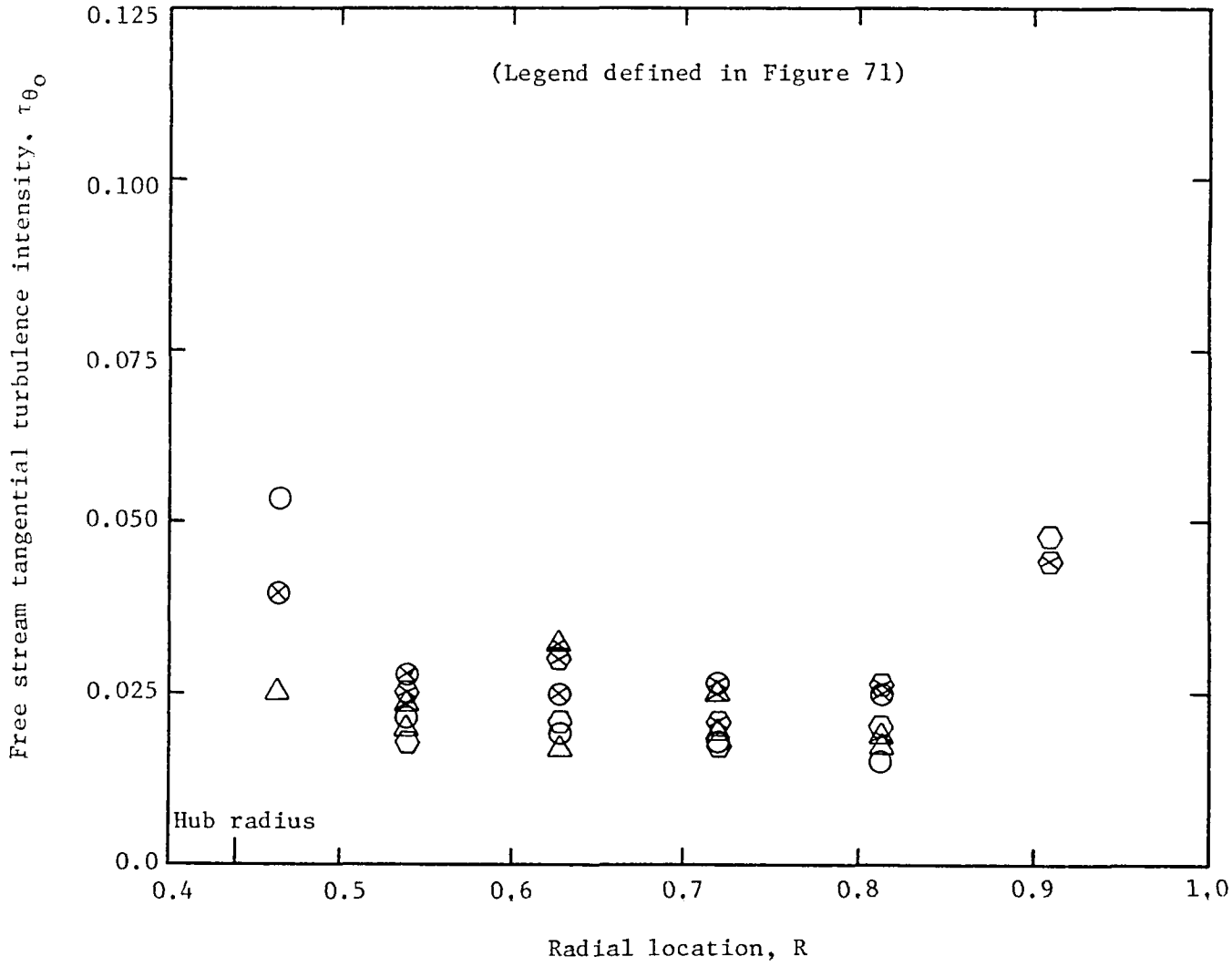

Figure 75. Radial variation of free stream tangential turbulence intensity for i = 10° and 15°

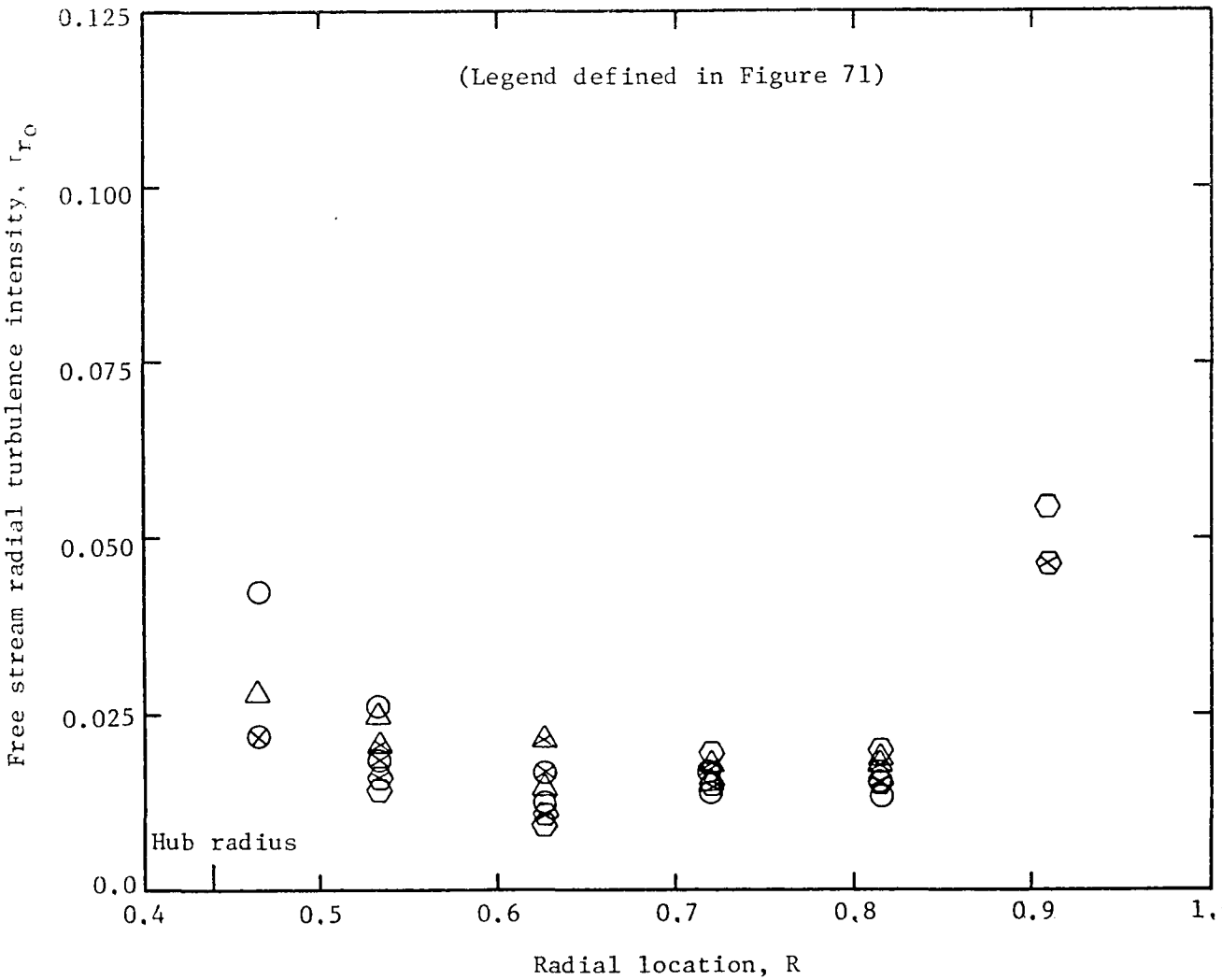

Figure 76. Radial variation of free stream radial turbulence intensity for i = 10° and 15°

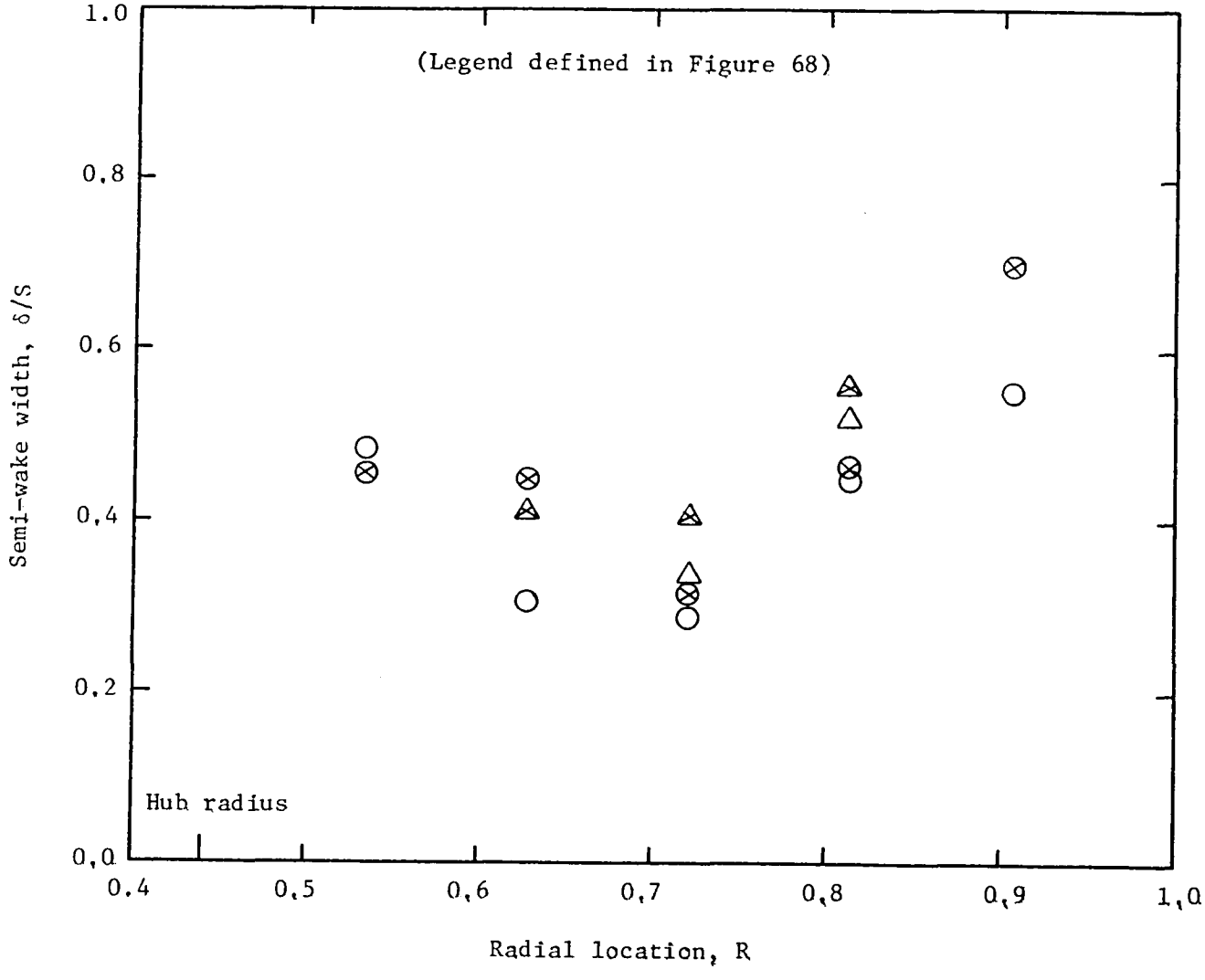

Figure 77. Radial variation of semi-wake width for $i = 10°$ and $15°$

the lowest value of wake width is at mid-radius (R = .721). A large increase in wake width is found for increasing radius beyond mid-radius. This represents the effects of the large radially outward transport of mass momentum, and energy in the rotor wake. A smaller increase in semi-wake width near the hub wall is also shown in Figure 77. This characteristic may result from the hub wall boundary layer and secondary flow effects on the rotor wake.

5.9.4 Momentum thickness

Momentum thickness variation with radius is shown in Figure 78. Data is shown for measurements made at the 10° and 15° operating conditions at stations 1 and 4 (defined in Table 3). Momentum thickness is shown in Figure 78 to increase with increasing radius above the mid-radius stations (from R = .721 to R = .815). The radially outward transport of mass, momentum, and energy may result in the larger momentum thickness measured for increasing radius. Since radial transport is larger for the 15° operating condition, the data shows a more pronounced increased in momentum thickness than that for the 10° incidence operating condition. Consistent with increased momentum thicknesses towards the end wall regions, were the larger semi-wake widths and defects in mean velocity measured at R = .814 compared to those measured at R = .721. The variations of momentum thickness for radial stations less than R = .721 do not show any conclusive trends. However, momentum thickness does appear to be approximately constant for some of the data in the mid-radius region at R = .628 and R = .721.

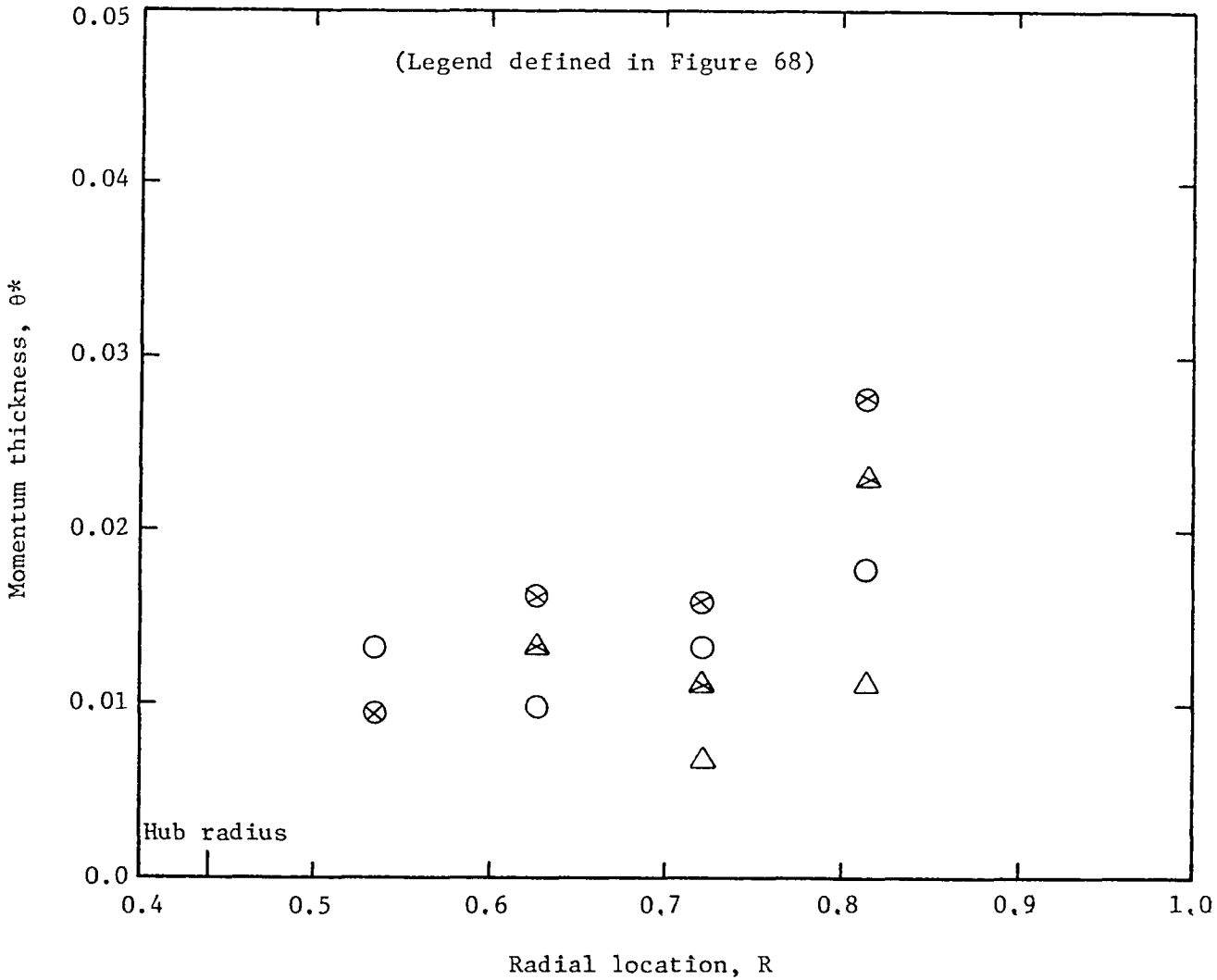

Figure 78. Radial variation of wake momentum thickness for i = 10° and 15°

5.10 Structure of Turbulence

5.10.1 Flatness factor

Variations of flatness factor across the rotor wake at mid-radius (R = .721) at a blade incidence of 10° is shown in Figure 79. Measurements are presented for both the near and far wake flow regions.

In the near wake region for Z < .2 the flatness factor variations across the rotor wake are found to be very large. Since a flatness factor variation from .4 to -.4 across the wake is not representative of an isotropic structure of turbulence, the complex turbulence characteristics of the rotor wake are evident. Turbulence is certainly not isotropic throughout the rotor wake in the near wake region. Part of the complex flatness factor behavior in the rotor wake will be a result of rotation and centrifugal force effects.

Flatness factor in the far wake region for Z > 1.0 has become almost constant with less variation across the rotor wake. This is a result of the very small Reynolds stress variations measured at these stations while turbulence intensities were found at about two to four percent in the wake and freestream.

Ermshaus (1970) has given the flatness factor variations in the far wakes of axisymmetric bodies and for the two-dimensional far wake of a circular cylinder. These measurements show a large variation of flatness factor throughout the wake. Flatness factors of .4 to .6 and -.4 to -.6 were found in the outer layers of these wakes with a linear variation from positive to negative in the inner layer. This same trend in the inner layer is exhibited in the near wake data shown in Figure 79 for the rotor wake.

Spacial errors exist in measuring the stress correlations (discussed in Section 5.3.8) used to calculate the flatness factors shown in Figure

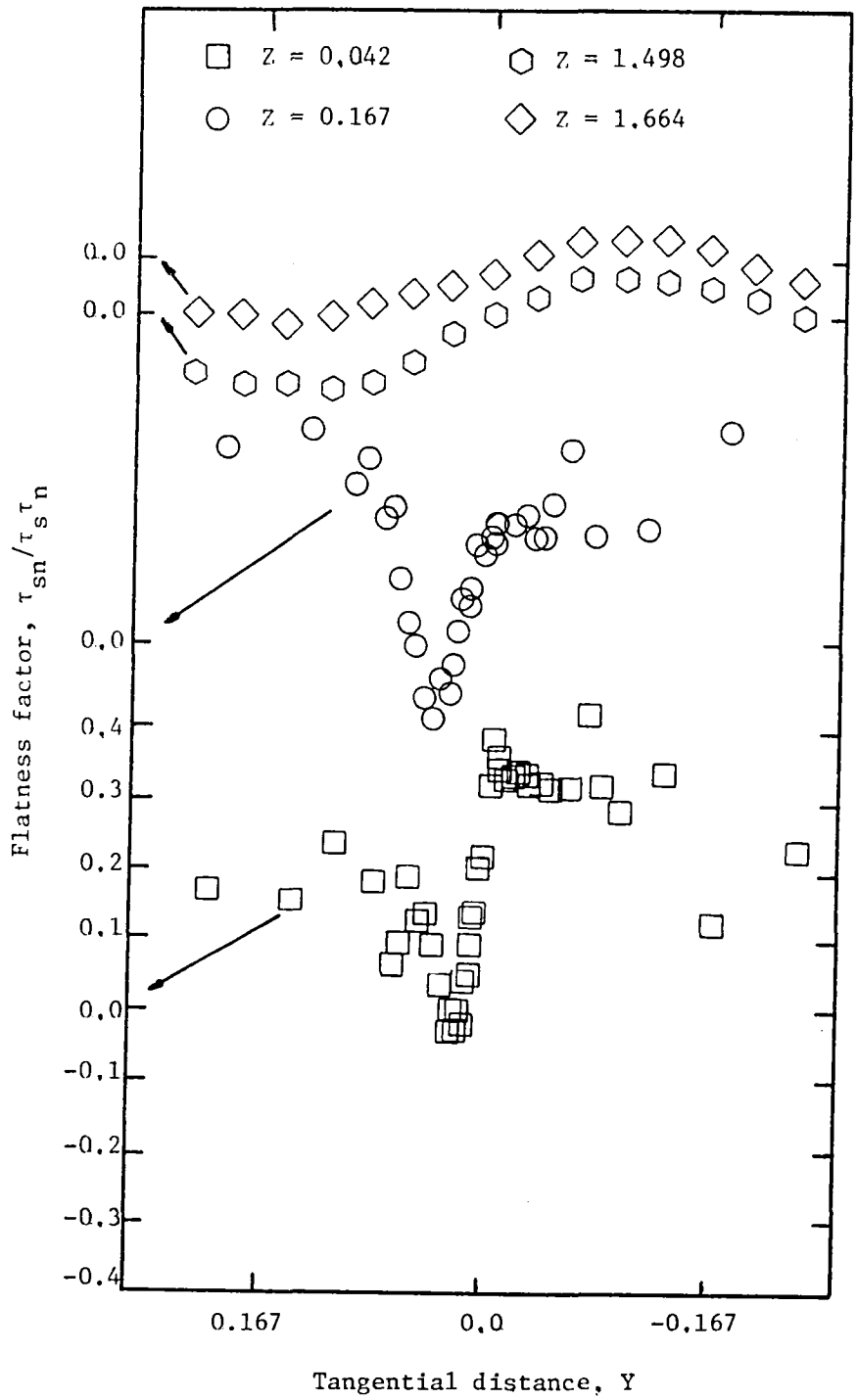

Figure 79. Flatness factor variation across the rotor wake for i = 10° and R = .721

79. However, the data does indicate that flatness factor variations in the rotor wake can be expected to be quite different than those found for two-dimensional shear flows.

5.10.2 Turbulence energy spectrum

5.10.2.1 Rotating probe spectra

Turbulent energy spectra taken with the spectrum analyzer are shown in Figures 80 and 81 for measurements made in the rotating frame of reference at mid-radius (R = .721) for a rotor blade incidence of 10°. For the data shown in Figure 80 the rotating tri-axial probe was located approximately at the wake centerline. The probe was located in the free stream for the energy spectrum shown in Figure 81. The fluctuating voltages e_1, e_2, and e_3 represent measurements from the tri-axial probe hot wires 1, 2, and 3, respectively.

In the near wake region (Z = .021) for the wake center measurements shown in Figure 80 the turbulent energy spectrum shows a cut off frequency of 4.0 KHz. The energy in the spectrum is defined as,

$$E_k \alpha f_K^{n_s} \quad . \tag{86}$$

The measurements for Z = .021 in Figure 80 seem to follow a $n_s = -7/3$ law from .3 KHz to 3.0 KHz. The eddy length in the above frequency range is approximately .26 cm to 2.6 cm. This eddy length size is of the order of that expected for the boundary layer thickness at the rotor blade trailing edge. The energy spectrum shown in the far wake seems to follow a $n_s = -5/3$ law in the frequency range from .1 KHz to 2.0 KHz. The -5/3 law is characteristic of isotropic turbulence. Here, the eddy size is .80 cm to 16.0 cm. While the smallest eddy size is similar in the near and far regions, the turbulence has become isotropic in the far wake.

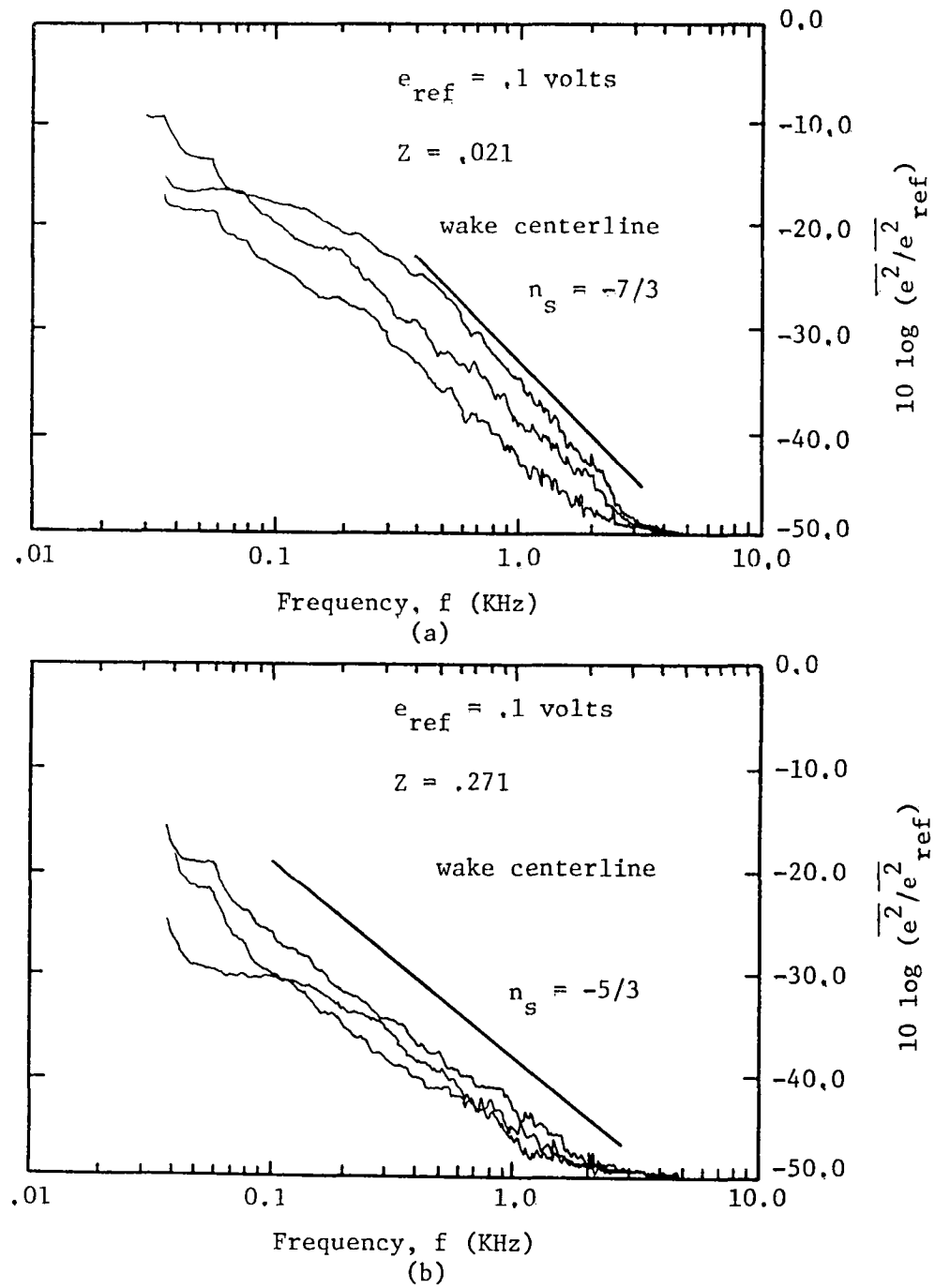

Figure 80. Turbulent energy spectra in the rotating frame of references at the wake centerline for Z = .021 and Z = .271 at i = 10°, R = .721

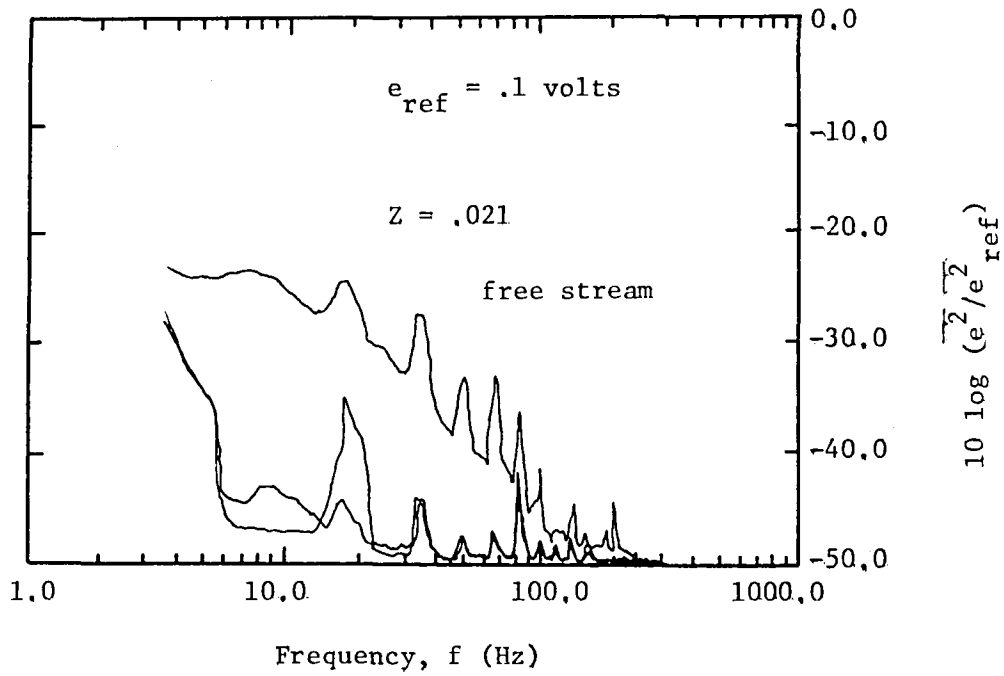

Figure 81, Turbulent energy spectrum in the rotating frame of reference in the free stream for Z = ,021 at i = 10°, R = ,721

A typical free stream turbulent energy spectrum measured by the tri-axial probe is shown in Figure 81 for R = .721, Z = .021 at the 10° incidence operating condition. The effect of the strut wakes on the free stream energy spectrum is clearly seen in Figure 81. Since the two upstream struts were located immediately next to each other, the energy spectrum shows distinct peaks at the blade passing frequency and its harmonics for one upstream disturbance. This characteristic is not evident beyond a frequency of 400 Hz. Since all energy in the free stream is found at low frequencies long eddies (approximately 7.0 cm) are characteristic for the turbulence in this region.

5.10.2.2 Stationary probe spectra

Turbulent energy spectra in the stationary frame of reference at mid-radius (R = .721) for Z = .206 at the 5° and 10° operating conditions are shown in Figure 82. Measurements are shown in Figure 83 at the far downstream station for Z = 1.498 at i = 5° and 10°, R = .721. As expected, distinct peaks are found at the rotor blade passing frequency and its harmonics for measurements at both Z = .206 and Z = 1.498. For the turbulent energy spectra at Z = .206, the blade passing harmonics disappear after the ninth harmonic for 5° and 10° incidences. At the far downstream station (Z = 1.498) the turbulent energy spectra in Figure 83 show no harmonics past the fourth harmonic. The energy within the peaks is representative of that contained in the periodic unsteadiness of mean velocity in the rotor wake in the stationary frame of reference. The disappearance of the fifth through ninth harmonics indicates the decay of steep tangential gradients of total mean velocity between Z = .206 (near wake) and Z = 1.498 (far wake).

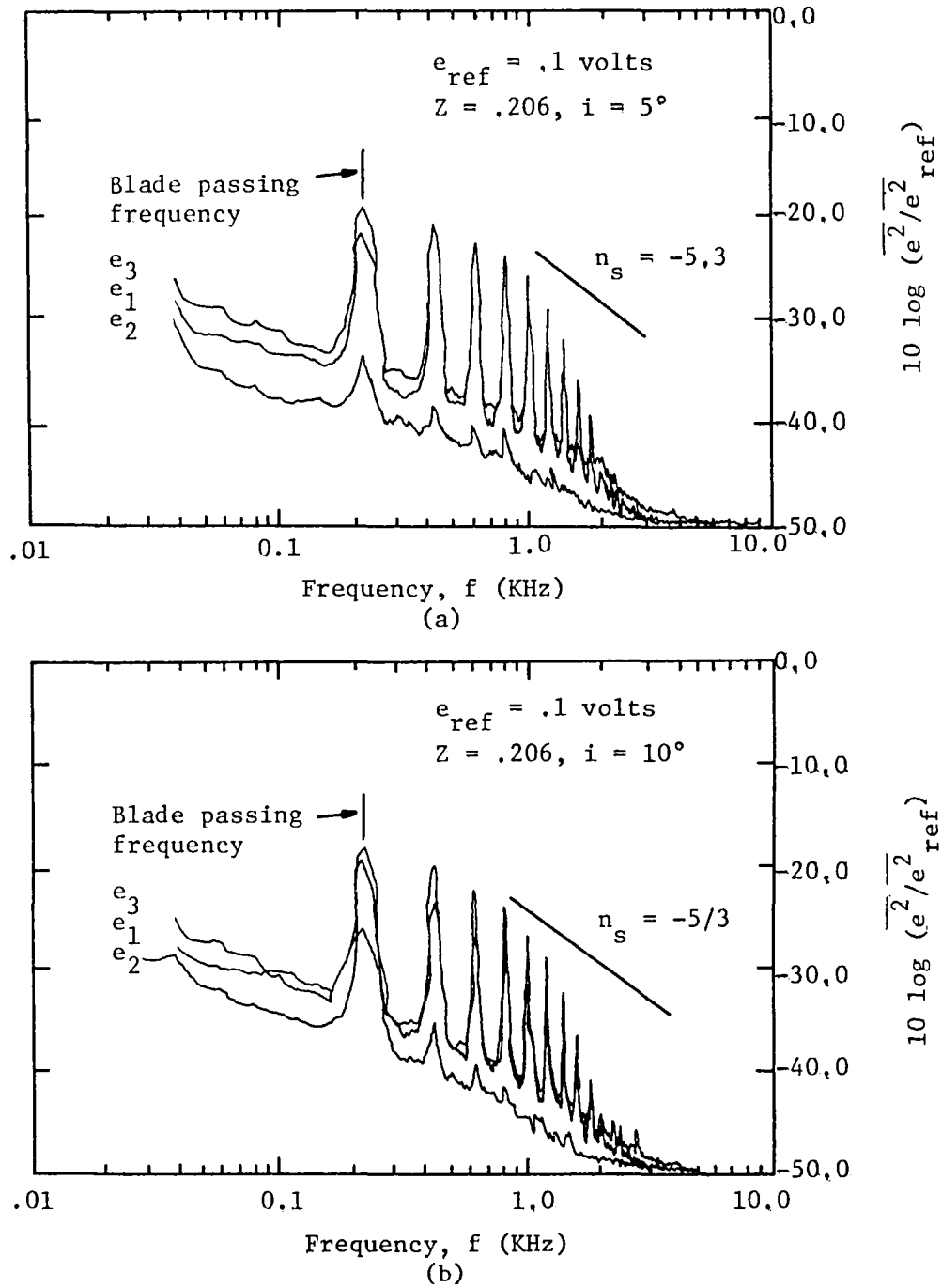

Figure 82. Turbulence energy spectra in the stationary frame of reference for Z = .206 at i = 5° and 10°, R = .721

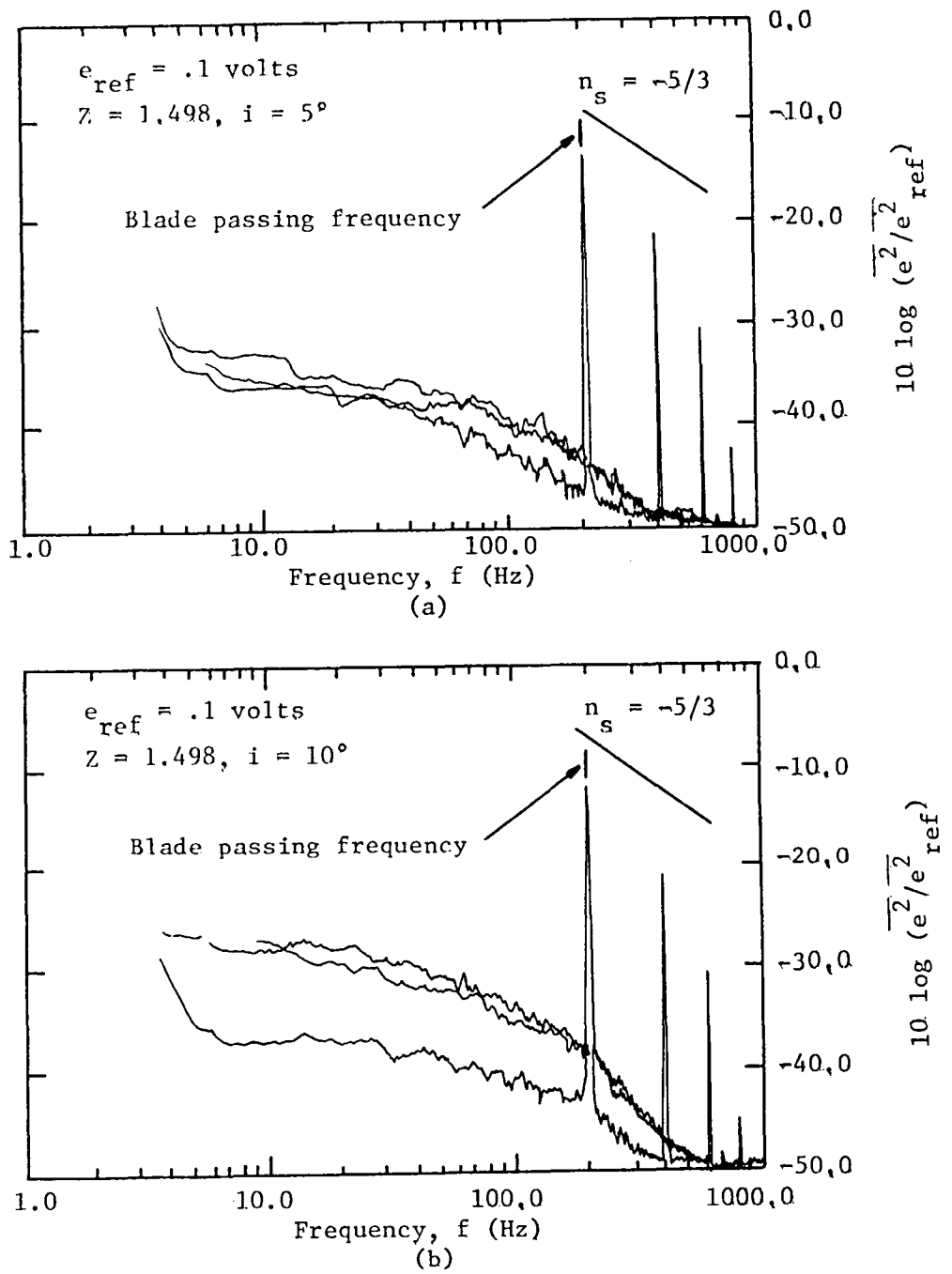

Figure 83. Turbulence energy spectra in the stationary frame of reference for Z = 1.498 at i = 5° and 10°, R = .721

As shown in Figure 82, the passage averaged turbulent energy spectra behind the rotor seem to follow the $n_s = -5/3$ law for Z = .206 between 1.0 KHz and 3.0 KHz. Here, the isotropic structure of turbulence is exhibited for eddy sizes of approximately .5 cm to 1.5 cm. The $n_s = -5/3$ law is shown in Figure 83 at Z = 1.498 in the frequency range from 200 HZ to 600 HZ. The eddy length in this range is 3.55 cm to 10.7 cm. The smallest eddy size in the rotor wake is shown to have increased by an order of magnitude between Z = .206 and Z = 1.498 for both 5° and 10° rotor blade incidences. The smaller eddies in the near wake dissipate or become elongated as the rotor wake decays in the far wake region.

Chapter 6

CONCLUSIONS

The characteristics of a rotor blade wake has been investigated both experimentally and theoretically. The rotating tri-axial probe measurements reported in this investigation represent the first systematic data in the near wake region of the rotor wake using this technique. The rotating tri-axial probe technique is shown to have small inherent errors in the near and far wake regions and to accurately measure the complex, three-dimensional nature of the rotor wake. The stationary tri-axial probe technique is shown to have small inherent errors in the far wake measurements. The momentum integral technique is shown to give a solution of the rotor wake which accurately predicts the nature of the three-dimensional flow phenomena in the far wake region.

The major conclusions derived on the basis of this investigation are:

1. The axial and tangential components of mean velocity profiles in the rotor wake are found to be highly asymmetric about the wake centerline. This characteristic is shown to be more pronounced for increased blade loading.
2. Large radial mean velocities in the rotor wake in the near wake region indicate a large radial migration of mass, momentum, and energy. This radial flow alters the rotor wake properties when compared to a corresponding two-dimensional wake.
3. Axial, tangential, and radial components of turbulence intensity were found to be highly asymmetric about the wake centerline.

4. The dominant stress vector in the rotor wake is found to deviate substantially from the streamwise direction with radial and streamwise Reynolds stresses of the same order.
5. Appreciable static pressure variations across the rotor wake exist in the near wake region. The distribution of static pressure across the wake is found to be very complex.
6. The axial and tangential velocity defects and maximum radial velocity in the rotor wake are found to decay very rapidly in the trailing edge region. These rates are substantially reduced in the near wake region.
7. The tangential mean velocity defect is found to decay slower than the axial component in the trailing edge region. In the near and far wake regions the tangential mean velocity defect decays more rapidly than the axial component.
8. The total mean velocity defect (resultant relative velocity) is shown to decay faster in the trailing edge region than that for an isolated airfoil wake. In the near wake region the decay rate was similar for the isolated airfoil and rotor wakes.
9. The maximum axial, tangential, and radial turbulence intensities in the rotor wake decay rapidly in the trailing edge and near wake region.
10. The radial component of turbulence intensity in the near wake region are found to be larger than the axial or tangential components.

11. The increase of wake width in the rotor wake shows a very unconventional behavior in the near wake region. The presence of an almost constant wake width region for increasing z shows the effects of three-dimensionality on the rotor wake flow.

12. Wake width in the far wake region is found to increase at a rate approximately given by $\sqrt{s/c}$. In this region the wake width is shown to increase for increased blade loading.

13. Momentum thickness is shown to decrease for increasing axial distance in the near wake region. This characteristic is attributed to the static pressure variations across the wake. Momentum thickness reaches an almost constant value in the far wake region.

14. Increased blade loading slows the decay rates of axial and tangential mean velocity defects. The maximum radial velocities in the wake are also found to increase for increased blade loading.

15. Increased blade loading increases the maximum axial, tangential, and radial turbulence intensities in the wake.

16. A larger wake width for the rotor wake is found for increased blade loading.

17. The momentum thickness for the rotor wake increases for increased blade loading.

18. The longitudinal radius of curvature of the rotor wake centerline in the near wake region is very large. The radius of curvature is shown to decrease for increased radius.

19. Similarity exists for axial and tangential components of mean velocity in the rotor wake. The similarity profiles for both components follow a Gaussian distribution ($e^{-0.693\eta^2}$).

20. Similarity was found in the outer layer of the rotor wake for axial, tangential, and radial components of turbulence intensity. The similarity profiles show a Gaussian distribution.

21. The resultant relative velocity defect in the rotor wake showed a good correlation with $c_d^{1/4}$ in the near and far wake regions.

22. The decay of axial and tangential components of mean velocity defects is slower near the hub and end wall regions as compared to that found at mid-radius.

23. The maximum radial velocity in the rotor wake shows a substantial increase for increasing radius above mid-radius.

24. All components of maximum and free stream turbulence intensities increases towards the hub and end walls.

25. Wake width is found to increase for increasing radial position above mid-radius. This characteristic may result from the large radial transport of mass, momentum, and energy in the rotor wake.

26. The momentum thickness for the rotor wake increases for increasing radius above mid-radius. This characteristic is more pronounced for increased blade loading.

27. The variation of flatness factor across the rotor wake in the near wake region shows a non-isotropic and complex structure of turbulence.

28. From turbulent energy spectrum measurements made in the rotating frame of reference, the structure of turbulence in the wake is found to be isotropic in the far wake region following a $n_s = -5/3$ law (Equation (86)). The turbulence followed a $n_s = -7/3$ law in the near wake region.

29. A higher harmonic content of the rotor wake exists in the near wake region as compared to that found in the far wake region.

30. The passage averaged turbulence followed a $n_s = -5/3$ law in the near and far wake regions.

APPENDIX

Since static pressure variations across the rotor wake have been experimentally measured (reported in Section 5.3.4) a study of the mechanisms that control this characteristic was undertaken. Static pressure variations across the rotor wake are studied below using the n momentum equation (s, n being the streamwise and principle normal directions, respectively) given by Raj and Lakshminarayana (1975),

$$U_r \frac{\partial U_n}{\partial r} + U_n \frac{\partial U_n}{\partial n} + U_s \frac{\partial U_n}{\partial s} + 2\Omega U_r \cos\beta - \frac{U_s^2}{R_c} + \frac{U_r U_n}{r} \cos^2\beta$$

$$= -\frac{1}{\rho}\frac{\partial p^*}{\partial n} - \{\frac{\partial}{\partial r}(\overline{u'_r u'_n}) + (1 + \cos^2\beta)\frac{\overline{u'_r u'_n}}{r} + \frac{\partial}{\partial n}\overline{u'^2_n} + \frac{\partial}{\partial s}(\overline{u'_n u'_s}) \quad (87)$$

where

$$p^* = P - \frac{1}{2}\rho\Omega^2 r^2 \quad . \quad (88)$$

Non-dimensionalizing Equation (87) with δ and U_{s_o} and neglecting shear stress terms, one derives the following equation,

$$\frac{U_r}{U_{s_o}} \frac{\delta(U_n/U_{s_o})}{\delta(r/\delta)} + \frac{U_n}{U_{s_o}} \frac{\delta(U_n/U_{s_o})}{\delta(n/\delta)} + \frac{U_s}{U_{s_o}} \frac{\delta(U_n/U_{s_o})}{\delta(s/\delta)} + \frac{2(\Omega r)U_r \cos\beta}{U_{s_o}^2 r}$$

$$+ \frac{U_r U_n}{U_{s_o}^2 (r/\delta)} \cos^2\beta - \frac{U_s^2/U_{s_o}^2}{R_c/\delta} = -\frac{1}{\rho}\frac{\partial p^*}{\partial(n/\delta)}\frac{1}{U_{s_o}^2} - \frac{\partial(u'^2_n/U_{s_o}^2)}{\partial(n/\delta)} \quad . \quad (89)$$

An order of magnitude analysis is perfomed on Equation (89) using the following assumptions where $\varepsilon << 1$:

$$n \sim \varepsilon \qquad U_n/U_{s_o} \sim \varepsilon$$

$$s \sim \delta \qquad U_r/U_{s_o} \sim 1$$

$$\delta/r \sim \varepsilon \qquad \overline{u'^2_n}/U_{s_o}^2 \sim \varepsilon$$

$$\Omega r/U_{s_o} \sim 1 \qquad R_c \sim S$$

$$U_s/U_{s_o} \sim 1 \qquad \delta/S \sim \varepsilon \quad .$$

The above assumptions are valid in the near wake region where the pressure gradient in the rotor wake is formed. The radius of curvature, R_c, is chosen to be of the order of blade spacing on the basis of the measured wake center locations shown in Figure 56.

The order of magnitude analysis is used to give the following expressions:

$$\frac{U_r}{U_{s_o}} \frac{\partial(U_n/U_{s_o})}{\partial(r/\delta)} \sim \varepsilon^2 \quad , \tag{90}$$

$$\frac{U_n}{U_{s_o}} \frac{\partial(U_n/U_{s_o})}{\partial(n/\delta)} \sim \varepsilon^2 \quad , \tag{91}$$

$$\frac{U_s}{U_{s_o}} \frac{\partial(U_n/U_{s_o})}{\partial(s/\delta)} \sim \varepsilon \quad , \tag{92}$$

$$\frac{2\delta(\Omega r)U_r \cos\beta}{U_{s_o}^2 r} \sim \varepsilon \quad , \tag{93}$$

$$\frac{U_r U_n}{U_{s_o}^2(r/\delta)} \cos^2\beta \sim \varepsilon^2 \quad , \tag{94}$$

$$\frac{U_s^2/U_{s_o}^2}{R_c/\delta} \sim \varepsilon \quad , \tag{95}$$

and

$$\frac{\partial(\overline{u_n'^2}/U_{s_o}^2)}{\partial(n/\delta)} \sim \varepsilon \quad . \tag{96}$$

Retaining terms that are of order ε in Equation (89) one gets,

$$\frac{U_s}{U_{s_o}} \frac{\partial(U_n/U_{s_o})}{\partial s} + \frac{2(\Omega r)U_r\cos\beta}{U_{s_o}^2 r} - \frac{U_s^2/U_{s_o}^2}{R_c} = -\frac{1}{\partial n}\frac{\partial p^*}{\partial n}\frac{1}{U_{s_o}^2} - \frac{\partial(\overline{u_n'^2}/U_{s_o}^2)}{\partial n} \quad . \tag{97}$$

The first term in Equation (97) can be written as,

$$\frac{U_s}{U_{s_o}} \frac{\partial(U_n/U_{s_o})}{\partial s} = \frac{U_s}{U_{s_o}} \frac{\partial[(U_n/U_s)(U_s/U_{s_o})]}{\partial s} \quad . \tag{98}$$

Since one knows that,

$$U_n/U_s = \tan \alpha \tag{99}$$

where α is the relative streamline angle, Equation (98) can be written as,

$$\frac{U_s}{U_{s_o}} \frac{\partial(U_n/U_{s_o})}{\partial s} = \frac{U_s}{U_{s_o}}\left[\frac{U_s}{U_{s_o}} \sec^2 \alpha \frac{\partial \alpha}{\partial s} + \tan \alpha \frac{\partial(U_s/U_{s_o})}{\partial s}\right] . \tag{100}$$

Since,

$$\frac{\partial \alpha}{\partial s} = \frac{1}{R_c} \tag{101}$$

and with α small,

$$\sec^2 \alpha \stackrel{\sim}{=} 1 \tag{102}$$

$$\tan \alpha \sim \alpha . \tag{103}$$

Equation (100) can be written as,

$$\frac{U_s}{U_{s_o}} \frac{\partial(U_n/U_{s_o})}{\partial s} = \frac{U_s^2}{U_{s_o}^2} \frac{1}{R_c} + \alpha \frac{U_s}{U_{s_o}} \frac{\partial(U_s/U_{s_o})}{\partial s} . \tag{104}$$

Substituting Equation (104) and (88) into Equation (97) one gets,

$$\alpha \frac{U_s}{U_{s_o}} \frac{\partial(U_s/U_{s_o})}{\partial s} + \frac{2(\Omega r)U_r \cos\beta}{U_{s_o}^2 r} = -\frac{1}{\rho} \frac{\partial p}{\partial n} \frac{1}{U_{s_o}^2} - \frac{\partial(\overline{u_n'^2}/U_{s_o}^2)}{\partial n} . \tag{105}$$

From the measured curvature of the rotor wake centerline shown in Figure 56, the radius of curvature is assumed to be very large. Thus, the streamline angle, α, is very small and Equation (105) can be written as,

$$-\frac{1}{\rho} \frac{\partial p}{\partial n} \frac{1}{U_{s_o}^2} = \frac{2(\Omega r)U_r \cos\beta}{U_{s_o}^2 r} - \frac{\partial(\overline{u_n'^2}/U_{s_o}^2)}{\partial n} . \tag{106}$$

Equation (106) indicates that static pressure variations in the rotor wake are controlled by Coriolis force effects and turbulence intensity. Figure 84 shows the static pressure variations across the wake as given

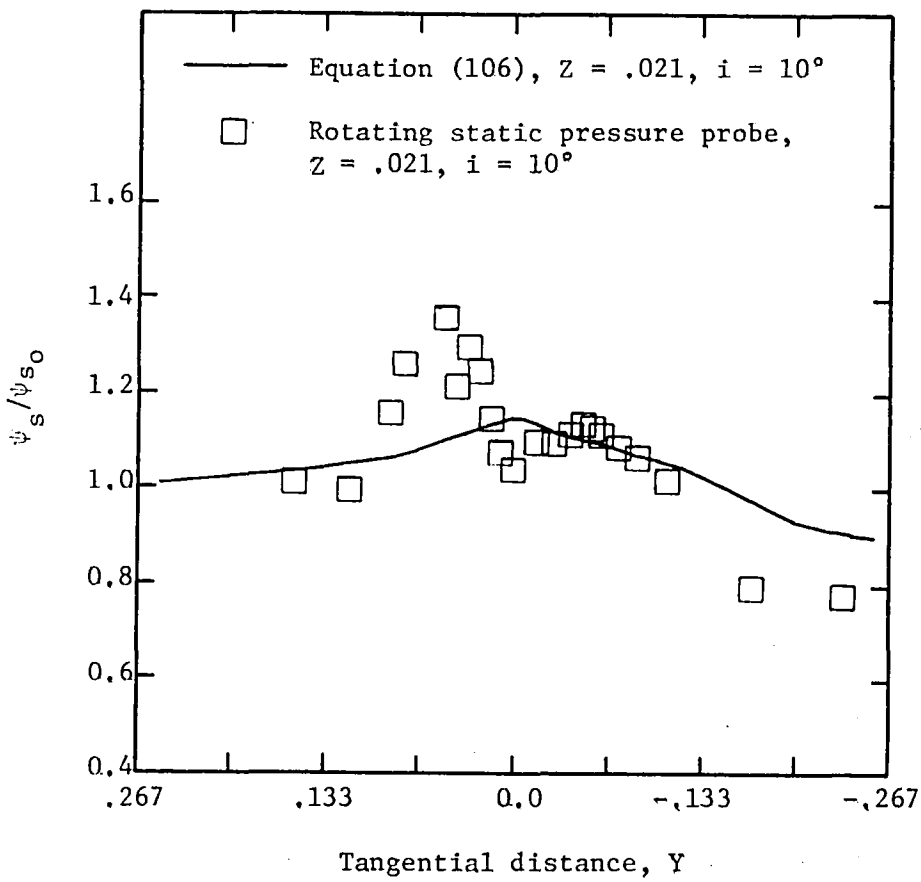

Figure 84. Static pressure in the rotor wake as given by Equation (106)

by Equation (106) compared to that which has been experimentally measured. The comparison is shown for static pressure variations in the near wake region at Z = .021, R = .721 for the 10° incidence operating condition. The effects of Coriolis force and turbulence intensity on static pressure in the wake are shown to correctly model some of the characteristics that had been experimentally measured. While the complex distribution of static pressure across the wake is not modeled, the turbulence intensity and Coriolis force effects in Equation (106) do account for some of the measured variations across the wake. It should be noted that the static pressure distribution across the rotor wake as given by Equation (106) is not presented as a prediction scheme. It is used only as a means to determine what mechanisms control the static pressure distribution in the wake.

REFERENCES

Bennett, J. C., "Measurements of Periodic Flow in Rotating Machinery," AIAA Paper No. 77-713, 1977.

Bruce, E. P., "The ARL Axial Flow Research Fan--A New Facility for Investigation of Time-Dependent Turbomachinery Flows," ASME Paper No. 74-FE-27, 1974.

Chen, L. and McCune, J., "Comparison of Three-Dimensional Quasi-Linear Large Swirl Theory with Measured Outflow from a High-Work Compressor Rotor," MIT-GTL Report No. 128, 1975.

Chevray, R. and Kovasznay, S. G., "Turbulence Measurements in the Wake of a Thin Flat Plate," AIAA Journal, Vol. 7, 1969.

Ermshaus, R., "Typical Features of Turbulent Wake Flows," Max Planck Inst., No. 46 (translated by Johns Hopkins Applied Physics Laboratory, CLR-3 T-650), 1970.

Evans, R. L., "Turbulence and Unsteadiness Measurement Downstream of a Moving Blade Row," Journal of Engineering for Power, Vol. 97, 1975, pp. 131-139.

Gallus, H. E., Private communication, 1977.

Goldstein, S., "On the Two-Dimensional Steady Flow of a Viscous Fluid Behind a Solid Body," Appendix by A. Fage, Proc. Royal Soc., Vol. 142, 1953.

Gorton, C. A. and Lakshminarayana, B., "A Method of Measuring the Three-Dimensional Mean Flow and Turbulence Quantities Inside a Rotating Turbo-Machinery Passage," Journal of Engineering for Power, Vol. 98, No. 2, 1976, pp. 137-146.

Hah, C. and Lakshminarayana, B., "Effect of Rotation on a Rotating Hot Wire," to be published in Journal of Physics E., Scientific Instruments, 1978.

Hah, C., Private communication, 1978.

Klein, A., "Comparative Measurements Behind a Compressor Rotor with a Space-Bound and Corotating Cylindrical Probes," Forschung im Ingenieurwesen, Vol. 40, No. 1, 1974, pp. 25-34.

Kool, P., DeRuyck, J., and Hirsch, C. H., "The Three-Dimensional Flow and Blade Wake in an Axial Plane Downstream of an Axial Compressor Rotor," ASME Paper No. 78-GT-66, 1978.

Lakshminarayana, B. and Poncet, A., "A Method of Measuring Three-Dimensional Rotating Wakes Behind Turbomachinery Rotors," Journal of Fluids Engineering, Vol. 96, No. 4, 1974, pp. 87-91.

Lakshminarayana, B., "The Nature of Flow Distortion Caused by Rotor Blade Wakes," AGARD CP 177, 1976.

Lieblein, S. and Roudebush, W. H., "Low-Speed Wake Characteristics of Two-Dimensional Cascade and Isolated Airfoil Sections," NACA TN 3771, 1956.

Mendelsohn, R. A., "Wind Tunnel Investigation of the Boundary Layer and Wake and Their Relation to Airfoil Characteristics--NACA 65,012 Airfoil with a True Contour Flap and a Beveled Trailing Edge Flap," NACA TN No. 1304, 1947.

Meusmann, G., "Zusammenhang der Strömungseigenschaften des Laufrades eines Axialgebläses mit denen eines Einzelflügels," Zeitschrift Für Flugwissenschaften, 6. Jahrgang, Heft 12, Dez. 1958.

Muhlemann, E., "Experimentelle Untersuchungen an einer axialen Gebläsestufe, Mitteilungen Aus Dem Institut Fur Aerodynamik, No. 12, 1946.

Pollard, D. and Gostelow, J. P., "Some Experiments at Low Speed on Compressor Cascades," Journal of Engineering for Power, Trans. ASME, July 1967, pp. 427-436.

Pratte, B. D. and Keffer, J. F., "The Swirling Turbulent Jet," Journal of Basic Engineering, Vol. 94, No. 4, 1972, pp. 739-748.

Preston, J. H., Sweeting, N. E., and Cox, D. K., "The Experimental Determination of the Boundary Layer and Wake Characteristics of a Piercy 1240 Aerofoil, with Particular Reference to the Trailing Edge Region," Gr. Brit. Aero. Res. Council, R and M, No. 2013, 1945.

Preston, J. H. and Sweeting, N. E., "The Experimental Determination of the Boundary Layer and Wake Characteristics of a Simple Joukowski Aerofoil, with Particular Reference to the Trailing Edge Region," Gr. Brit. Aero. Res. Council, R and M, No. 1998, 1943.

Raj, R., "On the Investigation of Cascade and Turbomachinery Rotor Wake Characteristics," Ph.D. thesis, Department of Aerospace Engineering, The Pennsylvania State University, November 1974.

Raj, R. and Lakshminarayana, B., "Characteristics of the Wake Behind a Cascade of Airfoils," Journal of Fluid Mechanics, Vol. 61, Pt. 4, 1973, pp. 707-730.

Raj, R. and Lakshminarayana, B., "On the Investigation of Cascade and Turbomachinery Rotor Wake Characteristics," NASA CR 134680, 1975.

Raj, R. and Lakshminarayana, B., "Three-Dimensional Characteristics of Turbulent Wakes Behind Rotors of Axial Flow Turbomachinery," Journal of Engineering for Power, Vol. 98, April 1976, pp. 218-228.

Ravindranath, A., "The Wake Characteristics of a Heavily Loaded Compressor Rotor," M.S. Thesis, Department of Aerospace Engineering, The Pennsylvania State University, to be submitted November 1978.

Reynolds, B., Lakshminarayana, B., and Ravindranath, A., "Characteristics of the Near Wake of a Compressor Rotor," AIAA Paper No. 78-1141, 1978.

Schmidt, D. P. and Okiishi, T. H., "Multistage Axial Flow Turbomachine Wake Production, Transport and Interaction," AIAA Journal, Vol. 15, 1977, p. 1138.

Schlichting, H., Boundary Layer Theory, McGraw-Hill, Inc., 1968, pp. 685-686.

Silverstein, A., Katzoff, S., and Bullivant, W. K., "Downwash and Wake Behind Plain Airfoils," NACA Report No. 651, 1939a.

Silverstein, A. and Katzoff, S., "Design Charts for Predicting Downwash Angles and Wake Characteristics Behind Plain and Flapped Wings," NACA Report No. 648, 1939b.

Speidel, L. and Scholz, "Untersuchungen über die Strömungsverluste in ebenen Schaufelgittern," VDI-Forschungsheft No. 464, 1957.

Spence, D. A., "Growth of the Turbulent Wake Close Behind an Aerofoil at Incidence," A.R.C. Technical Report, C.P. No. 125, 1952.

Thompkins, W. T. and Kerrebrock, J. L., "Exit Flow from a Transonic Compressor Rotor," AGARD, CP 177, 1975, p. 6-1.

Ufer, H., "Analysis of the Velocity Distribution at the Blade Tips of Axial-Flow Compressors," Technische Mitteilungen Krupp (Forschung Sberichte), Vol. 26, No. 2, 1968, pp. 33-45.

Wagner, J. H., Okiishi, T. H., and Holbrook, G. J., "Periodically Unsteady Flow in an Imbedded Stage of a Multistage, Axial-Flow Turbomachine," ASME Paper No. 78-GT-6, 1978.

Whitfield, C., Kelly, J, and Barry, B., "A Three-Dimensional Analysis of Rotor Wakes," Aeronautical Quarterly, Nov. 1972.

Yocum, A. M., "The Effects of Design and Operating Variables on the Response of an Axial Flow Fan to Inlet Flow Distortions," M.S. Thesis, Department of Mechanical Engineering, The Pennsylvania State University, August 1978.

1. Report No.	2. Government Accession No.	3. Recipient's Catalog No.
NASA CR-3188		

4. Title and Subtitle	5. Report Date
CHARACTERISTICS OF LIGHTLY LOADED FAN ROTOR BLADE WAKES	October 1979
	6. Performing Organization Code

7. Author(s)	8. Performing Organization Report No.
B. Reynolds and B. Lakshminarayana	PSU/TURBO R 78-4
	10. Work Unit No.

9. Performing Organization Name and Address	11. Contract or Grant No.
The Pennsylvania State University 233 Hammond Building University Park, PA 16802	NSG 3012
	13. Type of Report and Period Covered
12. Sponsoring Agency Name and Address	Contractor Report
National Aeronautics and Space Administration Washington, D.C. 20546	14. Sponsoring Agency Code

15. Supplementary Notes

Final report. Project Manager, Marcus F. Heidmann, V/STOL and Noise Division, NASA Lewis Research Center, Cleveland, Ohio 44135.

16. Abstract

The highly three-dimensional flow characteristics of a rotor or fan wake have been investigated both theoretically and experimentally. The research presented in this report is confined to a study of a low subsonic and incompressible wake flow downstream of a lightly loaded rotor. Theoretically, the equations of motion were solved using the momentum integral technique in the far wake region. An analytical solution for the three components of mean velocity and wake width is derived from the momentum integral equations using suitable approximations. This analysis showed good agreement with experimental results in the far wake region and correctly predicted the effects of varying blade loading on the overall properties of the rotor wake. The experimental investigation included measurements of mean velocity, turbulence intensity, Reynolds stress, and static pressure variations across the rotor wake at various axial and radial locations. Wakes were measured at various rotor blade incidences to discern the effect of blade loading on the rotor wake. Mean velocity and turbulence measurements were carried out with a tri-axial hot wire probe both rotating with the rotor and stationary behind the rotor. The rotating tri-axial probe measurements reported in this investigation represent the first systematic data in the near wake region of a rotor wake using this technique. Static pressure measurements across the rotor wake were made with a conventional static pressure probe rotating with the rotor. Radial, tangential, and axial components of mean velocities and turbulence intensities were found to decay very rapidly near the rotor blade trailing edge. Increased blade loading was shown to slow the decay rates of axial and tangential mean velocity defects and radial velocities in the wake. The presence of large radial velocities in the rotor wake indicated the extent of the interactions between one radius and another. Similarity in the profile shape was found for the axial and tangential components of mean velocity and in the outer layer for axial, tangential, and radial turbulence intensities. Appreciable static pressure variations across the rotor wake were found in the near wake region.

17. Key Words (Suggested by Author(s))	18. Distribution Statement
Turbomachinery Rotating blade wakes Axial flow fan	Unclassified - unlimited STAR Category 02

19. Security Classif. (of this report)	20. Security Classif. (of this page)	21. No. of Pages	22. Price*
Unclassified	Unclassified	191	A09

* For sale by the National Technical Information Service, Springfield, Virginia 22161

NASA-Langley, 1979

National Aeronautics and
Space Administration

Washington, D.C.
20546

Official Business
Penalty for Private Use, $300

THIRD-CLASS BULK RATE

Postage and Fees Paid
National Aeronautics and
Space Administration
NASA-451

POSTMASTER: If Undeliverable (Section 158
Postal Manual) Do Not Return